PEOPLE'S DEMOCRATIC REPUBLIC OF ALGERIA
MINISTRY OF HIGHER EDUCATION
AND SCIENTIFIC RESEARCH
UNIVERSITY OF SAAD DAHLEB BLIDA 1
INSTITUTE OF AERONAUTICS AND SPACE STUDIES
Department of space studies

END OF STUDIES' PROJECT

In view of obtaining the MASTER Diploma in Aeronautics
Option: Space propulsion

Influence of chemical kinetic model in hypersonic thermochemical non-equilibrium and ionized flow around lifting bodies DURING ATMOSPHERIC REENTRY

Made by:

- **SELAMI ABDERAHMANE**
- **DAOUD LYES**

Led by:

Supervisor: ALLOUCHE Rachid

Supervisor: RENANE Rachid

2021 / 2022

Abstract

As a part of the non-equilibrium phenomena which occur behind a strong shock wave, In general, these phenomena observed at hypersonic velocities, we present in this work the vibrational relaxation and the dissociation of the air mixture in a high temperature. Particularly, we interest to the simulation of the flow in the shock layer where the intense thermochemical non-equilibrium phenomena occur, The Park and Zeldovich chemical-kinetic models involves eleven species, N2, O2, NO, N, O, NO^+, $N2^+$,$O2^+$, N^+, O^+, e^- of a kinetic mechanism of 5, 17, 21, 31 reactions is applied. in order to achieve this, we have simulated a two-dimensional and three-dimensional viscous air flow in a chemical non-equilibrium with taking into account the turbulence models using ANSYS Fluent 19 around the Lobb's sphere, Cone flare, conical Circular body and Capsule fire II. Then we investigated the trajectory of shuttle re-entry. The results obtained present a good agreement with the scientific literature.

Keywords: Hypersonic flow, shock wave, dissociation, Euler equations, Navier-Stokes equations, turbulence.

Résumé

Dans le cadre des phénomènes de non-équilibre qui se produisent derrière une forte onde de choc, En général, ces phénomènes observés à des vitesses hypersoniques, nous présentons dans ce travail la relaxation vibrationnelle et la dissociation du mélange d'air à haute température. En particulier, nous nous intéressons à la simulation de l'écoulement dans la couche de choc où se produisent les phénomènes thermochimiques intenses de non-équilibre. Les modèles chimico-cinétique de Park et Zeldovich impliquent onze espèces, N2, O2, NO, N, O, NO+, N2+,O2+, N+, O+, e- d'un mécanisme cinétique de 5, 17, 21, 31 réactions est appliqué. pour y parvenir, nous avons simulé un écoulement d'air visqueux bidimensionnel et tridimensionnel dans un non-équilibre chimique en tenant compte des modèles de turbulence à l'aide d'ANSYS Fluent 19 autour de la sphère de Lobb, Cône flair, conique Circulaire corps et Capsule fire II. Ensuite, nous avons étudié la trajectoire de rentrée de la navette. Les résultats obtenus présentent un bon accord avec la littérature scientifique.

Mots clés : Écoulement hypersonique, onde de choc, dissociation, équations d'Euler, équations de Navier-Stokes, turbulence.

ملخص

كجزء من ظاهرة عدم التوازن التي تحدث خلف موجة صدمة قوية ، بشكل عام ، هذه الظواهر التي لوحظت بسرعات تفوق سرعة الصوت ، نقدم في هذا العمل الاسترخاء الاهتزازي وتفكك خليط الهواء في درجة حرارة عالية. على وجه الخصوص، نحن مهتمون بمحاكاة التدفق في طبقة الصدمة حيث تحدث ظواهر عدم التوازن الكيميائية الحرارية الشديدة، يشتمل النمرذج الكيميائي الحركي بارك و زيلدوفيتش على أحد عشر نوعًا: N2، O2، NO، N، O، NO +، N2 +، O2 + ، يتم تطبيق N +، O +، e- لآلية حركية للتفاعلات 5 ، 17 ، 21 ، 31. من أجل تحقيق ذلك، قمنا بمحاكاة تدفق هواء لزج ثنائي الأبعاد وثلاثي الأبعاد في حالة عدم توازن كيميائي مع مراعاة نماذج الاضطراب باستخدام ANSYS Fluent 19 حول كرة Lobb ، والتوهج المخروطي ، والجسم الدائري المخروطي والكبسولة النار II. ثم قمنا بالتحقيق في مسار عودة المكوك. النتائج التي تم الحصول عليها تتوافق بشكل جيد مع المؤلفات العلمية.

الكلمات المفتاحية: الجريان فوق الصوتي ، الموجة الصدمية ، التفكك ، معادلات أويلر ، معادلات نافيير-ستوكس ، الاضطراب.

Acknowledgment

We would like to thank God (Allah) the Almighty for having given us the favor of succeeding in our studies.

At first, we would like to thanks our advisors Mr. RENANE Rachid and Mr. ALLOUCHE Rachid, who were more than generous with their expertise and precious time. We are grateful for their valuable guidance and help throughout the execution of this work, they gave us the strength and knowledge to handle and complete this useful work.

Our sincere thanks to Ms ZMIT Oumaima for his technical support in simulation and the advice they gave us in the realization of this end of studies project.

We thank also all the teachers of the Institute of Aeronautics and Space Studies who contributed to our training and all our friends and of the promotion as well as all those who collaborated closely or remotely in the realization of this end of studies project.

Finally, we extend our heartfelt and sincere thanks to the members of the Jury who agreed to honor our work with their presence.

Dedications

To my dear parents who have always been there for me, and who have given me a magnificent model of hard work and perseverance.

To my sister Sabrina and brother Zakaria.

To my family.

To my friends

I dedicate this work.

SELAMI ABDERAHMANE

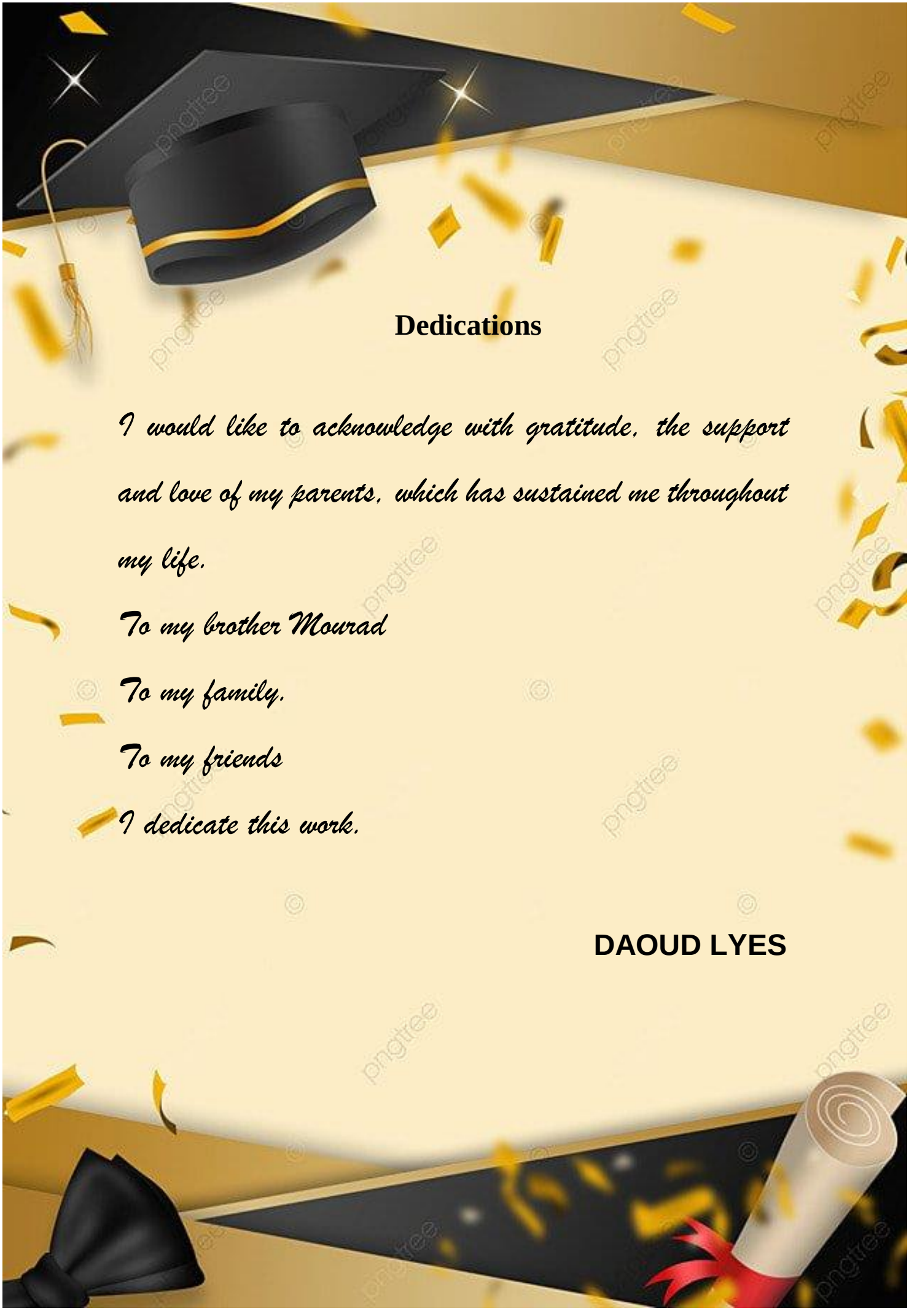

Dedications

I would like to acknowledge with gratitude, the support and love of my parents, which has sustained me throughout my life.

To my brother Mourad

To my family.

To my friends

I dedicate this work.

DAOUD LYES

Table of Contents

Summary

List of Figures:

List of tables :

Nomenclature:

α: Parameter of the Dirichlet distribution.

β: : Apex angle

***c*0:** Local sound velocity

***CV*:** Vibration-dissociation coupling..

***CVD*:** Vibration-dissociation-vibration coupling.

***C*:** Mass heat at constant pressure (J.kg-1.K-1).

***C*:** Mass heat at constant volume (J.kg-1.K-1).

: Constant pressure mass heat of the species (J.kg-1.K-1).

***Cvs*:** Mass heat at constant volume of the species (J.kg-1.K-1).

***C*v,s(rot):** Mass heat at constant volume of rotation of the species

***C*v,s(tr):** Mass heat with constant volume of translation of (J.kg-1.K-1).

***C*v,s(v):** Mass heat at constant volume of vibration of .(J.kg-1.K-1)

***D*:** Characteristic non-dimensional number of Damkölher

K: Number of events the pmf q

***l*0:** Chord

L: Characteristic length of the obstacle

M: Mach number

M*α*: The molar weight of the species α, respectively

θ^{vib}: Vibrational characteristic temperature

***Re*:** The Reynolds number

ρ: The density of the fluid

μ: Dynamic viscosity

,.: The Knudsen number

***τvi*:** The relaxation time of the vibrational mode

: Time required for a flow particle to move in the shock layer

***τch*:** Characteristic time for chemistry to occur

***u*0:** The local flow velocity

γ: Sweep angle

E: Total energy

e: Wing thickness.

Q~(*α*): Random pmf Q coming from a Dirichlet distribution with parameter α .

***qne*:** The net heat flux

$qradiativetransfer$**:** The heat flux radiative net

$qconvec-diffu$**:** The sum of the convective heat fluxes

$qconvectio$**:** The process of convection

$qdiffusio$**:** The process of diffusion

$\mathbf{R_u}$**:** The universal gas constant

Ttr: The translation temperature

T(vib): The vibrational temperature

Γ(s): The gamma function evaluated at s, for $s > 0$.

Γ(k,θ): Gamma distribution with parameters k and θ

v**:** Ith entry of the vector .

$v-$**:** The vector v with the i-th entry removed.

Xα: The mass

Introduction

Entry is the process by which a body coming from space encounters significant planet atmosphere along its trajectory, either descending from a planet orbit, or originating from eccentric hyperbolic orbits. Entry is one of the most intricate problems in the Aerospace field and involves complex dynamics and kinematics.

Re-entry The high Mach number flow around these vehicles is dominated by high-temperature thermo-chemical physics associated with molecular dissociation. ionization, skin friction between molecules engenders an important amount of heat which excites molecules in the air and release their vibrational energy and so the internal energy of these molecules **[1]**This high-temperature effect will influence the surface temperature and heat flux of the vehicle, which acts as a thermal load. Thus, the maximum temperature that a spacecraft experiences in its hypersonic flight exceed the limit temperature of any materiel due to the important drag and aerodynamic heating, so the reduction of heat transfer rate plays an important role. Accurate calculation of the heat load is therefore important when designing the flight trajectory. Although computational research in this field has expanded in recent times, further research on the combined effects of thermal non-equilibrium and chemical reactions using the latest computational techniques are needed to fully comprehend the flow physics in hypersonic non-equilibrium flows around re-entry vehicles and how to ensure better thermal protection of spacecraft with good flight quality.

In the other hand, the extent of the heat flux and heat load depends on the shape of the vehicle and its flight trajectory design (altitude, angle of attack). The need for a safer access to space dictates the review of operational capabilities and hence of design approach for manned reentry vehicles. Current systems such as the Space Shuttle, still fly at relatively low L/D (<1.5) but are reusable. Research has shown that reentry vehicle designs with high L/D could be designed to take advantage of aerodynamic lift during reentry **[2]**Higher L/D is desirable because it uses its ability of generating a significant lift force to dissipate energy in a controlled fashion during re-entry, being also capable of changing its trajectory to reach the landing site safely. So, a vehicle with high aerodynamic efficiency would have enhanced down-range and cross-range capability (more than twice that of the Space Shuttle). This leads to increase significantly the operational flexibility of re-entry rockets for use in deep space missions.

Earth's atmosphere presents a dense, fluid medium, which, at orbital velocities, is not all that different from a lake's surface. Re-entry vehicle must plan to hit the atmosphere at the precise angle and speed for a safe landing. If it hit too steeply or too fast, its risk making a big "splash," which would mean a fiery end. If its impact is too shallow, it may literally skip off the atmosphere and back into the cold of space. This subtle dance between fire and ice is the science of atmospheric re-entry. Thus, the goal of atmospheric re-entry is to put a space vehicle on the ground safely.

For this to happen several conditions must be met: the vehicle must sustain the intensive aero heating, the trajectory must ensure descent, aerodynamic load limits must not be exceeded, the vehicle must have minimal guidance capabilities to guarantee that the correct path is followed. Constraints are different depending on the type of vehicle, initial conditions, and if it is manned.

In this work, a study of the phenomena of thermochemical non-equilibrium in the shock layer and the reduction of aerodynamic heating.

First a description of the hypersonic re-entry flows and its characterization are presented briefly, followed by a relations presentation of RANKINE HUGONIOT allowing the parameters of the flow upstream to be linked to those downstream of a shock wave. Part of this chapter has been devoted to a bibliographical synthesis on heating reduction and aerodynamic drag techniques in hypersonic flows around lifting bodies with a brief prestation of our apport to the domain.

Secondly it would be interesting to treat, a mathematical and physical flow modulization of the reactive gas mixture in thermochemical non equilibruium in the general case.

In the third chapter, it was proposed to study a viscous two-dimensional hypersonic flow in thermochemical non-equilibrium around sphere blunt body. In the second part of this study, we explore the mission requirements: trajectory design and vehicle design of vehicles entering earth atmosphere with an application of blunt body, cone flare, conic body and capsule fire II to ward off the shock and reduce heating load rate. We consider what engineers must trade in designing missions that must plunge into dense atmospheres. In particular, this chapter focuses on the feasibility of using a numerical computational code for fluid dynamics to simulate such a flow under reentry conditions.

The last chapter provides an overall presentation of the results of the various studies envisaged from the trajectory simulations of different kinds of re-entry vehicles and finally, a general conclusion will be drawn.

Chapter 1:

Atmospheric reentry characteristics

1 Atmospheric reentry characteristics

1.1 Introduction

When a spacecraft enters the upper layers of the atmosphere, its speed is still very important (hypersonic speeds). The associated aerodynamic processes create extremely high temperatures, particularly on the nose, necessitating the use of a heat shield. Given the complexities of the phenomena that occur in hypersonic flows, they are currently the topic of extensive research**.** Given to the complexities of the phenomena that occur in hypersonic flows, they are currently the topic of extensive research. We present in what follows some peculiarities of the trajectories of these vehicles and the important characteristics linked to the new physicochemical characteristics of the flows envisaged around space vehicles.

1.2 Atmospheric re-entry characterization:

1.2.1 Atmospheric re-entry characterization

1.2.1.1 The atmosphere

The atmosphere is a mixture of several gases that surrounds earth, nitrogen and oxygen make up about 99% of the atmosphere in front of the total volume of the gas, up to altitudes approximately 90 km, the air mixed stay in nearly the same proportions due to fluctuating winds and General atmospheric turbulence in all direction. **[1].**

The earth's atmosphere has two major zones or shells that we can distinguish by their composition of air:

1.2.1.2 The homosphere

The region of homosphere is from the ground extends to 100 km consider as the lowest earth's atmosphere layer where the composition of air is uniform and the concentration of molecules are the same in this layer, it includes the troposphere, the stratosphere and the mesosphere.

1.2.1.3 The heterosphere

Is the upper part of the atmosphere between 100 km and 400 km in altitude, where the molecules are dissociated under form of ions and atoms and contains a higher proportion of lighter gases such as helium and hydrogen, it includes the exosphere and the thermosphere.

The most common criterion used is the temperature distribution for divide the atmosphere regions to the troposphere, stratosphere, mesosphere, thermosphere, and exosphere. **Fig 1.1** the layers of the atmosphere defined by the composition and temperature.

- The troposphere, from sea level up to about 10 km altitude;
- The stratosphere lying between 10 km and 50 km altitude;
- The mesosphere between 50 km and 80 km altitude;
- The thermosphere lying between 80 to 700 km;
- Exosphere: between 700 to 10,000 km.

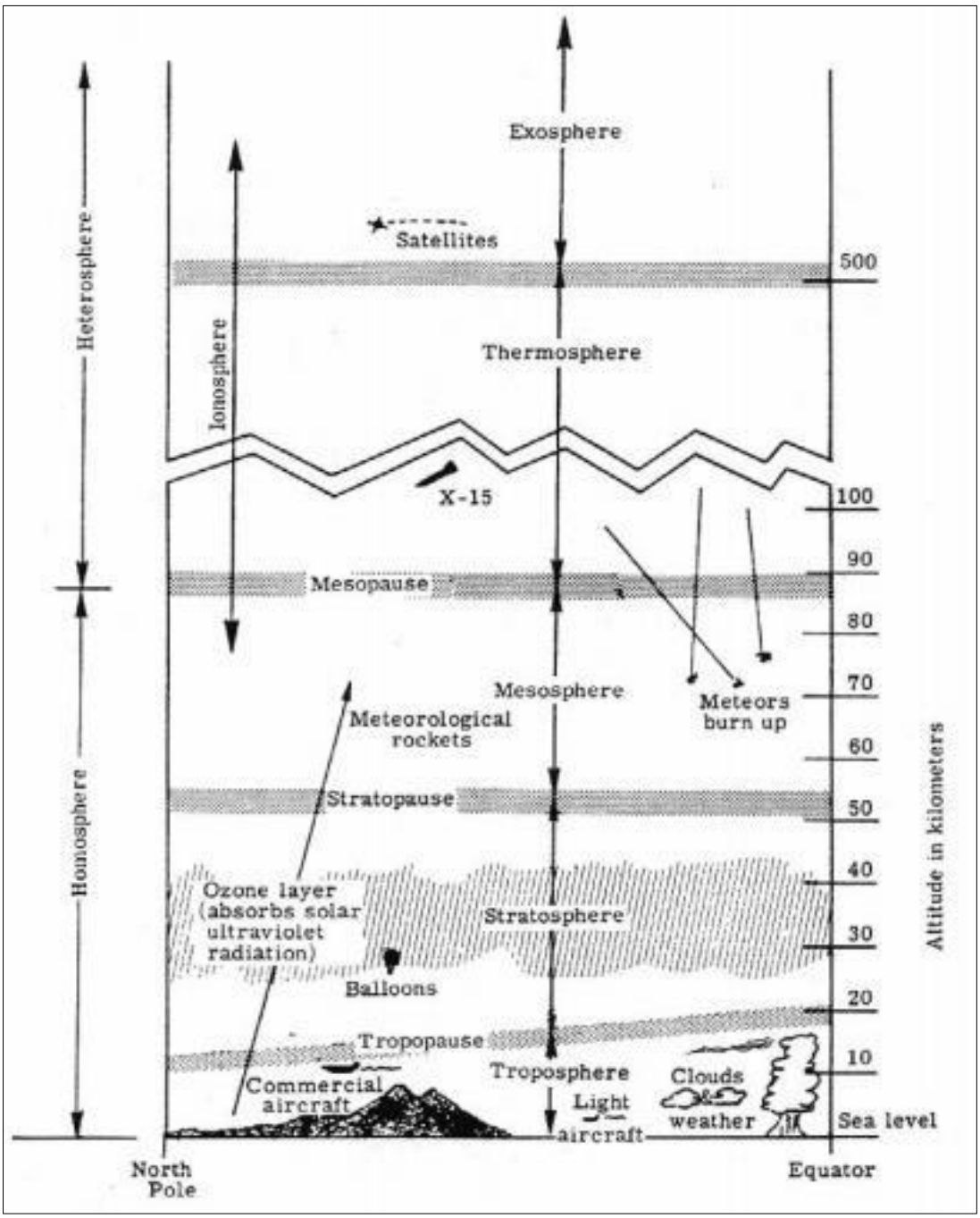

Figure 1-1: Atmospheric structure**. [1]**

1.2.2 Flows characterization:

Space shuttles experience several flow regimes during atmospheric reentry, ranging from rarefied to continuous medium **[2]**hypersonic to subsonic, laminar to turbulent. As a result, a flow depends on the flow regime, a speed regime, and a dynamic behavior.

1.2.2.1 Velocity regimes:

When studying compressible fluid flows, an essential value is the speed of sound. Sound is propagated as a series of longitudinal compression waves within a medium, and therefore its transmission speed is dependent on the fluid's compressibility **[3]** This is an important notion in aerodynamics for the study of transonic and supersonic flow and the various effects associated with these flow regimes.

The speed of sound in the air, considered a perfect gas, is expressed by:

$$C = \sqrt{\frac{\partial P}{\partial \rho}} \qquad (1.1)$$

P : the pressure (Pa)

ρ : the density (kg·m-3)

The equation of state makes it possible to rewrite it as a function of the specific gas constant r (287 J. kg-1.K−1 for air) and the temperature T in kelvins

$$C = \sqrt{\gamma r T} \qquad (1.2)$$

Flow regimes can be classified via their Mach number, defined as the ratio of the local velocity to the local speed of sound

$$Ma = \frac{V}{C} \qquad (1.3)$$

Ma: is the Mach number

V: is the speed of the object (relative to its environment)

c: is the speed of propagation or speed of sound in the environment under consideration.

The range of Mach numbers with associated fluid flow regimes are shown in **Fig 1.2**.When the local Mach number is less than unity the flow is said to be subsonic. Although

compressibility in a fluid is always present to some extent, flows may be treated as incompressible when changes in fluid density are negligible, which is for all practical purposes true of flows where $M < 0.3$.

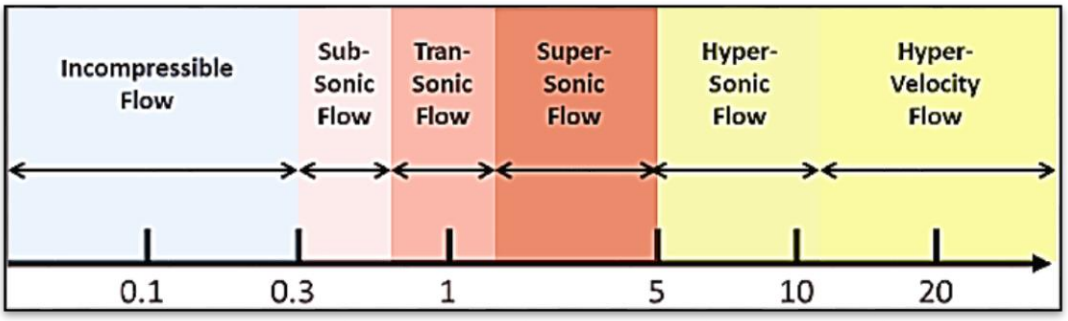

Figure 1-2: Mach number flow regimes**. [3]**

Flows in which the Mach number is greater than unity are known as supersonic. In a steady flow with a supersonic freestream, shock waves may form, which are the response of a fluid to a disturbance moving greater than the speed of information propagation. Although experiments show the thicknesses of these shock waves to be on the order of several hundred nanometers, on a macroscopic scale and in aerodynamic theory they are typically treated as an instantaneous increase in entropy. Shocks may also form when certain parts of the flow are locally supersonic due to fluid acceleration, in what is known as the transonic regime. Shock waves may be associated with a large increase in temperature, pressure and density and are therefore of great concern in aero-thermodynamic design **[3]**

For example, the elevated pressure and density can greatly reduce aerodynamic lift and increase drag. An accurate assessment of a vehicle's aerodynamic properties is essential for mission profile design as well as the development of thermal protection systems (TPS), control systems and avionics packages. The transition to the hypersonic flight regime is commonly defined at Mach 5, though its true definition is when a combination of effects, which will be discussed below, begins to manifest them.

Although the presence of strong shock waves in supersonic flows is problematic for the design of supersonic vehicles, the hypersonic flight envelope is susceptible to an even wider array of problems. First and foremost, hypersonic vehicles fly at even higher velocities, resulting in significant freestream kinetic energy. Reentry vehicles returning from orbit enter the Earth's atmosphere at least at low earth orbit (LEO) velocities of roughly 7.8 km/s **[3]**
The kinetic energy of the flow is converted mainly to thermal energy through recompression as well as viscous dissipation effects that occur within a boundary layer, resulting in extremely

large heat fluxes to the body. Furthermore, the large freestream Mach numbers result in smaller deflection angles for oblique shocks emanating from the body. Consequently, the hot shock layer is located even closer to the vehicle, increasing heat fluxes. Other shocks propagating from the body may also lead to shock-shock interaction, which generates extremely high temperature and pressure regions. **[4]**

1.2.2.1.1 Some hypersonic aircraft

- Experimental hypersonic aircraft HTV-2 (Mach 20)
- Hypersonic glider Avangard (Mach 20)
- Hypersonic glider "Advanced Hypersonic Weapon" in development by the US Army (Mach 17)
- Anti-aircraft missile 40N61 of the future missile defense system S-400F2 and S-500 (Mach 12). **[5]. [6]**
- Sprint anti-missile missile (Mach 10).
- Russian hypersonic aerobalistic missile Kinjal (Mach 10).
- Chinese nuclear-powered hypersonic glider, DF-ZF/Wu-14 (Mach 10).
- Prototype X-43 Scramjet hypersonic unmanned aircraft (just under Mach 10).
- Missile of the American anti-ballistic system THAAD (Mach 8)

1.2.2.1.2 Dynamic behavior

The dynamic behavior of the flow is defined by the Reynolds number Re, which defines the ratio of inertial forces to viscous forces

$$R_{eL} = \frac{\rho u_0 L}{\mu} \qquad (1.1)$$

Where μ is its dynamic viscosity and ρ is the density of the fluid, and L is a characteristic length of the obstacle.

- There are three major regimes exist: **[5]**

- The laminar regime kn $<10^5$, in which viscosity forces predominate. For external Flows, this limit value is valid.
- A transient flow regime in which the flow fluctuates between laminar and turbulent.
- The turbulent regime kn $>10^5$, which appears at much larger Reynolds numbers, and is characterized by three-dimensional random occurrences that are irregular in space and time **[5].**

Because the density of the earth's atmosphere varies with altitude, a hypersonic vehicle such as a planetary entry capsule or a reusable launch vehicle will experience widely diverse flow regimes along its flight trajectory **[5].**

The flow regime is described using the Knudsen number, kn. It is defined by the report:

$$K_n = \frac{l}{L} \tag{1.2}$$

Where l indicates the average free path of the particles and L is the characteristic length of flow. There are three types of reentry regimes in terrestrial atmospheric reentry:

- Continuous regime, $kn \leq 10^{-3}$, at altitudes below 80 km, the pressure and density of the fluid for this regime are high enough to completely define different macroscopic quantities that characterize the fluid.
- The intermediate regime, $10^{-3} \leq kn \ll 1$, for altitudes lying between 80 to 100 kilometers. The flow is commonly described by the NS equations, but wall slip conditions are also required.
- The rarefied regime, $kn \gg 1$, the density and pressure of which are extremely low. It is required to use a microscopic technique to characterize the fluid's evolution in this situation (Boltzmann equations). At very high altitudes, above 100 km, where air pressure is low, this type of flow is common.

The flow is described by solving the original Navier-Stokes's equations, which are predicated on the assumption that the medium is continuous. As a result, we concede that the volume, which we will call "fluid particle," is large enough to hold a huge number of molecules but tiny enough to define a "local" value and an infinitesimal volume element, permitting differential and integral calculus to be justified. **[6].**

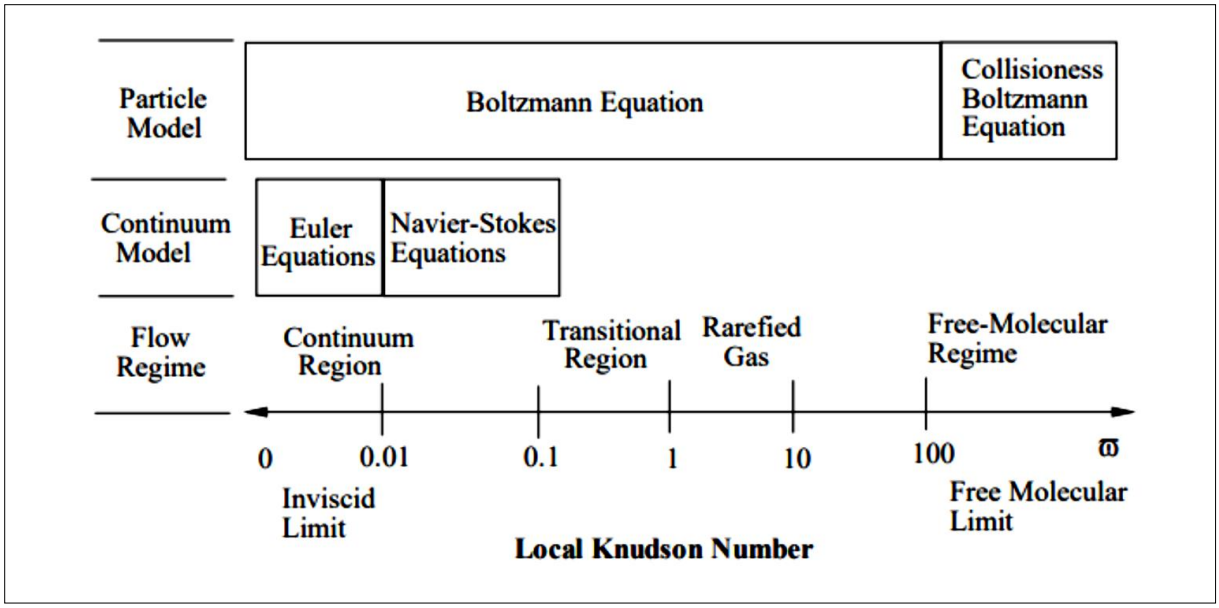

Figure 1-3: Different approach for the Knudsen number limits**. [5]**

When the flow state undergoes thermochemical non-equilibrium, thus, when a hypersonic vehicle crosses a shock wave that occurs upstream, the kinetic energy of the flow, which is very substantial, is transferred to the internal energy of the particles by collisions. Collisions cause because of its power chemical reaction and/or excite the degrees of freedom of the particles, such as rotation, vibration, and electronics (the modes of rotation and vibration only concern molecules). In such situations, there are three sorts of collisions**. [6]**

Elastic collisions, in which only the energy associated with the modes of translation is implicated. Throughout a collision, particles transfer some of their kinetic energy (translation-translation exchanges). These collisions assist in bringing the environment closer to translational equilibrium. It's the transnational relaxation phenomena.

Inelastic collisions occur when particles exchange energy through translation as well as rotational, vibrational, and electronic degrees of freedom. As a result, various sorts of exchanges exist, including vibration translation (VT), vibration vibration (VV), rotation translation (RT), and so on. At temperature T, these exchanges will push the medium towards a state of local thermodynamic equilibrium

Chemical reactions like dissociation, ionization, and particle charge exchange are produced by reactive collisions.

1.2.3 **The dynamics of gases at high temperatures in continuous hypersonic regime**:

1.2.3.1.1 Normal shockwave

The shock wave is thought to represent a surface of discontinuity perpendicular to the flow, dividing an upstream region (index (1)) from a downstream region (index (2)) in the configuration we're looking at. This shock wave is stationary.

As a result, by applying balance equations to these discontinuities, we'll be able to relate the properties of the flow upstream and downstream of the shock wave, and hence the values that characterize these two zones.

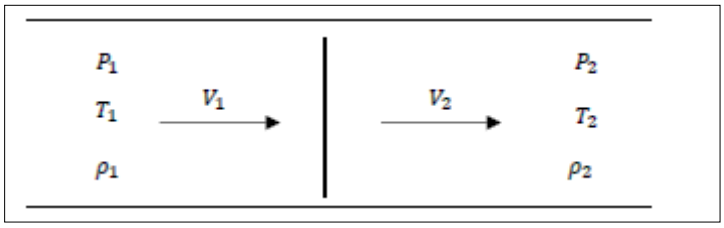

Figure 1-4: A normal shock configuration for the balance sheet**. [7]**

Relations de Rankine-Hugoniot

The Rankine-Hugoniot relations make it possible to establish the link between the two states upstream and downstream of a shock wave in a one-dimensional flow. We consider the wave shock as a surface of discontinuity perpendicular to the flow, separating an upstream region (index "1") from a downstream region (index "2"). This shock wave is stationary, that is to say, is stationary with respect to the frame of reference of the study.

In addition to these assumptions used, we can also consider that

- All streamlines are parallel to each other and perpendicular to the surface of the shock, the one-dimensional flow along the direction
- There is no chemical reaction, and the fluid remains in thermodynamic equilibrium.

We are now going to write the different conservation equations, making it possible to link state (1) upstream of the shock, to state (2) downstream of the shock [8]as result , We develop the various conservation equations that will allow us to relate state (1) to state (2). It's as simple as that to maintain mass conservation.

$$\rho 1 \upsilon 1 = \rho 2 \upsilon 2 \qquad (1.6)$$

Because the shock is infinitely thin perpendicular to the flow, the section remains constant (A1=A2). $K_n = \frac{l}{L}$

One acquires momentum as a result of this.

$$m\dot{}\upsilon 2 - m\dot{}\upsilon 2 = p1A1 - p2A2 \qquad (1.7)$$

Assume that the flow rate remains constant and that the only source of variation in momentum is pressure forces. Because (A1 = A2) and (1. 5) are used, we can conclude:

$$p1 + \rho 1\upsilon 12 = p2 + \rho 2\upsilon 22 \qquad (1.8)$$

The energy balance is simply written in the absence of effort and heat input:

$$h_1 + \frac{u_1^2}{2} = h_2 + \frac{v_2^2}{2} \qquad (1.9)$$

By introducing the state equation to these equations, we obtain four equations, allowing, from the knowledge of the state (1), to calculate the four unknowns, $p2$, $\rho 2$, $\upsilon 2$, $h2$ which characterize the state (2). Mass balance: **[7].**

- **For a perfect gas**

We add the equation of state of the gas which is fairly simple in this situation, for example, in the form:

$$p=\rho rT$$

To achieve simple ratios, we will now try to display the upstream and downstream Mach numbers. As a result, we have for the energy equation:

$$C_pT_1 + \frac{v_1^2}{2} = C_pT_1\left(1 + \frac{v_1^2}{2C_pT_1}\right) = C_pT_1\left(1 + \frac{\gamma - 1}{2}M_1^2\right) \qquad (1.10)$$

The energy balance equation is as follows

$$\frac{T_2}{T_1} = \frac{1 + \frac{\gamma - 1}{2} M_1^2}{1 + \frac{\gamma - 1}{2} M_2^2} \tag{1.11}$$

The equation for momentum balance can now be transformed using

$$p_1 + \rho_1 v_1^2 = p_1 \left(1 + \frac{\rho_1 v_1^2}{p_1} \right) = p_1 \left(1 + \gamma M_1^2 \right) \tag{1.12}$$

So here's the second relation we're looking for:

$$\frac{p_2}{p_1} = \frac{1 + \gamma M_1^2}{1 + \gamma M_2^2} \tag{1.13}$$

The evolution of the ratio can be quickly deduced using the equation of state of ideal gases:

$\rho 2 / \rho 1$

The upstream and downstream Mach numbers must now be connected. The mass balance is employed in this process:

$$\frac{\rho_2}{\rho_1} = \frac{v_1}{v_2} = \frac{M_1 c_1}{M_2 c_2} \tag{1.14}$$

The first and third members of this equality can be transformed by employing:

$$\rho = \frac{p}{rT} c = (\gamma r T)^{\frac{1}{2}} \tag{1.15}$$

To get:

$$\frac{p_2}{p_1} = \frac{M_1}{M_2} \left(\frac{T_2}{T_1} \right)^{\frac{1}{2}} \tag{1.16}$$

Changes in Mach numbers have previously been linked to pressure and temperature ratios. We may establish the following relationship between the upstream and downstream Mach numbers by simple substitution:

$$\frac{1+\gamma M_1^2}{1+\gamma M_2^2} = \frac{M_1}{M_2}\left(\frac{1+\frac{\gamma-1}{2}M_1^2}{1+\frac{\gamma-1}{2}M_2^2}\right)^{\frac{1}{2}} \tag{1.17}$$

This second-degree equation can be easily solved by elevating everything to the square and treating, $M22$, for example, as an unknown function of, $M12$. $M22=M12$ is a simple solution that has been discarded. We finally:

$$M_2^2 = \frac{2+(\gamma-1)M_1^2}{2\gamma M_1^2+1-\gamma} \tag{1.18}$$

The equation 1.19, when combined with the formulas previously discovered for the pressure, temperature, and density ratios, now gives the value of these ratios as a function of the number of upstream Mach numbers (for example). As a result, we have:

$$\frac{T_2}{T_1} = \left(\frac{2\gamma}{\gamma+1}M_1^2 - \frac{\gamma-1}{\gamma+1}\right)\left(\frac{\gamma-1}{\gamma+1} + \frac{2}{(\gamma+1)M_1^2}\right) \tag{1.19}$$

Similarly, we discover:

$$\frac{p_2}{p_1} = \frac{2\gamma}{\gamma+1}M_1^2 - \frac{\gamma-1}{\gamma+1} \tag{1.20}$$

Finally, using the state equation

$$\frac{\rho_2}{\rho_1} = \frac{p_2}{p_1}\frac{T_1}{T_2} = \frac{2+(\gamma-1)M_1^2}{1+(\gamma-1)M_1^2} \tag{1.21}$$

Like $\rho 1 v 1 = \rho 2 v 2$

Finally, using the state equation:

$$\frac{v_1}{v_2} = \frac{2+(\gamma-1)M_1^2}{1+(\gamma-1)M_1^2} \tag{1.22}$$

Taking into account all of these connections, we can observe that $M1 \to \infty$ also has $T2 \to \infty$and $2 \to \infty$. The ratios of densities and velocities, on the other hand, have a finite limit:

$$\lim_{M_1\to\infty} \frac{\rho_2}{\rho_1} = \lim_{M_1\to\infty} \frac{v_2}{v_1} = \frac{\gamma+1}{\gamma-1} \tag{1.23}$$

Obtaining the relationship between the total pressures on both sides of the shock may also be beneficial. To accomplish this, we write

$$\frac{p_{12}}{p_{i1}} = \frac{p_{i2}}{p_2}\frac{p_2}{p_1}\frac{p_1}{p_{i1}} \tag{1.24}$$

The normal member's second ratio is (1.27), whereas the first and third simply correspond to the isentropic relation. So, in the end, we:

$$\frac{p_{i2}}{p_n} = \left(\left(\frac{\gamma-1}{\gamma+1} + \frac{2}{(\gamma+1)M_1^2}\right)^{\gamma}\left(\frac{2\gamma}{\gamma+1}M_1^2 - \frac{\gamma-1}{\gamma+1}\right)^{\frac{-1}{\gamma-1}}\right. \tag{1.25}$$

The last relation we'll look at is the one that shows how entropy changes as a result of a shock wave. To accomplish this, we write:

$$\frac{s_2-s_1}{c_v} = \ln\left(\frac{p_2}{p_1}\left(\frac{\rho_1}{\rho_2}\right)^{\gamma}\right) \tag{1.26}$$

The last relation we'll look at is the one that shows how entropy changes as a result of the shock wave. To do so, we use the following formula: **[7]**

$$\frac{s_2 - s_1}{c_v} = \ln\left(\left(\frac{1}{\gamma+1}\right)^{\gamma+1} 2\gamma M_1^2 - \gamma + 1\right)\left(\frac{2}{M_1^2} + \gamma - 1^{\gamma}\right) \qquad (1.27)$$

For M1 = 1, we can see that the entropy variation balances out (infinitely weak shock wave). The fluctuation of entropy is positive for M1>1, but negative for M11. We can see that a standing normal shock wave can only exist in a supersonic flow because the last hypothesis is impossible according to the second law of thermodynamics.

A strong shock arises upstream of a re-entry vehicle during a hypersonic flow surrounding it. Numerous practical applications require a study of the physicochemical processes which appear downstream of intense shocks where the Mach number is very high. These shocks produce high temperatures and, therefore, a deviation from the behavior of an ideal gas is observed **Fig 1.5**.

The sudden increase in the internal energy of the gas through the shock manifests itself first as an increase in the translational and rotational thermal stirring energy of the molecules.Then, an evolution towards a state of equilibrium, characterized by the equipartition of energies, thanks to collisions between particles.

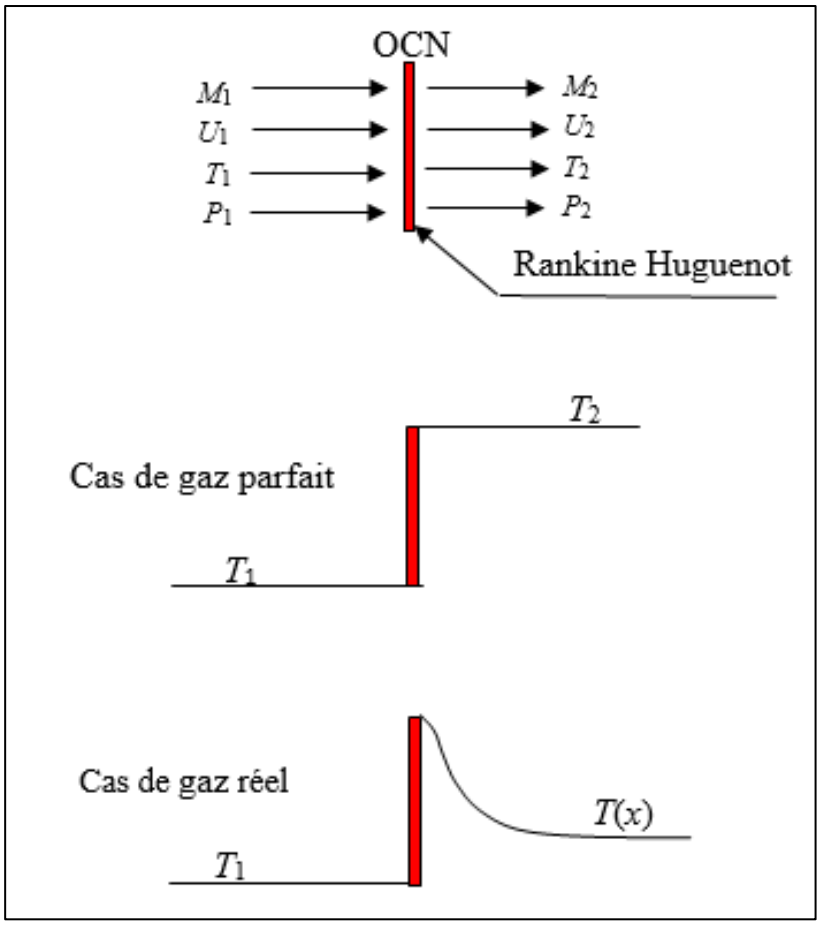

Figure 1-5: Effects of real gas on the temperature behind the shock wave**. [9]**

1.2.3.1.2 **Shock wave in hypersonic flow:**

The formulae for pressure, density, and temperature following the shock wave reach a mathematical limit when the Mach number of the upstream flow grows progressively hypersonic. **[10]**

Oblique shock wave equations

$$\frac{T2}{T1}=\left(\frac{2\gamma}{\gamma+1}M_1^2\sin^2\sin^2\beta-\frac{\gamma-1}{\gamma+1}\right)\left(\frac{\gamma-1}{\gamma+1}+\frac{2}{(\gamma+1)M_1^2\sin^2\sin^2\beta}\right) \quad (1.28)$$

$$\frac{P2}{P1}=\frac{2\gamma}{\gamma+1}M_1^2\sin^2\sin^2\beta-\frac{\gamma-1}{\gamma+1} \quad (1.29)$$

$$\frac{\rho2}{\rho1}=\frac{(\gamma+1)M_1^2\sin^2\sin^2\beta}{2+(\gamma-1)M_1^2\sin^2\sin^2\beta} \quad (1.30)$$

$$\frac{P2}{P1} \approx \frac{2\gamma}{\gamma+1} M_1^2 \sin^2 \sin^2 \beta \tag{1.31}$$

$$\frac{\rho_2}{\rho_1} \approx \frac{\gamma+1}{\gamma-1} \tag{1.32}$$

The hypersonic limit for the density ratio is 6 for a perfect atmospheric gas approximation using. Hypersonic post-shock dissociation of O2 and N2 into O and N, on the other hand, lowers, permitting larger density ratios in nature. The temperature ratio of hypersonic is:

$$\frac{T_2}{T_1} = \frac{2\gamma(\gamma-1)}{(\gamma+1)^2} M_1^2 \sin^2 \sin^2 \beta \tag{1.33}$$

Normal shock wave equations

$$\frac{T_2}{T_1} = \left(\frac{2\gamma}{\gamma+1} M_1^2 \right) \tag{1.34}$$

$$\frac{P_2}{P_1} = \left(\frac{2\gamma}{\gamma+1} M_1^2 \right) \tag{1.35}$$

$$\frac{v_2}{v_1} = \frac{\gamma+1}{\gamma-1} \tag{1.36}$$

However, the state equation h = cpT, which was proposed to complete this system, is insufficient to capture the effects of genuine gases arriving at high temperatures. This equation of state is a simplified version of the relations, which is derived from the assumption cp =constant: **[10]**

$$h(T) = h(T_0) + \int_{T_0}^{T} c_{p(\tau)d\tau} \tag{1.37}$$

It is impossible to view cp as a constant at high temperatures due to the gradual stimulation of interior levels of molecules. It is no longer possible to solve the Rankine-Huguenot equations

analytically when a realistic equation of state is taken into consideration, which becomes a nonlinear function of temperature.

1.2.4 Physicochemical phenomena in the shock layer:

When the free stream Mach number is increased from a supersonic value, the temperature behind the shock wave rises, in the event of an external flow, the internal energy modes of the molecules are stimulated. Even at extremely high Mach levels, the temperature can rise to the point where the diatomic molecules dissociate. If the Mach number is raised much higher, some species may get ionized. Radiation may emit or absorbed by the gas. The gas cools as it expands across the flow field. This allows the constituents to recombine, causing the internal energy levels to relax. High-temperature effects refer to the thermochemical excitation of vibration, dissociation, ionization, and radiation. As a result, the flow properties diverge from the ideal gas values. To be vibrated excited, a molecule must endure a particular number of collisions (typically a few hundred). This quantity, although, changes based on the chemical species under consideration, as well as the amount of kinetic energy involved in collisions, and hence the medium's temperature. For the oxygen molecule to dissociate, 200,000 collisions are required.

Because only the translational and rotational modes of internal energy are fully stimulated at low temperatures (800 K), a combination of gases can be described as a mixture of calorically perfected gases with constant specific heats. When the temperature of the air is raised over 800 K, the molecules may experience vibrational excitation, causing the specific heats to become a function of the temperature; the gas is then considered to be thermally perfect. Chemical reactions can occur when the temperature rises, and air becomes a chemically reactive mixture of thermally ideal gases.

$O2$dissociation ($O2 \rightarrow 2$) begins about 2000 K for air at 1 atm pressure, and the molecular oxygen is completely dissociated around 4000 K. As seen in **Fig 1.6**, N 2 dissociation ($N2 \rightarrow 2$) begins at this temperature and is essentially completely dissociated by 9000K. Ion's form ($N \rightarrow N + e-, \rightarrow O + e-$), and the gas forms a partly ionized plasma, above a temperature of 9000 K. **[11]**

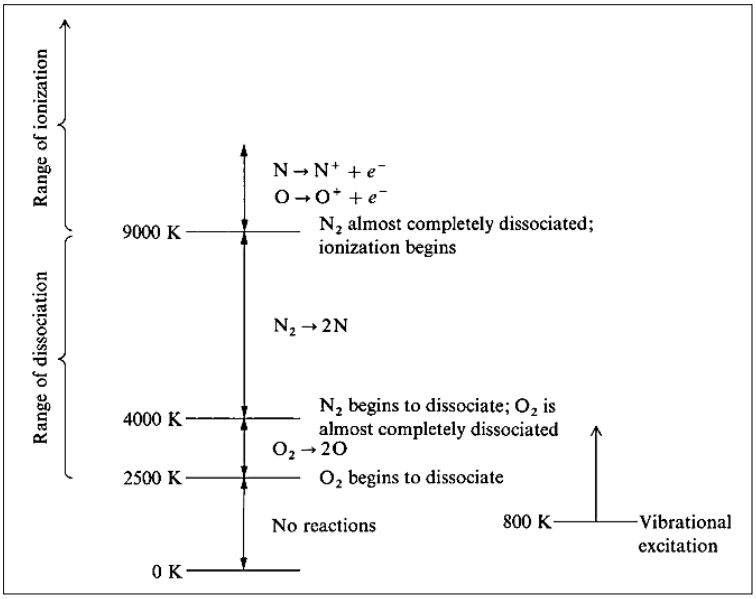

Figure 1-6: Depicts the dissociation and ionization ranges in air at 1 atm pressure. **[11]**

Fig 1.6 provides a direct link to **Fig 1.7**. The flying zones linked with various chemical effects in air are depicted on this velocity-altitude map. The effective beginning and end of various sections where these effects are prominent are denoted by the 10 and 90% labels. In the lower-left corner and mentally "ride up" the flight route in reverse, we will arrive at our destination. At about V= 1 km/s, vibrational excitation is initially observed in the flow field as the velocity increases. The vibrational mode is virtually fully activated at a higher velocity of roughly 2.5 km/s, and oxygen dissociation initiated. The shaded zone labeled "oxygen dissociation" is affected by this impact. At roughly 5 km/s, O2 dissociation is virtually complete, and N2 dissociation begins. The darkened zone labeled "nitrogen dissociation" is affected by this impact. The N2 dissociation is finally complete above 10 km/s, and ionization begins. The fact that zones of diverse dissociations and ionization are so distinct on the velocity-altitude map, with little overlap, is fascinating. **[11]**

Finally, based on **Fig 1.7**, we can make the following general observation. The entry flight pathways slash through large regions of the velocity-altitude map that are critical for chemical reactions and vibrational stimulation.

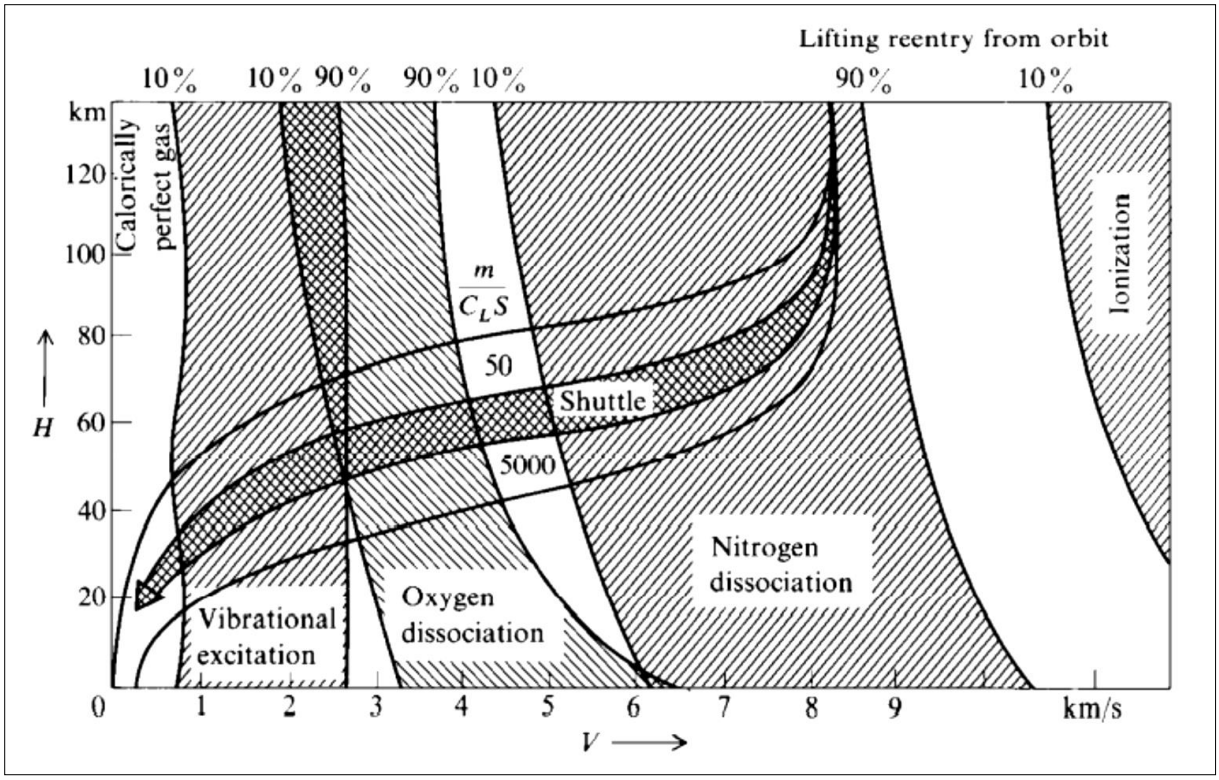

Figure 1-7: Superimposed zones of vibrational excitation, dissociation, and ionization on a velocity-amplitude map**. [12]**

The above-mentioned high-temperature effects are triggered and propagated via molecular collisions. In general, these phenomena have predictable time scales for reaching equilibrium; in translational mode, only a few collisions are required to achieve equilibrium. In rotational mode, around 10 collisions are required, while in vibrational mode, about 200,000 collisions are required **[12]**A molecule must collide with other molecules several times to obtain complete excitation of a vibrational energy mode, for example. A chemically reactive medium must do the same to reach its equilibrium composition at a given pressure and temperature. As a result, the vibrational mode's relaxation duration is clearly longer than the other modes.

When the relaxation time of the vibrational mode $\tau vib$is compared to the time required for a flow particle to move in the shock layer τec, three flow states can be distinguished: $\tau vib \ll \tau ec$The flow is considered to be in thermochemical equilibrium $\tau vib \gg \tau ec$ Vibrationally, the flow is frozen. After passing the shock wave, the thermodynamic condition remains unchanged. $\tau vib \sim \tau ec$ because the vibration temperature of each vibrating molecule may differ from the translation-rotation temperature of the mixture, the flow is in vibrational equilibrium, also known as thermal equilibrium.

1.2.4.1 Chemical environment evaluation:

Flow chemistry includes a huge variety of processes and microscopic phenomena, which are normally contained in a series of chemical reactions, each with its own kinetics, and which yet include numerous forward and backward reactions. It's a difficult task to account for the chemical state of a mixture. The ultimate stable state is equilibrium.

Different perspectives on chemical non-equilibrium could be used. Damkölher proposed a characteristic non-dimensional number (Da) to account for the chemical non-equilibrium of a gas mixture. In the same location, he proposed comparing a characteristic time for chemistry to occur (τch) with a characteristic time for flow (τec)

$$D_a = \frac{\tau_{ec}}{\tau_{ch}} \qquad (1.38)$$

$\tau ch \gg \tau ec$ with in a frozen flow $Da \rightarrow 0$ chemical processes do not have time to develop. When traveling through a shock wave. Because the thickness of the shock reflects only a few mean free pathways of a particles, the flow behavior rapidly changes. For a few collisions, however, the rotating mode can relax and approach equilibrium. Everything happens as if the gas downstream of the shock has the same composition as the gas upstream. When a flow is exposed to a large amount of expansion, it might get frozen. **[13]**

$\tau ch \ll \tau ec$ for chemical equilibrium flow: $Da \rightarrow \infty$ when compared to the flow's time scale, chemical reactions where the approach to equilibrium is incredibly fast. To put it another way, the gas's chemical composition changes to local temperature and pressure conditions in a very short amount of time, and hence over a very small distance. Chemical equilibrium is achieved at each point in the flow. As a result, the local composition of the gas is entirely determined by local pressure and temperature, or any other combination of variables.

$\tau ch \sim \tau ec$ the flow is a Chemical non-equilibrium, the chemical composition of the gas varies depending on the flow parameters. It will require more time or space to reach equilibrium.

1.3 State of art

The flow temperatures after strong shockwaves increase rapidly when vehicles fly at hypersonic speeds. The hypersonic thermochemical non-equilibrium phenomena such as vibration, dissociation and ionization occur in high flow temperatures.1,2 With the increase of hypersonic aerodynamic heating effect, the ionized species around the hypersonic vehicle will generate a plasma layer and cause the blackout with communication difficulty.3 What’s worse,

the structures seriously damaged by the extreme thermal loads may cause the flight mission to fail. Therefore, it's necessary to effectively predict the hypersonic aerodynamic heating environments for the optimal design of Thermal Protection System (TPS) and the flight safety of a hypersonic vehicle.

Lots of researches have been done to effectively predict the hypersonic aerodynamic heating environments of vehicles in thermochemical non-equilibrium air flows. Wang et al.compared the performances of Dunn & Kang, Gupta, Park (1988) and Park (1991) chemical kinetic models in hyper-sonic aerodynamic heating environments calculations. They considered that the difference in wall heat fluxes was mainly caused by the chemical reaction rates of different kinetic models. Tchuen and Zeitoun11 researched the method of computing the backward reaction rate by using different equilibrium constants. They found that the flow field structure, shockwave shape and surface properties were seriously affected by the equilibrium constants chosen. The equilibrium constants obtained from the fitting of experimental data were more reliable than those calculated by the theoretical formulations. Clarey and Greendyk utilized the Park's two-temperature model to analyze the thermochemical non-equilibrium flows around a reentry vehicle. They found that the differences in the maxmum number densities of electrons, temperature modes and species concentrations along the stagnation streamline calculated by the two-temperature and three-temperature models were very small. Edwards presented an implicit multi-grid algorithm for computing hypersonic viscous flows with thermal and chemical non-equilibrium. He obtained the distributions of temperature and pressure along the stagnation streamline by using the 11 species chemical reaction model. Prakash et al. developed a fifth-order shock-fitting numerical method to simulate the hypersonic thermochemical non- equilibrium flows over blunt bodies. The new method was capable of capturing the hypersonic flow field with high- order accuracy but without any oscillations near the shock- wave. In addition, Farbar et al. studied the effect of electron thermal non-equilibrium on hypersonic flow fields; Zeng et al. proposed a new method to express the vibrational thermal conduction in numerical calculations of hyper- sonic thermochemical non-equilibrium flows.

In this study, a theoretical methodology for thermochemical non-equilibrium flow combing with the HLLC scheme is applied to study the hypersonic thermochemical non-equilibrium environment of an entry configuration in ionized flow. The high temperature flow after shockwave is treated as a mixture of 11 species (N2, O2, NO, O, N, NO+, N+2 , O+2 , N+, O+, e). A two-temperature controlling model is utilized and the Gupta's thermochemical non- equilibrium model8 is used. In order to effectively verify the reliability of the method above, the method is taken to calculate the hypersonic aerodynamic heating environments of

two different aerodynamic shapes in advance. The method is then applied to research the effects of ionization and wall catalysis on the hypersonic thermochemical non-equilibrium environment of the entry configuration in ionized flow **[14].**

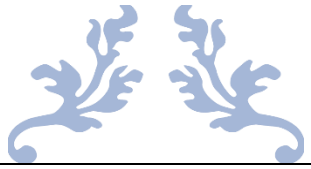

Chapter 02

Mathematical and physical model

2 Introduction:

The governing equations for a multi-species gas that is both thermally excited and chemically reactive are discussed in this chapter. The Navier-Stokes's equations, which are statements of global continuity, provide the basis for these equations: total mass conservation, total momentum conservation, and total energy conservation. The Navier-Stokes's equations are based on the continuum postulate, which asserts that there are a large number of molecules within a computational volume, and that the average statistical properties of the molecules accurately represent the properties of the fluid in this elementary region.

The sum of a molecule's translational, rotational, vibrational, and zero-point energies is its total energy. Only translational and electronic energies exist for a single atom. Each of the species in the combination is considered to act like a perfect gas.

Separate and independent temperatures are presented to characterize the thermal state of the gas.

2.1 Governing equations

2.1.1 Species conservation:

For species in a mixture, the mass conservation equation is dictated by:

$$\underset{1}{\frac{\partial \rho_\alpha}{\partial t}} + \underset{2}{\frac{\partial}{\partial x}\left(\rho_a u - \left(-q_{\alpha x}^D\right)\right)} + \underset{3}{\frac{\partial}{\partial y}\left(\rho_\alpha u - \left(-q_{ay}^D\right)\right)} = \underset{4}{\dot{w}_\alpha} \tag{2.1}$$

In the above equation,

- The term (1) represents the rate of change of mass of species αper unit volume in a cell centered at point (x, y)
- In term (2), o$\rho_\alpha u$represents the x- component of flux of mass of species α, convicted across cell walls o $q_{\alpha x}^D$ is the component of species diffusion flux across cell walls.
- Term (3) has the same meaning as term (2) but in the y- direction
- Term (4) represents the mass production rate of species αdue to chemical reactions. Clearly $\Sigma \dot{w}\alpha Ns\alpha$=1is zero, since mass is conserved in chemical changes.

2.1.2 Global continuity:

Summing the Nsindividual species mass conservation equations yield the total mass conservation for the mixture as a whole. The global continuity equation looks like this

$$\frac{\partial \rho}{\partial t}+\frac{\partial}{\partial x}(\rho u)+\frac{\partial}{\partial y}(\rho u)=0 \tag{2.2}$$

- Term (1) is the rate of change of mass of the mixture per unit volume in a cell centered at (x, y).
- Terms (2) and (3) are x and y components of the mass flux.

Conservation of momentum

For mixing, the momentum conservation equation is written

$$\frac{\partial \rho u_i}{\partial t}+\frac{\partial \rho u_i u_j}{\partial x_j}=-\frac{\partial p}{\partial x_i}+\frac{\partial}{\partial x_j}\left[\mu\left(\frac{\partial u_i}{\partial x_j}+\frac{\partial u_j}{\partial x_i}\right)-\frac{2}{3}\mu\frac{\partial u_k}{\partial x_k}\delta_{ij}\right] \tag{2.3}$$

The 1st term in equation (2-3) represents the rate of change of the i[th] component of momentum per unit volume in a VCE centered at point j x , the 2ndterm represents the flux of the i[th] component of the momentum by convection through the faces of the VCE with the velocity u_j , the 3rd term represents the forces of the pressure on the faces of the VCE in the i[th] direction, and the 4th term represents the viscous forces acting on the faces of the VCE in the i[th] direction.

Conservation of vibrational energy

The equation for the conservation of vibrational energy is given by

$$\frac{\partial \rho e_v}{\partial t}+\frac{\partial \rho e_v u_j}{\partial x_j}=\frac{\partial}{\partial x_j}\left(\eta_v\frac{\partial T_v}{\partial x_j}\right)+\frac{\partial}{\partial x_j}\left(\rho\sum_{5}^{s=1}h_{v,s}D_s\frac{\partial \xi_s}{\partial x_j}\right)+\sum_{s=mol}[\omega_s^{VT}+\omega_s^{VE}+\omega_s^{VV}]+\sum_{s=mol}\omega_{c,s}\hat{D}_s \tag{2.4}$$

The terms in equation (2-4) represent: (1) the rate of change of energy vibrational per unit volume in the VCE centered at j x , (2) the flow of energy vibrational by convection with the velocity u_j , (3) the conduction of vibrational energy through the faces of the VCE due to vibrational temperature gradients, (4) the diffusion of the vibrational energy through the faces of the VCE due to the concentrations elements, (5) the exchange of energy (relaxation) between the modes of vibration and translation due to collisions between constituents in the VCE, (6) the exchange of energy between vibration and electronic modes, (7) vibration-vibration exchange, (8) term that represents vibrational energy lost or gained due to dissociation or recombination.

It should be noted that the equation of the conservation of vibrational energy does not concern than molecules.

Conservation of total energy

The equation for conservation of total energy is given by the following equation

$$\frac{\partial \rho E}{\partial t}+\frac{\partial \rho H u_j}{\partial x_j}=\frac{\partial}{\partial x_j}\left(\eta\frac{\partial T}{\partial x_j}+\eta_v\frac{\partial T_v}{\partial x_j}+\eta_e\frac{\partial T_e}{\partial x_j}\right)+\frac{\partial}{\partial x_j}\left(\rho\sum_{5}^{s=1}h_s D_s\frac{\partial \xi_s}{\partial x_j}\right)+\frac{\partial}{\partial x_j}\left[u_i\mu\left(\frac{\partial u_i}{\partial x_j}+\frac{\partial u_j}{\partial x_i}\right)-\frac{2}{3}u_i\mu\frac{\partial u_k}{\partial x_k}\delta_{ij}\right]-Q_{ra}^{6} \quad (2.5)$$

In equation (2-5), the six terms represent: (1) the local rate of change of the total energy per unit volume, (2) the enthalpy convection with the velocity j u , (3) the conduction composed of the three contributions of translation, vibration and electronics, (4) the diffusion of the enthalpy due to concentration gradients, (5) the power induced by the viscous forces, (7) radiative power lost due to electronic transitions.

Thermochemical modeling

Thermodynamic relationships

The analysis of flows at high temperature necessarily implies knowledge thermodynamic properties of gas. It is therefore necessary to determine the expressions of the different energies possessed by the constituent species of the mixture gas and other derived quantities such as: specific heats and enthalpies...etc. Statistical mechanics provides precise methods for the calculation of thermodynamic properties, in this section, we present the necessary notions making part of this discipline particularly we are interested in the mechanics of BOLTZMAN

Nallowing to develop the thermodynamic relations which describe the properties of the gaseous mixture statistically which leads us to consider the microscopic state of the gas.

The microscopic description of gases

In statistical thermodynamics, we are interested in the microscopic state of the gas; in considering that gas is made up of a large number of molecules. A molecule is a collection of atoms bound together by intermolecular forces; the simple model is that of a diatomic molecule.

When the temperature of a gas is raised, the molecular agitation increases. Energy exchanges during collisions between gas particles give rise to different physico-chemical phenomena.

First, the molecules are vibrational excited. Consider for example an oxygen molecule O2, the energy of the molecule is distributed over different modes corresponding to its degrees of freedom: translation, rotation, vibration, excitation electronic.

Indeed, the molecule can move in space, in other words, the center of mass of the molecule can move, it therefore has translational energy (**Fig 2.1.a**).It can rotate around the three orthogonal axes defining a reference in space, it therefore has a rotational energy (**Fig 2.1.b**). The two oxygen atoms O, which compose, can vibrate around an equilibrium position within the molecule [8]the molecule therefore has a vibrational energy (**Fig 2.1.c**). Finally, the electrons are moving in orbits around the nucleus of each oxygen atom. Therefore, the molecule has electronic energy (**Fig 2.1.d**). Each of these energies is quantified, i.e. that it can only take certain discrete values.

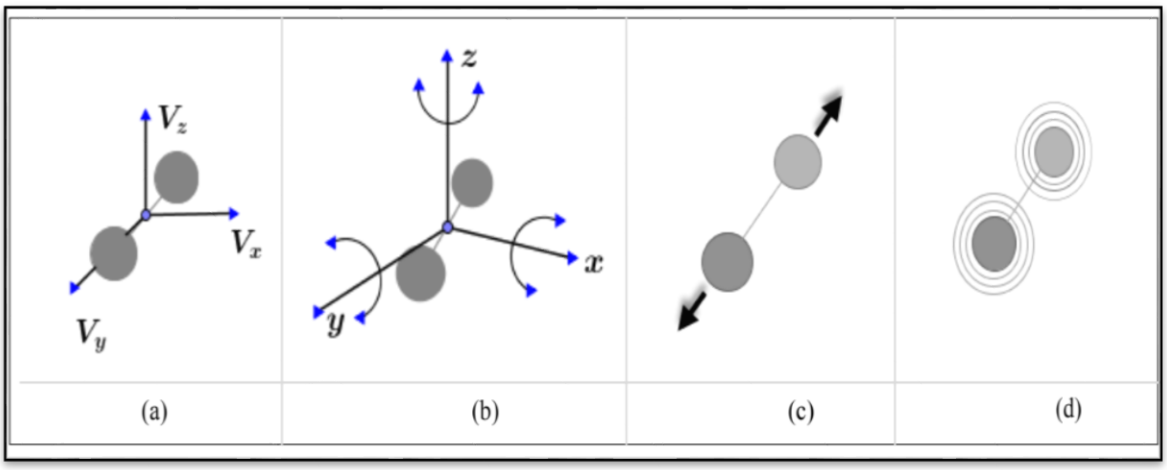

Figure 2-1: Energy modes of molecules. **[9]**

2.1.2.1 Thermodynamic quantities of a perfect gas:

If the different forms of energy of a particle, atom or molecule, are assumed to be independent of each other, i.e. if there is no coupling between the different degrees of freedom of the particle (degrees of translation, rotation, vibration, electronic and nuclear), the energy of a particle has the value of a particle

$$E = E^{t}_{i\ translation} + E^{\gamma}_{j\ rotation} + E^{\gamma}_{k\ vibration} + E^{\ell}_{l\ electronical} + E^{\kappa}_{m nuclear} \tag{2.6}$$

2.1.2.2 Boltzmann distribution and partition functions

The Boltzmann distribution is a probability law or distribution used in statistical physics to determine the distribution of particles between different levels of energy, it gives the number of molecules N_j which populate an energy level j characterized by an energy ε_j , this distribution function is given by [15] [8]

$$N_j = N \cdot g_j \frac{e^{-\frac{\varepsilon_j}{k_E T}}}{Q} \tag{2.7}$$

With: $= \sum_j N_j$ is the number of molecules, g_j is the degeneracy or the number of energy states ε_j .

Q is the partition function; it is a function that describes the statistical properties of a system in thermodynamic equilibrium, its expression is given by

$$Q = \sum_j g_j e^{\frac{-\varepsilon_j}{k_B T}} \tag{2.8}$$

The average energy per unit mass of species α in energy mod i can be represented as

$$e_i = R_\alpha T^2 \left(\frac{\partial \log(Q_a)}{\partial T} \right) \tag{2.9}$$

At constant volume, the corresponding specific heat capacity is given. $c^{(i)}_{v,\alpha}$ as

$$C_{v,\alpha} = \left(\frac{\partial \mathrm{e}\alpha(\mathrm{i})}{\partial \mathrm{T}} \right) \tag{2.10}$$

Translation: For weakly interacting particles, the translational mode yields the following relations:

$$Q_{\alpha}^{(tr)} = \left(\frac{2\pi M \alpha k T(i)}{N_a h^2} \right) V \tag{2.11}$$

$$e_{\alpha}^{(tr)} = \frac{3}{2} R_{\alpha} T \tag{2.12}$$

$$C_{v,\alpha}^{(tr)} = \frac{3}{2} R_{\alpha} \tag{2.13}$$

Rotation: For the rotational mode of energy, the following relations are found at sufficiently high temperatures:

$$Q_{\alpha}^{(rot)} = \frac{1}{\Lambda} \frac{\mathrm{T}}{\theta_{\alpha}(\mathrm{rot})} \tag{2.14}$$

$$e_{\alpha}^{(rot)} = R_{\alpha} T$$

$$C_{v,\alpha}^{(rot)} = R_{\alpha}$$

Where

- Λ is a symmetry factor that is 2 for homo nuclear and 1 for heteronuclear molecules. The characteristic temperature for rotation is written as follows in terms of the molecule's moment of inertia i:

$$\theta = \frac{h^2}{8\pi^2 k I} \tag{2.15}$$

Vibration: The following relations are found for a frequency harmonic oscillator: [16]

$$Q_{\alpha}^{(vib)} = \frac{1}{1-e^{\frac{-\theta}{T}}} \qquad (2.16)$$

$$e_{\alpha}^{(vib)} = \frac{R_{\alpha}\theta\alpha}{e^{\frac{\theta_{\alpha}^{xib}}{T}}} - 1$$

$$C_{v,\alpha}^{(vib)} = \frac{R_{\alpha}\left(\frac{\theta_{\alpha}^{vib}}{\mathrm{T}}\right)^{2} e^{\frac{\theta_{\alpha}^{ub}}{T}}}{\left[e^{\frac{\theta}{T}} - 1\right]^{2}} \qquad (2.17)$$

The above relationships were calculated using an infinite number of vibrational energy states. The number of vibrational states is assumed to be finite at sufficiently high temperatures that dissociation occurs, and the upper vibrational level is assumed to correspond to dissociation energy. The following are the results in this case:

$$\theta_{\alpha}^{vib} = \frac{hV}{k} \qquad (2.18)$$

Zero-point energy:

Since the zero-point energy is constant, the following relations are obtained for it:

$$Q_{\alpha}^{0} = e^{\frac{-\theta_{\alpha}^{0}}{T}} \qquad (2.19)$$

$$e_{\alpha}^{0} = -R_{\alpha}\theta_{\alpha}^{0}$$

$$C_{v,\alpha}^{0} = 0$$

The specific heat capacity of a component at constant volume is calculated as follows:

$$C_{v,\alpha} = C_{v,\alpha}^{(tr)} + C_{v,\alpha}^{(rot)} + C_{v,\alpha}^{(vib)} \qquad (2.20)$$

A component's specific heat capacity at constant pressure is defined as:

$$C_{p,\alpha} = \left(\frac{\partial h\alpha}{\partial \mathrm{T}}\right) \qquad (2.21)$$

Where the enthalpy per unit is the species α mass and is expressed as

$$h_\alpha = e_\alpha + \frac{\rho_\alpha}{P_\alpha} \tag{2.22}$$

The partial pressure of each species is derived by assuming that it acts like a thermally perfect gas and obeys the perfect gas equation.

$$P_\alpha = \rho_\alpha R_\alpha \mathrm{T} \tag{2.23}$$

Using the above equation Cp,α can be expressed as[27]

$$C_{p,\alpha} = C_{v,\alpha} + R_\alpha = C_{v,\alpha} + \frac{R_u}{M} \tag{2.24}$$

2.1.2.3 Mixture properties:

Summing all of the partial densities and partial pressures of all species yields the mixture density and mixture pressure:

$$\rho = \sum \rho\alpha \tag{2.25}$$

$$P = \rho R_u T^{(Tr)} \sum X_\alpha / M_\alpha \tag{2.26}$$

Where

- $X\alpha = \rho\alpha/\rho$ is the mass fraction
- $M\alpha$is the molar weight of the species α
- $R_u$is the universal gas constant
- Ttr is the translation temperature.
- Translational and rotational modes are given the same temperature.

$T_{n2}{}^{vib}$,$_2{}^{vi}$,$T_{NO}{}^{vib}$ .For the vibrational modes of the molecular components, separate temperatures is introduced. When considering flows in thermal equilibrium, numerical simulations assign a same temperature to all modes. The translational pressure is the only factor that affects the pressure.

The sum of kinetic and interior energies is defined as the total energy E per unit mass:

$$E = \frac{1}{2}\left(u^2 + v^2\right) + \sum X_\alpha e_\alpha \tag{2.27}$$

Where

- eα is the total specific energy per unit mass of the species α,
- u and v are the velocity components x, y indirections, respectively. The mixture's specific heat capacities are provided by

$$C_v = \sum X_\alpha C_{v,\alpha} \tag{2.28}$$

$$C_p = \sum X_\alpha C_{p,\alpha} = C_v + R_u \sum X_\alpha / M_\alpha \tag{2.30}$$

The ratio of specific temperatures is calculated as follows:

$$\gamma = \frac{C_p}{C_v} = 1 + \frac{R_u}{C_v} \sum \frac{X_\alpha}{M_\alpha} \tag{2.31}$$

The total enthalpy per unit mass is calculated as follows [16]

$$\mathrm{H} = \mathrm{E} + \frac{\mathrm{p}}{\rho} \tag{2.32}$$

2.1.3 Chemical kinetic model:

The chemical source names are formed from reactions that take place between the gas's constituents. A mass transfer mechanism occurs between species as reactions occur. The term wα on the right-hand side of the species conservation equation represents this. Eq. 2.1

The formulas for these mass transfer rates are determined in this section. Several separate elementary chemical reactions between species in the gas can take place at the same time.Consider the rth chemical reaction of Nr elementary reactions between Ns chemically reacting species:

$$\sum v'_{\alpha,r} X_\alpha = \sum v''_{\alpha,r} X_\alpha \tag{2.33}$$

Where

- $v'_{\alpha,}$ and $v''_{\alpha,}$ represent the stoichiometric mole numbers of reactants and products of reaction r , respectively.
- $X_\alpha$is the molar concentration of the species α.

There is a forward and backward portion to the chemical reaction equation, eq. 2.34. The forward and backward reaction rates are calculated as follows:

- Forward:

$$\frac{d\left[X_\alpha\right]_r^f}{dt}=\left(v_{\alpha,r}^{''}-v_{\alpha,r}^{'}\right)\left[k_{f,r}\prod_{\alpha=1}^{N_s}\left[X_\alpha\right]^{v_{\alpha,r}^{'}}\right] \tag{2.34}$$

- Backward:

$$\frac{d\left[X_\alpha\right]_r^b}{dt}=\left(v_{\alpha,r}^{*}-v_{\alpha,r}^{'}\right)\left[k_{b,r}\prod_{\alpha=1}^{N_s}\left[X_\alpha\right]^{v_{\alpha,r}^{*}}\right] \tag{2.35}$$

Where

- K_f, r and $K_{b,r}$ are the forward and backward reaction rate coefficients of reaction r, which are both affected by the temperature of the reaction.
- The net rate for the above general reaction r can be written as

$$\frac{d\left[X_\alpha\right]}{dt}=\frac{d\left[X_\alpha\right]_r^f}{dt}-\frac{d\left[X_\alpha\right]_r^b}{dt}=\left(v_{\alpha,r}^{*}-v_{\alpha,r}^{'}\right)\left[k_{f,r}\prod_{\alpha=1}^{N_s}\left[X_\alpha\right]^{v_{\alpha,r}}-k_{b,r}\prod_{\alpha=1}^{N_s}\left[X_\alpha\right]^{v_{\alpha,r}^{'}}\right] \tag{2.36}$$

The equation above is a general form of the law of mass action, which assures that total mass is preserved during a chemical reaction. The mass rate of species production per unit volume is calculated as follows:

$$w_\alpha=\frac{d}{dt}\left(\rho_\alpha\right)=M_\alpha\sum_{r=1}^{N_r}\frac{d}{dt}\left[X_\alpha\right]_r \tag{2.37}$$

When the necessary equations for the forward and backward rate coefficients are provided for a collection of Nr reactions, a chemical kinetic model is defined. Experimentally measured forward reaction rates are common. Many reactions have empirical relationships that can be connected in the form of:

$$K_{f,r}=C_{f,r}T_{f,r}^{n_{f,r}}e^{\frac{-E_{f,r}}{kT_{f,r}}} \tag{2.38}$$

Where

- $E_{f,r}$is the activation energy
- $C_{f,r}$is a constant

The Arrhenius equation is known as equation 2.39. Experimental data is used to determine the parameters $C_{f,}$, $n_{f,r}$, and the activation energy $E_{f,r}$ for various reactions. The backward reaction rate coefficients are presented under the normal assumptions.

$$k_{b,r} = \frac{k_{f,r}\left(T_{b,r}\right)}{k_{eq,r}\left(T_{b,r}\right)} \tag{2.39}$$

2.1.3.1 Dissociation

In chemistry, the dissociation energy of a bond (D0) refers to one of the measurements of the energy of a chemical bond. It corresponds to the change in enthalpy during homolytic cleavage1 with reagents and products of the hemolysis reaction at 0 K (absolute zero). Moreover, the dissociation energy of a bond is sometimes called the enthalpy of dissociation of a bond. However, these terms are not strictly equivalent because the enthalpy of dissociation of a bond refers to the dissociation reaction under normal conditions of temperature and pressure. This leads to a difference of about 1.5 kilocalorie per mole (kcal/mol), or 6 kJ/mol, in the case of a hydrogen bond in a large organic molecule

2.1.3.2 Chemical equilibrium constant

In chemistry, equilibrium constant characterizes the steady state of a chemical system. It is therefore associated with a state of the system that cannot evolve spontaneously. The value of the equilibrium constant depends only on the chemical reaction considered and the temperature. Equilibrium constants are usually given at 25 °C.

The main equilibrium constants are presented in the following table.

Table 2-I: The main equilibrium constants**.**

Constante d'équilibre	**Symbole**	**Type d'équilibre**
Produit ionique de l'eau	Ke	Dissociation de l'eau
Produit de solubilité	Ks	Équilibrehétérogèneentreunesubstancefaiblementsolubleetsesionsdansunesolutionsaturée
Constante de dissociation (Constante d'acidité et Constante de basicité)	Ka et Kb	Dissociation d'un acide faible ou d'une base faible
Constante de complexation	ßn	Formation d'un ion complexe
Constante de partage ou de distribution	KD	Équilibre de distribution entre des solvants non miscibles

.

The constants defined in the expression of the equilibrium constant, which appears in the expression of the inverse constant of the reaction velocity are listed in the table below and the equilibrium constant (Keq) is defined as follows

$$K_{eq}(T) = \exp\left(C_0 + C_1 z + C_2 z^2 + C_3 z^3 + C_4 z^4\right), z = \frac{10000}{T} \qquad (2.30)$$

2.1.4 Model of chemical kinetics

Modern studies of the properties of gases through which an intense shock wave passes take into account the important effect that play, in the assessment of internal energy, the dissociation (if it is a poly atomic gas) and ionization. The energy delivered to the passage of the front is indeed large enough to excite these "distant" degrees of freedom, therefore, a wave shock of 7,000 m/s passing through the ambient air leaves oxygen fully dissociated, nitrogen half dissociated, and a proportion of electrons in the region of 0.1%.

Considering, the Earth's atmosphere a binary mixture of 21% of O2 and 79% of N2 (by volume) and neglecting argon (about 1%) and all traces of the other constituents.

Behind the normal shock wave, these species dissociate and ionize, forming new species, thus the air presents itself as a reactive gas mixture formed from the species next: N2, O2, NO, N, O ,ionized species: NO+, O+, N+, O+ and free electrons.

It is necessary to adopt a kinetic model to describe the reactive medium and to study the velocities reactions and the production rates of the species to determine the parameters thermodynamic and chemical properties of the reactive mixture.

Three reaction schemes of increasing complexity are presented above

2.1.4.1 1- Model has three reactions:

As a first approximation we use the approximate air model has 3 reactions and 5 components commonly called Zeldovich's model.

$$O_2 + N_2 = 2O + N_2 \quad (r = 1)$$

$$N_2 + O = NO + N \quad (r = 2)$$

$$NO + O = O_2 + N \quad (r = 3)$$

2.1.4.2 Model has six reaction

The mechanism can be completed by introducing three additional types of collisions reactive between O2 and N, NO and N2 respectively.

2.1.4.3 Model has 17 reactions

$$N_2 + M = 2N + M \quad (r = 1 \text{ à } 5)$$

$$O_2 + M = 2O + M \quad (r = 6 \text{ à } 10)$$

$$NO + M = N + O + M \quad (r = 11 \text{ à } 15)$$

$$NO + O = N + O_2 \quad (r = 16)$$

$$N_2 + O = NO + N \quad (r = 17)$$

Considering a catalyst M whose role is simply to allow the dissociation reaction or recombination, the first 15 elementary dissociation reactions can be written in a more compact form, as follows two types of reactions are distinguished in the model:

Dissociation reactions: These are the reactions r = 1 to 15, the dissociation of the molecules behind the shock thus results in a decrease in temperature. The preponderance of molecular nitrogen in the mixture increases the area of imbalance due to the fact that the nitrogen molecule which has a characteristic temperature of significant dissociation, dissociates with difficulty.

Exchange reactions: Are the reactions r = 16 and r = 17 (sometimes called ≪shuffle reactions≫) Exchange reactions are the two most important reactions for oxide formation nitric, in the air.

2.1.4.4 Model of 21 reactions

The chemical reactions model used is proposed by Park (1985) which is applied to seven air species (O, N, NO, O2, N2, NO+ , e) with 24 elementary reactions. The primary chemical reactions con-idered between species are

$$O_2 + M = O + O + M \ \ (r = 1 \text{ à } 6)$$
$$N_2 + M = N + N + M \ (r = 7 \text{ à } 12)$$
$$NO + M = N + O + M \ (r = 13 \text{ à } 18)$$
$$O + N_2 = NO + N \ (r = 19)$$
$$NO + O = O_2 + N \ (r = 20)$$
$$N + O = NO^+ + e^- \ (r = 21)$$

In these equations, M represents (O, N, NO, O2, N2, e^-). The 3 fist equations are dissociation–recombination reactions, whereas Eqs. 4 and 5 are exchange reactions. Equation 6 is an associative-ionization reaction, and its inverse is a dissociative–recombination reaction. The associative-ionization mechanism in Eq.6 dominates for shock speeds below 9 km⁄s; the present study focuses on the lower-temperature regime; for higher temperatures, the chemistry model must include O2, O, and N2 [17]

2.1.4.5 Model of 31 reactions

In this study, a theoretical methodology for thermochemical non-equilibrium flow is applied to study the hypersonic thermochemical non- equilibrium environment of an entry configuration in ionized flow. The high temperature flow after shockwave is treated as a mixture of 11 species (N2, O2, NO, O, N, NO+, N2+, O2+, N+, O+, In order to effectively

verify the reliability of the method, the method is taken to calculate the hypersonic aerodynamic heating environments of an aerodynamic shape in advance.The method is then applied to research the effects of ionization and wall catalysis on the hypersonic thermochemical non-equilibrium environment of the entry configuration in ionized flow.

$$N2 + M = 2N + M \ (r=1 \text{ à } 6)$$

$$O2 + M = 2O + M \ (r = 7 \text{ à } 12)$$

$$NO + M = N + O + M \ (r = 13 \text{ à } 18)$$

$$N2 + O = NO + N \ (r=19)$$

$$NO + O = O2 + N \ (r=20)$$

$$N + e = N^{+} + e^{-} + e^{-} \ (r=21)$$

$$O + e = O^{+} + e^{-} + e^{-} (r=22)$$

$$N + O = NO^{+} + e^{-} \ (r=23)$$

$$N + N = N2^{+} + e^{-} \ (r=24)$$

$$O + O = O2^{+} + e^{-} \ (r=25)$$

$$O^{+} + N2 = N2^{+} + O \ (r=26)$$

$$NO^{+} + O = O^{+} + NO \ (r=27)$$

$$NO^{+} + O2 = O2^{+} + NO \ (r=28)$$

$$NO^{+} + N = N^{+} + NO \ (r=29)$$

$$O + O_2^{+} = O2 + O^{+} \ (r=30)$$

$$N + NO^{+} = \ NO + N^{+} \ (r=31)$$

2.2 Turbulence model

2.2.1 Introduction:

In the literature, three main methods to modelling turbulent flows are provided.

Statistical Navier Stokes equations modelling, direct simulation, and large-scale simulation are examples of these. **[18]**The modelling and simulation of turbulence are fundamentally different.

2.2.2 Direct Simulation (DNS):

The direct numerical simulation of turbulence (DNS) involves numerically solving the Navier-Stokes's equations in space and time with physically consistent accuracy, in order to resolve all of the important turbulent scales whose size is dictated by the fluid's viscosity. If the mesh is fine enough, the time step is short enough, and the numerical scheme is designed to minimize dissipation errors **[18]**. Because it necessitates considerable computing power, this technology is difficult to apply to moderately complex industrial applications.

2.2.3 Large Eddy simulation (LES):

This technology is intermediate between statistical approach (RANS) and simulation (DNS). Indeed, large structures that depend on the geometry of the flow are directly simulated (DNS) while smaller **[18]**much more scales are modelled (RANS).This means that large scales that transmit mass, quantity of movement, and energy must be clearly represented without the use of a model, whereas small vortex-nary structures, are modelling.

2.2.4 Statistical modelling (RANS):

RANS (Reynolds Averaged Navier Stokes), is used to describe the mean movement of turbulent flow **[18]**. The mixing-length model, two-level models, the Algebraic Stress Model (ASM), and the second-order Reynolds Stress Model are among the models that have been created (RSM). It's a model that produces good results while requiring minimal IT resources.
Averaged equations:

Direct simulation of the instantaneous Navier-Stokes's equations is still limited to low Reynolds number flows and simple geometric designs. When we're looking for realistic flows, an alternative is to be just interested in average quantities and hence to acquire the system of equations that these quantities verify. To do so, practice the Reynolds decomposition on the problem's unknowns and apply the set average operator to the instantaneous equations. Averaged equations are the new equations obtained **[19]**

The solution of the general equations of viscous fluid motion, which include the continuity and Navier-Stokes's equations, is required for many flows of technical significance. As a result,continuity equation can be written as:

$$\frac{\partial u_i}{\partial x_i} = 0 \tag{2.41}$$

And the momentum equation

$$\frac{\partial u_t}{\partial t} + u_j \frac{\partial u_t}{\partial x_j} = -\frac{1}{\rho}\frac{\partial p}{\partial x_i} + \nu \frac{\partial^2 u_t}{\partial x_j \partial x_j} \tag{2.42}$$

2.2.4.1 The equations of mean motion

In the case where the flow is turbulent, decomposing the instantaneous variables (such as velocity components and pressure) into a mean value and a fluctuating value is desirable.

$$u_{t(s,t)} = U_{(s,t)} + u_{(s,t)} \tag{2.43}$$

$$p_{t(\dot{x},t)} = p_{t(x,t)} + P'_{t(x,t)} \tag{2.44}$$

When measuring flow quantities, we are more interested in mean values than fluctuating values. Instead of that, solving numerically the Navier-Stokes's equation would necessitate an extremely fine grid to resolve all turbulent scales, as well as a fine time resolution.
We get the following result for the mean field by introducing the Reynolds decomposition into the continuity equation and obtaining the ensemble mean:

$$\frac{\partial U_i}{\partial x_i} = 0 \tag{2.45}$$

We get the velocity fluctuations by subtracting this equation from the equation of instantaneous motion continuity:

$$\frac{\partial u_i}{\partial x_i} = 0 \tag{2.46}$$

As a result, we can see that both the mean and fluctuation quantities confirm the continuity equation.

The following are the three components of the average velocity:

$$\frac{\partial U_i}{\partial t} + U_j \frac{\partial U_i}{\partial x_j} + u_j \frac{\partial u_i}{\partial x_j} = -\frac{1}{\rho}\frac{\partial P}{\partial x_i} + v\frac{\partial^2 U_i}{\partial x_j \partial x_j} \tag{2.47}$$

The incompressibility criterion for fluctuations implies that:

$$u_j \frac{\partial u_i}{\partial x_j} = \frac{\partial u_i}{\partial x_j} \tag{2.48}$$

The Reynolds tensor is therefore defined as follows

$$R_{ij} = -\rho \overline{u_i \dot{u}_j} \tag{2.49}$$

Finally, the averaged equations are written as

$$\frac{\partial U_i}{\partial t} + U_{,} \frac{\partial U_i}{\partial x_j} = -\frac{1}{\rho}\frac{\partial P}{\partial x_i} + \frac{1}{\rho}\frac{\partial}{\partial x_j}\left(\overline{\tau_{ij}} + R_{ij}\right) \tag{2.50}$$

Where,

$$\bar{\tau}_{iJ} = \mu\left(\frac{\partial U_l}{\partial x_j} + \frac{\partial U_j}{\partial x_i}\right) \tag{2.51}$$

2.2.4.2 The problem of closure:

We have four unknown functions $U1$,$U2$, $U3$, and P, as well as four equations, the continuity equation and the three NAVIER-STOKES equations, with the Reynolds equations substituting the NAVIER-STOKES equations, for a turbulent issue, we have the 6 unknown functions of the Reynolds tensor $u_i\, u_j$ therefore we have 10 unknown functions but only 4 equations in the general case. The system, is not closed. To solve this problem, you'll need to find a sufficient number of additional equations.

This is the central problem of turbulence, problem of closure. For this, many researchers have invested in the field and several contributions of resolution models have been proposed. Among these models we can cite:

2.2.5 Classification of turbulence models:

There are two types of models in general:

- First-order models (turbulent viscosity models), which involve modeling Reynolds stresses directly using a turbulent viscosity.
- Second-order models: The Reynolds stresses are directly estimated **[20]**There are numerous types of turbulence models for first-order models dependent on the number of equations of fluctuating motion added to the conservation equations:

2.2.5.1 The zero-equation model:

This is a model that uses only the average field equations to find an expression for the Reynolds $uiuj$constraint based on the average values **[21]**Because of their limited uses, zero equation models are being employed less and less in comparison to other models (they completely ignore the locality characteristics of turbulence).

2.2.5.2 One equation model:

In these models, a transport equation is solved for a turbulent variable (typically the turbulent kinetic energy) and an algebraic expression is used to generate a second turbulent quantity (usually the turbulent length scale) **[21]**

2.2.5.3 Two-equation model:

The turbulent kinetic energy k and its dissipation $\varepsilon$are described by two transport equations [21]The Reynolds stress tensor is calculated using an assumption that links the Reynolds stress tensor to velocity gradients and eddy viscosity:

2.2.5.4 K-epsilon (k-ε) model

The most frequent model used in Computational Fluid Dynamics (CFD) to simulate mean flow characteristics for turbulent flow conditions is the K-epsilon (k-ε) turbulence model.

It's a two-equation model that uses two transport equations to give a general explanation of turbulence (PDEs) **[22]**The K-epsilon model was created with the goal of improving the mixing-length model. The turbulent length scale is calculated as follows:

$$l = \frac{k^{\frac{3}{2}}}{\varepsilon} \tag{2.52}$$

- The k-ε focus on the mechanisms that influence the turbulent kinetic energy (per unit mass) k.

❖ If we know k and ε, we may present turbulent viscosity as follows::

$$v_t \propto \vartheta l \propto C_\mu k^{\frac{1}{2}} \frac{k^{\frac{3}{2}}}{\varepsilon} = C_\mu \frac{k^2}{\varepsilon} \tag{2.53}$$

In turbulence theory, we consider the $k-\varepsilon$model:

$$k_t = \alpha\left(\frac{k^2}{\varepsilon} k_x\right)_x - \varepsilon \tag{2.54}$$

$$\varepsilon_t = \beta\left(\frac{k^2}{\varepsilon} \varepsilon_x\right)_x - \gamma \frac{\varepsilon^2}{k} \tag{2.55}$$

Where

- k is the turbulence kinetic energy.
- $\varepsilon$is the dissipation rate of turbulent energy.
- α, $\beta and \gamma$are positive constants.

Advantages:

➢ Calculations are more stable and converge more quickly.

Disadvantages: [22]

➢ Unfavorable predictions for:

- swirling and rotating flows,
- flows with strong separation,
- axisymmetric jets,
- certain unconfined flows

➢ Valid only for fully turbulent flows.

2.2.5.4.1 The transport equations for the standard model k – ε:

The kinetic energy of turbulence, k, and its dissipation rate, are computed using the corresponding transport equations: **[21]**

$$\frac{\partial k}{\partial t} + U_j \frac{\partial k}{\partial x_j} = v_t \left[\frac{\partial U_t}{\partial x_j} + \frac{\partial U_j}{\partial x_j}\right] \frac{\partial U_i}{\partial x_j} + \frac{\partial}{\partial x_j}\left[\frac{v_t}{\sigma_k} \frac{\partial k}{\partial x_j}\right] + v \frac{\partial^2 k}{\partial x_t \partial x_j} - \varepsilon \tag{2.56}$$

$$\frac{\partial \varepsilon}{\partial t}+U_j\frac{\partial \varepsilon}{\partial x_j}=\left[\frac{\nu_t}{\sigma_k}\frac{\partial \varepsilon}{\partial x_j}\right]+C_{\partial 1}\nu_t\left[\frac{\partial U_i}{\partial x_j}\frac{\partial U_j}{\partial x_l}\right]\frac{\partial U_t}{\partial x_j}\frac{\partial}{k}-C_{\partial 2}\frac{\partial^2}{k} \quad (2.57)$$

The various closure coefficients of the k model is given as

- $C\epsilon 1$, $C\epsilon 2$ are constants,
- σk, $\sigma \varepsilon$are the turbulent Prandtl numbers for k and $\boldsymbol{\varepsilon}$respective.

The various closure coefficients of the k – $\boldsymbol{\varepsilon}$model is given as

Table 2-II: The constants of the model k-values.

$C\mu$	$C\epsilon 1$	$C\epsilon 2$	$\sigma k,$	$\sigma \varepsilon$
0.09	1.44	1.92	1	1.3

2.2.5.4.2 k-omega k-ω model

The K-omega ($k-\omega$) model is a two-equation model, meaning it adds two additional transport equations to explain the flow's turbulent features. This model also solves two more PDEs.

The conventional k equation is solved, but it is employed as a length determining equation. From its definition $\omega\propto$., this quantity is commonly referred to as specific dissipation.

2.2.5.4.3 The transport equations for the standard model k –ω:

The following transport equations yield the turbulent kinetic energy (k) and the specific rate of dissipation (ω).

$$\frac{\partial(\rho k)}{\partial t}+\frac{\partial(\rho k U_j)}{\partial x_j}=P-\beta^*\rho\omega k+\frac{\partial}{\partial x_j}\left[\left(\mu+\sigma_k\frac{\rho k}{\omega}\right)\frac{\partial K}{\partial x_j}\right] \quad (2.58)$$

2.5.4.6.2 The constants and auxiliary functions for the model k –ω

The various closure coefficients of the k – ω model is given as

Table 2-III: The various closure coefficients of the k – $\boldsymbol{\varepsilon}$model**.**

σk	$\sigma\omega$	$\beta*$	γ	$Clim$	$\beta 0$
0.6	0.5	0.09	1325⁄	78⁄	0.0708

2.2.5.4.4 2.5.4.7 k−ωSST model:

The k−ωSST model predicts flow separation better than most RANS models and a high performance under adverse pressure gradients.

- It can account for the transfer of the primary shear stress in boundary layers with a negative pressure gradient.
- In places with high normal stress, such as standstill and severe acceleration, the SST model creates some substantial turbulence levels. [22]

  The turbulent viscosity is then calculated in the following manner:

$$v_T = \frac{a_1 k}{\max\left(a_1\omega, SF_2\right)} \tag{2.59}$$

2.2.5.4.5 The transport equations for the model k −ωSST [31

$$\frac{\partial \mathrm{k}}{\partial \mathrm{t}} + \mathrm{U_j}\frac{\partial \mathrm{k}}{\partial \mathrm{x_j}} = \mathrm{P_k} - \beta^{*}\mathrm{k}\omega + \frac{\partial}{\partial \mathrm{x_j}}\left[\left(\mathrm{v} + \sigma_{\mathrm{k}}\mathrm{v_T}\right)\frac{\partial \mathrm{k}}{\partial \mathrm{x_j}}\right] \tag{2.60}$$

$$\frac{\partial \omega}{\partial \mathrm{t}} + \mathbf{U}_{\mathrm{j}}\frac{\partial \omega}{\partial \mathrm{x}_1} = \alpha\mathbf{S}^2 - \beta\omega^2 + \frac{\partial}{\partial \mathrm{x}_1}\left[\left(\mathrm{v} + \sigma_{\mathrm{k_T}}\mathbf{v}_{\mathrm{T}}\frac{\partial \omega}{\partial \mathrm{x}_1}\right] + 2\left(1 - \mathrm{F}_1\right)\sigma_{\omega 2}\frac{1}{\omega}\frac{\partial \mathrm{k}}{\partial \mathrm{x}_1}\frac{\partial \omega}{\partial \mathrm{x}_1}\right. \tag{2.61}$$

2.2.5.4.6 The constants of the model $k-\omega SST$

The various closure coefficients of the $k-\omega SST$ model are given as:

Table 2-IV: The various closure coefficients of the $k-\omega SST$.

a1	a2	β1	β2	β∗	σk1	σk2	σω1	σω2
59⁄	0.44	340⁄	0.0828	9100	0.85	1	0.5	0.856

2.2.5.4.7 Model to N≥2 equations:

Despite the fact that two-equation models produce good results in a variety of applications, this is not the case for some complex flows, such as gradient verses fed flows. **[22]**

2.3 Wall function:

Some mature turbulence models, are only valid in fully formed turbulence and do not function well in the vicinity of the wall. The employment of so-called wall functions, which can model the near wall region. The first cell center must be positioned in the log-law zone to assure the accuracy of the outcome. Wall functions are empirical equations used to fulfill the physics of the flow in the near wall region.

Rather than specifying boundary conditions at the wall, wall functions are utilized to bridge the inner region between the wall and the turbulence fully formed region in order to provide near-wall boundary conditions for the momentum and turbulence transfer equations. **[23]**. It should be noted that when employing the wall functions approach, the boundary layer does not need to be resolved, resulting in a significant reduction in mesh size and computing

domain. Approximations of "log - layer," are wall functions. The “law of the wall” describes the velocity profile.

$$u(y) = u\tau\kappa(\ln y + C) \tag{2.62}$$

Where

- κ is von Karmar constant
- The constant C is affected by the roughness of the wall as well as the friction velocity.

Wall law:

The wall y+ is a non-dimensional number that determines whether the influences in the wall-adjacent cells are laminar or turbulent, and hence indicates which part of the turbulent boundary layer they resolve.

In a turbulent boundary layer, the subdivisions of the near-wall area can be summarized as follows **[24]**

a) y + < 5: viscous sublayer region (velocity profiles are considered to be laminar, and viscous stress dominates wall shear): **[23]**
b) 5 < y+ < 30: buffer region (both viscous and turbulent shear dominates)
c) 30 < y+ < 300: Fully turbulent portion or log-law region (corresponds to the region where turbulent hear predominate.

Hypersonic Weakly Ionized External

2.4 Introduction

In a hypersonic flow around a blunt body, the presence of a strong bow shock converts the high kinetic energy into numerous internal energy modes causing dissociation and ionization of species.

Ionization has been known to be of particular importance in low-density environments and during atmospheric reentry. Under these conditions, the air must be considered weakly ionized. The plasma around the vehicle traditionally perturbs the communication between the vehicle and the ground control station because the plasma absorbs radio waves **[25]**Furthermore, the plasma affects the surface heat transfer rate, the static temperatures, and the species densities, which are of importance to optimize the design of a hypersonic vehicle.

In previous studies, weakly ionized hypersonic flows were numerically simulated using an electric field model assuming that the movement of electrons was tied to those of the ions. One of the first electric field models was developed by Bird **[26]**where no explicit electric field calculation is made, and so the ions and electrons are not accelerated but the electrons move

with the ions. In later work, Bird modified the method to include a calculation of the electric field as a function of the electron temperature and the gradient of the electron number density **[27]**This equation can be derived from the electron momentum conservation equation using the assumption of negligible inertial effects, negligible friction due to collisions, zero magnetic field, and constant translational temperature. The movement of the electrons is still tied to the ions in this method. In Bird's approach, the assumption of isothermal electrons may not be justified and the assumptions of charge neutrality and coupling of electrons to ions may not be applicable throughout the shock layer **[28]**

In the work of Gallis and Harvey **[29]** a similar approach was made but the assumption of isothermal electrons was not made and the gradient of electron pressure used instead. This approach helps in keeping the simulation time step to correspond to that of the heavy particles. However, this method suffers from the same limitations as that presented by Bird [**[26]**but allows for variable electron temperature. The electric field model created by Gallis and Harvey **[29]** is one of the most popular models used for continuum hypersonic flows. The electric field models are consistent with the ambipolar diffusion assumption, which requires negligible inertial effects, negligible viscous effects, zero magnetic field, and negligible electron–ion momentum exchange through collisions in the charged particle momentum conservation equations and quasi neutrality of the plasma. Unfortunately, the flow is neither quasi neutral in the plasmas heath nor at the interface of the bulk plasma and the ambient neutral gas upstream of the shock layer **[28]**. Charge separation occurs in these regions due to the difference in transport coefficients of the charged particles due to the differences in their masses. To calculate the self-induced electric field without the assumptions of quasi neutrality zero net current or ambipolar diffusion, the electrostatic Poisson's equation must be solved. This was carried out for very rarefied flows surrounding spacecraft in low Earth orbit by Bartel and Justiz **[30]** and Justiz and Dalton **[31]**; however, these simulations are for flow fields of significantly different structures than the shock layer being considered in this study. Coupling the Poisson's equation to the governing equations of a thermochemical weakly ionized flow in the continuum flow regime is one of the objectives of this study.

Another objective of this study is to increase the accuracy of the existing numerical models of the weakly ionized gas in the flow regimes where thermodynamic non equilibrium effects are present. The Poisson's equation is solved together with simplified charged particle momentum conservation equations, which do not assume charge neutrality, zero net current or

ambipolar diffusion. The simplification of the momentum equations of the charged particles requires certain assumptions that are difficult to justify a priori **[32]**; more details are given in the body of this paper.

The ambipolar assumption relies on the simplification of these equations in addition to the assumptions that the density fluxes of electrons and ions must be equal (Γe ΓI) and the plasma must be quasi neutral (Ne NI). By relaxing these two assumptions needed to applied ambipolar diffusion, this study aims to model the physics of the problem more realistically.
We begin by showing in Sec. II the set of governing equations used, followed by the numerical procedure in Sec. III, which includes the conditions of the numerical simulations. The boundary conditions, results, and conclusion are given in Secs. IV–VI.

2.5 Governing Equations

In this section, the governing equations and the ionization model are presented as well as the different approaches used to estimate or calculate the electric field and transport effects of charged particles.

The basic governing equations in the given flight regime are given by Josyula and Bailey and Lee], and the conservation equations for non-equilibrium plasma are given by Appleton and Bray **[33]**.
Additionally, Poisson's equation and the simplified charged particle momentum equations are included to avoid the use of any of the traditional electric field models or ambipolar diffusion assumption.

2.5.1 Species Mass Conservation

The species s mass conservation equation is given by Eq. (2.63):

$$\frac{\partial}{\partial t}\left(\rho_s\right)+\frac{\partial}{\partial x^j}\left(\rho_s u^j\right)=-\frac{\partial}{\partial x^j}\left(\rho_s V_s^j\right)+\dot{\omega}_s \tag{2.63}$$

In Eq. (2.63), the diffusion velocity of species s given by Eq. (2.64):

$$V_s^j=u_s^j-u^j \tag{2.64}$$

The mixture density is the sum of the individual densities of each species; the mass-average velocity component of the fluid mixture is the sum of the mass fluxes of species s due to convection divided by the mixture density; the sum of the "source and sink" term of each species, representing the production and destruction of the given species, is equal to zero; and the sum of the mass flux due to diffusion is equal to zero, as given by the following equations, respectively. These four equations are used to simplify the governing equations given in this section:

$$\rho = \sum_s \rho_s \tag{2.65}$$

$$u^j = \sum_s \rho_s u_s^j / \sum_s \rho_s = \frac{1}{\rho} \sum_s \rho_s u_s^j \tag{2.66}$$

$$\sum_s \dot{\omega}_s = 0 \tag{2.67}$$

$$\sum_s \rho_s V_s^j = 0 \tag{2.68}$$

The primary species of air considered in the present study are diatomic oxygen (O2), atomic oxygen (O), diatomic nitrogen (N2), atomic nitrogen (N), nitrogen oxide molecules (NO), nitrogen oxide ions (NO), and electrons (e−). The significant reactive collisions constituting ω_ s and the respective reaction threshold for the forward (dissociation or ionization) process given in parentheses are **[34]**

$$N_2 + M \rightarrow 2N + M(9.76eV) \tag{2.69}$$

$$O_2 + M \rightarrow 2O + M(5.12eV) \tag{2.70}$$

$$NO + M \rightarrow N + O + M(6.49eV) \tag{2.71}$$

$$N_2 + O \rightarrow NO + N(3.27eV \tag{2.72}$$

$$NO + O \rightarrow O_2 + N(1.37eV \tag{2.73}$$

$$N + O \rightarrow NO^{+} + e^{-} \left(2.76eV\right) \tag{2.74}$$

$$NO + M \rightarrow NO^{+} + e^{-} + M\left(9.25eV\right) \tag{2.75}$$

In these equations, M represents any species in the gas mixture. Equations (2.69-2.71) are dissociation–recombination reactions, whereas Eqs. (2.72) and (2.73) are exchange reactions. Equation (2.74) is an associative-ionization reaction, and its inverse is a dissociative–recombination reaction. The associative-ionization mechanism in Eq. (2.73) dominates for shock speeds below 9 km⁄s; whereas for higher velocities, the electron-impact ionization given by Eq. (2.74) dominates. The present study focuses on the lower-temperature regime; for higher temperatures, the chemistry model must include O2+ , O+, and N2+ **[35].**

As in the work of Josyula and Bailey [9], the dissociation rates are calculated using

$$k_f\left(T_{\text{eff}}\right) = C_f^{*} T_{\text{eff}}^{\eta} \exp\left(\theta_d / T_{\text{eff}}\right) \tag{2.76}$$

The constants C

f, η, and θd are obtained from experiments; they are given in the works of Park [14] for Eqs. (8–12) and Wray [18] for Eq. (13). The effective temperature (Teff TTvp) is given in the work of Park to characterize dissociation reactions involving diatomic species, whereas (Teff TeTvp) when the impact particle is an electron and (Teff T) for reactions involving only mono-atomic species. The recombination (or backward) reaction rate depends only on the temperature of the impacting particles, and is therefore evaluated from

$$k_b\left(T_{\text{eff}}\right) = \frac{k_f\left(T_{\text{eff}}\right)}{K_{\text{eq}}\left(T_{\text{eff}}\right)} \tag{2.77}$$

The equilibrium constant (Keq) is obtained from the same refer-ences as Cf, η, and θd given previously. The effective temperature (Teff T) is given in the work of Josyula for all backward reactions. **[36]**

2.6 Species Momentum Conservation

$$\frac{\partial}{\partial t}\left(\rho_s u_s^i\right) + \frac{\partial}{\partial x^j}\left(\rho_s u^i u^j\right) + \frac{\partial}{\partial x^j}\left(\rho_s u^i V_s^j + \rho_s u^j V_s^i\right) \tag{2.78}$$

$$+\frac{\partial p_s}{\partial x^i}-\frac{\partial \tau_s^{ij}}{\partial x^j}=F_{\text{ele,s}}^i+F_{\text{int},s}^i \tag{2.79}$$

The source terms in the previous equation consist of the interaction force owing to collisions (Fiint;s) and the electric field force (Fiele;s),which acts only on the charged particles. The interaction force term (Fiint;s) is the summation of the elastic terms Fiela;s) and the in elastic terms (Fiinela;s). since all species are asumed to share the total momentum in proportion to their relative mass density, the contribution of inelastic interaction force terms may be neglected (Fiinela;s~ 0); and the electric field force per unit volume Fiele;s) is approximated as

$$F_{\text{eles}}^i \approx N_s \in Z_s E^i \tag{2.80}$$

In Eq. (2.80), the elastic interaction force terms (Fiela;s) can be obtained through the standard method of kinetic theory by assuming that the species velocity distribution functions have Max wellian forms corresponding to the mean velocities of the species [37]

$$F_{\text{cla},s}^i=-N_s M_s \sum_r\left(\frac{M_r}{M_s+M_r}\right)v_s^*\left(u_s^i-u_r^i\right) \tag{2.81}$$

The equation of state is obtained by assuming that each species obeys the perfect-gas law

$$p_s=\rho_s R_s T_s \tag{2.82}$$

Using Eq. (2.82), the electron momentum conservation equation is defined as

$$\begin{aligned}&\frac{\partial}{\partial t}\left(\rho_e u_e^i\right)+\frac{\partial}{\partial x^j}\left(\rho_e u^i u^j\right)+\frac{\partial}{\partial x^j}\left(\rho_e u^i V_e^j+\rho_e u^j V_e^i\right)+\frac{\partial p_e}{\partial x^i}-\frac{\partial \tau_e^{ij}}{\partial x^j}\\&=-N_e\varepsilon E^i-N_e M_e\sum v_{er}^*\left(u_e^i-u_r^i\right)\end{aligned} \tag{2.83}$$

And the ion momentum conservation equation is defined as

$$\begin{aligned}&\frac{\partial}{\partial t}\left(\rho_l u_l^i\right)+\frac{\partial}{\partial x^j}\left(\rho_l u^i u^j\right)+\frac{\partial}{\partial x^j}\left(\rho_l u^i V_l^j+\rho_l u^j V_l^i\right)+\frac{\partial p_I}{\partial x^i}-\frac{\partial \tau_l^{ij}}{\partial x^j}\\&=N_l Z_l\varepsilon E^i-N_l M_l\sum\left(\frac{M_r}{M_l+M_r}\right)v_{lr}^*\left(u_I^i-u_r^i\right)\end{aligned} \tag{2.84}$$

2.7 Total Momentum Conservation

Summing the individual species momentum equations, substituting Eq. (2.85), and noticing that the overall average collisional inter-action force is zero because of conservation of momentum during collisions, the total momentum conservation equation is obtained as in the work of Josyula and ailey **[36]**:

$$\frac{\partial}{\partial t}\left(\rho u^i\right)+\frac{\partial}{\partial x^j}\left(\rho u^i u^j\right)+\frac{\partial p}{\partial x^i}-\frac{\partial \tau^{ij}}{\partial x^j}=\sum_s N_s \varepsilon Z_s E^i \tag{2.85}$$

2.8 Electric Field Model

The ionized relaxation zone in a hypersonic air plasma flow field is described in **Fig 2.2**. For hypersonic flows with temperatures higher than 4000 K, nitrogen oxide molecules ionize by means of an associative-ionization reaction, producing free electrons in the flow-field. The disparity between the electron and ion diffusion coefficient causes an excess of free electrons ahead of the shock wave, leaving positive ions behind the shock and causing a space charge separation (see "region across shock wave" in **Fig 2.2**. The given space charge separation creates an induced electric field responsible for the net force applied to the flow field. The ionized relaxation zone is approximately quasi neutral. Near the wall of the vehicle, the plasma is positively charged with respect to the wall, which is at a lower electric potential, to balance the density flux of ions and the density flux of electrons impacting the surface. The non-neutral region between the relaxation zone and the wall forms a plasma sheath (see "sheath" region in **Fig 9**). The gas is typically assumed quasi neutral between the shock and the body excluding the sheath.

As explained by Josyula and Bailey in many circumstances of interest, the pressure gradient and the electric field term in Eq. (2.86) dominate the momentum balance of electrons. Because of the small mass of electrons, the inertial terms, which are the first three terms in the left-hand side of Eq. (2.86), can be neglected. Since the viscous stress owing to electrons is generally negligible, the viscous term is also neglected. In addition, it is assumed that there is no conduction current in the flow, which neglects the last term in the right-hand side of Eq. (2.86). These derivation and assumptions were shown by Lee enabling an approximate

evaluation of the electric field generated by a charge separation as a function of the electron pressure gradient Ei

$$E^i = -\frac{1}{\varepsilon N_e}\frac{\partial p_e}{\partial x^i} = -\frac{k_b T_e}{\varepsilon}\frac{\partial\left[\ln\left(p_e\right)\right]}{\partial x^i} \tag{2.86}$$

Where Ei1 refers to the axial component Ex and Ei2 refers to the radial component Ey of the electric field. For a spatially homogeneous electron temperature, this form states that the electrons achieve Boltzmann equilibrium with the field [9]. Alternatively, the electric field may be evaluated using ambipolar diffusion theory, which is consistent with the assumptions made to derive Eq. (2.86). For an insulated surface, a positive space charge develops at the boundary, as shown in the sheath region of **Fig 2.2**, due to the significant difference in the transport coefficients (diffusion and mobility) of electrons and ions. This positive charge develops as the faster-moving electrons leave the ions behind, flowing to the surface and causing a negative surface charge density. The positive charge buildup in the sheath region limits the electron density flux to the surface and enhances the density flux of ions. The electrons are attracted by the ions in the sheath and are repelled by the negative charge surface. The opposite is true for ions. Since the surface is insulated, current continuity demands that the net current to the surface be zero; therefore, the density fluxes of electrons and ion must be equal, ergo defining the ambipolar condition:

$$\boldsymbol{\Gamma}_e = N_e V_e = \boldsymbol{\Gamma}_I = N_l V_I = \boldsymbol{\Gamma}_a = -D_a \nabla N$$

$$D_a = D_l\left(1+\frac{T_e}{T_l}\right) \tag{2.87}$$

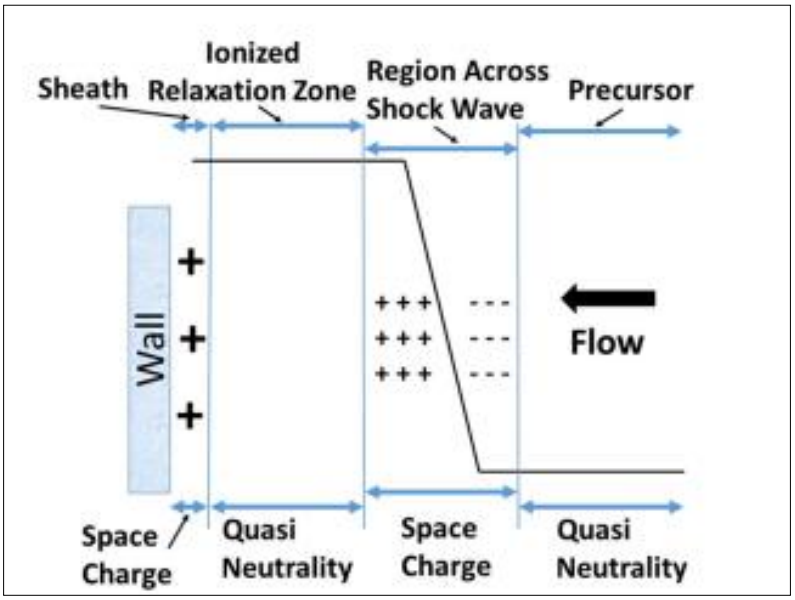

Figure 2-2: Relaxation zone in the shock layer.

The ambipolar diffusion condition assumes that ions and electrons diffuse at the same rate (Ve∼ VI), ions are accelerated by the faster-moving electrons and the electrons are slowed down by the massive slow-moving ions, and quasi neutrality is maintained (N Ne NI). The ambipolar electric field approximation due to equating the density fluxes is given by

$$E = \left(\frac{D_I - D_e}{b_I + b_e} \right) \frac{\nabla N}{N} \tag{2.88}$$

The ambipolar diffusion assumption neglects the plasma sheath region and the charge separation in the shock region. In these two regions, the ambipolar diffusion assumption is not valid and the plasma is not quasi neutral **[38].**

To calculate the self-induced electric field without assuming charge neutrality, zero net current, or ambipolar diffusion, the electro-static Poisson's equation must be solved, which is defined as

$$\nabla \left(\grave{o}_0 \nabla \phi \right) = -\varepsilon \sum_l \left(Z_l N_l - N_e \right) = -\varepsilon \left(N_{NO^+} - N_e \right) = -q_{\text{charge}} \tag{2.89}$$

$$E = -\nabla \phi$$

If the individual species are analyzed separately, the total charge density (q charge) can be obtained and the electric field can be established self-consistently. Solving Poisson's equation requires more stringent time stepping and grid refinement than the electric field model in Eq. (22).

2.9 Electron Energy Conservation

The electron energy conservation equation is

$$\frac{\partial}{\partial t}\left[\rho_e\left(e_e\right)\right]+\frac{\partial}{\partial x^j}\left[\rho_e u^j\left(\frac{1}{2}u^2+e_e\right)\right]+\frac{\partial q_e^j}{\partial x^j}+\frac{\partial}{\partial x^i}\left(u^i p_e\right) \\ =-\sum_f \dot{N}_{e,f}E_{i,f}+P_e+Q_{T-e}-Q_{c-v}+\dot{\omega}_e e_e \tag{2.90}$$

Where (ee) is the electron internal energy given by

$$e_e=\frac{3}{2}\frac{k_b T_e}{M_e} \tag{2.91}$$

For Max wellian distribution. The work done by the electric field on electrons, which is the volumetric joule heating, is

$$P_e=-N_e\varepsilon E^i u_e^i \tag{2.92}$$

The translational energy transfer rate of the elastic collisions of heavy species and electrons is derived from Lee

$$Q_{T-e}=2M_e N_e\sum_{r\neq c}\frac{\nu_{er}^{**}}{M_r}\left(\frac{3}{2}k_b T-\frac{3}{2}k_b T_e\right) \tag{2.93}$$

Where the second effective collision frequency (ver) can be approximated by the first effective collision frequency (ver) given by Eqs. (2.92) and (2.93). Qe–v is the electron-vibration energy transfer, N_ e;f is the rate of ionization by the fth electron-impact ionization process, and Ei;f is the first ionization energy. Finally, the electron heat flux vector is defined as in Ref. , and the cross sections needed to calculate κ 0e and κe are obtained from the work of Gnoffo et al. **[39]:**

$$q_e^j=-\kappa_e^{'}\frac{\partial T_e}{\partial x^j}+\rho_e h_e V_e^j=-\kappa_e^{'}\frac{\partial T_e}{\partial x^j}+\frac{5}{2}N_e k_b T_e V_e^j \tag{2.94}$$

2.10 Total Energy Conservation

The total energy conservation equation is obtained by summation over all species, where (ρe) represents the total energy:

$$\frac{\partial}{\partial t}\left[\rho\left(\frac{1}{2}u^2+e\right)\right]+\frac{\partial}{\partial x^j}\left[\rho u^j\left(\frac{1}{2}u^2+e\right)\right]+\frac{\partial q^j}{\partial x^j}+\frac{\partial}{\partial x^i}\left(u^i p\right) \tag{2.95}$$

$$-\frac{\partial}{\partial x^j}\left(u^i\tau^{ij}\right)=\sum_s N_s\varepsilon Z_s E^i u_s^i \tag{2.96}$$

$$\rho e=\sum_{s\neq e}\rho_s C_{v,s}T+\frac{1}{2}\sum_{s\neq c}\rho_s u^i u^i+\sum_{s=\text{ Datomic}}\rho_s e_{v,s}$$

$$+\left(\rho_e C_{v,e}T_e+\frac{1}{2}\rho_e u^i u^i\right)+\sum_{s\neq e}\rho_s h_s^0+\sum_{s\neq e}\rho_s e_{\text{cl},s} \tag{2.97}$$

The excited electronic state (eel;s) is obtained from Lee and the translational–rotational temperature T of the diatomic species is obtained from Eq. (2.98). The vibrational temperature of the diatomic species (Tv;s) is calculated by inverting the expression for the energy obtained in a harmonic oscillator of species s

$$e_{v,s}=\left(\frac{k_b}{M_s}\right)\left[\frac{\theta_{v,s}}{\exp\left(\frac{\theta_{v_s}}{T_{v,s}}\right)-1}\right] \tag{2.98}$$

The total pressure p is the sum of the partial pressures:

$$p=\sum_{s\neq e}\rho_s R_s T+\rho_e R_e T_e \tag{2.99}$$

Lastly, the total energy equation is completed by defining the total heat flux vector as

$$q^j=-\kappa\frac{\partial T}{\partial x^j}-\sum_{s=\text{ Diatamic}}\kappa_{E,s}\frac{\partial T_{v,s}}{\partial x^j}-\kappa_e\frac{\partial T_e}{\partial x^j}+\sum_s\rho_s h_s V_s^j \tag{2.100}$$

2.11 Vibrational Energy Conservation

In both models presented in this study, four independent vibrational energy conservation equations are used: one for each diatomic species. The vibrational energy conservation equation is solved only for the diatomic species using the Landau–Teller formalism **[40]**The vibrational energy conservation equation is given as

$$\frac{\partial}{\partial t}\left(\rho_s e_{v,s}\right)+\frac{\partial}{\partial x^j}\left(\rho_s e_{\varepsilon,s}u^j\right)=\frac{\partial}{\partial x^j}\left(\kappa_{v,s}\frac{\partial T_v}{\partial x^j}\right)-\frac{\partial}{\partial x^i}\left(\rho_s e_{v,s}V_s^j\right)$$

$$+Q_{T-v}+Q_{c-v}+\dot{\omega}_s e_{v,s} \tag{2.101}$$

In Eq. (2.101), the vibrational energy ev;s represents the total energy in the vibrational manifold, which in this case is assumed as a simple harmonic oscillator. The vibration–vibration exchanges (Qv−v) and their effect on the population depletion model are neglected in the present study, and the translation–vibration exchanges (QT−v) are

$$Q_{T-\varepsilon} = \frac{\rho_s \left(e^*_{v,s} - e_{\varepsilon,s} \right)}{\tau^*_s} \tag{2.102}$$

Where the relaxation time is computed as

$$\tau^*_s = \frac{\sum_r X_r}{\frac{\sum_r X_r}{\tau^*_{r,k}}} \tag{2.103}$$

The electron-vibration energy exchange for the nitrogen molecules is assumed to also be the Landau–Teller form as in Lee **[41]**As explained by Bourdon and Vervisch **[42]**, the coupling of the electron energy with the vibrational energy of diatomic nitrogen is strong due to the exchange processes being very efficient for N2 in comparison to the other molecules of O2, NO, and NO; therefore, this energy exchange term is generally simplified as

$$Q_{e-\gamma} = \frac{\rho_s \frac{M_s}{M_e} \left(e^{**}_{v,s} - e_{v,s} \right)}{\tau_{es}} \tag{2.104}$$

The previous assumption is only valid for certain values of the reduced electric field (E⁄N), where N is the total number density of the gas. “For a reduced electric field on the interval 4 Td < E⁄N < 110 Td (Townsend) in air, the most efficient mechanism for electron energy loss is the excitation of the vibrational levels of nitrogen [molecules (N2)],” where (1 Td 10−21 V · m2) **[25]**.

In the previous equations, the values of ev;s and ev;s are obtained from

$$e^*_{v.s} = \left(\frac{k_b}{M_s} \right) \left[\frac{\theta_{vs}}{\exp\left(\frac{\theta_{Es}}{T} \right) - 1} \right] \tag{2.105}$$

$$e^{**}_{v,s} = \left(\frac{k_b}{M_s} \right) \left[\frac{\theta_{vs}}{\exp\left(\frac{\theta_{vs}}{T_e} \right) - 1} \right] \tag{2.106}$$

And the relaxation times (τr;k) are computed using the expression from Millikan and White . Josyula and Bailey **[36]** and Lee **[37]** should be consulted for more information about the various coefficients and the derivation of the energy conservation equations used in this study.

Chapter 03

Numerical modeling

3 Numerical modeling

3.1 Introduction:

To deal with a fluid mechanics problem, which is all the more true for other branches of physics, the resolution can be established either by an approach:

– analytical: the great advantage of this approach is that it provides exact solutions. However, it is limited for very simple cases by making a number of assumptions.

– experimental: this is surely the approach that best represents reality. On the other hand, it is often difficult to implement and requires some time to resolve all the problems that may be encountered. Not to mention that it can become very expensive very quickly.

– numerical: it makes it possible to make fewer assumptions than an analytical approach and makes it possible to deal with relatively complex problems. Moreover, it can be less expensive than an experimental approach. On the other hand, it is limited by the order of the numerical methods used, the precision of the model and the means of calculation implemented.

Numerical modeling is the transcription of the physical phenomenon into computer language, the efforts and progress made in numerical methods and more particularly in CFD show all the interest that we have for it. On the other hand, the two experimental and numerical approaches are often associated and complementary: before any experimental realization, a preliminary CFD study is often carried out to better identify and gauge the problem. Then, the experiment comes in the final phase to confirm these results.

Simulation almost always comes in the form of a computer program or tools. These are commonly referred to as simulation environments.

3.2 Computational Fluid Dynamics code

CFD codes are structured around numerical algorithms that can be tackle fluid problems. All codes contain three main elements

The pre-processor transforms the input of a flow problem into a suitable form for the use by the solver. The Pre-processing stage involves:

- The computational domain: Definition of the geometry
- Grid generation: the subdivision of the domain into a number of small, subdomains (or control volumes).
- Fluid properties definition.
- Define the solution of a flow problem (velocity, pressure, Temperature) in every signal cell, by the specification of appropriate boundary conditions at cells.

- The accuracy of CFD solutions is governed by number of cells in the grid. In general, the larger numbers of cells better the solution accuracy. Both the accuracy of the solution &it's cost in terms of necessary computer hardware & calculation time are dependent on the fineness of the grid.

3.3 Solver

The FLUENT CFD code has extensive interactivity, so we can make changes to the analysis at any time during the process. This saves time and enables to refine designs more efficiently. The numerical solution of Navier–Stokes's equations in CFD codes usually implies a discretization method: it means that derivatives in partial differential equations are approximated by algebraic expressions which can be alternatively obtained by means of the The governing equations are non-linear and coupled. Several iterations of the solution loop must be performed before a converged solution is obtained. The result is a set of algebraic equations through which mass, momentum, and energy transport are predicted at discrete points in the domain.

Because the governing equations are non-linear and coupled, several iterations of the solution loop must be performed before a converged solution is obtained and each of the iteration is carried out as follows:

1. Fluid properties are updated in relation to the current solution; if the calculation is at the first iteration, the fluid properties are updated consistent with the initialized solution.
2. The three momentum equations are solved consecutively using the current value for pressure so as to update the velocity field.
3. The pressure–velocity coupling is made by the SIMPLE algorithm, as in FLUENT default options:. Since the velocities obtained in the previous step may not satisfy the continuity equation, one more equation for the pressure correction is derived. Once solved, it gives the correct pressure so that continuity is satisfied.
4. Their equations for scalar quantities such as turbulence, chemical species and radiation are solved using the values of the other variables in the original equation.
5. Finally, the convergence of the equations set is checked and all the procedure is repeated until convergence criteria are met.

3.4 Post-Processing:

This is the final step in CFD analysis, [34] and it involves the organization and interpretation of the predicted flow data and the production of CFD images and animations

3.5 Mesh

A mesh is a partition of space or a domain in cells called mesh. Usually convex, it is used to solve an EDP; the mesh must be made in such a way as to minimize the diffusion of the digital error. As well as topological forms of mesh are often two-dimensional triangles or quadrangles, and tetrahedrons, cubes or three-dimensional hexahedrons

3.5.1 Mesh components

- Cell: control volume dividing geometry.
- Face: border of a cell.
- Edge: border of a face.
- Node: mesh point.

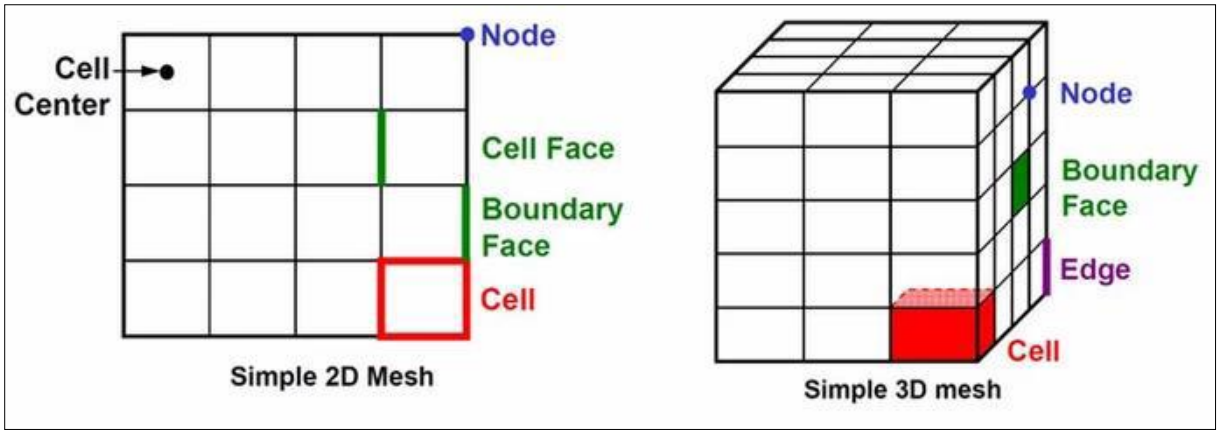

Figure 3-1: Mesh component**.**

3.5.2 Mesh types

3.5.2.1 Structured grid

Refers to that the number of grid cells subordinate to any internal node is the same for all grids within a given computational domain or geometry, and the connection relationship between adjacent cell nodes is apparent boundary without having to store all the information of grids.

3.5.2.2 Body-Fitted Structured Grids

Various configurations can be used depending on the orientation of the grid lines in order to get the requirements for smoothness and continuity of cell sizes, as indicated by the letter to which they are most similar: Grids of the H-type, C-type, O-type, I-type.

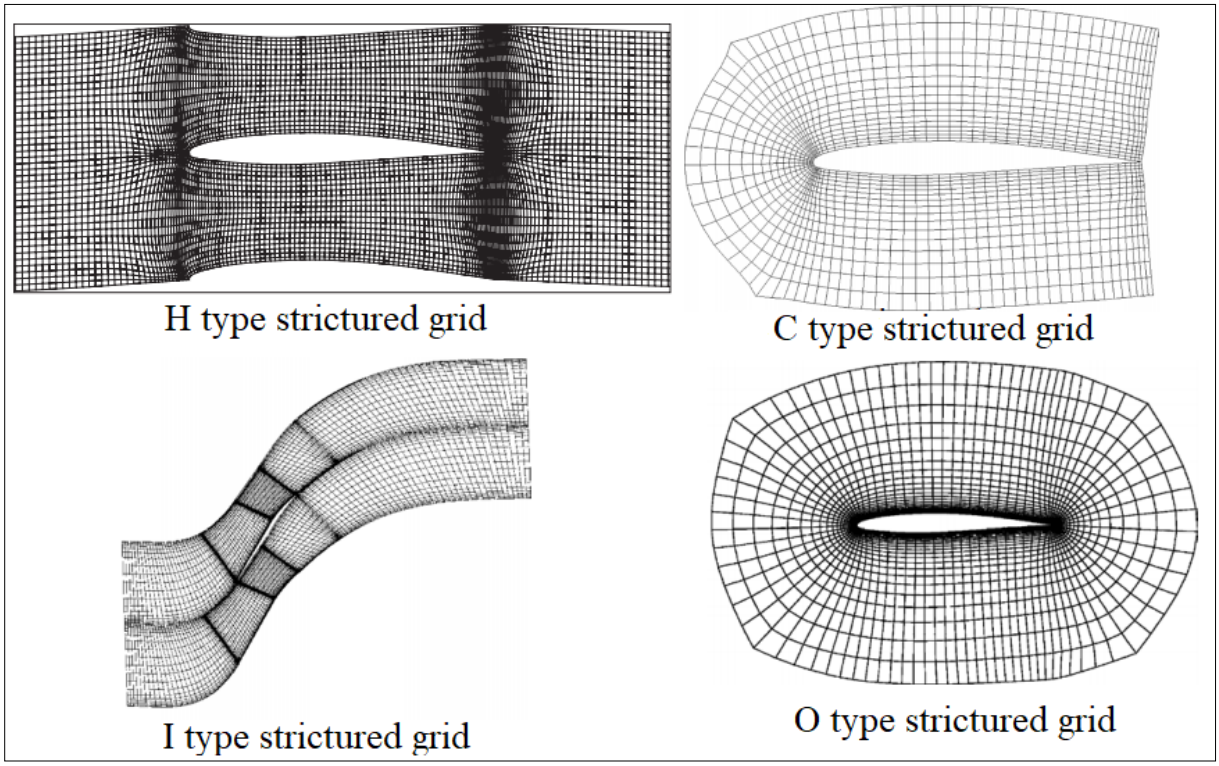

Figure 3-2: Boddy fitted structured grid**. [43]**

.

3.5.2.3 Unstructured mesh:

The elements of this type of mesh are generated arbitrarily without any constraint as to their disposition **[43] [44]**

- In a two-dimensional mesh (2D), the elements that make it up are triangle-type or quadrilateral.
- In three dimensions (3D), we have elements such as tetrahedrons, prisms, hexahedrons and pyramids.

3.5.2.4 Hybrid mesh:

Hybrid meshes contain a variety of elements, such as a mix of triangular and quadrangular elements. This mesh is mostly used to discretize difficult fluid mechanics issues. The four-node elements discretize the rest of the domain of analysis, while the triangles cover the regions around the contact surfaces **[44]**

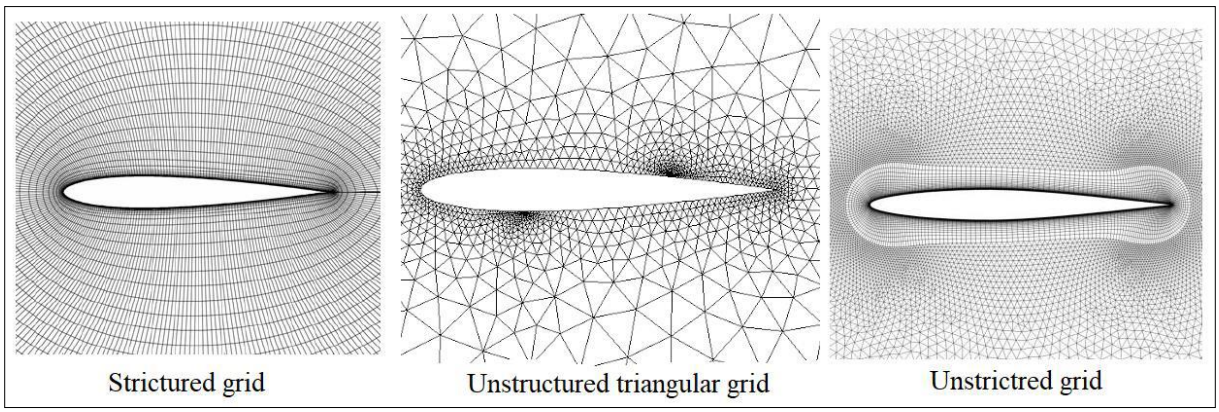

Figure 3-3: Mesh types**. [44]**

Structured	Unstructured
Domain must verify some constraints	Valid for arbitrary domains
More restrictive for dealing with non-constant element size	More flexible for dealing with non-constant element size
Preferable for aligning elements with boundaries / material properties	Can be used for aligning elements with boundaries / material properties
Easier to developed	More complex to develop

Figure 3-4: Structured vs unstructured mesh**. [43]**

3.5.2.5 General mesh generation techniques:

To have a good quality of mesh there are some techniques that allow to achieve a good result, depends on**:[35]**

- ✓ A faithful representation of surfaces
- ✓ A good accuracy of the solution
- ✓ Minimization of calculation times
- ✓ Reduced disk space usage
- ✓ Good Resolution in high-gradient regions.

3.5.2.6 Mesh generation

The generation of the mesh is an important step which will help us to have a good result on our CFD analysis using the necessary parameters that we must follow by using a fine mesh in the vicinity of the object where the phenomena are more dominated, on the other hand, a coarse mesh far from the object to reduce the calculation time and avoid numerical errors between refined and unrefined areas by a transition.

Quality of a mesh:

Mesh Quality refers to the properties of a mesh that allow a numerical PDE simulation to be run effectively **[44]**.With fidelity to the underlying physics, and with the precision required for the problem.

3.5.2.6.1 The different quality criteria

Mesh quality is determined by a number of factors, [44]which are briefly discussed in this section.

3.5.2.6.1.1 Clustering

Ensure that the mesh must be refined enough to resolve the primary features for the analyzed flow [43]The resolution depends on the parameters that control the interior and the initial boundary mesh

3.5.2.6.1.2 Smoothness

The transition from one face or cell to the next in a high-quality mesh should be smooth. Large changes in size between consecutive faces or cells will result in a poor computational grid

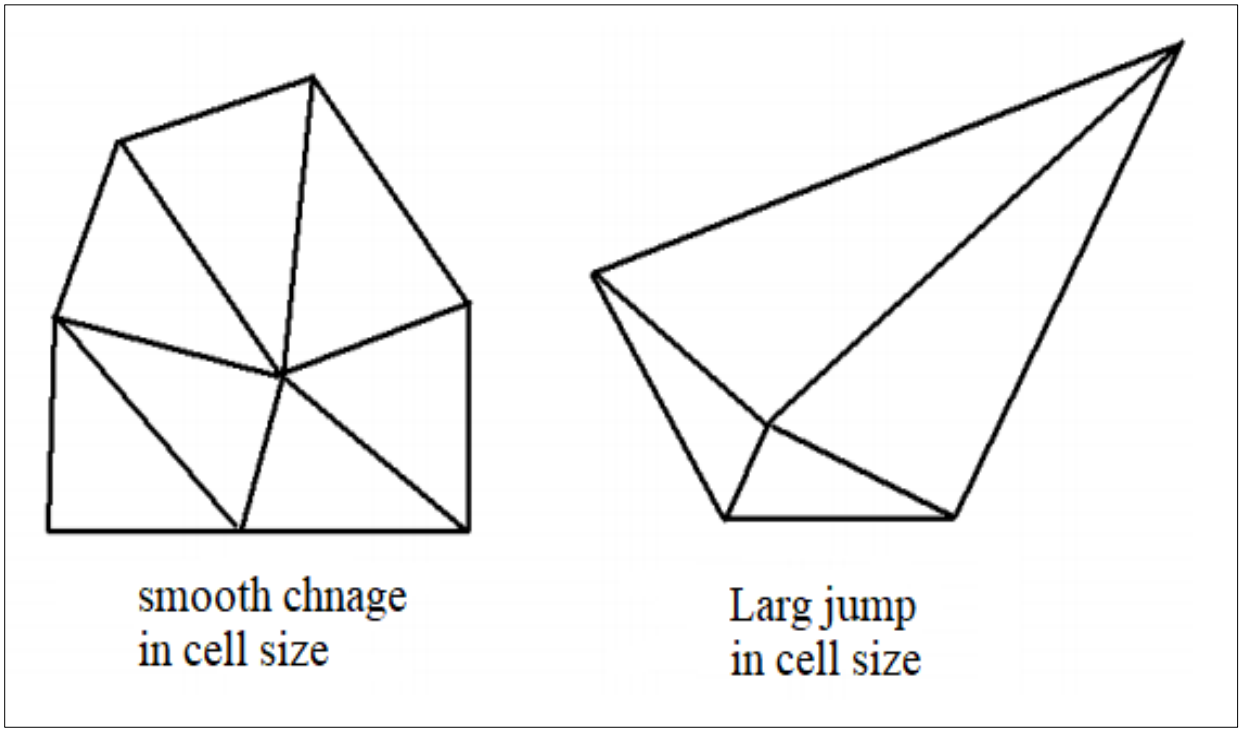

Figure 3-5: Smooth and Non-Smooth Transitions in Cell Size**. [44]**

3.5.2.6.1.3 Aspect ratio

The ratio of the longest edge length to the smallest edge length is the aspect ratio of a face or cell. The aspect ratio is defined differently for each element type and applies to triangular, tetrahedral, quadrilateral, and hexahedral elements. **[35]**

- For an equilateral face or cell, the aspect ratio will be 1.
- For less regularly-shaped faces or cells, the aspect ratio will be greater than 1, since the edges differ in length.
- For triangular and tetrahedral faces and cells, as well as pyramids, we should usually focus on improving the skewness, which will improve the smoothness and aspect ratio as well.

3.5.2.6.1.4 Skewness

One of the most important quality indicators for a mesh which refers to how close a face or cell is to being ideal (i.e., equilateral or equiangular). A number of 0 represents an equilateral cell (optimal) and a value of 1 suggests a fully degenerate cell (worst). **[44]**

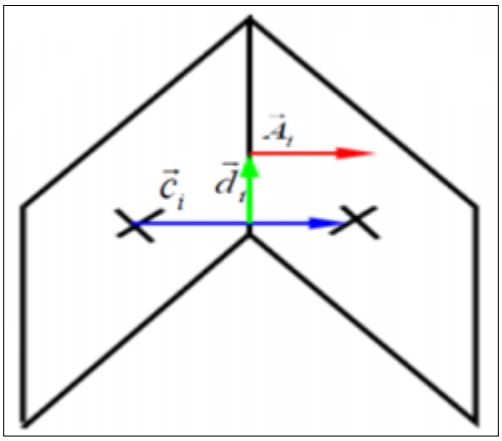

Figure 3-6: Skewness: the distance between the common face center (black dot) and intersection of the common face and line connecting the cell centers. **[44]**

Two methods for determining skewness:

1. Equilateral Volume deviation: Applies only for triangles and tetrahedrons

$$\text{skewness} = \frac{\text{optimal cell size} - \text{cell size}}{\text{optimal cell size}} \tag{3.1}$$

2. Normalized Angle deviation

$$\text{Skewness} = \max\left[\frac{\theta_{max} - \theta_e}{180 - \theta_e}, \frac{\theta_{min} - \theta_e}{\theta_e}\right] \quad (3.2)$$

Where

- θmax= largest angle in the face or cell;
- θmin = smallest angle in the face or cell;
- θe = angle for an equiangular face/cell (60 for tets and tris, and 90 for quads and hexes), Applies to all cell and face shapes **[45]**

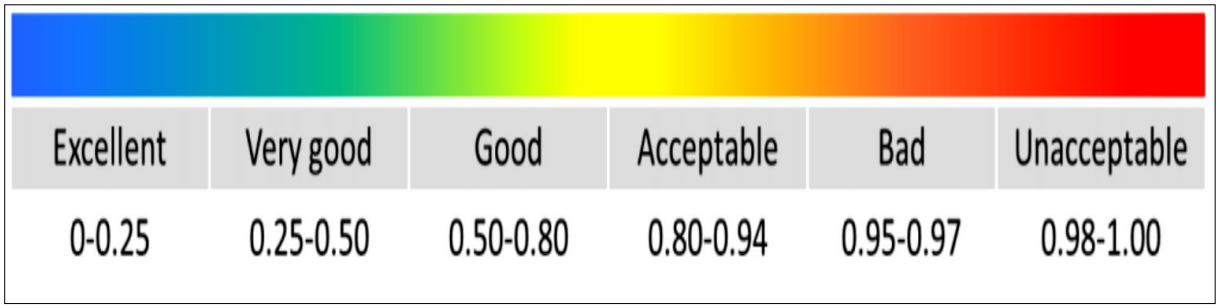

Figure 3-7: Skewness mesh metrics spectrum**. [45]**

3.5.2.6.1.5 Non-orthogonality:

This is a very important parameter of which we measure the angle between the line connecting two cell centers and the normal of their common face. **[45]**

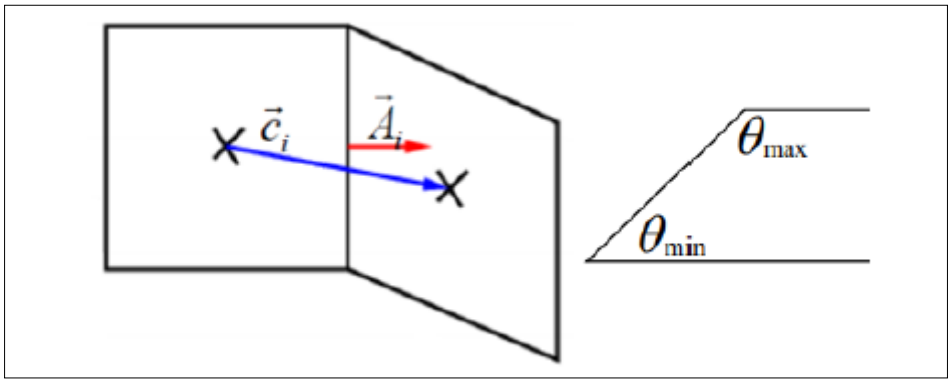

Figure 3-8: Orthogonality: the vector connecting two cell centers and the surface normal vector of their common face**. [45]**

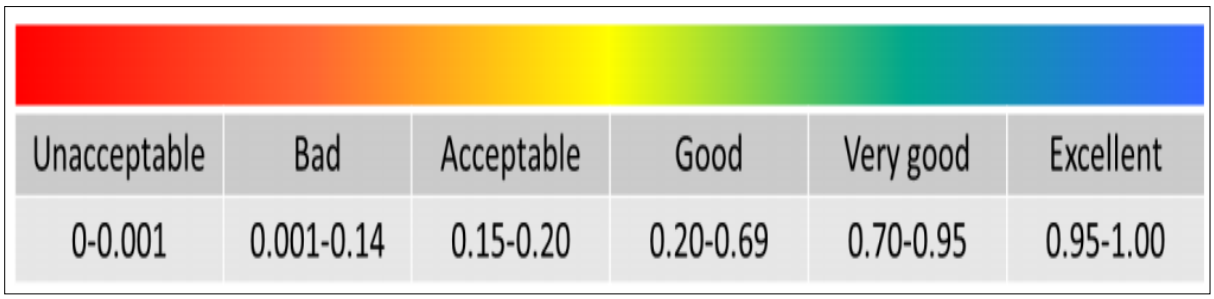

Unacceptable	Bad	Acceptable	Good	Very good	Excellent
0-0.001	0.001-0.14	0.15-0.20	0.20-0.69	0.70-0.95	0.95-1.00

Figure 3-9: Orthogonal Quality mesh metrics spectrum**.**

3.6 Problem and resolution

We aim in this work to perform a simulation of two-dimensional and three-dimensional, viscous and chemically unbalanced hypersonic flows around re-entry atmospheric blunt bodies. We have made the hypothesis of a chemical flow at vibrational equilibrium; and ionization phenomena: for upstream speeds up to 6000 ms-1 **[46]**the radiation only becomes significant from 8000 ms-1 **[46]**

First, the problem was treated around a simple rounded body "half sphere" The rounded body chosen for the simulation was the sphere of "Lobb", to better understand the phenomenon and master the calculation code, then, an attempt was made to carry out a study around a delta profile of a representative shuttle orbiter configuration with the same Lobb sphere radius to determine the re-entry trajectory design.

Finally, we investigated the conceptual design of a re-entry vehicle, by varying the shape and geometry of the vehicle in order to evaluate its impact on performance. We studied the classes of shape optimization in vehicles, con-flare shape, conic body, and capsule fire II.

3.6.1 Mesh and geometry

3.6.1.1 Part A. study of physicochemical processes in a shock layer around a blunt body

The rounded body chosen for the simulation was the "Lobb" sphere experiment performed on a sphere-cone body with **[47] [9]**

The radius of the sphere is R = 6.35mm;

The length of the cylinder is 1.3m.

The study was simulated under the flowing free stream conditions:

Table 3-I: Lobb sphere free stream boundary condition**. [46]**

α	$M\infty$	$Reaction.\ N$	$T\infty[k]$	$\rho\infty(kg/m3)$	$P\infty\ [Pa]$	K	ω
0°	15.35	5	293	$7.896\ 10^{-3}$	664	3245.962	64.607

3.6.1.1.1 Two-dimensional case

3.6.1.1.1.1 Geometry creation

Is the first step in simulation which consists in drawing the geometry of the problem: the body and the surrounding fluid domain, with the ANSYS DesignModeler software.

The geometry was created in a way that the simulation will be run using the axisymmetric Navier-Stock's equations; therefore, a two-dimensional symmetric geometry is created, with an axis defined at the radial center of the studied body. This technique makes it possible to reduce the computational domain used and consequently reduce the calculation time.

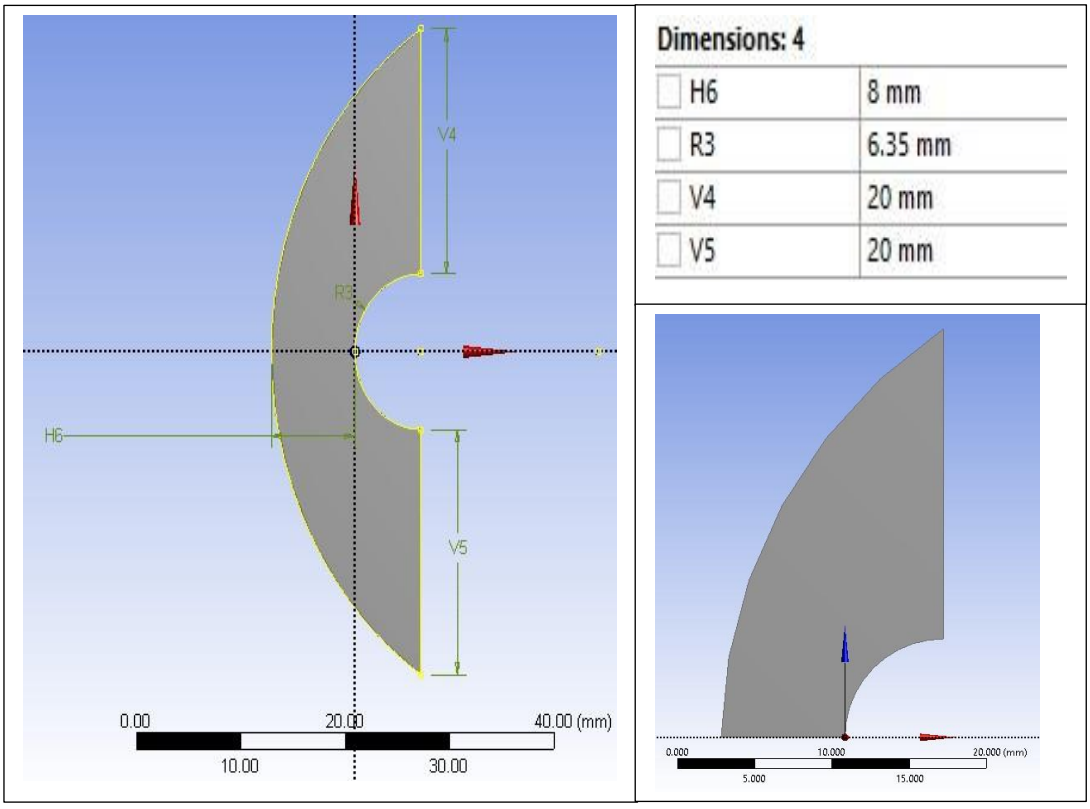

Figure 3-10: Lobb sphere Geometry creation**. (Original)**

3.6.1.1.1.2 Mesh construction

Our geometry is quite simple where the flow is practically the shape of geometry. So, using a quadrilateral cell mesh, we will have flow alignment with our mesh, whereas with triangular cells never will. This last point will guarantee a minimum of digital diffusion. Consequently, an initial 2D structured mesh with quadrilateral cells was carried out.

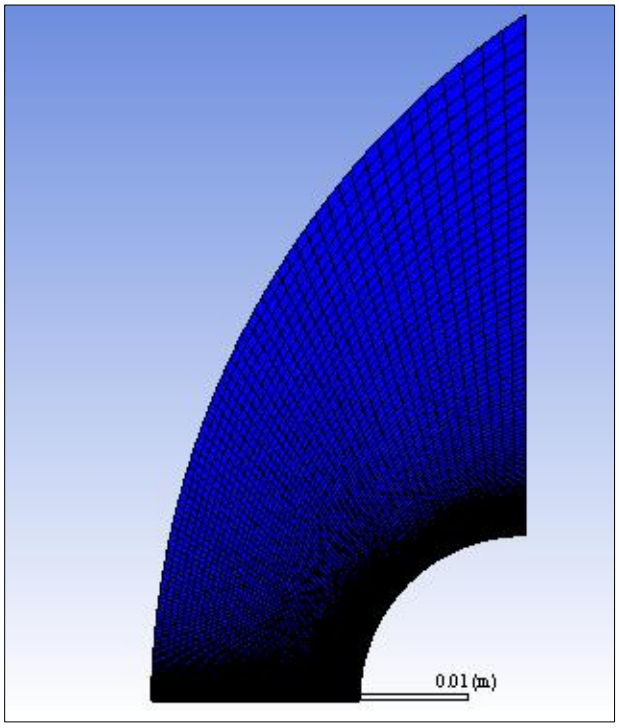

Figure 3-11: Lobb sphere Geometry mesh**. (Original)**

3.6.1.1.1.3 Identification of the boundary conditions

In order to simplify our work later on ANSYS Fluent, we should label each boundary in the geometry by creating named selections (inlets, the outlet, body and the symmetry surface) so we can:

- ✓ Define the boundary conditions of the problem
- ✓ Define the conditions on the mesh at the level of the different selections

In 2D, to express the outputs, inputs, etc., the different edges of the geometry must be selected

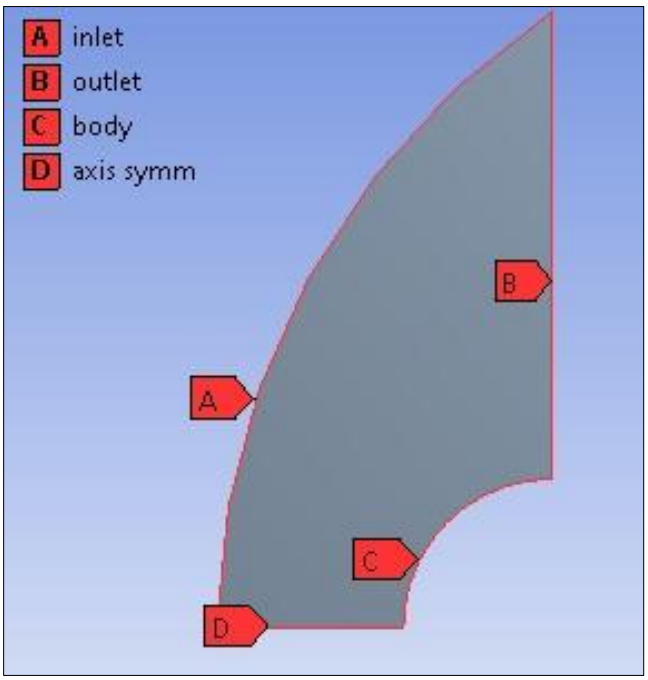

Figure 3-12: Lobb sphere identification of boundary conditions**. (Original)**

3.6.1.1.2 Three-dimensional case

3.6.1.1.2.1 Geometry creation

The geometry was created in a way that the simulation will be run using Navier-Stock's equations in 3D.

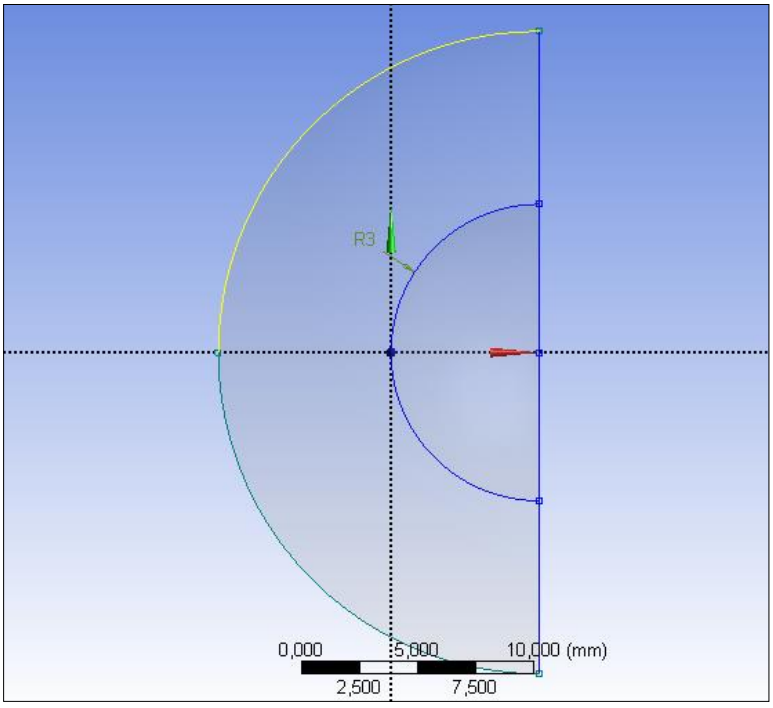

Figure 3-13: Lobb sphere geometry creation 3D**. (Original)**

3.6.1.1.2.2 Mesh construction

Our geometry is quite simple where the flow is practically the shape of geometry. So, using a quadrilateral cell mesh, we will have flow alignment with our mesh.
Consequently, an initial 3D structured mesh with quadrilateral cells was carried out.

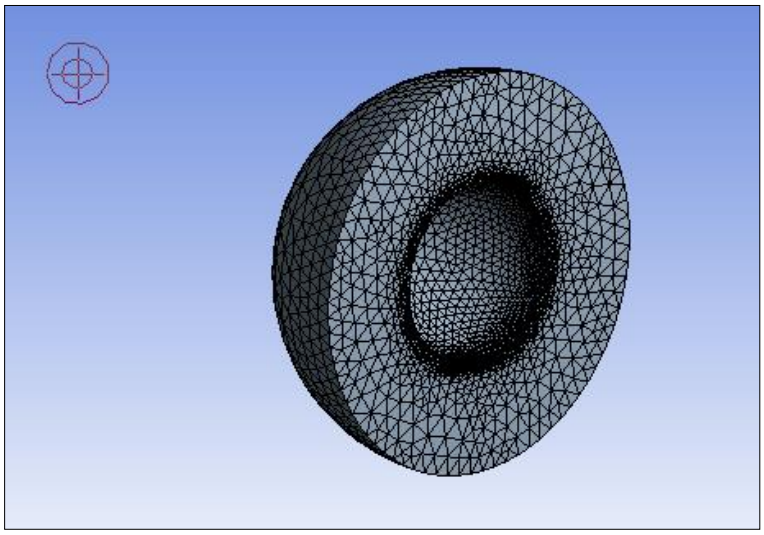

Figure 3-14: lobb sphere geometry mesh 3D**.**

3.6.1.1.2.3 Identification of the boundary conditions

In order to simplify our work later on ANSYS Fluent, we should label each boundary in the geometry by creating named selections (inlets, the outlet, body and the symmetry surface) so we can:

- ✓ Define the boundary conditions of the problem;
- ✓ Define the conditions on the mesh at the level of the different selections.

In 3D, to express the outputs, inputs, etc., the different edges of the geometry must be selected.

3.6.1.2 Conical Geometry

The second geometry is A 2D DART (Delft Aerospace re-entry test vehicle) model, re-entry vehicle has been used to simulate a chemical non-equilibrium flow to investigated the conceptual design of a re-entry vehicle compared with the previous delta body shape. [45]

Table 3-II: Cone flare body free stream boundary condition**. [47]**

α	$M\infty$	$Reaction.\ N$	$T\infty[k]$	$\rho\infty(kg/m3)$	$P\infty\ [Pa]$	K	ω
0°	15.35	17	293	$7.896\ 10^{-3}$	664	3245.962	64.607

3.6.1.2.1 Two-dimensional case

3.6.1.2.1.1 Geometry creation

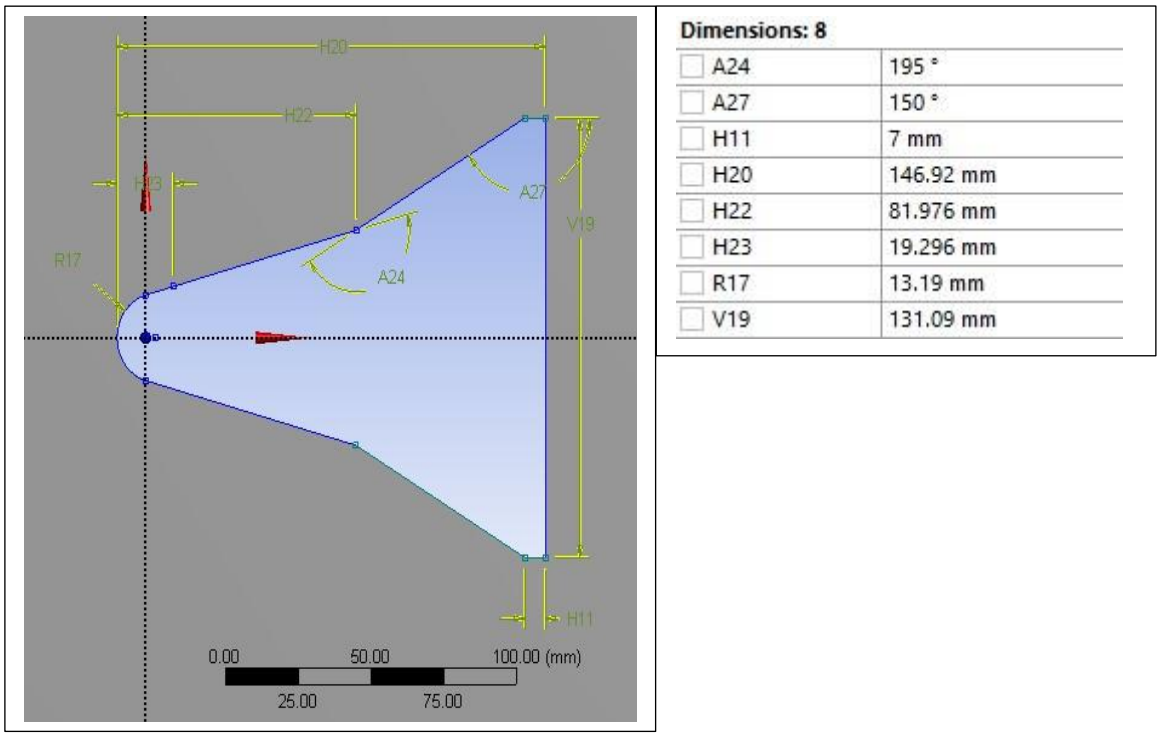

Figure 3-15: Cone-flare geometry creation**.**

3.6.1.2.1.2 Mesh construction

In this model, hybrid meshing is used. The majority of the domain's space is made up of an unstructured grid. All triangles method is inserted in meshing. To establish a structured grid around the (re-entry) vehicle's boundary, edge sizing and inflation are used. The structured grid is made up of 5 layers, each with a thickness of 1 millimeter, and it is used to investigate fluctuations in variables such as temperature, pressure, and Mach number near the boundary. Curvature guides the mesh size function which result in a fine mesh.

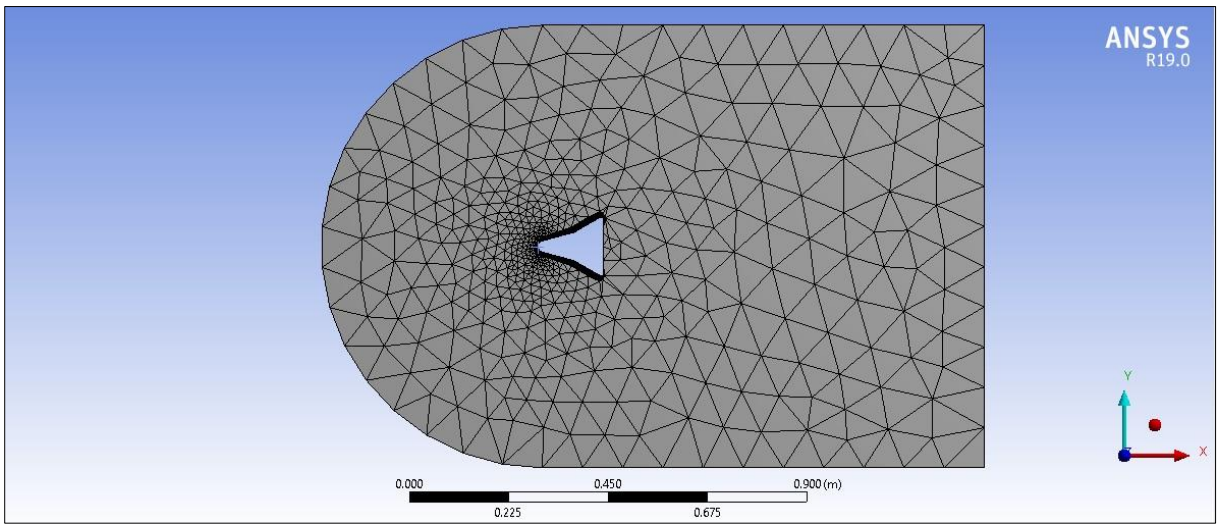

Figure 3-16: Cone-flare geometry mesh**.**

3.6.1.2.2 Three-dimensional case

3.6.1.2.2.1 Geometry creation

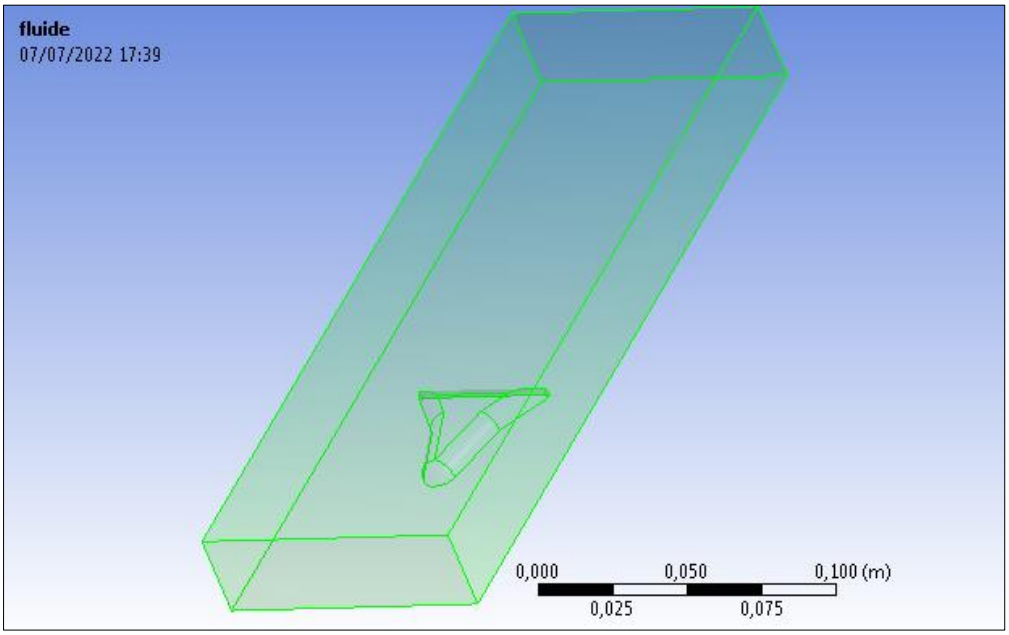

Figure 3-17: Cone-flare geometry creation 3D**.**

3.6.1.2.2.2 Mesh construction

In this model, hybrid meshing is used. The majority of the domain's space is made up of an unstructured grid. All triangles method is inserted in meshing. To establish a structured grid around the (re-entry) vehicle's boundary, edge sizing and inflation are used.

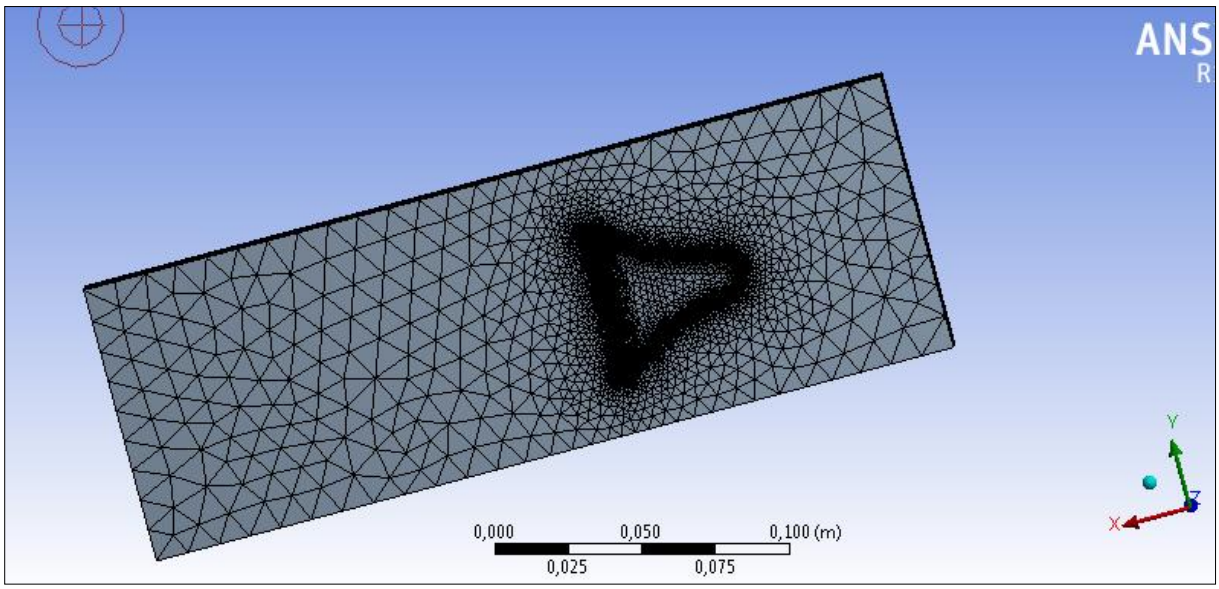

Figure 3-18: Cone-flare geometry mesh 3D**.**

3.6.1.3 Conic body

3.6.1.3.1 Two-dimensional case

3.6.1.3.1.1 Geometric creation

The geometrical sketch of the ELECTRE vehicle is shown in **Fig 3.19**. The Gupta's 5-species chemical reaction model is employed consistent. A fully catalytic wall boundary condition is assumed at the vehicle surface with a constant temperature of 343 K.

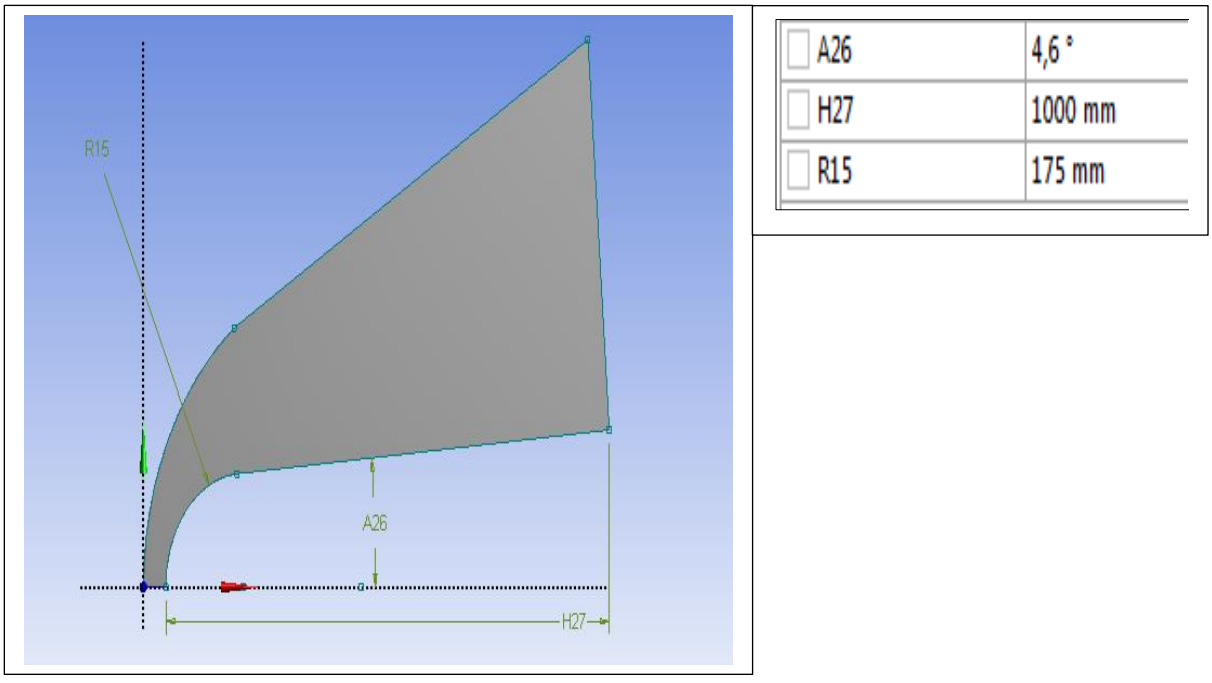

Figure 3-19: Conic body Geometric creation**.**

3.6.1.3.1.2 Mesh construction

A grid independence study is performed with three levels of grid refinement: A (80 x 60), B (80 x 90), and C (80 x 120). All the grids are constructed with normal spacing of 1 x 10^6 m at the surface to ensure that the cell Reynolds number is on the order of one. The resulting grid C is illustrated in **Fig 3.20**.

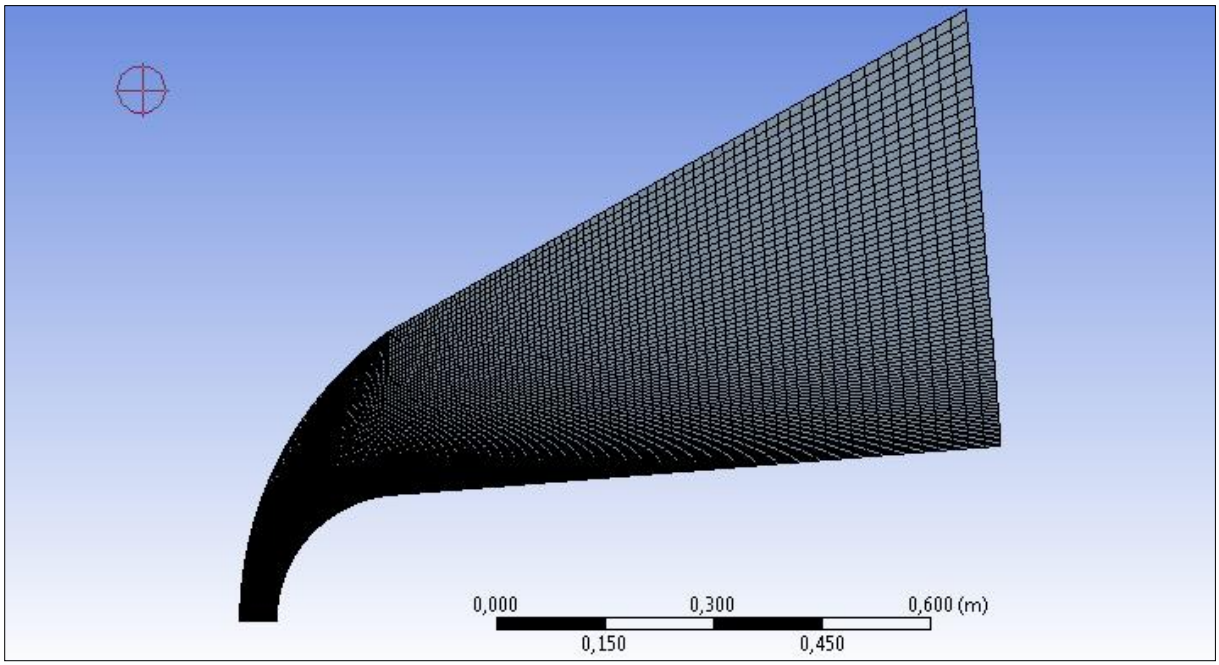

Figure 3-20: Conic body geometry mesh

3.6.1.3.2 Three-dimensional case

3.6.1.3.2.1 Geometric creation

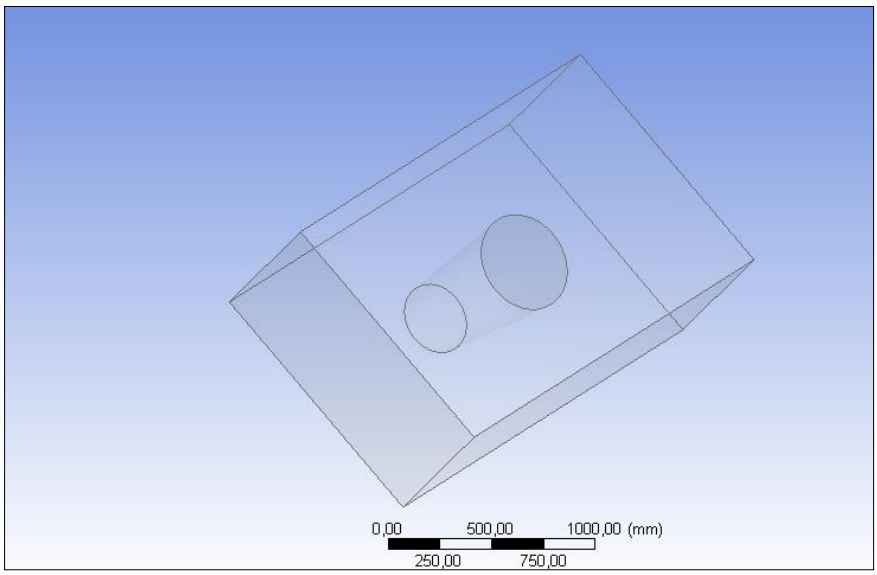

Figure 3-21: Conic body geometric 3D**.**

3.6.1.3.2.2 Mesh construction

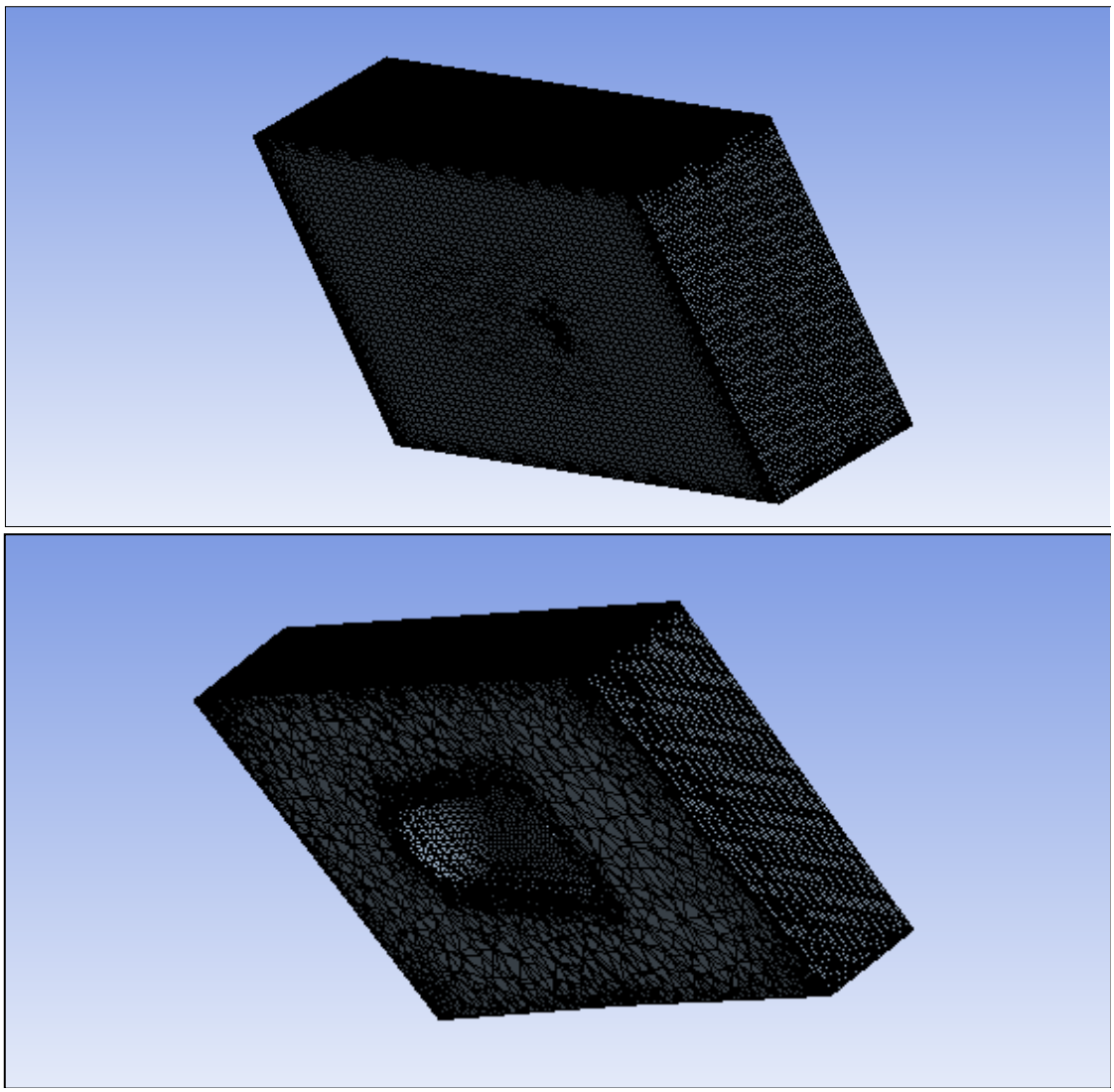

Figure 3-22: Conic bodies geometric mesh 3D**.**

3.6.1.4 Capsule fire II

3.6.1.4.1.1 Geometric creation

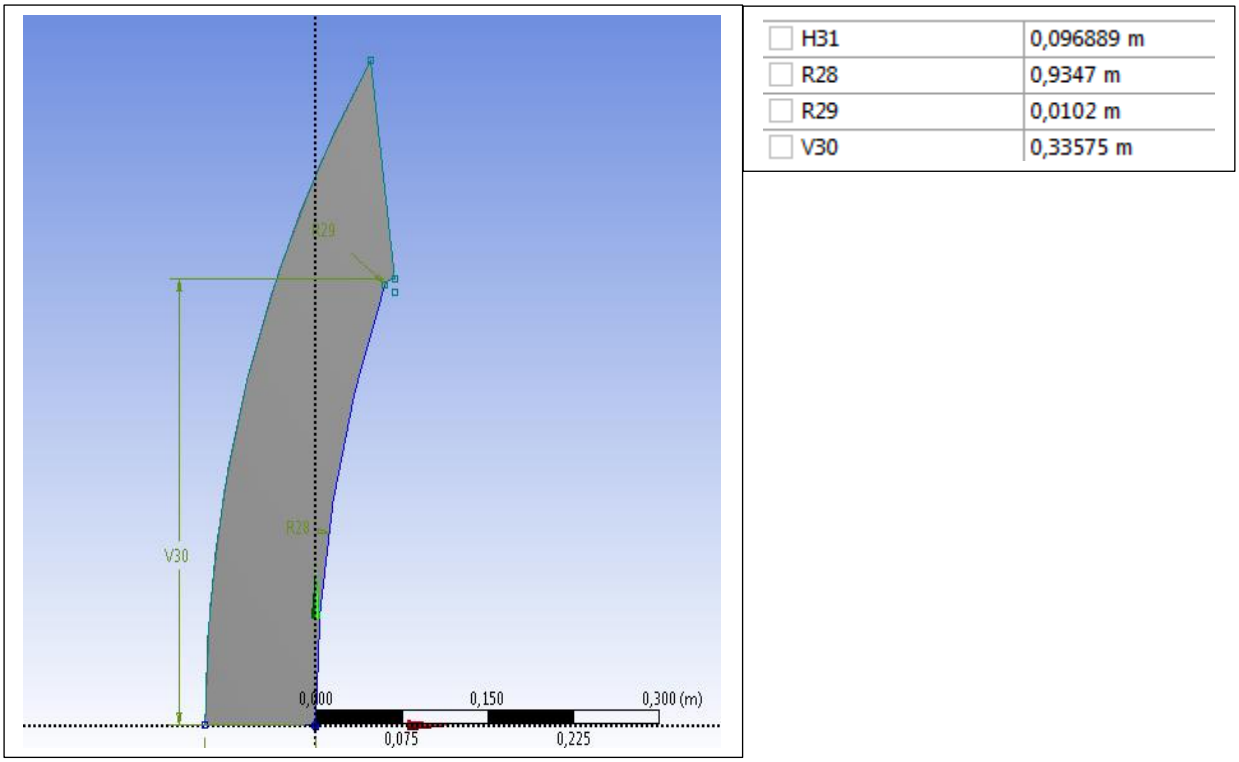

Figure 3-23: Capsule fire II geometry creation**.**

3.6.1.4.1.2 Mesh construction

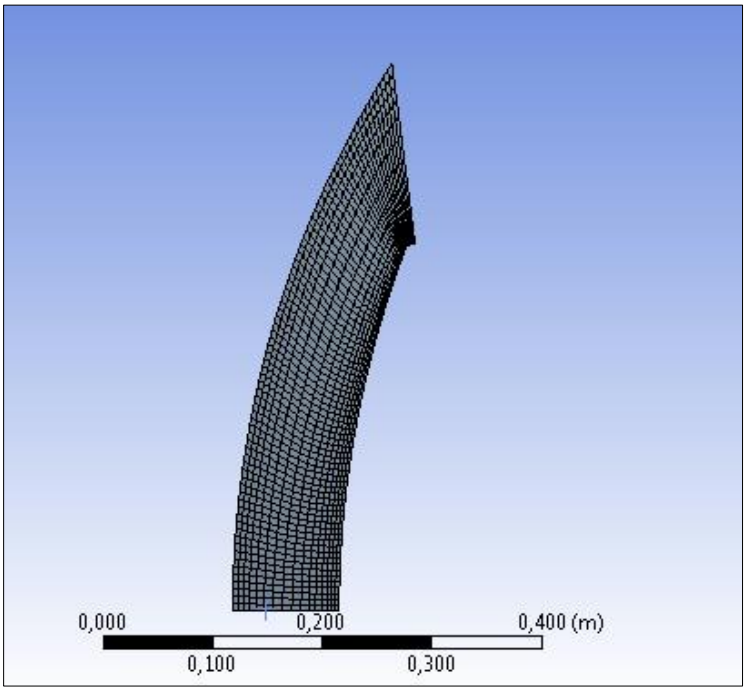

Figure 3-24: Capsule fire II geometry mesh**.**

3.6.2 Setting in data and simulation

3.6.2.1 Choice of calculation mode:

FLUENT Launcher appear, where we can specify the dimensionality of the problem (2D or 3D), as well as other options:

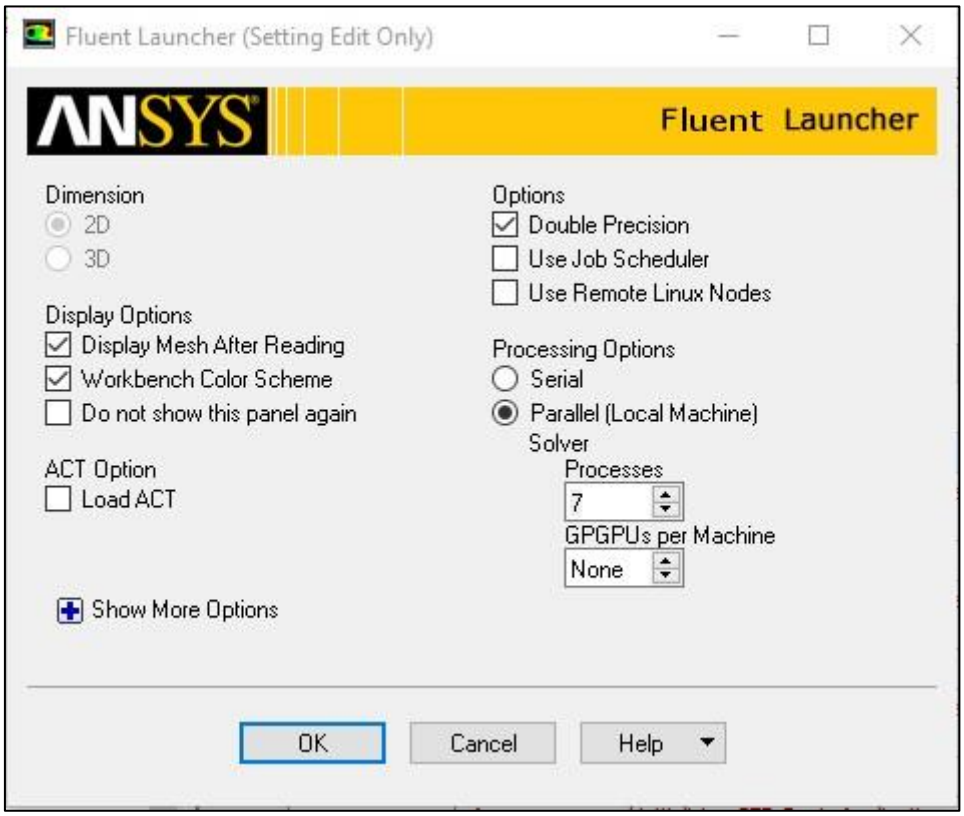

Figure 3-25: Choice of calculation mode and type of dimension**.**

Under Processing Options select Parallel Settings tab allows to specify settings for running Ansys FLUENT in parallel. Parallel processing takes away the computation from single core to multiple cores. For most cases, the single-precision mode is the mode that we will use. However, certain types of problems may benefit from the use of a double precision version.

3.6.2.2 Choice of solver:

In the steps that follow, we will select a solver and specify physical models, material properties, and zone conditions for our simulation using the Setting Up Physics ribbon tab ANSYS Fluent allows us to choose one of the two numerical methods:

- ✓ The pressure-based approach was traditionally developed for low-speed incompressible flows.
- ✓ The density-based approach was traditionally used for high-speed compressible flows.

The velocity field is obtained from the momentum equations in both methods:

- ✓ In the density-based approach, the density field is obtained from the continuity equation while the pressure field is determined from the equation of state.
- ✓ In the pressure-based approach, the pressure field is extracted by solving a pressure or pressure correction equation which is obtained by manipulating continuity and momentum equations.
- ✓

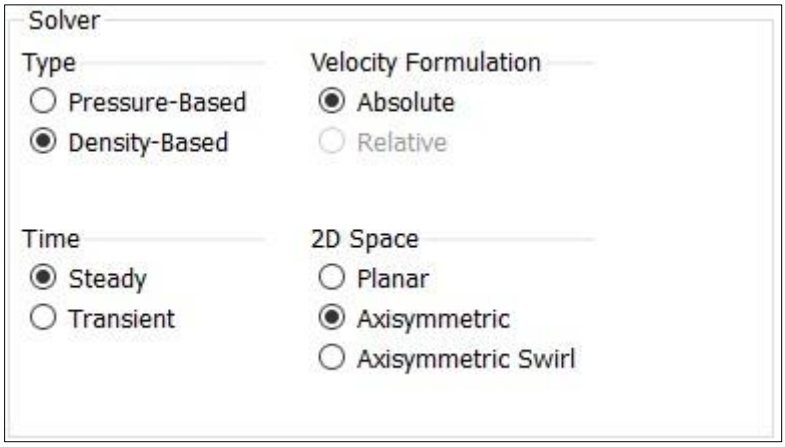

Figure 3-26: Choice of solver**.**

The two numerical methods employ the same finite-volume discretization process, but the approach used to linearize and solve the discretized equations is different. using either method, the governing integral equations for the conservation of mass, momentum, and for energy and other scalars such (turbulence and chemical species) will be solved by Ansys Fluent as follow:

a) The density-based solver
   - Solves the governing equations of continuity, momentum, energy and species transport simultaneously.
   - Governing equations for additional scalars will be solved afterward and sequentially.
   - Because the governing equations are non-linear (and coupled), several iterations of the solution loop must be performed before a converged solution is obtained.
   - Each iteration consists of the steps illustrated in **Fig3.26**

These steps are continued until the convergence criteria are met.

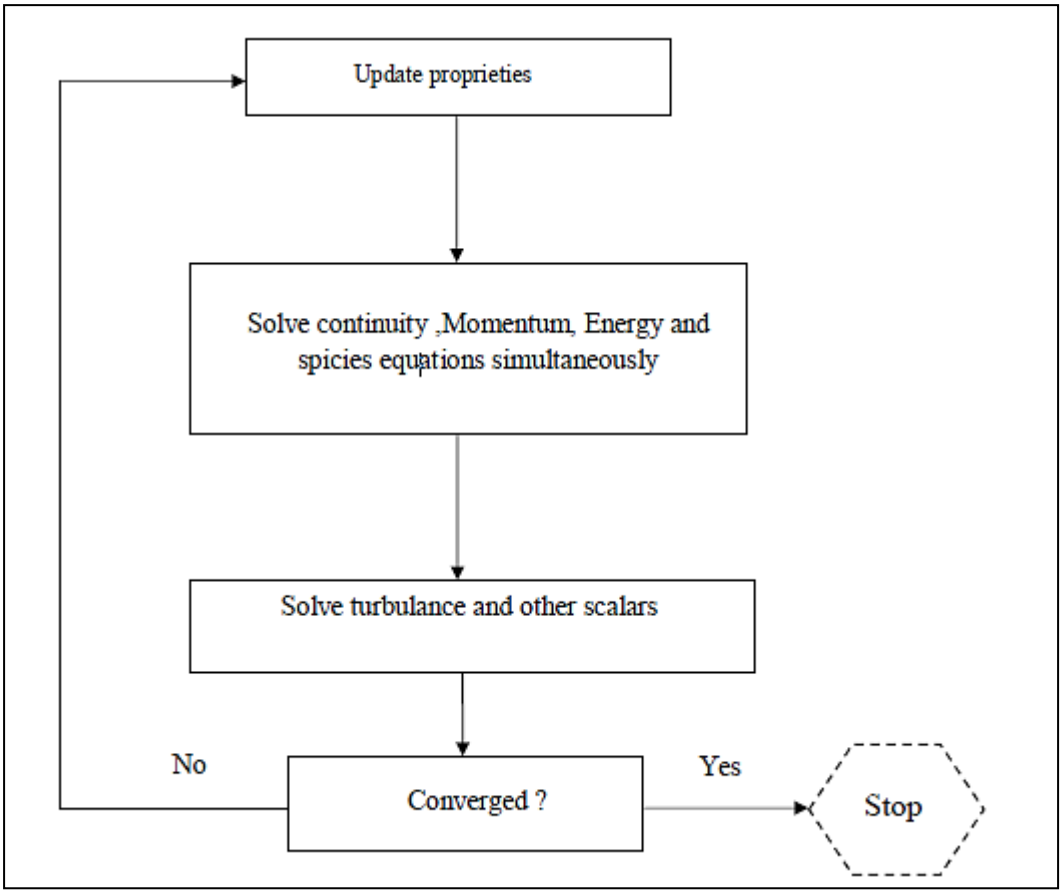

Figure 3-27: Overview of the Density-Based Solution Method.

b) In the pressure-based model, since the governing equations are nonlinear and coupled to one another, the solution process involves the following iterations:
   - The solver employs an algorithm which belongs to a general class of methods called the projection method, where, the constraint of mass conservation (continuity) of the velocity field is achieved by solving a pressure equation.
   - The pressure equation is derived from the continuity and the momentum equations in such a way that the velocity field, corrected by the pressure, satisfies the continuity.
   - The solution process involves iterations wherein the entire set of governing equations is solved repeatedly until the solution converges.

We are studying a hypersonic flow, therefore, the stationary density-based solver with an axisymmetric space was chosen

The geometry was created with the fact that the simulation will be run using the axisymmetric Navier-Stock's equations, this technique has an advantage of:

- ❖ Reduce the number of meshes used
- ❖ Consequently, reduce the calculation time.

3.6.3 Choice of model

Ansys fluent represent the different models available. We first activate the energy equation

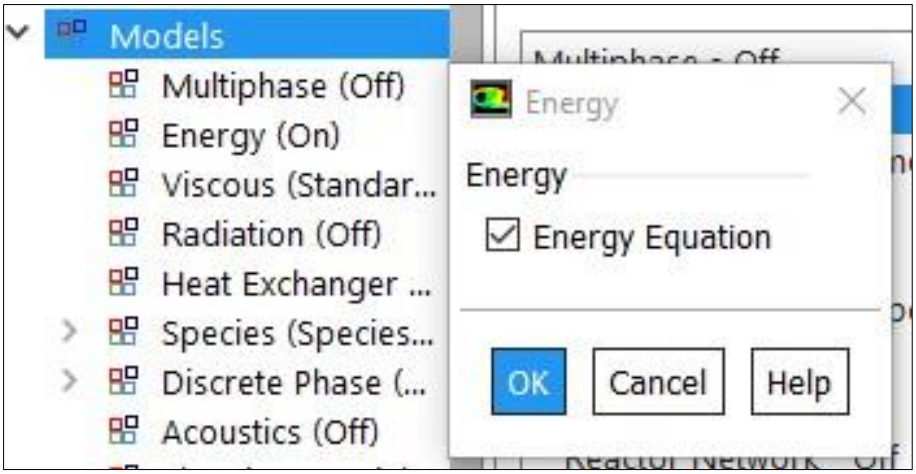

Figure 3-28: Choice of model and activation of the Energy Equation**.**

3.6.3.1.1 Choice of turbulence model

The successful choice of turbulence model depends on:

- Flow physics
- Computer resources available

Project requirements

- Accuracy
- Turnaround time
- Near-Wall treatments

The turbulence model must be selected carefully and upon the following procedures to decide the appropriate model that fine with physical flow:

- Determine whether the flow is turbulent by calculating Re.
- Estimate $y+$ before generating the mesh.
- Begin with standard k-ε and change to kw standard, SST.
- Use wall functions for wall boundary conditions.

The kw sst is the model that have been choose for our simulation since it is a hydride model combining the near wall and the free stream treatment and provides more accurate prediction of flow separation. This ensures that the appropriate model is utilized throughout the flow field while we are simulating a flow over a thin viscous boundary layer where turbulence is strongly damped and phenomena due to molecular viscosity are predominant.

By another method ANSYS fluent allows to uses a function called "Wall Function" which connects the wall to the outer layer.

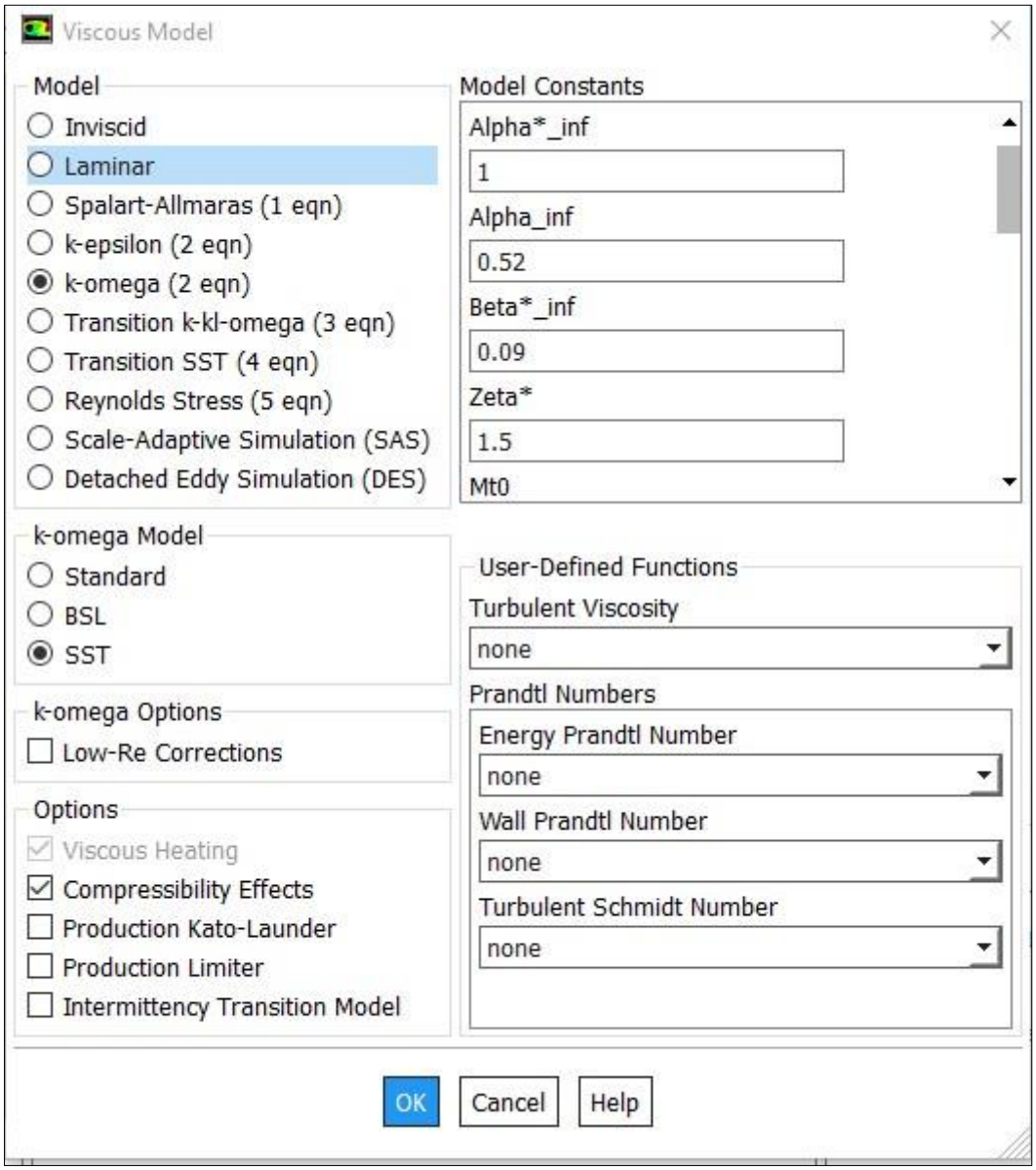

Figure 3-29: Choice of turbulence model**.**

3.6.3.1.2 Building a Model for Species Reactions and Transport

The mixing and transport of chemical species can be modelled by solving conservation equations describing convection, diffusion and reacting sources for each component species. Fluent offers the possibility of defining the reaction process simulation as follow:

First, we select species transport and volumetric reactions under reaction type to introduce reactions. The laminar finite-rate model computes the chemical source terms using Arrhenius expressions, and ignores the effects of turbulent fluctuations. It's the model that was chosen in our study.

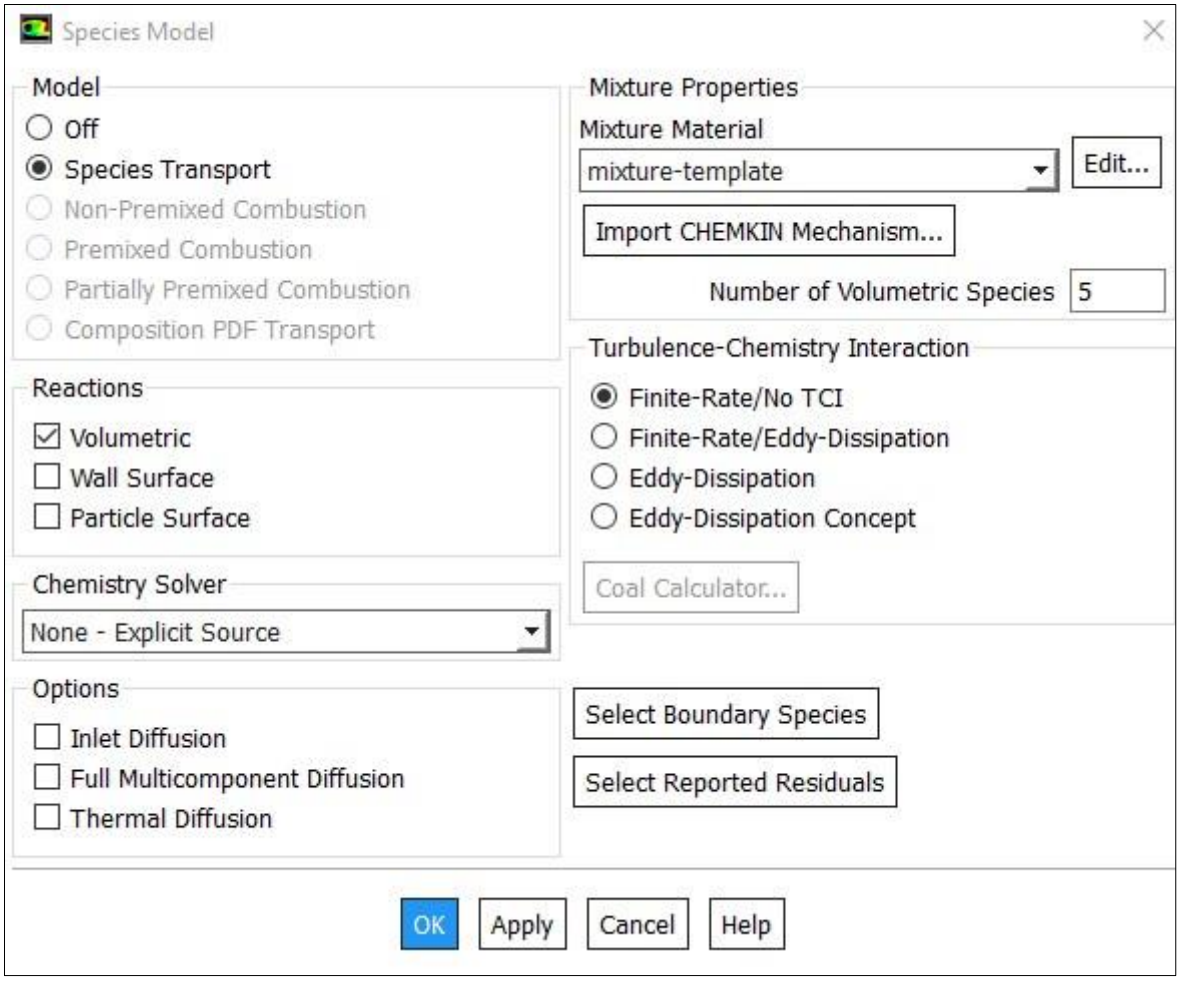

Figure 3-30: Species reaction model**.**

Because the air is considered as a reactive mixture, Fluent offers the possibility of specifying the different species of the mixture, from its database of we have created a reactive mixture of the species ($O2$, $N2$, NO, O, N).

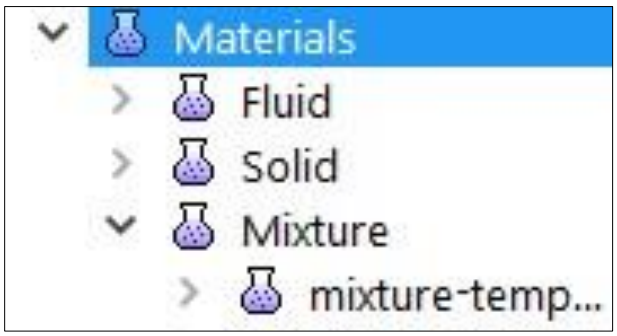

Figure 3-31: Choice of mixture material**.**

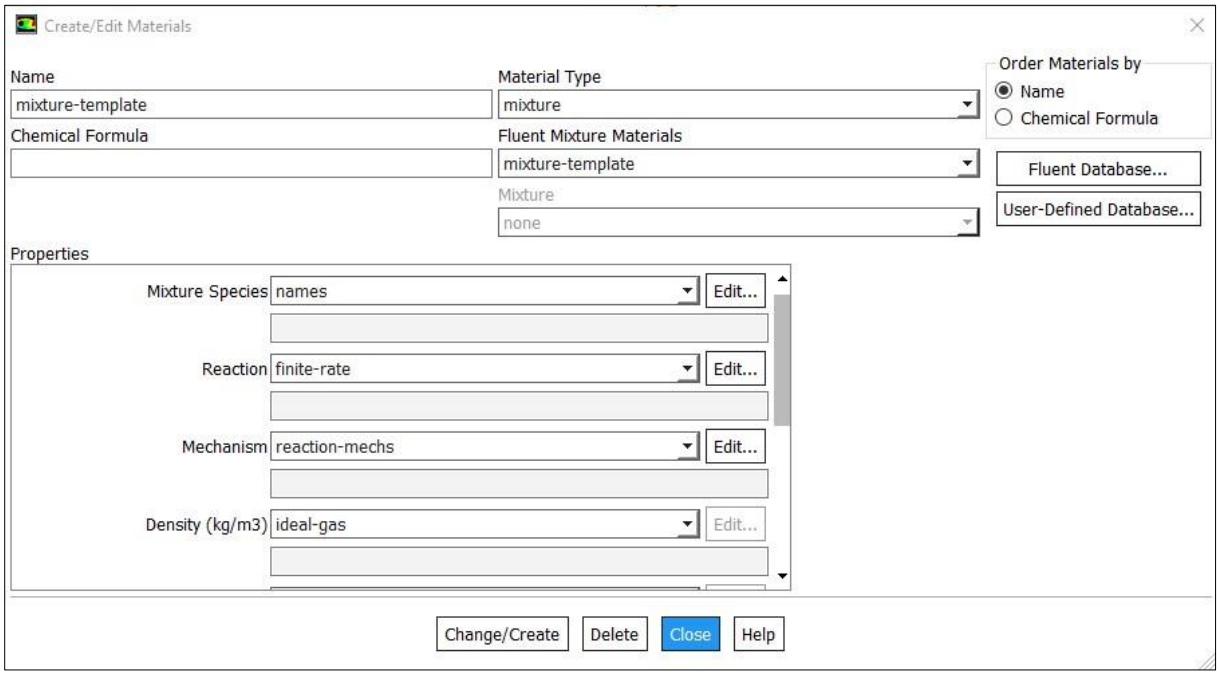

Figure 3-32: Create and edit materiel**.**

The appropriate Reaction model will be displayed in the Reaction drop-down list in the Edit Material dialog box. The reactions are modeled in the following form:

$$O2 + m = 2O + m$$

$$N2 + m = 2N + m$$

$$NO + m = N + O + m$$

$$N2 + O = NO + N$$

$$NO + O = N + O2$$

Where M is the catalyst which can be any of the five species ($O2$, $N2$, NO, O, N). Our reactions are reversible so we activate the Include Backward Reaction option and therefore the velocity exponent for each species is equivalent to the stoichiometric coefficient of that species which is the constant $v'i$,"i,in Equation 3.4. (Stoic. Coefficient = Rate Exponent),

$$\sum_{i=1}^{N} v'_{i,r}\mathcal{M}_i \rightleftharpoons_{k_{b,r}}^{k_{f,r}} \sum_{i=1}^{N} v''_{i,r}\mathcal{M}_i \tag{3.3}$$

In Fluent and for reversible reactions the molar production rate of species s from reaction r is given by:

$$R_{i,r} = \Gamma\left(v''_{i,r} - v'_{i,r}\right)\left(k_{f,r}\prod_{j=1}^{N}\left[C_{j,r}\right]^{\eta'_{j,r}} - k_{b,r}\Pi_{j=1}^{N}\left[C_{j,r}\right]^{v'_{j,r}}\right) \tag{3.4}$$

Where

$v'i$, stoichiometric coefficient for reactant i in reaction r

v"i, stoichiometric coefficient for product i in reaction r

v' , rate exponent for reactant species j in reaction r

v"j, rate exponent for product species j in reaction r

Because we are using the laminar finite-rate we have to enter the following parameters for the Arrhenius rate.

Pre-Exponential Factor

$$k_{f,r} = A_r T^{\beta_r} e^{-\frac{E_r}{RT}} \tag{3.5}$$

Activation Energy the constant Er, in the precedent equation

Temperature Exponent the value for the constant βrin the Arrhenius equation

Third-Body Efficiencies the values for γj, in following Equation

$$\Gamma = \sum_{j}^{N} \gamma_{j,r} C_j \tag{3.6}$$

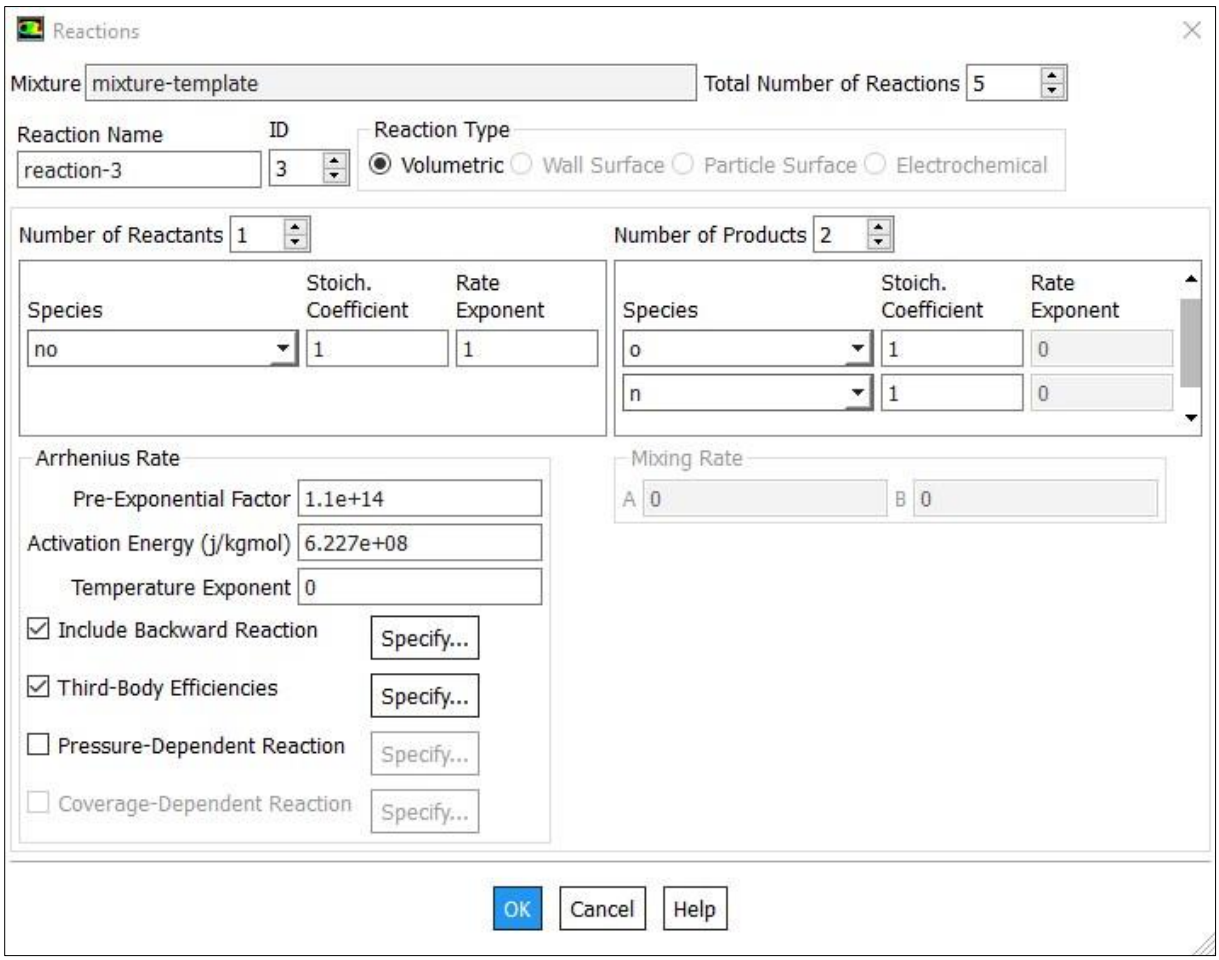

Figure 3-33: Reactions**.**

3.6.3.1.3 Boundary condition specifications

ANSYS Fluent provides different types of boundary zone types for the specification of flow inlets and exits. In Our study we have chosen the following types:

Pressure far field for ⟨*Inlet_flow*⟩

Pressure far-field boundary condition model the free-stream compressible flow at infinity, with static conditions specified and free-stream Mach number, this boundary condition is applicable only when the density is calculated using the ideal-gas law. And since the number of Mach, the pressure, temperature and mass composition of the mixture (76.7% of N2 and 23.3% of O) at the inlet are givens so “Pressure far field" is the appropriate entry condition for our problem.

Pressure outlet for ⟨*Outlet_Flow*⟩

In our case the condition does not require any specification because the flow is supersonic at the outlet, all the flow quantities are extrapolated from the interior **[48]**

The Average Pressure Specification option at the pressure outlet boundary allows the pressure along the outlet boundary to vary, but maintain an average equivalent to the specified value in the Gauge Pressure input field. The pressure variation allowed in this boundary implementation slightly diminishes the reflectivity of the boundary as compared with the default uniform pressure specification.

In the density-based solver in our study, the face pressure at the boundary equals the value specified in the Pressure Outlet where the computed average pressure value does not match the specified pressure value at the boundary then the weak average pressure enforcement can be used.

Wall boundary condition for Body

Wall boundary conditions are used to link fluid and solid regions. in our study we used these two wall boundary conditions,

The Dirichlet boundary condition allows to select the fixed temperature condition. we will need to specify the temperature at the wall surface. And the Neumann boundary condition by specifying the Heat flux option under thermal condition for a set heat flux condition. A zero-heat flux condition can be used to define an adiabatic wall.

Axis boundary condition for symmetry axis

The axis boundary type is used as the center line of a cylindrical-polar quadrilateral, hexahedral mesh or an axisymmetric geometry like the case in our study. We do not need to define any boundary conditions at axis boundaries.

3.6.3.1.4 Solution:

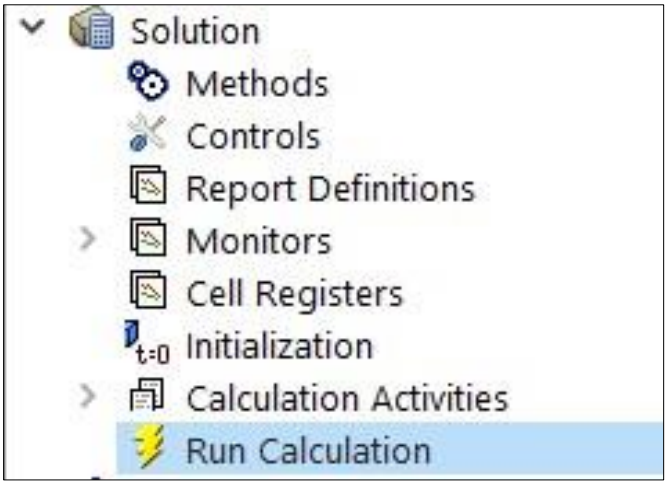

Figure 3-34: The Solution dialog box**.**

3.6.3.1.5 Choice of the formulation algorithm:

The Solution Methods task page allows specify different parameters to be used in the calculation.

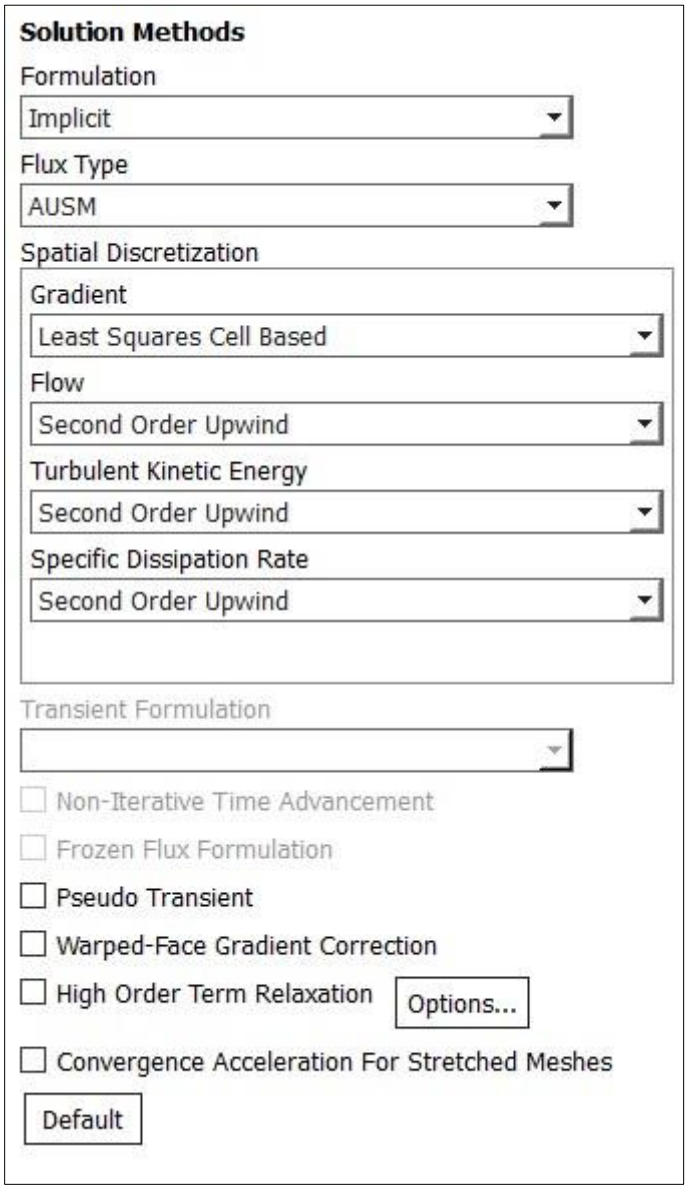

Figure 3-35: Solution method**.**

3.6.3.1.5.1 Choice of the formulation algorithm:

Formulation provides available types of solver formulations: Implicit and Explicit:

Implicit: The unknown value for a given variable in each cell is computed using a relation that includes both unknown and existing values from adjacent cells. Therefore, each unknown value will appear in several equations in the system, and these equations must be solved simultaneously to give the unknown quantities.

Explicit: The unknown value for a given variable in each cell is computed using a relation that includes just the existing values. Therefore, each unknown value will appear in only one equation in the system and to determine the unknow value we can solve one at a time the equation for the unknown values in each cell.

If we choose the implicit option of the density-based solver, we get a system of linear equations with N equations for each cell in the domain, where N is the number of coupled equations in the set because each equation in the coupled set of governing equations is linearized implicitly with respect to all dependent variables in the set

If we choose the explicit option of the density-based solver, as in the implicit option, this too will result in a system of equations with N equations for each cell in the domain and likewise, all dependent variables in the set will be updated at once because each equation in the coupled set of governing equations is linearized explicitly.

Flux Type provides a list of the convective flux types Roe-FDS and AUSM: will appear in several equations in the system, and these equations must be solved simultaneously to give the unknown quantities.

Explicit: The unknown value for a given variable in each cell is computed using a relation that includes just the existing values. Therefore, each unknown value will appear in only one equation

3.6.3.1.5.2 The choice of the spatial discretization scheme

3.6.3.1.5.2.1 Choice of Gradient method

Gradients of solution variables are needed for constructing values of a scalar at the cell faces, and so for computing secondary diffusion terms and velocity derivative. The gradients are computed in our study according to Least-Squares Cell-Based which has more accurate results, minimizes false diffusion and is less computationally intensive.

3.6.3.1.5.2.2 The choice of the precision of the diagrams used

When first-order accuracy is desired, quantities at cell faces are determined by assuming that the cell center values of any field variable represent a cell-average value and hold throughout the entire cell; the face quantities are identical to the cell quantities. While, when second-order accuracy is desired, quantities at cell faces are computed using a multidimensional linear reconstruction approach. In this approach, higher-order accuracy is achieved at cell faces through a Taylor series expansion of the cell-cantered solution about the cell centroid [48]

When the flow is aligned with the grid the first-order discretization may be acceptable, when the flow is never aligned with the grid, the second order discretization will generally give more accurate results. For complex flow, even with grid aligned flows, it's required to use the second order discretization to minimize the numerical diffusion.

For most cases, it is possible to use the second-order scheme from the start of the calculation. In some cases, we may need to start with the first-order scheme and then switch to the second-order scheme after a few iterations.

In summary, while the first-order discretization generally yields better convergence than the second-order scheme, it generally will yield less accurate results, especially on tri/tet grids.

3.6.3.1.6 Control of the solution

The Solution Controls task page allows you to set common solution parameters

Courant Number sets the fine-grid Courant number (time step factor) when the density-based solver is used

Setting Under-Relaxation Factors

The default under-relaxation parameters for all variables are set suitable for many problems. But for some particularly nonlinear problems it is prudent to reduce the under-relaxation factors initially (e.g., some turbulent).

We should alter the default under relaxation factor only if the residuals continue to increase after the first 4 to 5 iteration; in this case we need to reduce the under-relaxation factor from their default value to about 0.2, 0.5, 0.5 and 0.5.

3.6.3.1.6.1 Solution limits

The Solution Limits dialog box allows to improve the stability of the solution

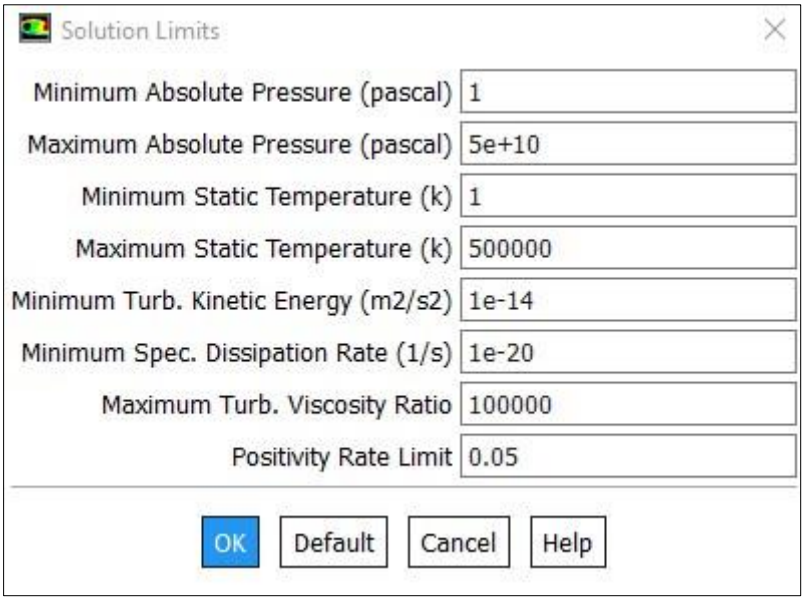

Figure 3-36: Solution limits**.**

ANSYS FLUENT applies limiting values for pressure, static temperature, and turbulence quantities. The purpose of these limits is to keep the absolute pressure or the static temperature from becoming 0, negative, or excessively large during the calculation, and to keep the turbulence quantities from becoming excessive.

Typically, we will not need to change the default solution limits. If pressure, temperature, or turbulence quantities are being reset to the limiting value repeatedly (as indicated by the appropriate warning messages in the console), we should check the dimensions, boundary conditions, and properties to be sure that the problem is set up correctly and try to determine why the variable in question is getting so close to zero or so large. In very rare cases, we may need to change the solution limits, for example in our case we know that the temperature will accede the minimum set temperature so only in this case that we have to change the solution limits**.[46]**

Positivity Rate Limit control the reduction of temperature by a default value of 0.2 means that the temperature should not decrease from one iteration to the next by more than 20% of its previous value. If the temperature change exceeds this limit, the time step in that cell is reduced to bring the change back into range and a "time step reduced" warning is printed. Rapid reduction of temperature is an indication that the temperature may become negative.

3.6.3.1.7 Solution initialization

Before starting our CFD simulation, we must provide ANSYS Fluent with an initial boundary condition of the solution flow.

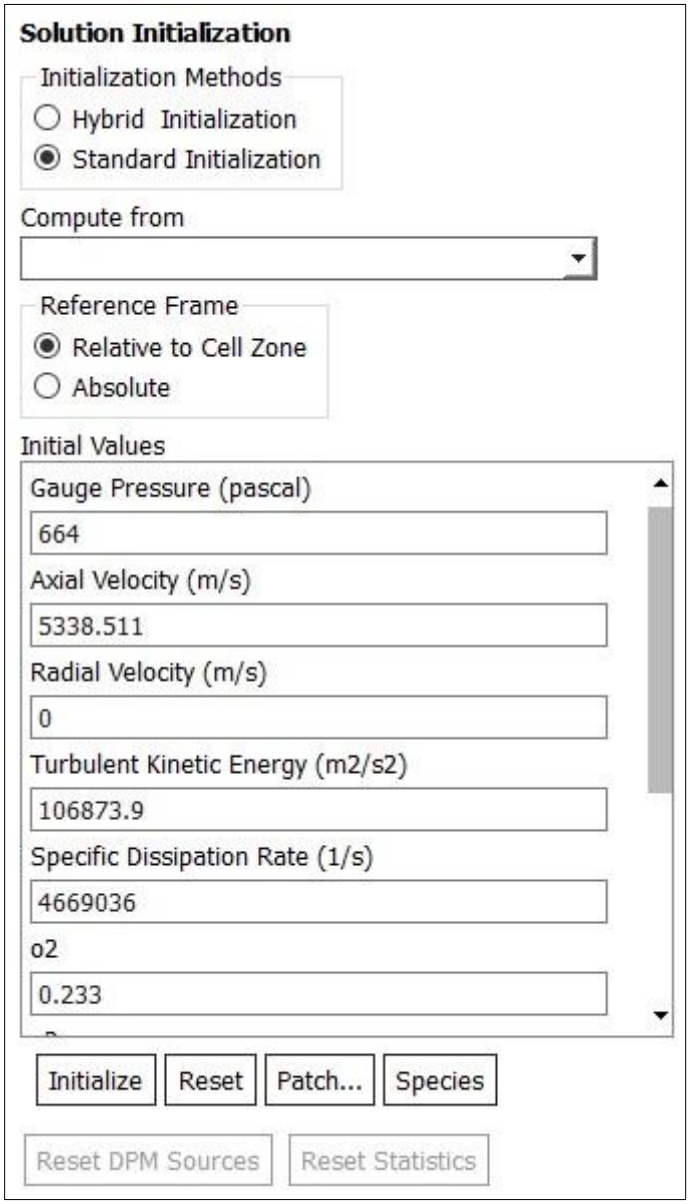

Figure 3-37: Solution initialization**.**

To obtain the most exact solution possible, the Fluent solver proceeds by successive iterations to solve the matrix system obtained by discretization of the equations by a finite volume method.

The iteration procedure requires that all the variables are initialized before the start of the calculation. An initialization improves the stability and the speed of convergence. In some

cases, a correct initial solution is necessary **[47].** For our calculation, we set a velocity field equal to the entry velocity in the whole domain as the starting point of the iterations.

The solver starts from the initial solution and due to an iterative algorithm of resolution of the matrix system obtained by discretization, will perform iterations. If all goes well, each iteration must modify the current solution to replace it with a solution closer to the exact solution sought. With each iteration and for each equation an error, called residue, is calculated compared to an exact solution of the system. A calculation diverges if the residuals increase during iterations.

3.6.3.1.8 Calculation control

The Run Calculation task page allow us to start the solver iterations

Number of Iterations

- For steady flow calculations: sets the number of iterations to be performed.
- For unsteady calculations: using the explicit unsteady formulation, this will specify the number of time steps, since each iteration will be a time step.

Select solution steering option so that we can choose the flow type (hypersonic in our study). The Courant number defines the time step size. In our case for density-based implicit solver:

- The Courant number is not limited by stability constraints.
- Default value is 5.

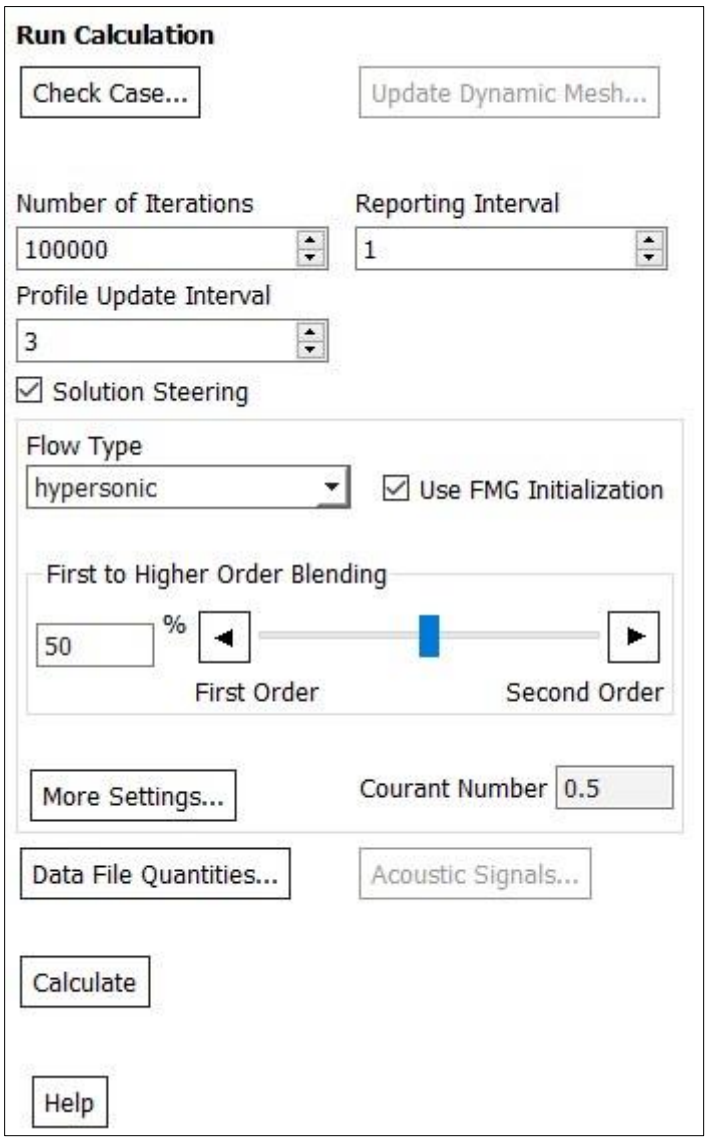

Figure 3-38: Run calculation**.**

Convergence and stability

At convergence, the following should be satisfied:

- ✓ Overall mass, momentum, energy, and scalar balances are achieved.
- ✓ Monitoring convergence using residual history:
- ✓ Generally, a decrease in residuals by three orders of magnitude indicates at least qualitative convergence. At this point, the major flow features should be established.
- ✓ Scaled energy residual should decrease to 10-6 (for the pressure-based solver).
- ✓ Scaled species residual may need to decrease to 10-5 to achieve species balance.
- ✓ Monitoring quantitative convergence :
- ✓ Monitor other relevant key variables/physical quantities for a confirmation.
- ✓ Ensure that overall mass/heat/species conservation is satisfied.

Convergence can be accelerated by:

- ✓ Supplying better initial conditions
- ✓ Starting from a previous solution (using file/interpolation when necessary).
- ✓ Gradually increasing under-relaxation factors or Courant number
- ✓ Excessively high values can lead to solution instability convergence problems
- ✓ You should always save case and data files before continuing iterations
- ✓ Default settings provide a robust Multigrid setup and typically do not need to be changed.

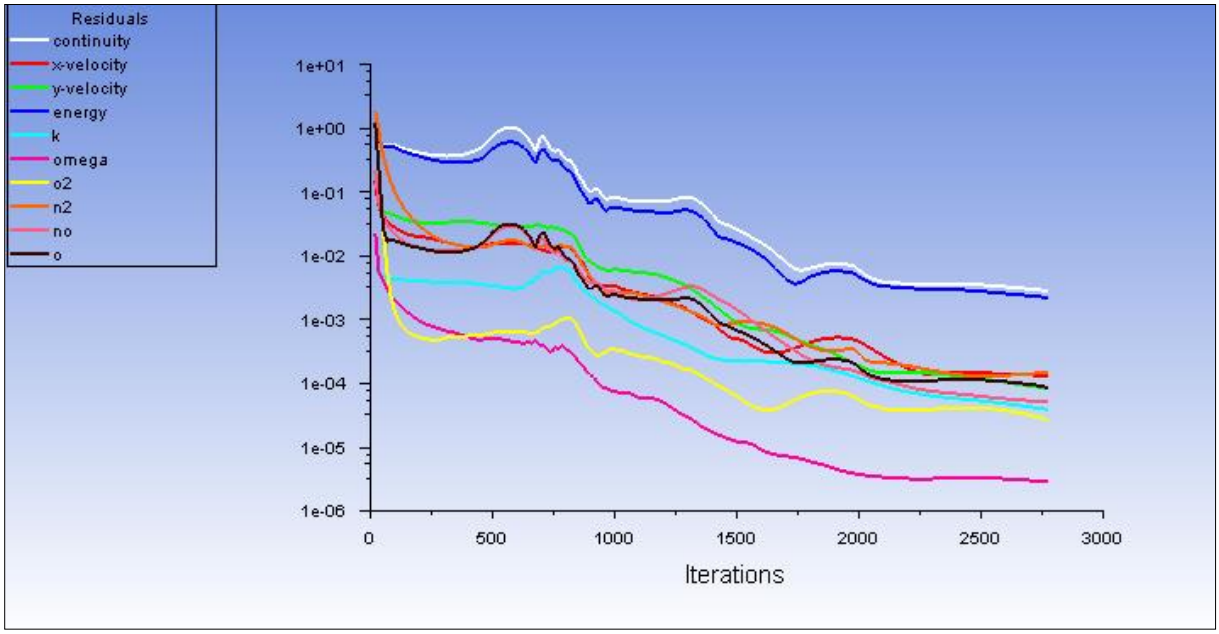

Figure 3-39: The evolution of the residues for the initial mesh**.**

3.6.4 Grid independence study:

Prior to performing the CFD simulations, a grid independence study was conducted over 4 grid resolutions. Because the heat transfer occurring between the surrounding air and the vehicle wall played a key role in this study, particular effort was made to ensure the near-wall mesh quality.

In this study, to strike a balance between accuracy on the one hand side and computational time and memory consumption on the other hand side the mesh should be constructed with reasonable mesh densities. This means that not every region of a spatial simulation domain is of particular importance for the solution of the numerical problem. So, the idea is to use a finer mesh in simulation domains where a high resolution is necessary and simultaneously reduce the memory consumption by applying a gradient mesh in regions of hight importance.

To overcome this issue, the region located near from the wall was meshed with a gradient structured mesh. Which allows to mark or to refine cells inside or outside a specified range of a selected field variable function?

We will observe the effect of refining the mesh on the flow results. And we will stop the process until the number of cells changes will be equal to 0 which means that the result of the study is independent of the mesh and so the temperature will remain the same for more cells number.

And because we are interested in the temperature evaluation in our study, we chose to refine the mesh where the gradient of temperature is important. The first is the default defined by Automatic Mesh Sizing. Each Adaptation contains mesh refinements based on the previous results field.

3.6.4.1 Lob sphere grid independence study

The table below compares the different maximum values of the temperature of the fluid for the five different densities of meshes.

Table 3-III: Lobb sphere grid independency**. (Original)**

Adaption	initial	Adption1	Adaption2	Adaption3	Adaption4
Cells	2550	4875	20690	129963	150963
Noeuds	5680	7950	37546	89125	97802
T(K)	8000	8500	9300	10470	11620

We notice on the table above, that, the less dense mesh (2550), the maximum value of the temperature of the flow is weak compared to the two denser meshes. We have adapted the mesh until the number of cells changed became 0.

The sensitivity test with respect to the mesh was performed for five different mesh densities, by comparing the flow temperature profiles under the same boundary-Axis_symm line- so that we can notice the maximum value of the temperature just behind the shock and the distance of the relaxation zone. The figure shows that for the initial mesh the temperature varies from a minimum value of the free stream temperature to a maximum value of 8000k in a distance of 0. 05m.The Temperature profiles shows that every time we adapt the mesh, the maximum temperature increases while the relaxation distance decreases from adapt 1 until it became invariable in adapt 5 to a temperature of 10470 in a distance less of 0.02.

The result become independent of mesh from adapt 3 cause the variation of temperature is no longer observed during the refinement, so we can consider that the “adapted 3 mesh” is

the optimum mesh where the temperature result is stable even if we refine the mesh more and more.

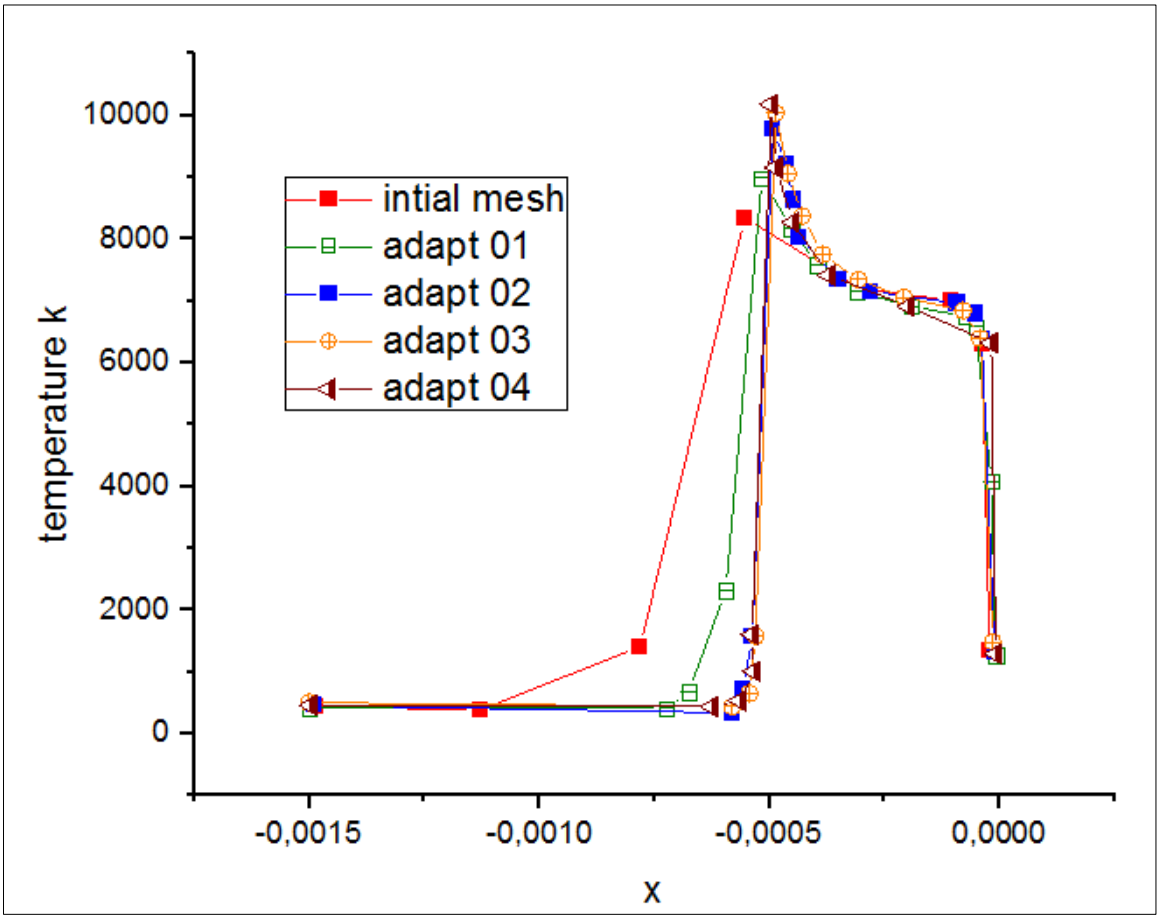

Figure 3-40: Lobb sphere grid independency**.**

3.6.4.2 Conical body grid independency

The sensitivity test with respect to the mesh was performed for four different mesh densities.

Table 3-IV: Conical body grid independency**.**

Adaption	initial	Adption1	Adaption2	Adaption3
Cells	15302	40703	151635	572744
Noeuds	9323	35498	110535	378518
T(K)	7000	7100	7900	8200

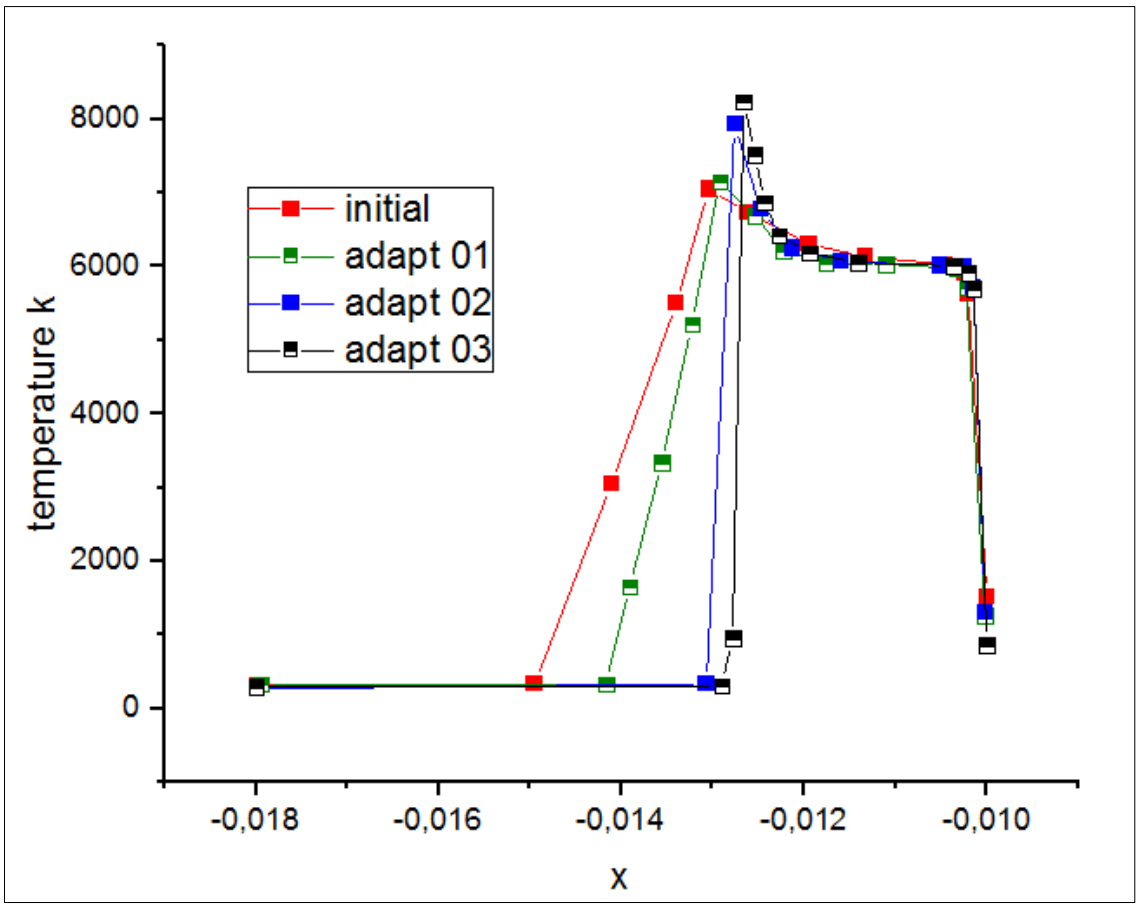

Figure 3-41: Conical body grid independency**.**

3.6.5 Turbulence model independency

We used the k w SST turbulence model which is the appropriate model to deal with the small viscous distance between the wall and the shock wave. So, to ensure the good precision in the determination of the proprieties of the boundary layer which is a small viscous area we have ensured that y+ is less than 5 far from the wall and less than 1 in the zone close to the wall for our deferent geometries as shown in **Fig (42,43,44,45).**

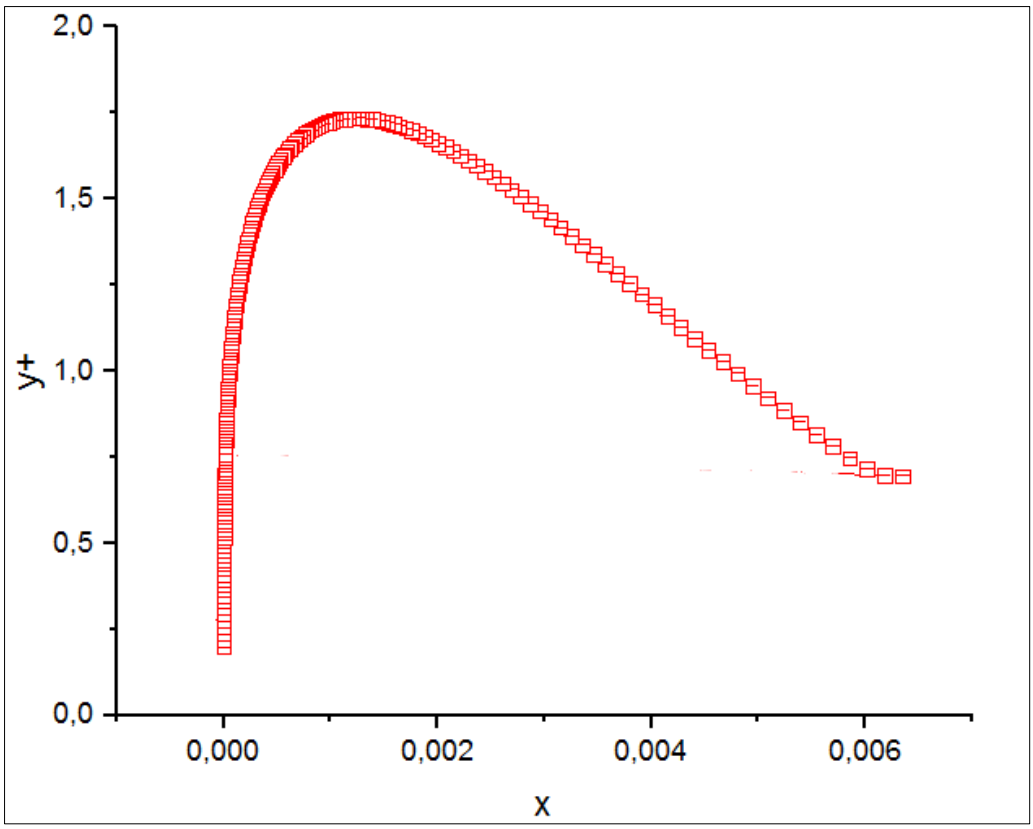

Figure 3-42: Lobb sphere Y+ wall profile of k ω *SS*.

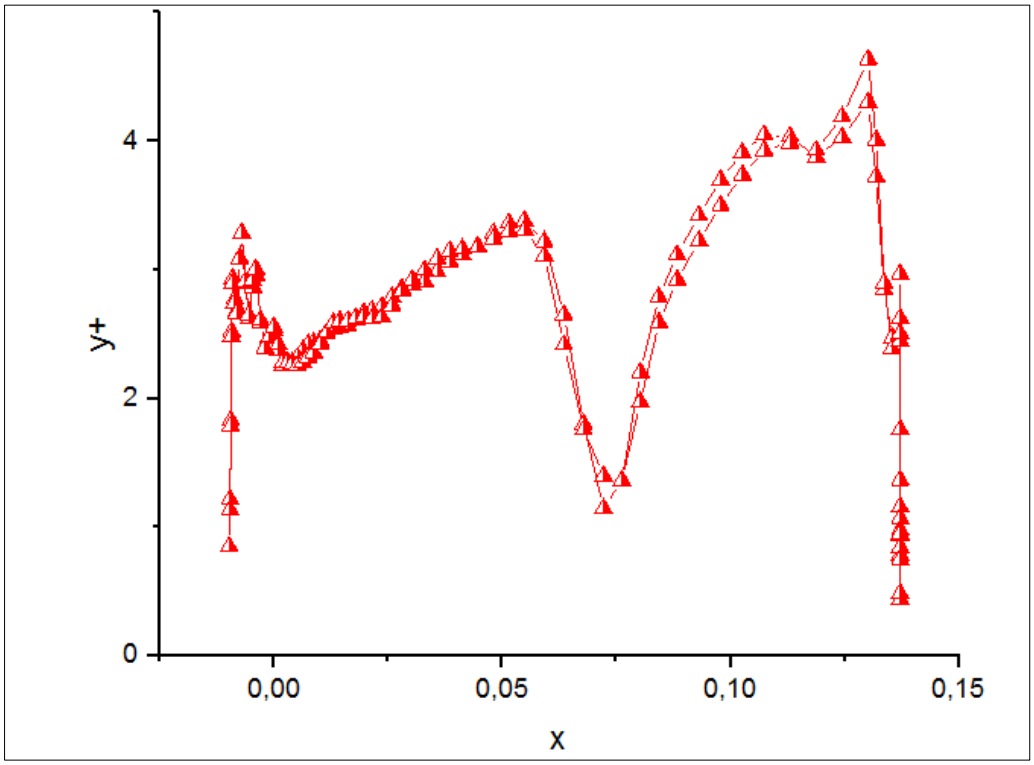

Figure 3-43: Cone-flare Y+ wall profile of k ω *SST* model.

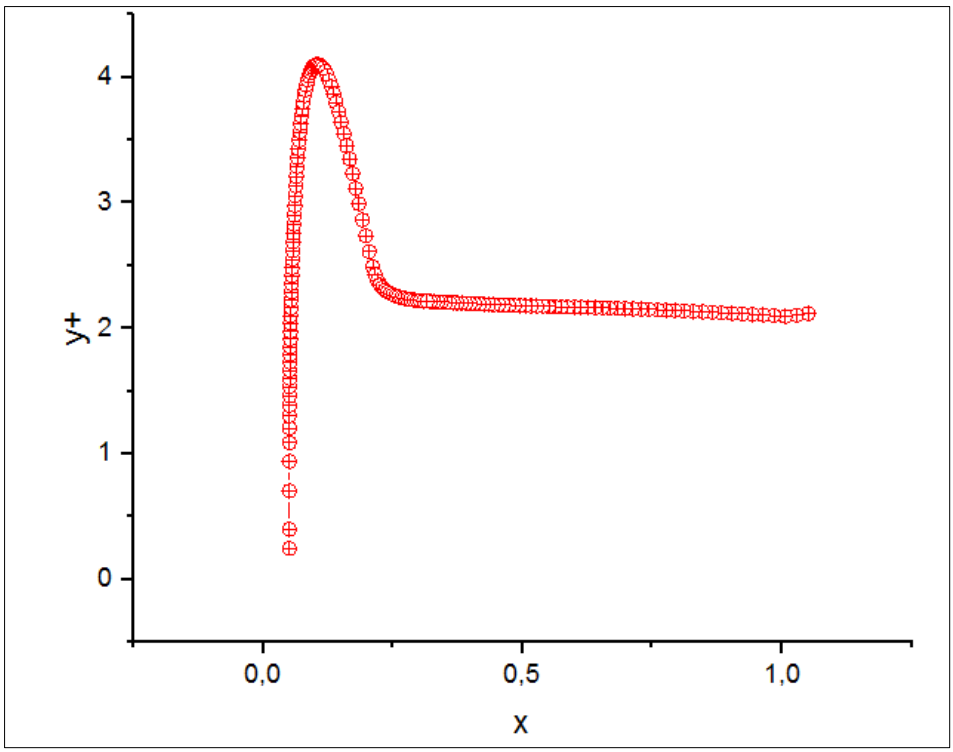

Figure 3-44: Conic body Y+ wall profile of k *ω SST* model**.**

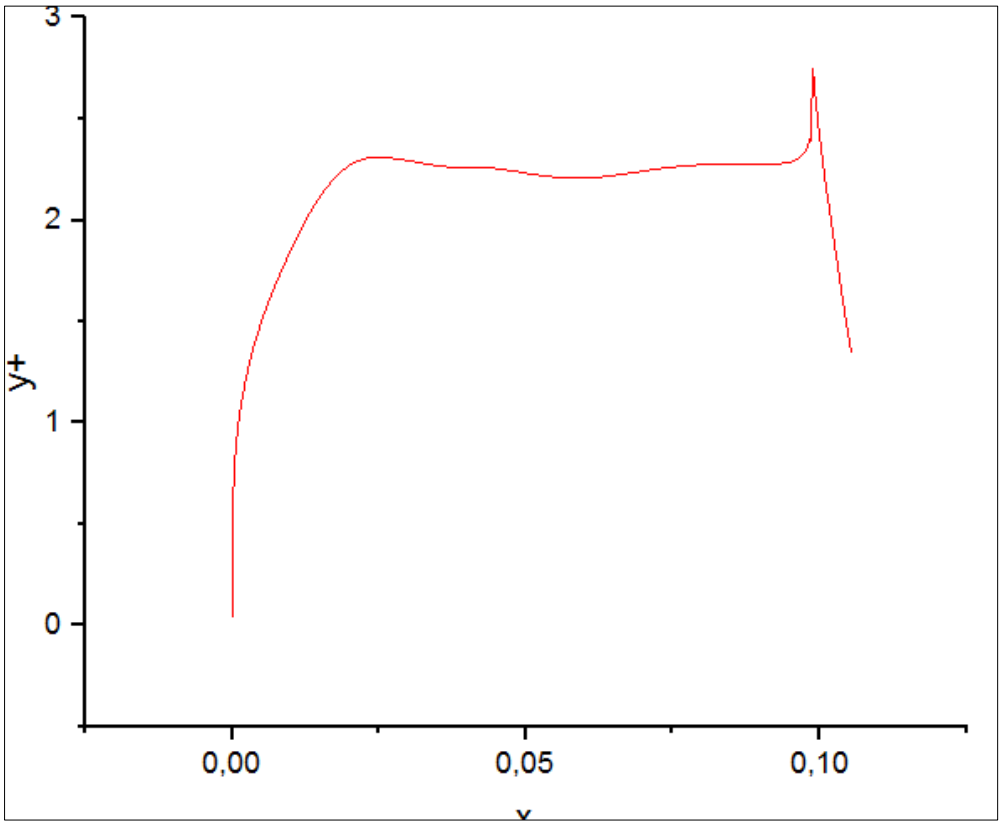

Figure 3-45: Capsule fire II Y+ wall profile of k *ω SST* model.

3.7 Conclusion

Our main object in this chapter was to perform a simulation of a hypersonic chemical non-equilibrium flow under the ANSYS environment. First, we presented the simulation software used (ANSYS software), geometry and mesh were studied for every signal body, specifying the main steps followed under the Fluent calculation code. It should be noted that the methods of the numerical solution cited previously for example the stability, the convergence are all controlled and checked during our simulations made. Finally, we presented the last step of our CFD process, i.e., the grid dependency and turbulence model verification.

In the next chapter, we will present the results obtained during the simulation around various geometries studied and validating them by comparison with the scientific literature.

Chapter 04

Results and Discussion

4 Introduction

This chapter is reserved for the presentation of the various results characterizing a flow hypersonic around a blunt body out of thermochemical equilibrium, for each configuration, a comparison with experimental or other numerical data is carried out.

Re-entry mission requirement affects the vehicle design. Deceleration, heating and accuracy are the major parameters that affect the trajectory which are drives by the design. So as an aerospace engineer our work is to trade-off between the trajectory and the vehicle design until we reach some compromise vehicle that satisfies mission requirements.

We used Ansys fluent simulations to balance all the competing mission requirements by approaching them on two broad fronts

- Thermochemical non equilibrium effect around blunt body
- Trajectory design, which includes changes to
  - Re-entry flight-path;
  - Re-entry altitude;
  - Re-entry Velocity.
- Vehicle design, which includes changes to
  - Vehicle shape.

Trajectory design involves the vehicle's velocity as it enters the effective atmosphere which defines the re-entry initial conditions. The vehicle design improves the vehicle's shape to modulate the drag force

In this chapter, we present:

- Lobb sphere blunted nose, cone flare and conic body to study the thermochemical non equilibrium effect in re-entry hypersonic flow ;
- The capsule fire II to study the vehicle design of a reusable re-entry vehicle (lifting body) compared with a blunt body.

4.1 Thermochemical non equilibrium flow study

4.1.1 Change in Mach number of flow after shock

Fig 4.1 represents the iso-Mach contours shows a drop in Mach number just after the shock wave which reaches a value less then unity because the flow is perpendicular to the wall so in this area the shock is considered to be a normal shock wave where the flow become subsonic downstream.

While there is a creation of an oblique shock wave in the other parts around the sphere, the downstream Mach number is not necessarily less than unity.

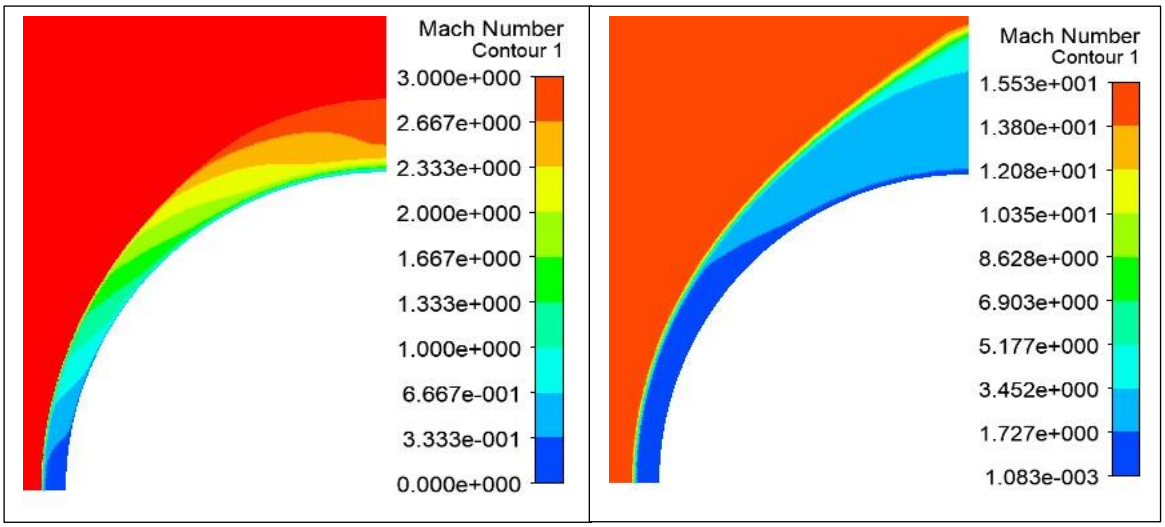

T = 293 K
ρ = 7.896 e-03 kg/m^3
P= 664 Pa
M= 15.35

Figure 4-1: Variation in Mach number in relaxation zone**.**

4.1.2 Change in flow temperature through relaxation zone

The high kinetic energy in the flow interacts with the surface of the vehicle and the kinetic energy transforms to thermal energy, forming a strong bow-shaped shock wave in the fore body of the vehicle. **Fig 4.2** shows the normal shock wave formation in front of the body. The shock wave formation compresses and slowdown the hypersonic upstream flow suddenly to a subsonic regime, there the molecules kinetic stored energy transforms to thermal energy by colliding intensively among themselves causing the abrupt temperature rise from 293k free stream temperature to 10470 k.

The maximum temperature behind the shock decreases until it reaches the equilibrium temperature of approximately 6000K in a distance of 0.50 mm. the appearance of the reactions of dissociation and exchange in the shock wave (chemical phenomena) which are endothermic phenomena, molecules absorb energy to recombinant or to break the links between them which cause a decrease in temperature to the wall by approximately 40% it's maximum value.

During this process, because the number of collisions required to reach equilibrium in the translational and rotational relaxation is fer less than that required for the vibrational equilibrium, the translational and rotational relaxation time is much shorter than the vibrational relaxation time. [49]

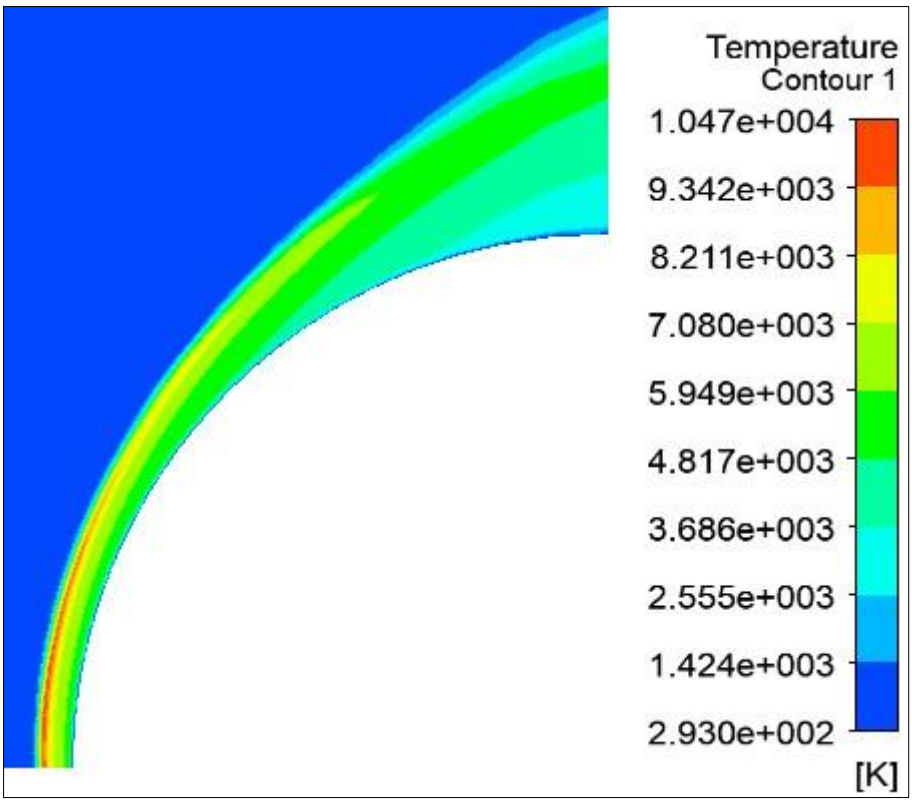

T = 293 K
ρ = 7.896 e-03 kg/m^3
P= 664 Pa
M= 15.35

Figure 4-2: Variation in temperature in relaxation zone**.**

Validation:

By comparing our result of **Fig 4.3** with that of Tristan **[8]**which shows the variation of the temperature along the relaxation range, one notices a good agreement between the two results in terms of pace and in quantitative term **[9]**

The slight difference is due to the fact that Tristan [8]considered a flow out of vibrational equilibrium. As vibrational relaxation is no longer instantaneous, its energy contribution is weaker. This lost energy is found in the form of temperature and in the form of kinetic energy; this is why the temperature of the mixture is higher and the shock moves away from the obstacle compared to the case of vibrational equilibrium **[50]**

Table 4.1 illustrates that this result agrees well with the experimentally determined value with an error of 2.89% [51]and the numerical values obtained in the literature [52] [53]

Table 4-I: Position of the shock of the Lobb sphere**. [8]**

Source Shock position [mm]	Shock position [mm]
Present results	0.536
Tristan	0.535
Tchuen	0.598
Joly et al	0.557
S'eror Lobb	0.552±0.032

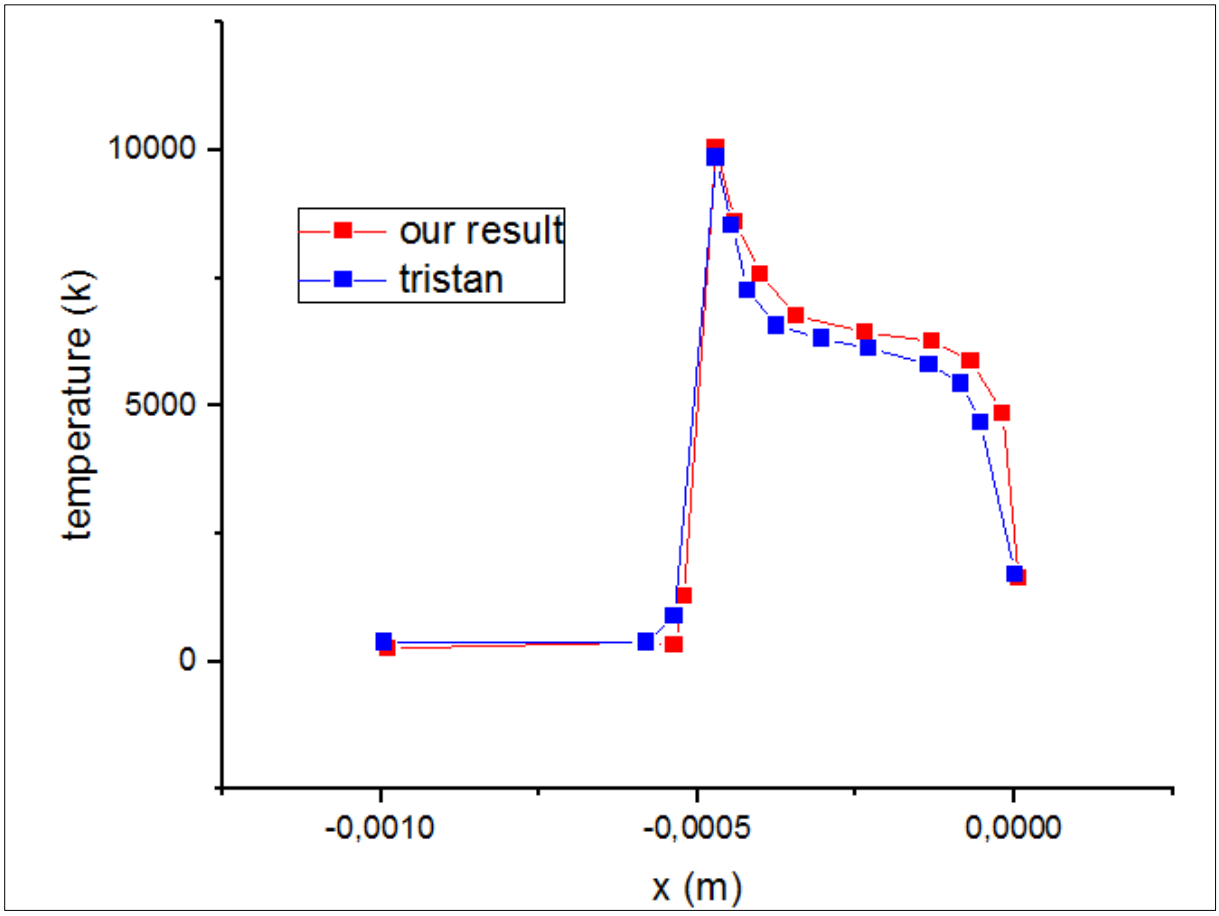

Figure 4-3: Comparison in temperature along the stagnation line**.**

4.1.3 Pressure field variation

The detachment shock is clearly obvious on the pressure field, the temperature increases gradually before it reaches its maximum value 20000Pa due to the compression waves created because of the abrupt deceleration from hypersonic to subsonic regime by the normal shock as describe earlier. The pressure decreases in the relaxation zone in parallel with the temperature

due to endothermic phenomena. Again, comparing our results in **Fig4.4** with that of Tristan in **Fig4.5.**

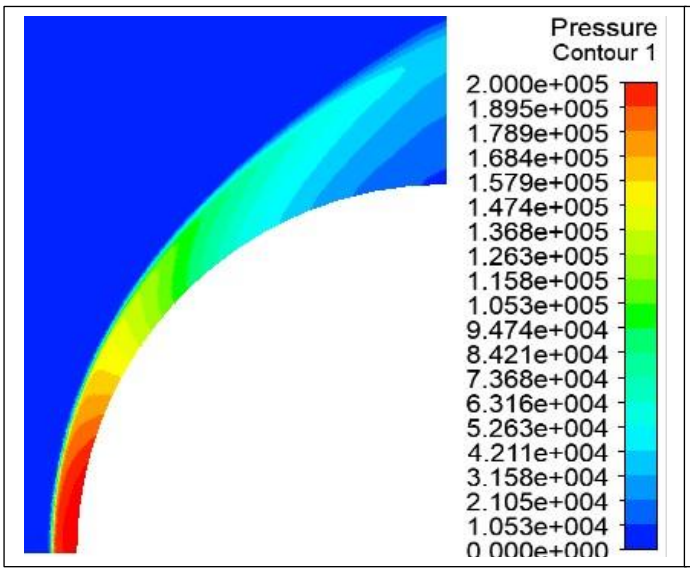

Figure 4-4: Pressure field along the relaxation range**.**

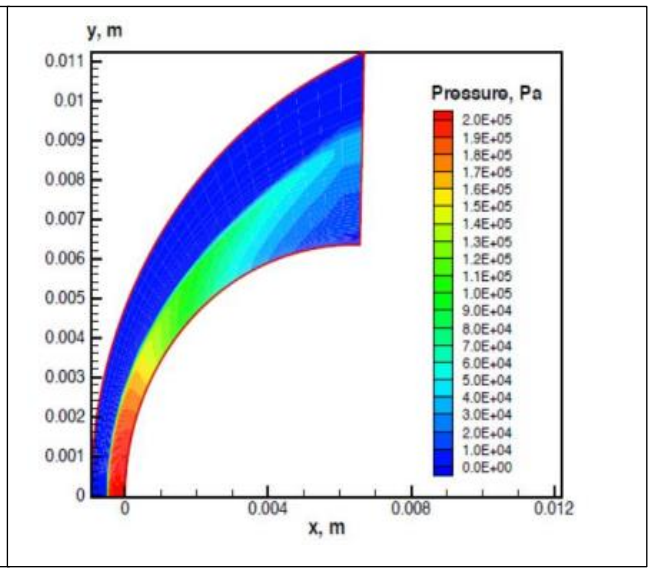

Figure 4-5: Pressure field along the relaxation range. "Tristan **[8]"**

4.1.4 Mass fractions of species

As mentioned before, the nitrogen molecule starts to dissociate at around 4000 K and the oxygen molecular at 2000K. It is apparent that with increasing temperature, the degree of dissociation increases. Crossing the shock in the post-shock region these two endothermic components start to dissociate and therefore non-existent species appears, which are nitrogen and oxygen atoms as well as nitrogen monoxide.

The characteristic temperature of the O2 molecules is twice lower than of N2 molecules what explain the dissociation of oxygen molecules at more than 95% while nitrogen molecules dissociate at less than 10% of their respective values at infinity upstream.

The disappearance of the O2 and N2 molecules makes the O and N molecules appear parallel and this is well represented and noticed by the curves **Fig 4.6**, that the formation rates of O and N are almost equal to the disappearance rates of O2 and N2 respectively but opposites in signs. In addition, the dissociated nitrogen atoms recombining to produce molecular nitrogen, atomic nitrogen interacts with oxygen molecules and there for closing to the wall, recombination reactions releasing energy appear as can be shown in **Fig 4.8.**

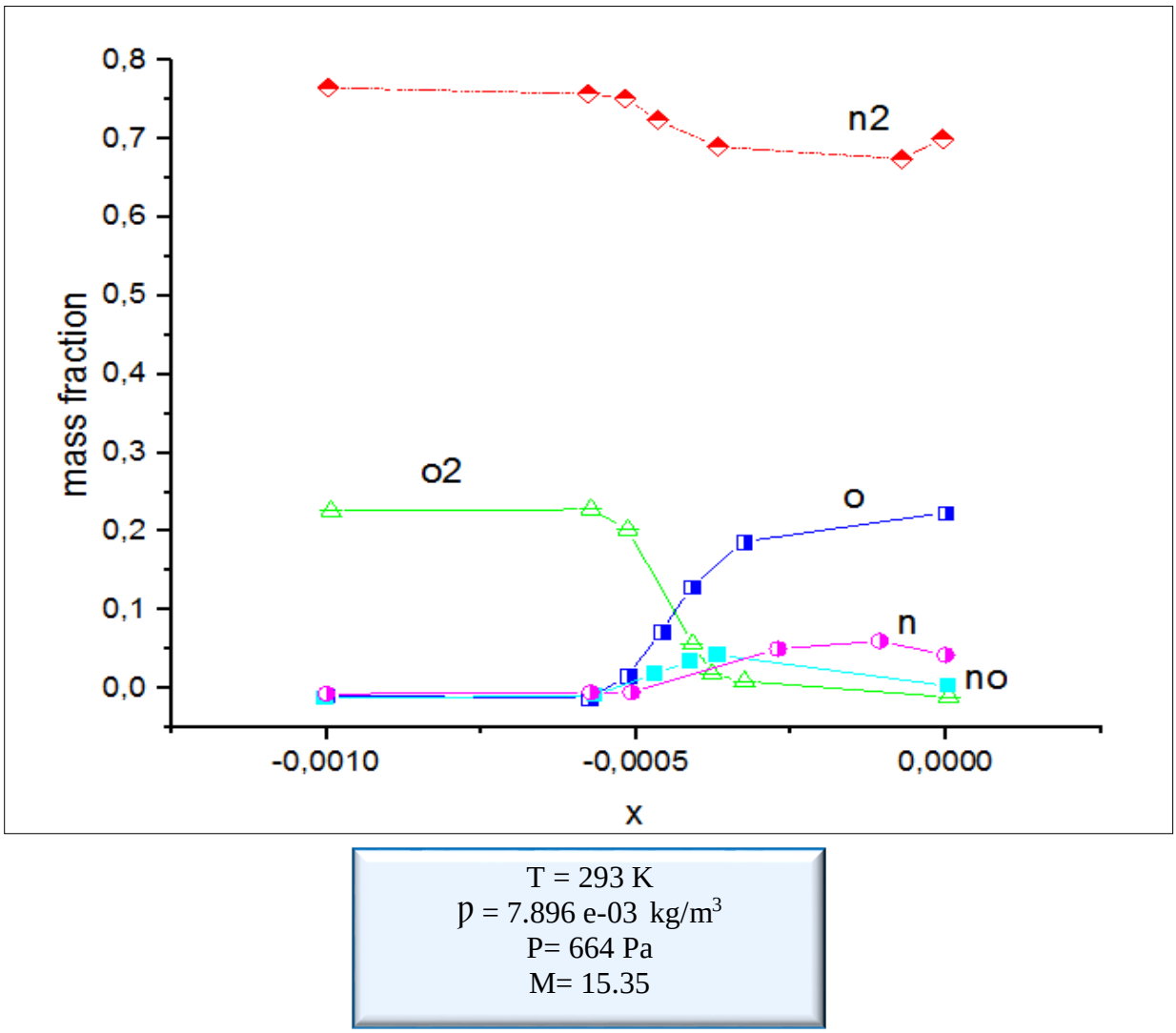

Figure 4-6: The mass fractions of the species along stagnation line**.**

Nonetheless, it can be seen that nitrogen does not dissociate completely, although the temperature was as high as 10470 K, it was not sufficient to dissociate all the molecules. This is primarily due to the high degree of thermal non-equilibrium, yielding an insufficient number of collisions for full dissociation. **[54]**

4.1.5 Mass fraction

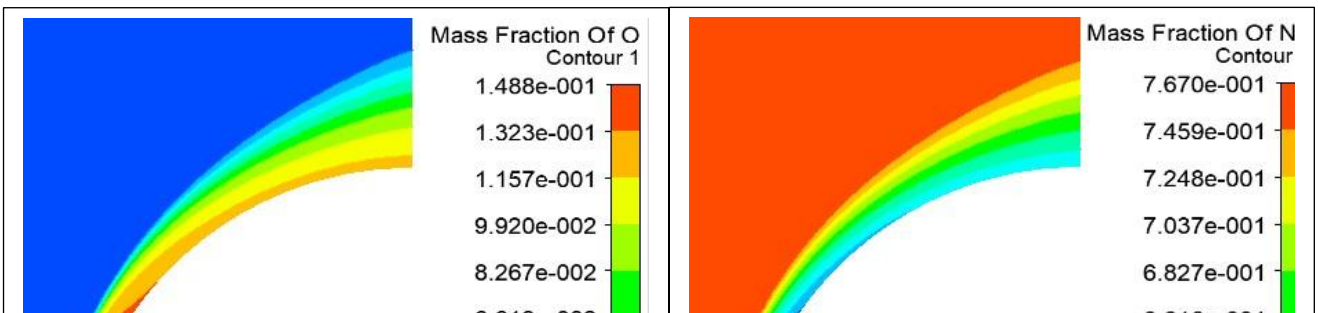

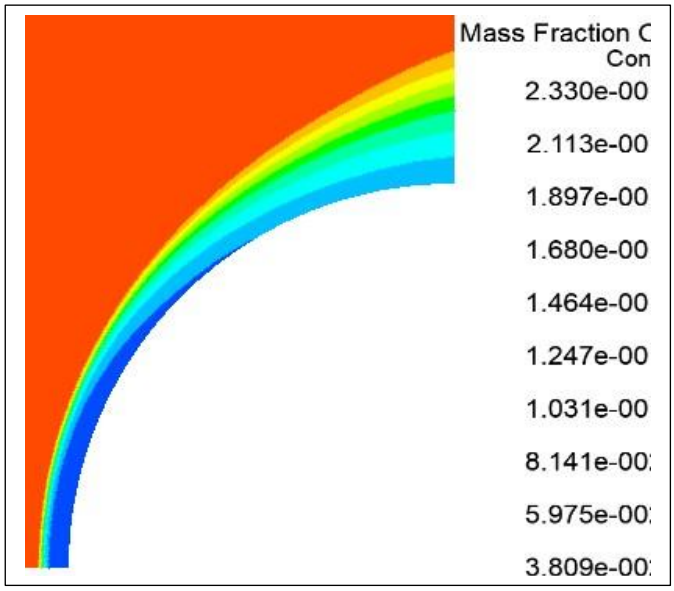

T = 293 K
ρ = 7.896 e-03 kg/m^3
P= 664 Pa
M= 15.35

Figure 4-7: Major species mass fraction**.**

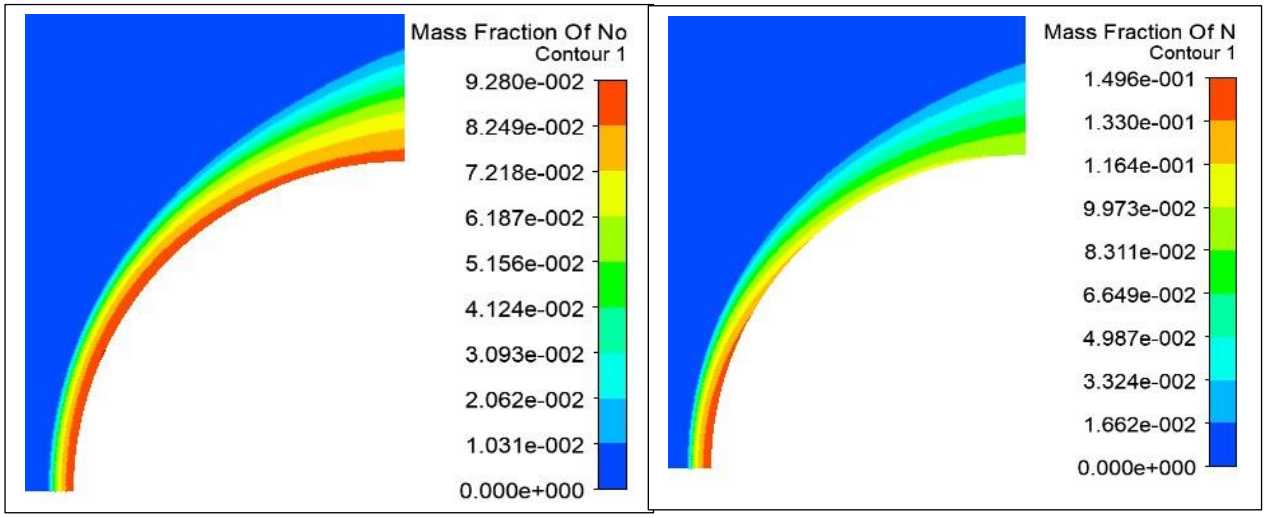

Figure 4-8: Minor species mass fraction**.**

4.1.6 Mach number effect

At 26 Mach number, it was observed that the maximum temperature in the flow field reaches 17 500 K. However, the shock standoff distance is the shortest as shown in **Fig 4.9**,

because the wave compression is done more quickly compared to 15.35 and 18 Mach numbers **Fig 4.11** and therefor the temperature just after the shock is the highest **Fig 4.10**.

Because the characteristic time of dissociation is less than the recombination time and from **Fig 4.9**, we notice that the relaxation zone decreases for high Mach numbers this allows the appearance of N and O masse fractions only **Fig 4.12,16** due to the short reaction time which explain the important dissociation process **Fig 4.13,15** counter to the recombination process which increases for low Mach numbers as shown in **Fig 4.14** for they have the available time to recombined.

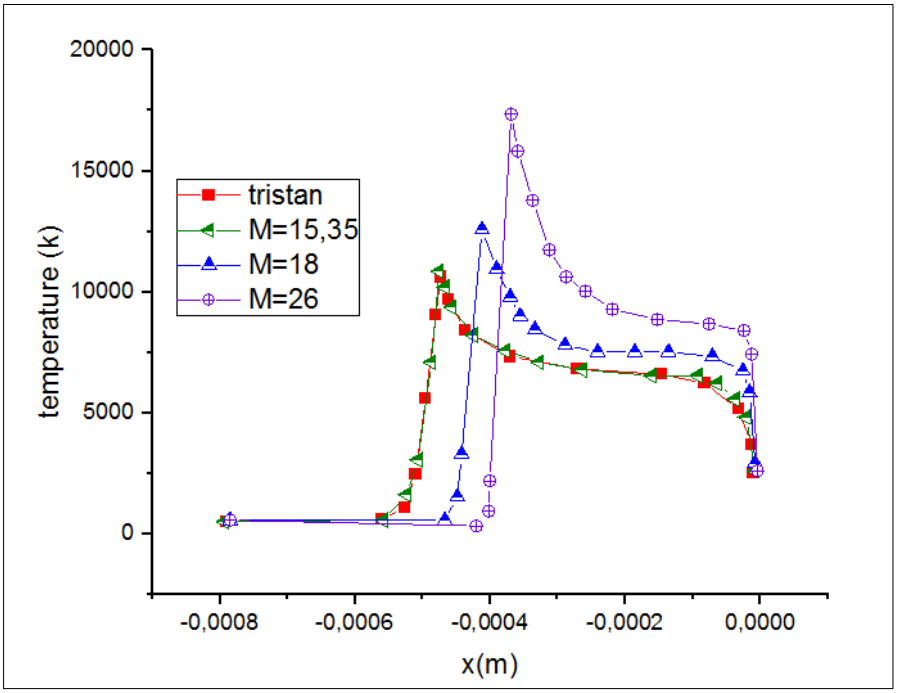

T = 293 K
p = 7.896 e-03 kg/m^3
P= 664 Pa

Figure 4-9: Temperature distribution along the stagnation line at deferent Mach number**.**

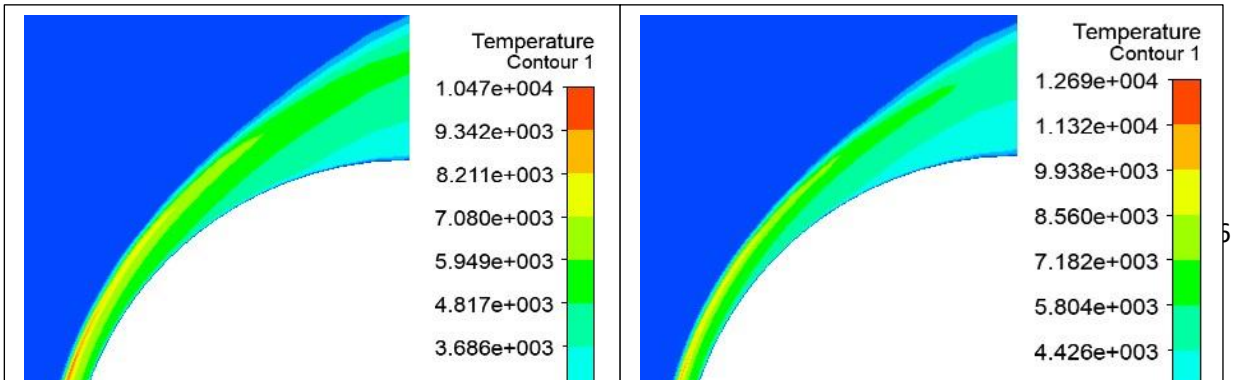

Fig A **Fig B**

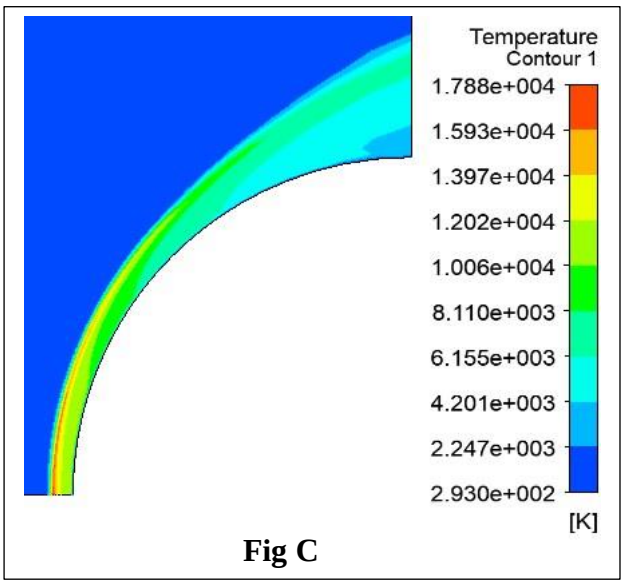

Fig C

T = 293 K
ρ = 7.896 e-03 kg/m^3
P= 664 Pa
Fig A) M = 15.35
Fig B) M = 18
Fig C) M = 26

Figure 4-10: Temperature field along relaxation zone at different Mach numbers**.**

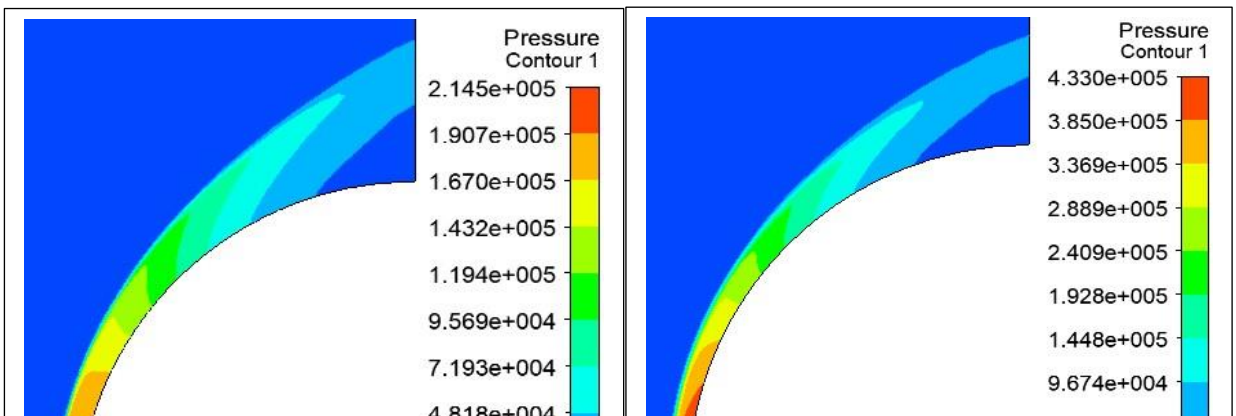

Fig A

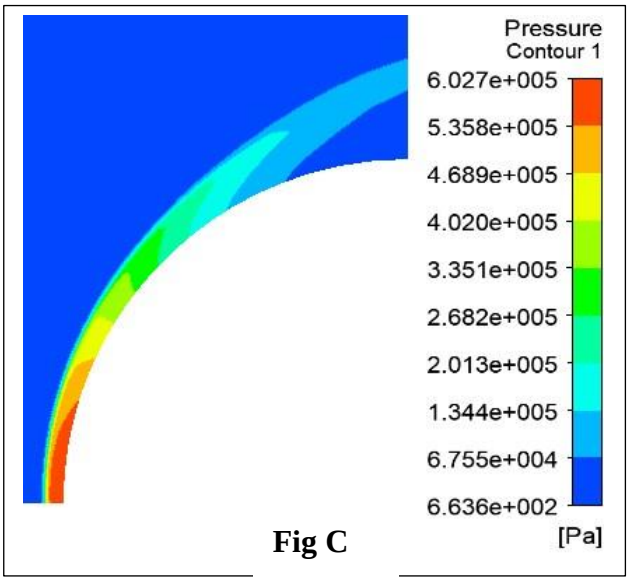

Fig C

Fig B

T = 293 K
ρ = 7.896 e-03 kg/m^3
P= 664 Pa
Fig A) M = 15.35
Fig B) M = 18
Fig C) M = 26

Figure 4-11: Pressure field along relaxation zone at different Mach numbers**.**

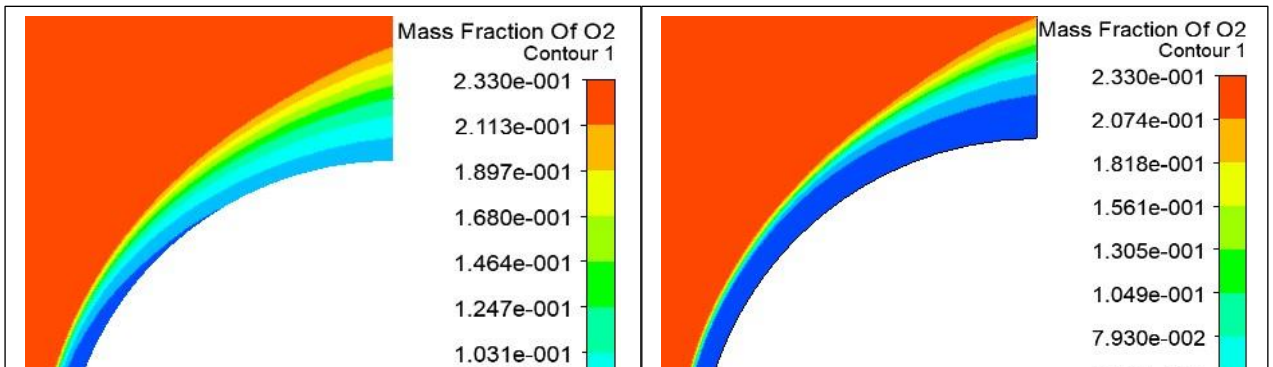

Fig A

Fig B

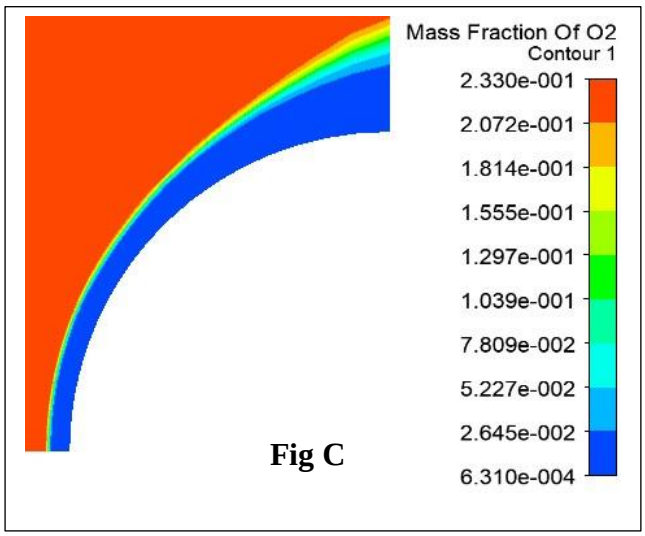

Fig C

T = 293 K
ρ = 7.896 e-03 kg/m^3
P= 664 Pa
Fig A) M = 15.35
Fig B) M = 18
Fig C) M = 26

Figure 4-12: Mass fraction of O2 along relaxation zone at different Mach numbers**.**

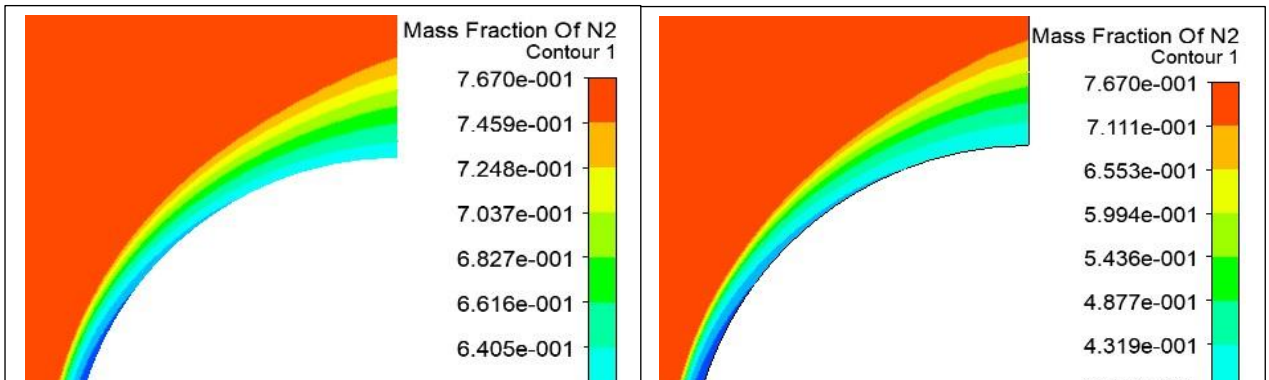

Fig A

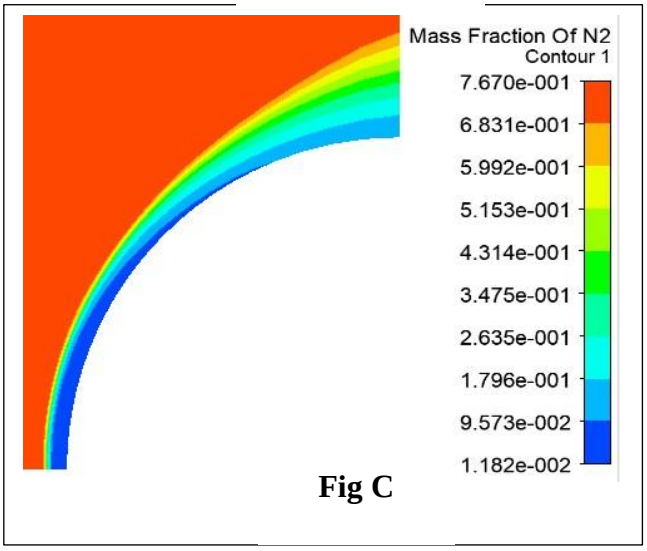

Fig C

Fig B

T = 293 K
ρ = 7.896 e-03 kg/m^3
P= 664 Pa
Fig A) M = 15.35
Fig B) M = 18
Fig C) M = 26

Figure 4-13: Mass fraction of N2 along relaxation zone at different Mach numbers**.**

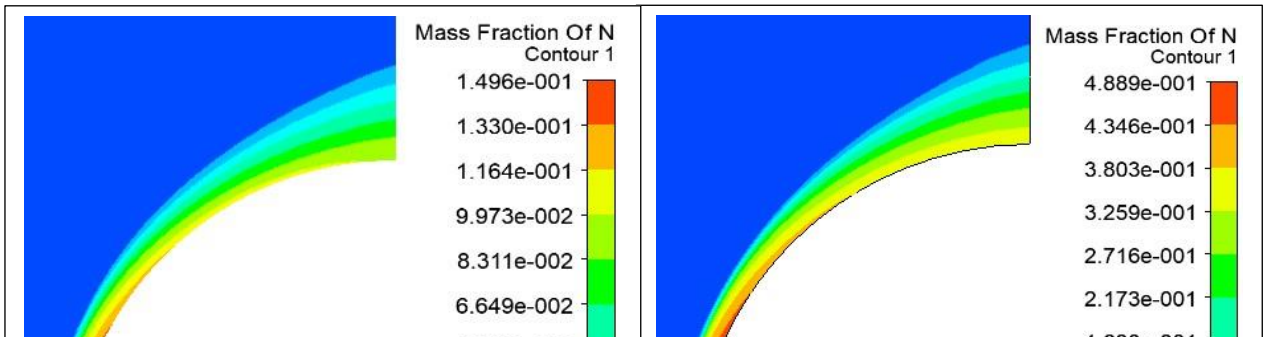

Fig A

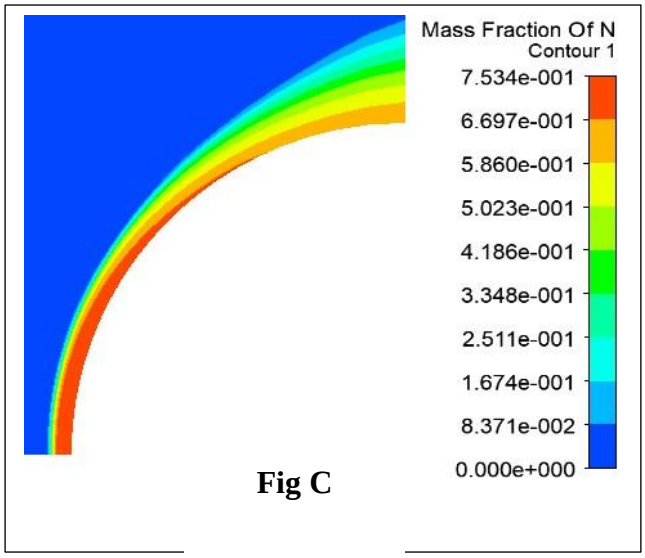

Fig C

Fig B

T = 293 K
ρ = 7.896 e-03 kg/m^3
P= 664 Pa
Fig A) M = 15.35
Fig B) M = 18
Fig C) M = 26

Figure 4-14: Mass fraction of N along relaxation zone at different Mach numbers**.**

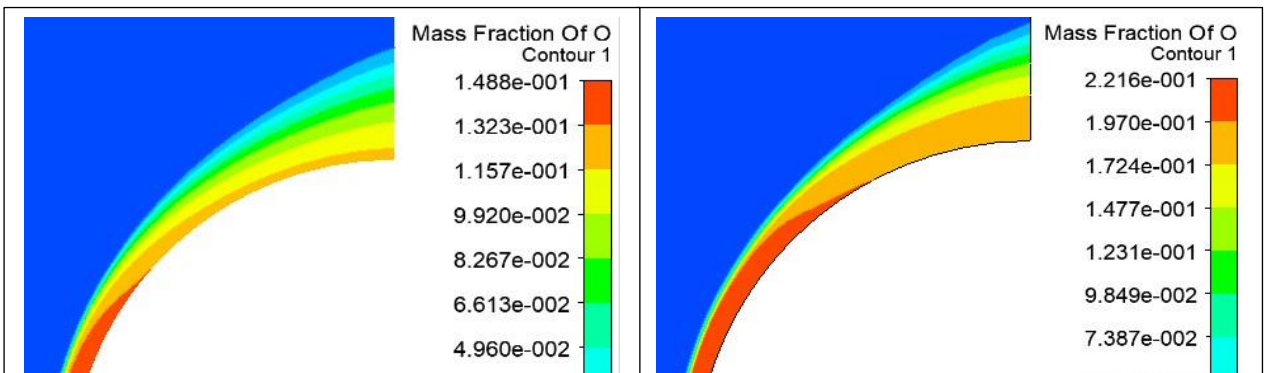

Fig A **Fig B**

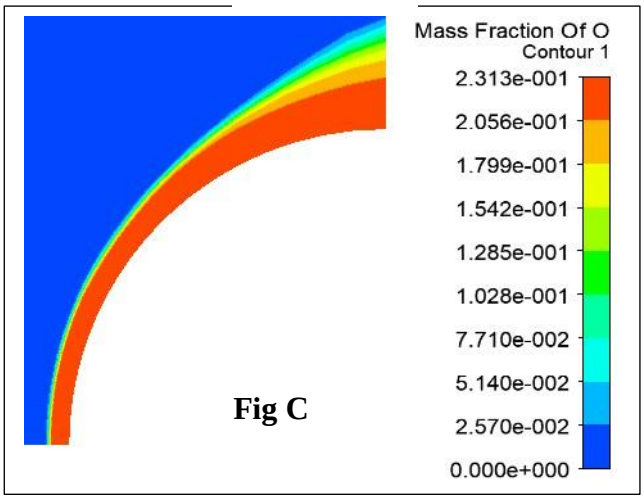

Fig C

T = 293 K
ρ = 7.896 e-03 kg/m^3
P= 664 Pa
Fig A) M = 15.35
Fig B) M = 18
Fig C) M = 26

Figure 4-15: Mass fraction of O along relaxation zone at different Mach numbers**.**

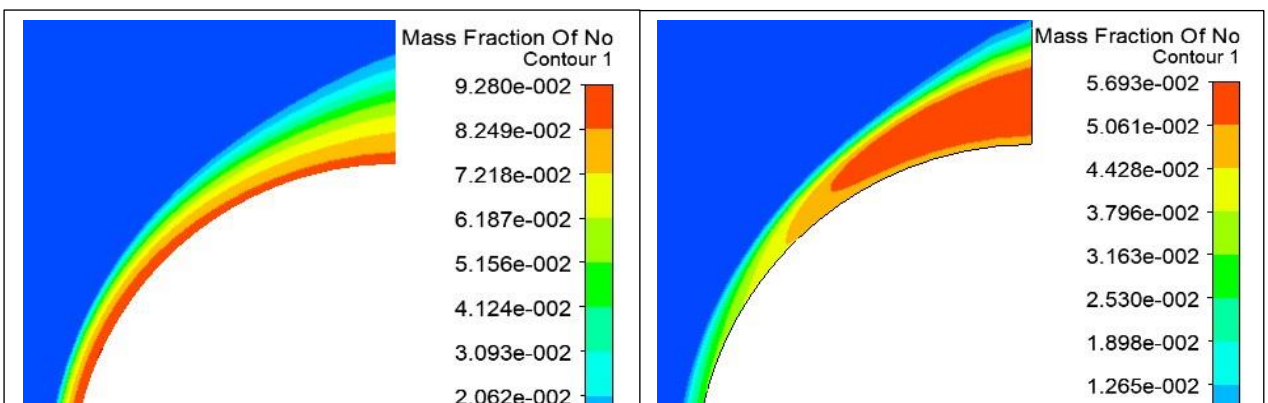

Fig A **Fig B**

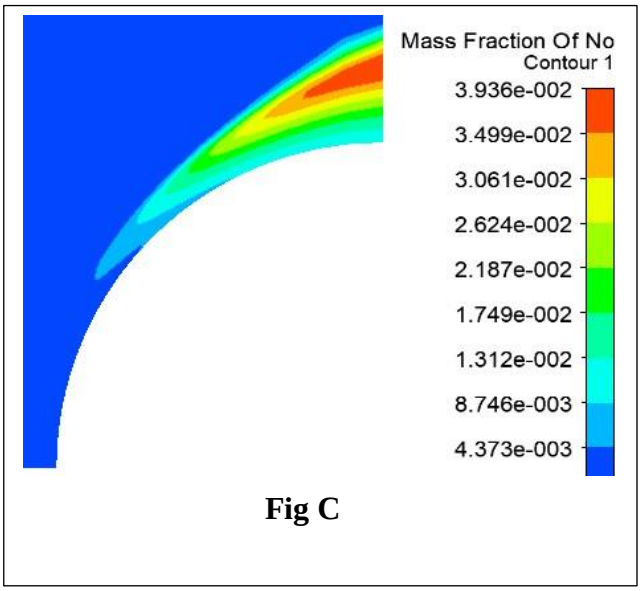

Fig C

T = 293 K
ρ = 7.896 e-03 kg/m^3
P= 664 Pa
Fig A) M = 15.35
Fig B) M = 18
Fig C) M = 26

Figure 4-16: Mass fraction of NO along relaxation zone at different Mach numbers**.**

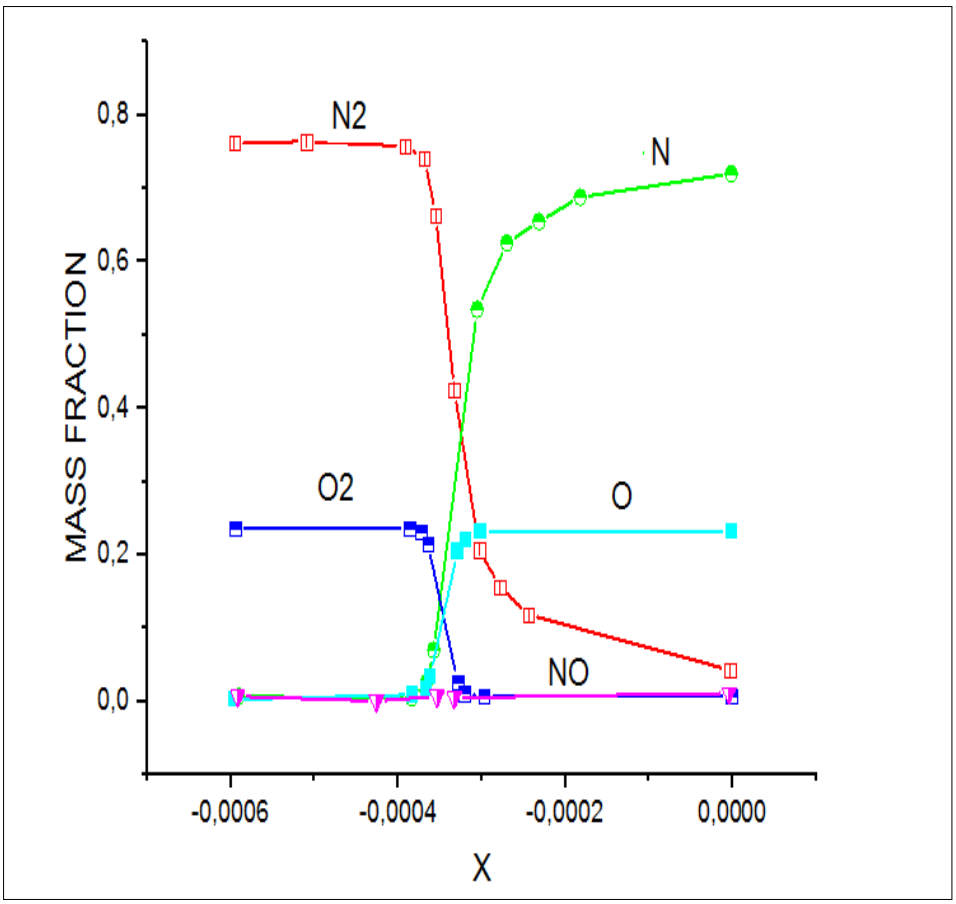

T = 293 K
ρ = 7.896 e-03 kg/m^3
P= 664 Pa
M = 26

Figure 4-17: The mass fractions of the species along stagnation line**.**

4.1.7 Effect of chemical model

The 17 and 21 reactions kinetic models decreases the maximum temperature by 12.5% and 13% compared to the 5 reactions kinetic model, this is due to the presence of a catalyst in the 17 and 21 reactions models, there are a greater number of effective collisions than in the absence of a catalyst (5 reaction kinetic model) at the same temperature because a catalyst accelerates the reaction by providing a new path way involving lower amount of activation energy, that what explain the decrease in temperature in the 17 and 21 reactions models more as shown in **Fig 4.18 [55]**

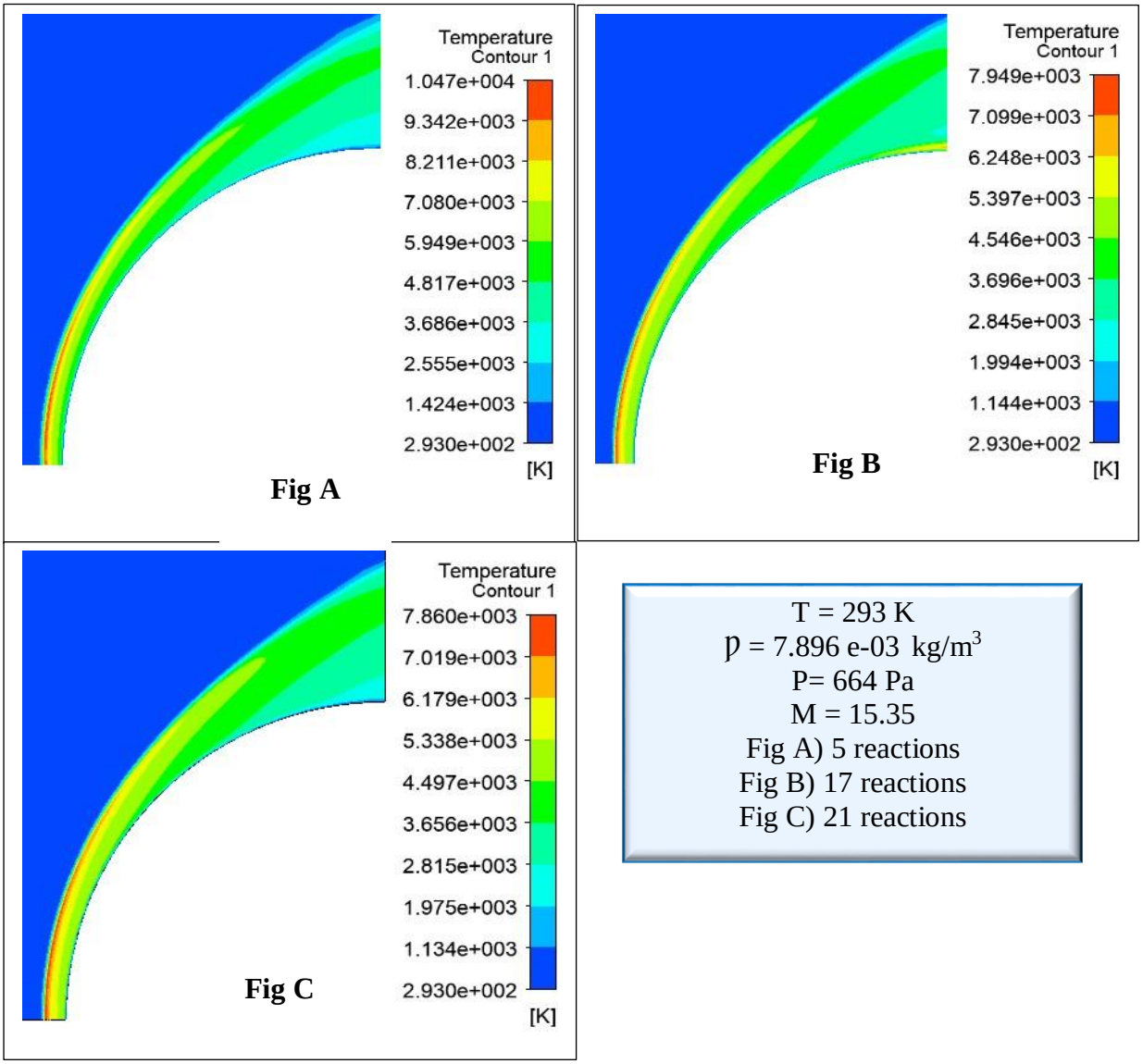

Figure 4-18: Temperature fields along relaxation zone at different models of reactions**.**

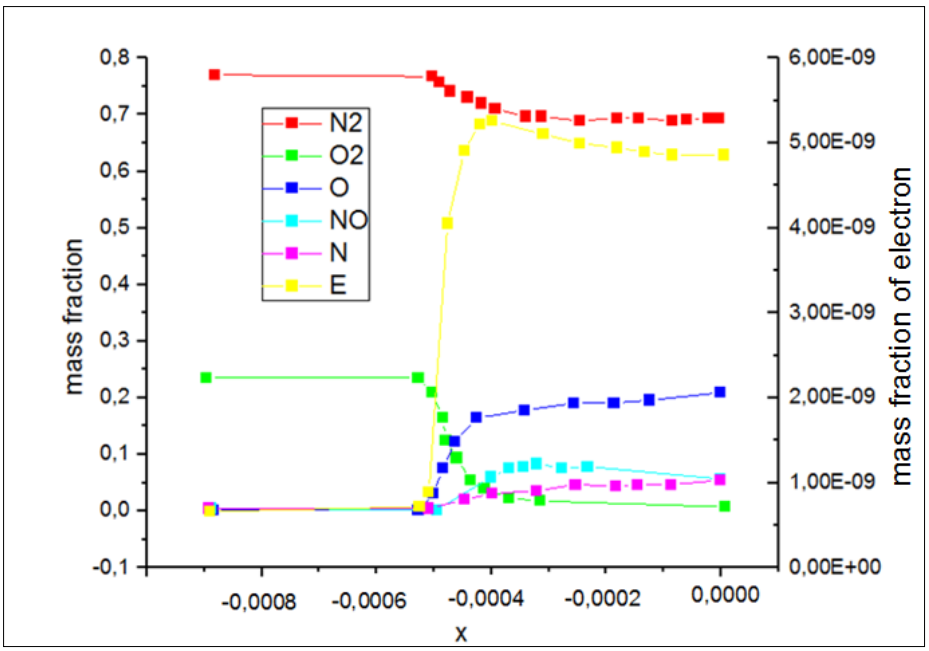

T = 293 K
ρ = 7.896 e-03 kg/m^3
P= 664 Pa
M = 15.35
21 reactions

Figure 4-19: The mass fractions of the species along stagnation line**.**

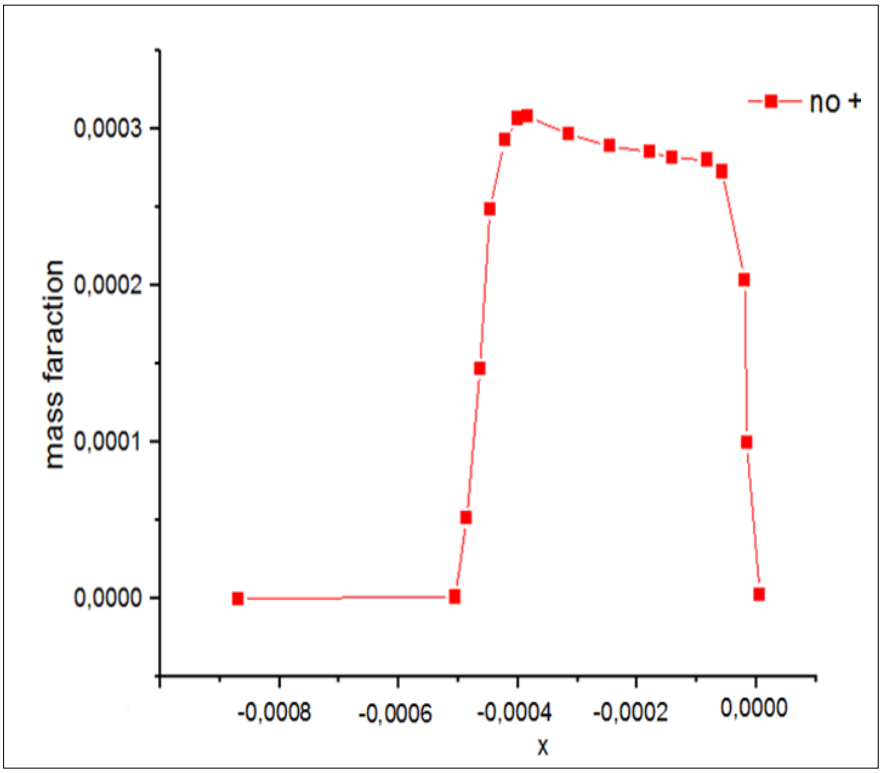

Figure 4-20: Mass fractions of NO+ along the stagnation line**.**

The similar difference is observed on species mass fractions plotted in **Fig 4.19**, except that some species (N,O) increases. The maximum value of electron mass fraction is around 5 £ 1029 and the mass fraction of the ionized species NO+ is significantly small than those of the neutral species as it will be shown in **Fig 4.20**. **[55]**

The chemical reactions on neutral species of gas with vibrational non-equilibrium do as previously, and in the second step the electron-electronic relaxation is included with weakly ionized gas. One can see that the effects observed previously increase with the temperature. A difference in order of 8 percent lower exists with ionization.

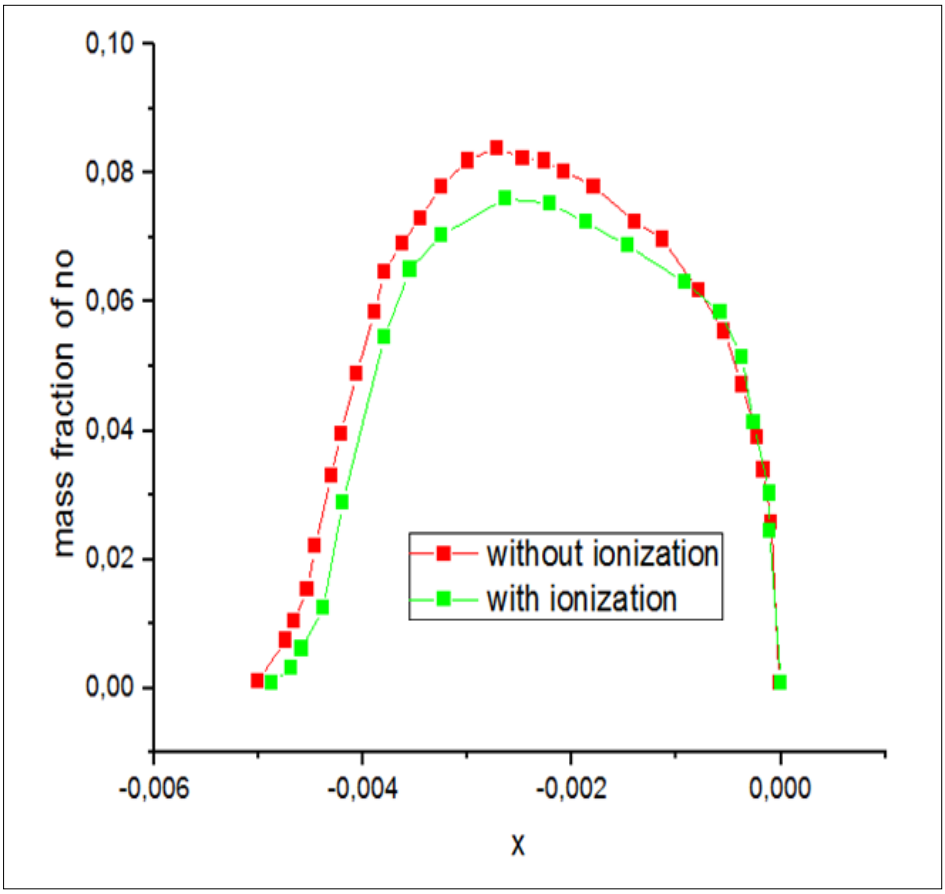

Figure 4-21: NO mass fraction along the stagnation line**.**

The YNO profiles obtained with and without ionization at M1 1⁄4 15:3 along stagnation line are compared in **Fig 4.21**. The peak concentration of nitric oxide is 10 percent lower with ionization. Such phenomena can be explained by the fact that N and O atoms are used in ionization case for the production of NO and NO+ molecules. Furthermore, this decrease is

similar to the decrease observed in the peak of temperature which acts and affects the kinetic of the chemical reactions.

4.1.7.1 Effect of 31 reaction

Consider now the impact of the gas model on the bulk gas properties. The translational temperature profiles along the stagnation line for the three models, the freestream velocity of 9 km⁄s. A comparison of temperatures obtained with the seven- and 11-species models shows that they are nearly identical inside the shock, as well as in the region between the shock and the boundary layer. In the boundary layer, the impact of the higher degree of ionization becomes visible, with the temperature for the 11-species model lower by over 1000 K. A comparison with the five-species model shows a counterintuitive result, with the ionization reactions resulting in a visibly higher translational temperature. Such a pattern differs from that at higher velocities, where the ionization either decreases the maximum or almost does not change it **[56]**

The difference between the five- and 11-species models is largest near the wall, where it reaches over 80% in both density and temperature (so that there is no visible impact on gas pressure). **[57]**

Generally, the impact of ionization on the bulk gas properties in the shock region becomes significant at 9 km⁄s **[57]**

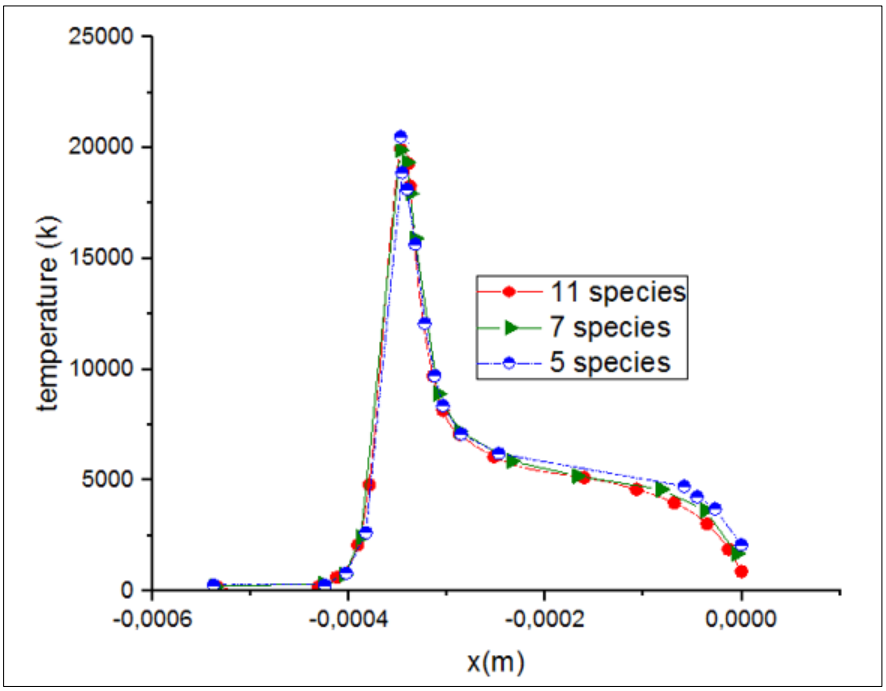

Figure 4-22: Impact of gas model on gas along the stagnation streamline at 9 km⁄s**.**

4.1.7.1.1 Mole fraction

The species concentrations along the stagnation line are shown in **Fig 4.23**.The simulation results eventually reach equilibrium values in agreement with the reference simulation. It is noteworthy that ions and free electrons, not present in the baseline solution, are reproduced with good accuracy.

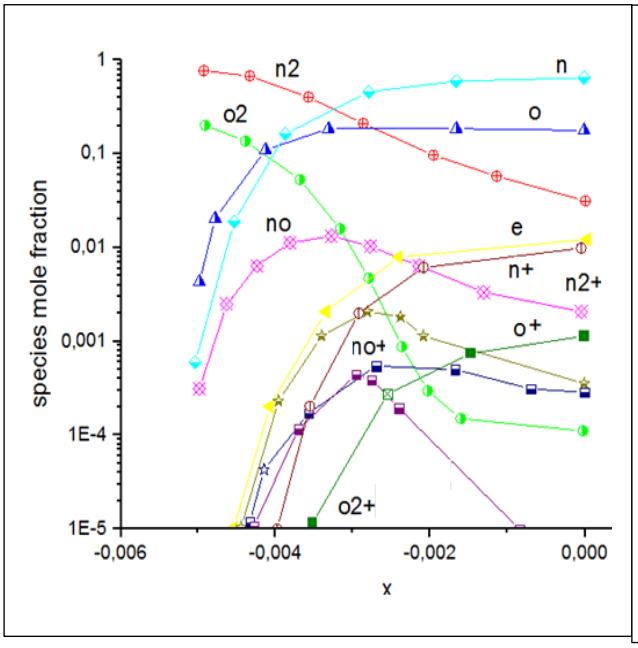

Fig A: The mole fractions of the species along stagnation line

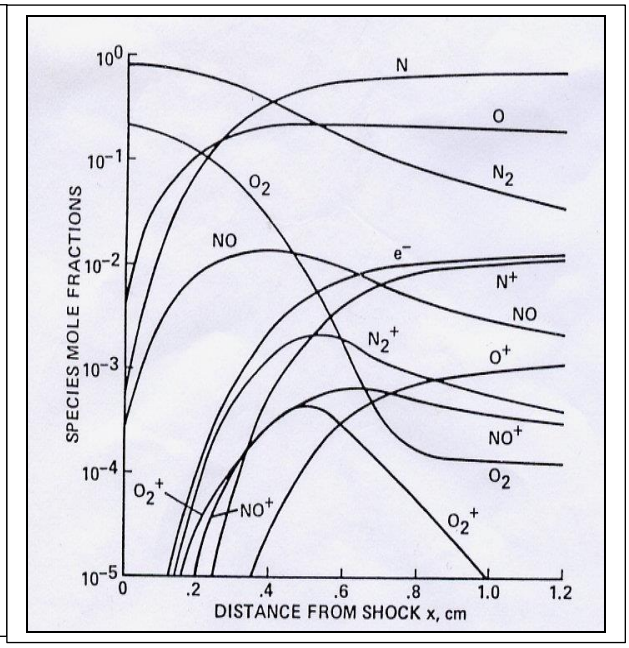

Fig B: Chul park s mole fraction.

P = 0.1 Torr
V = 10km/s
31 reactions

Figure 4-23: Comparison between our results and chul park results**.**

4.1.8 Effect of three dimension

4.1.8.1 Pressure

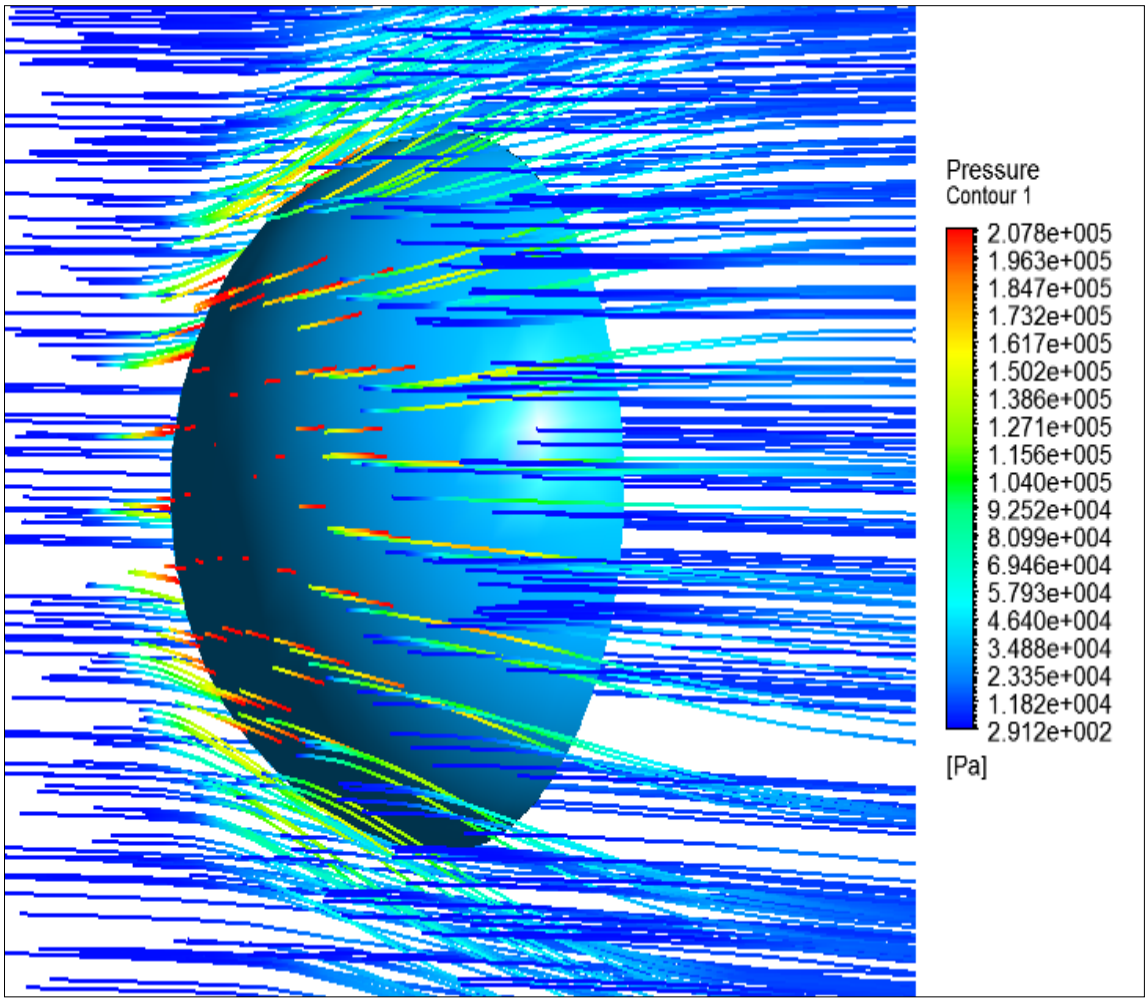

Figure 4-24: Pressure field along relaxation zone**.**

4.1.8.2 Temperature

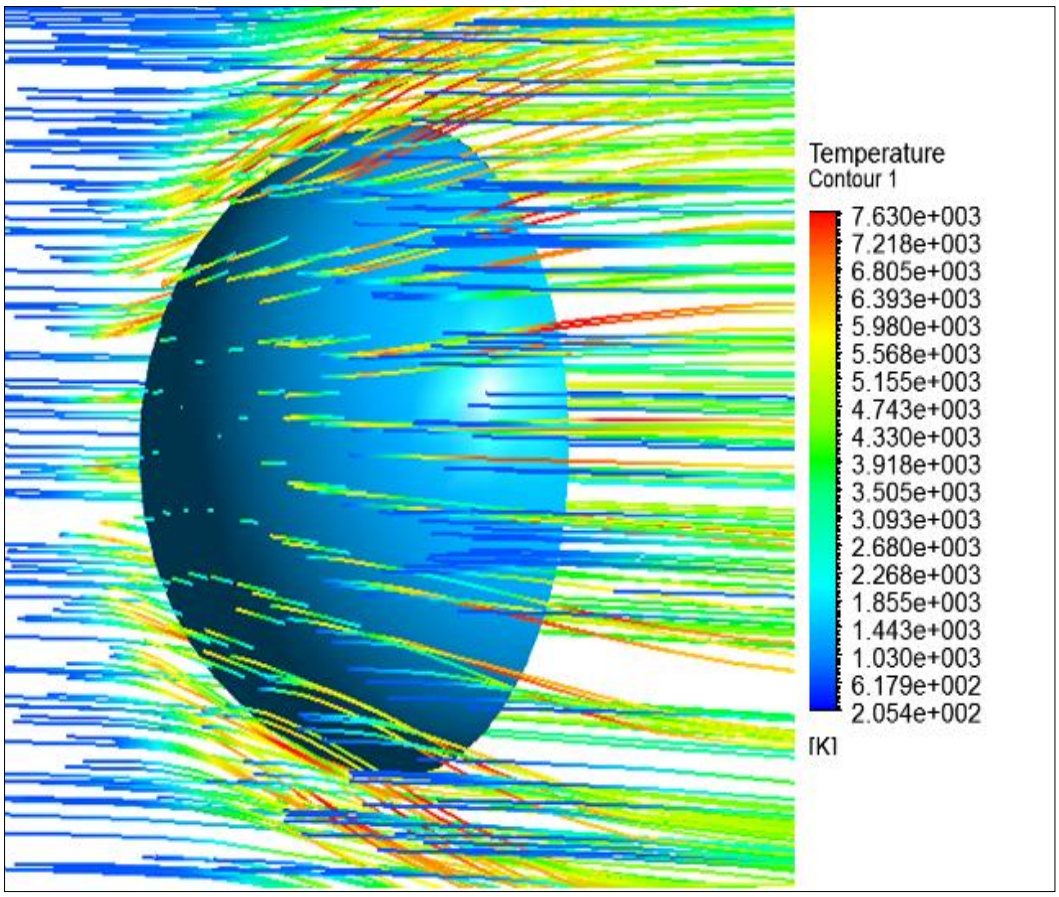

Figure 4-25: Temperature field along relaxation zone**.**

4.1.8.3 Mach number

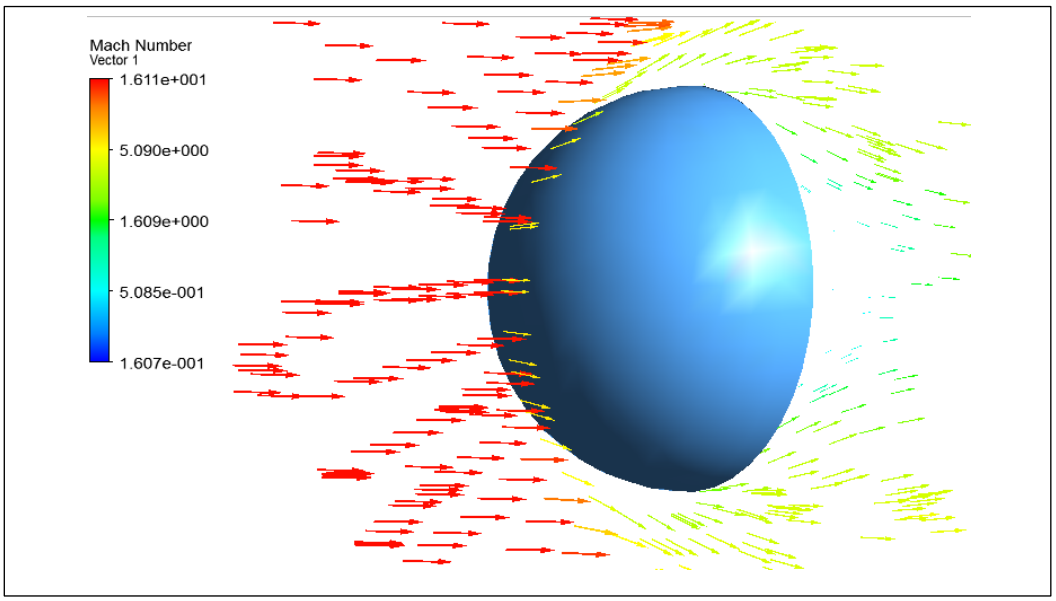

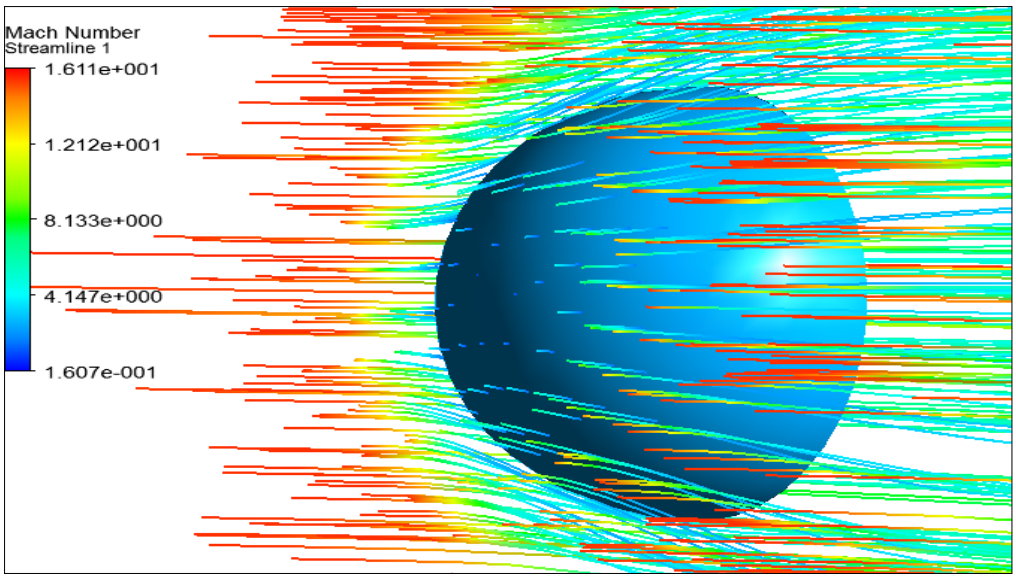

Figure 4-26: Mach number field along relaxation zone**.**

4.2 Result of Hypersonic Flow over a Cone flare

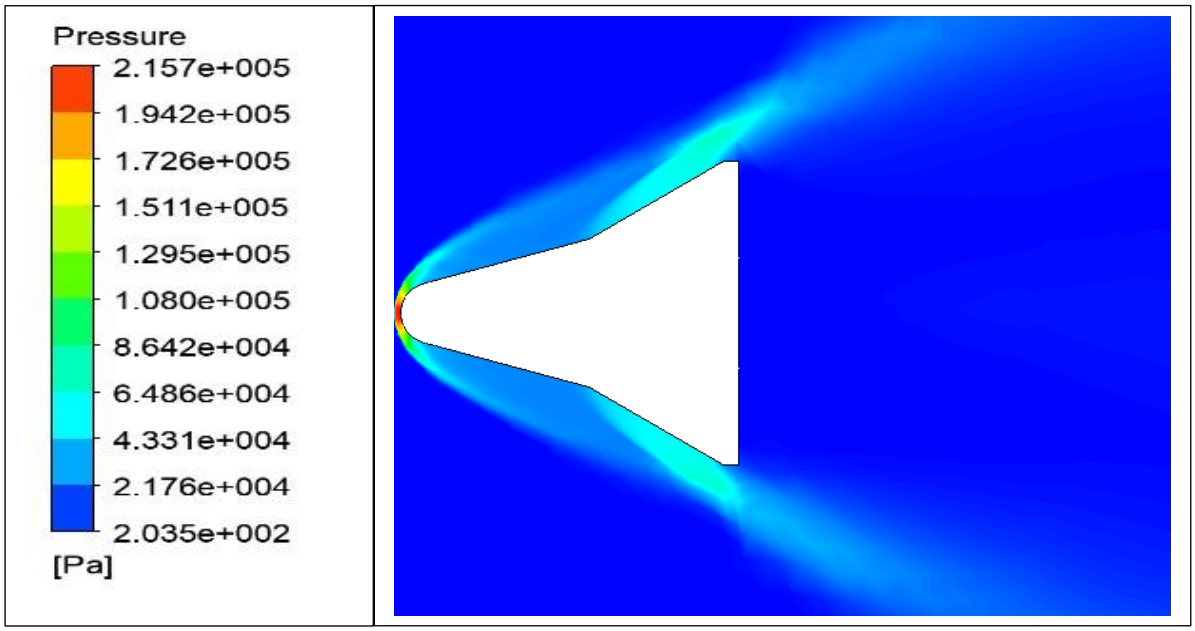

T = 293 K
ρ = 7.896 e-03 kg/m^3
P= 664 Pa
M = 15.35
17 reactions

Figure 4-27: Pressure contour along cone flare**.**

4.2.1 Validation

Fig 4.28 shows the experimental scleren graph. This graph shows the shock wave pattern and the fluent generated shock wave pattern for the same experimental input so we are comparing the both graphs for validation. One notices a good agreement between the two results**.[34]**

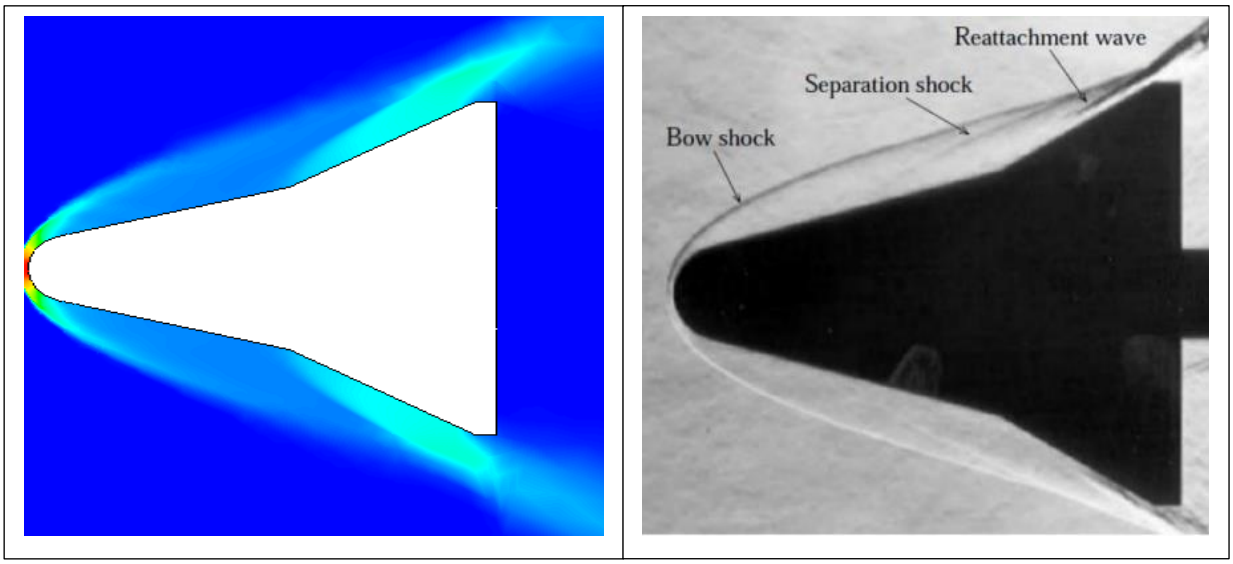

Figure 4-28: Comparison of Experimental Result with analytical result**.**

4.2.2 Temperature

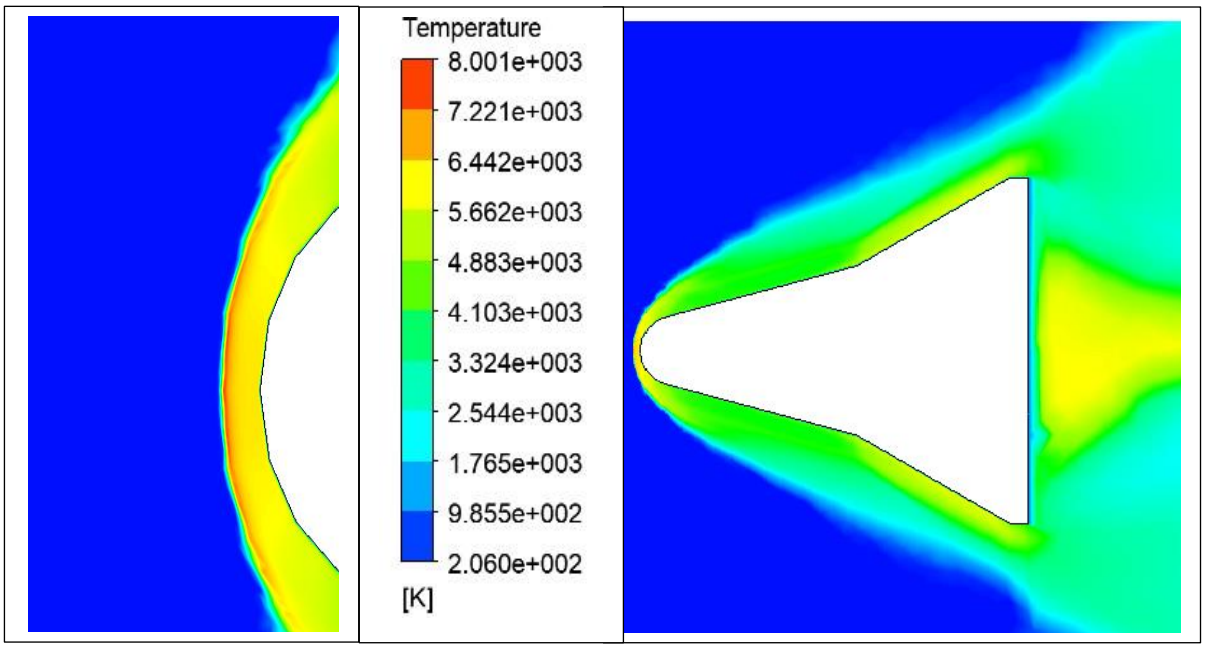

T = 293 K
ρ = 7.896 e-03 kg/m^3
P= 664 Pa
M = 15.35
17 reactions

Figure 4-29: Temperature contour along cone flare**.**

4.2.3 Reaction effects

We notice in **Fig 4.30** the formation of NO molecules where the flow is decelerated due to the compression waves that give more time for the recombination process, in the other hand, **Fig4.31** shows that the O2 and N2 dissociation layer contract in the flap region due to the formation of NO molecules.

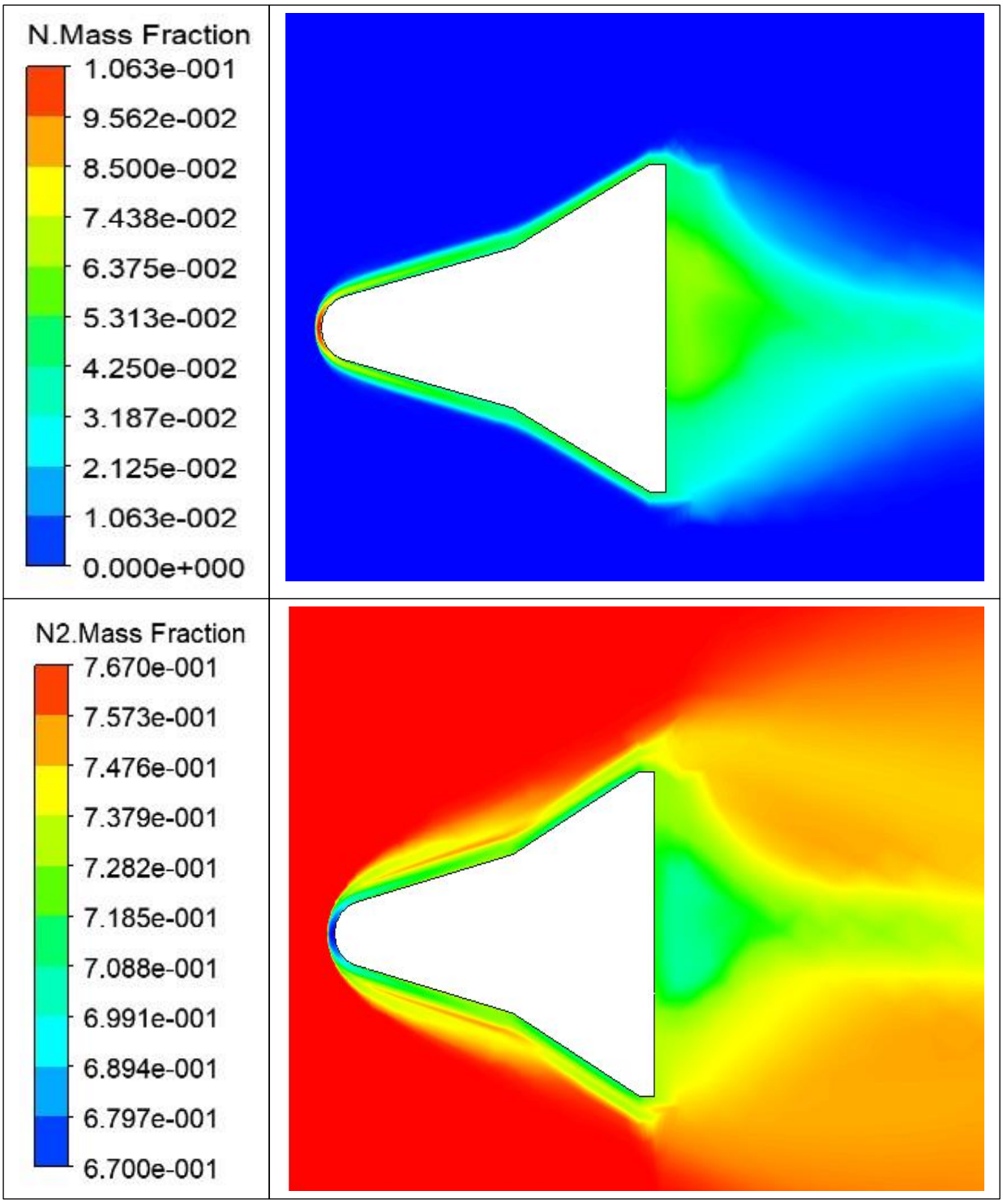

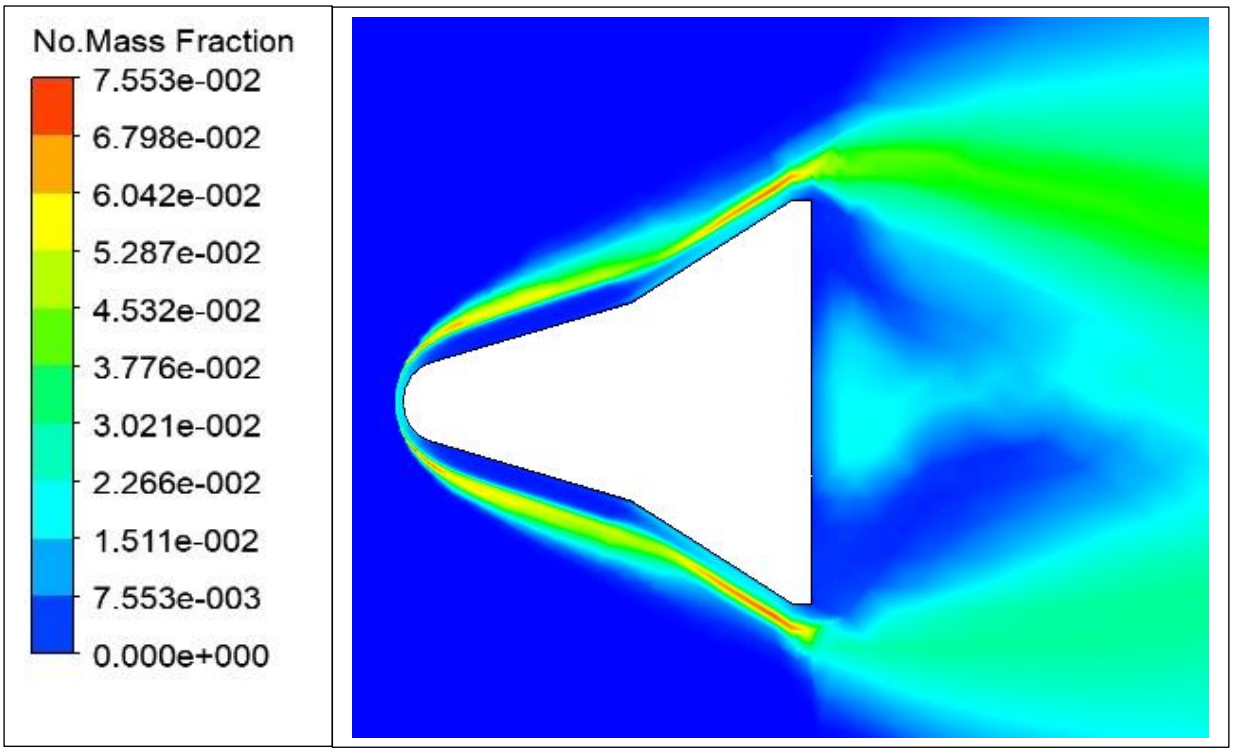

T = 293 K
ρ = 7.896 e-03 kg/m^3
P= 664 Pa
M = 15.35
17 reactions

Figure 4-30: Major species field along cone flare**.**

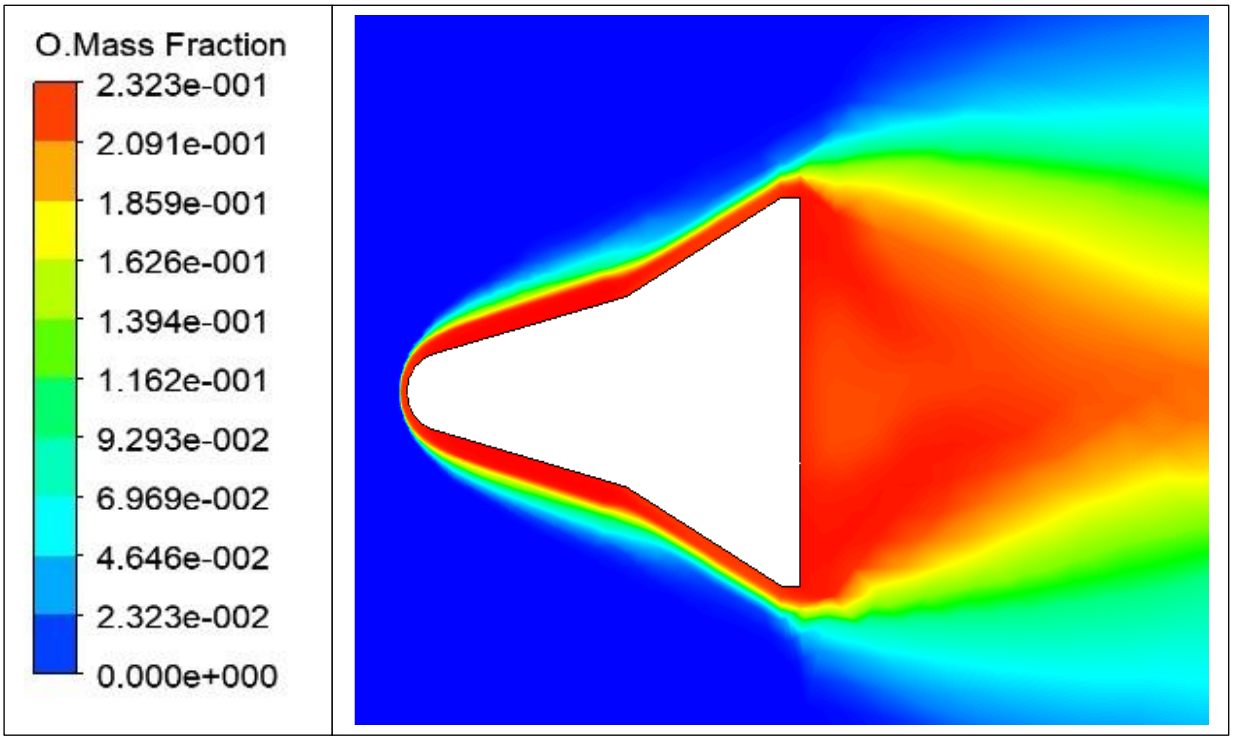

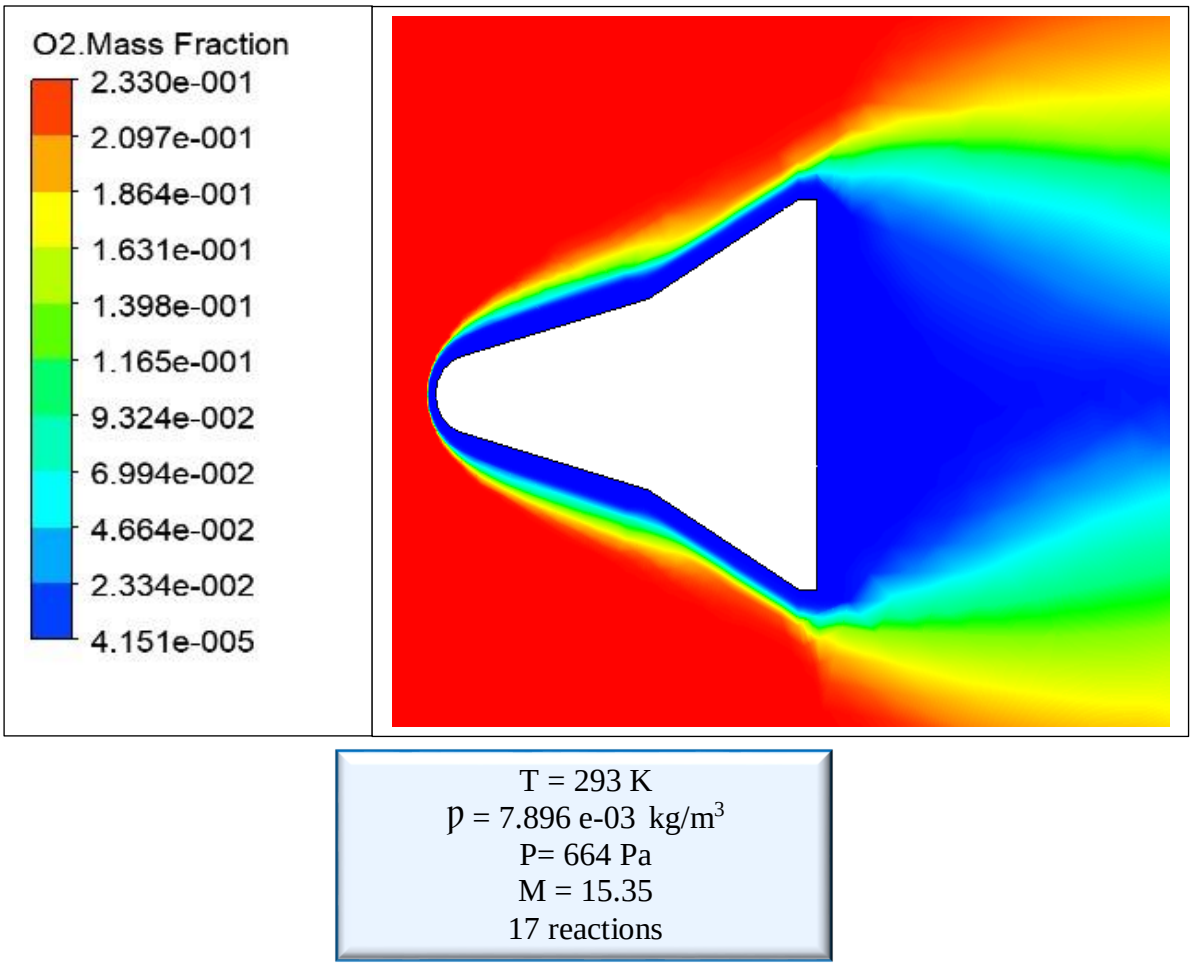

Figure 4-31: Minor species field along cone flare**.**

4.2.4 Results of cone flare in 3D

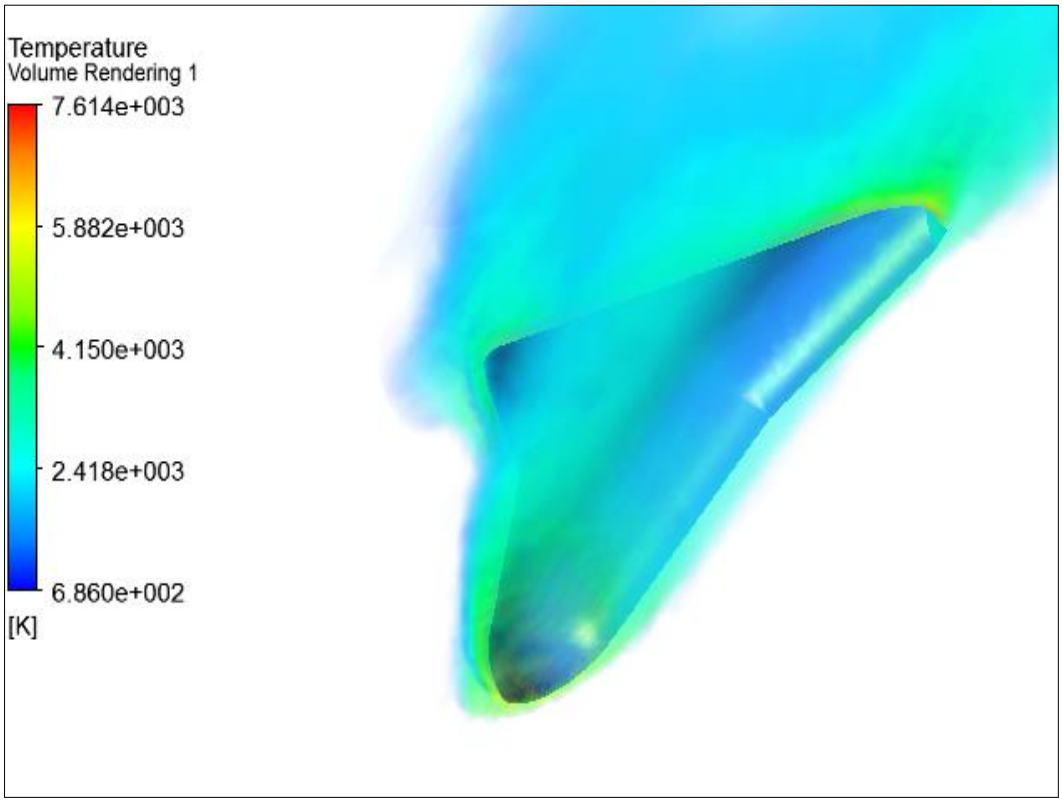

Figure 4-32: Temperature along cone flare in 3D**.**

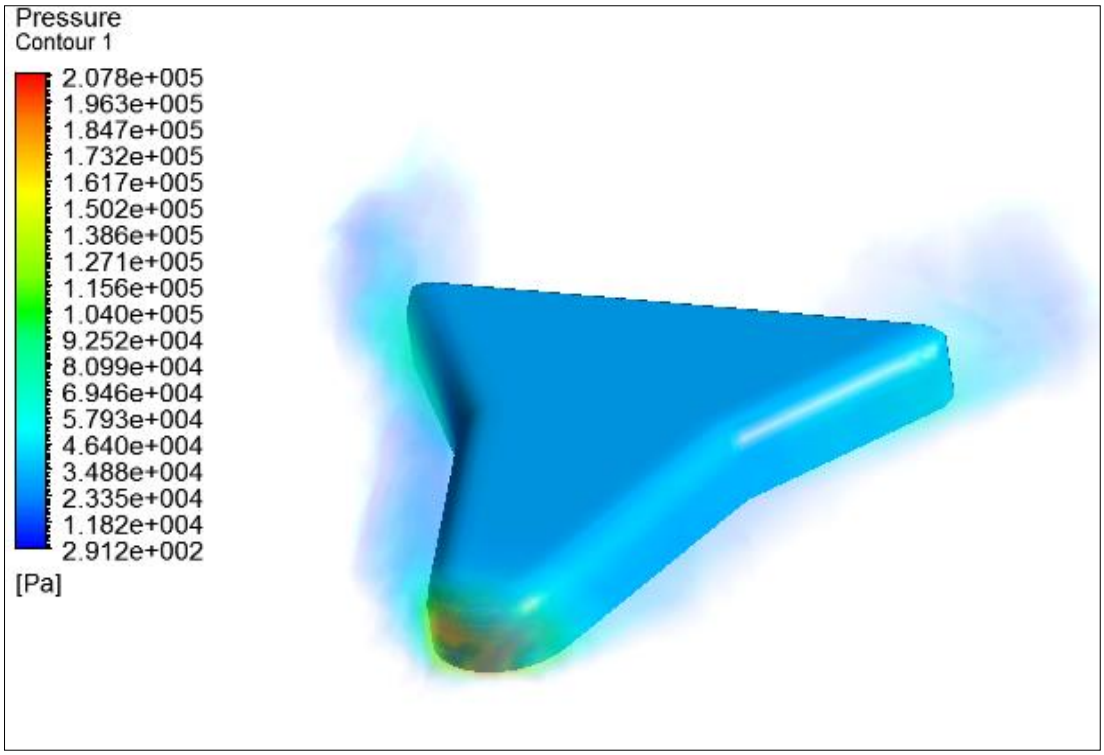

Figure 4-33: Pressure along cone flare in 3D**.**

4.3 Result of Hypersonic Flow over a Circular Cone body

4.3.1 Mach number

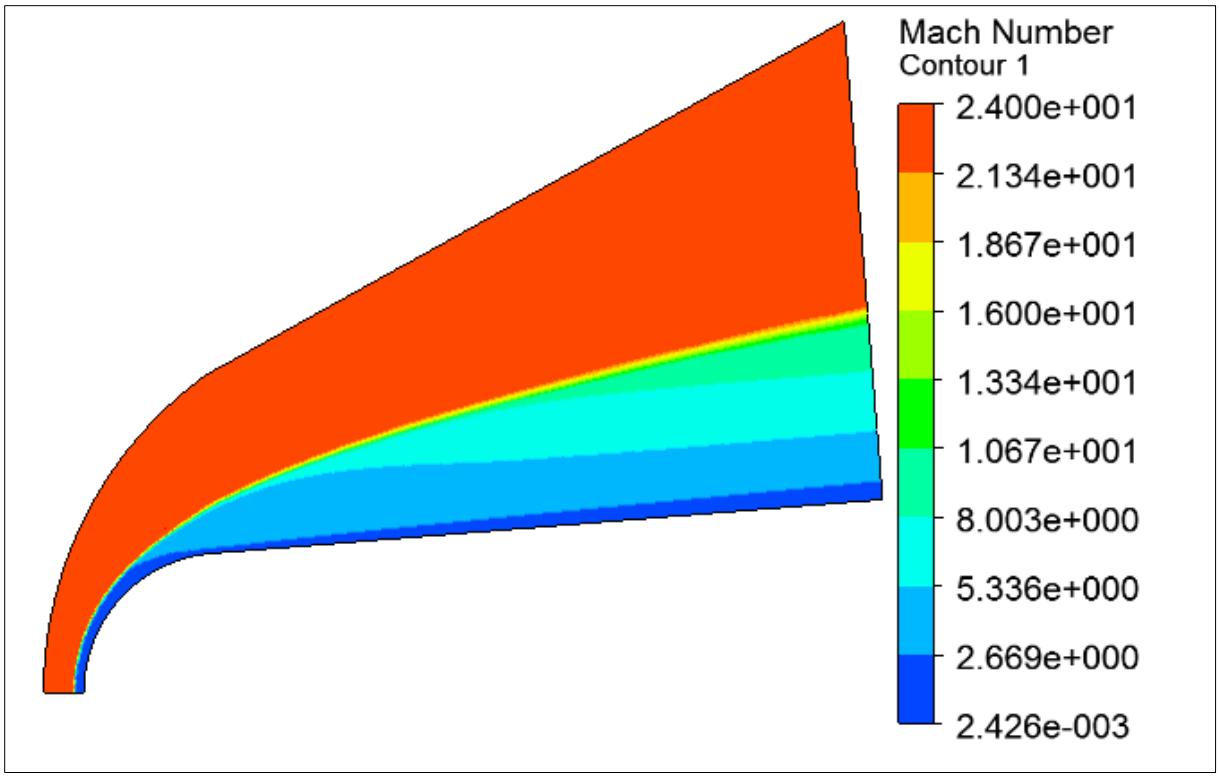

Figure 4-34: Mach number contour along conical body**.**

4.3.2 Temperature

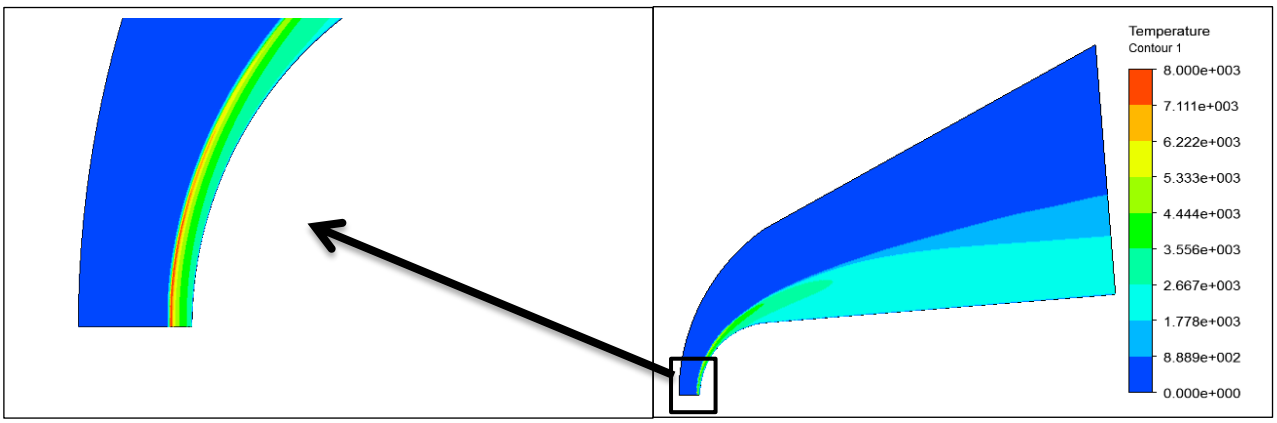

Figure 4-35: Temperature contour along conical body**.**

4.3.3 Pressure

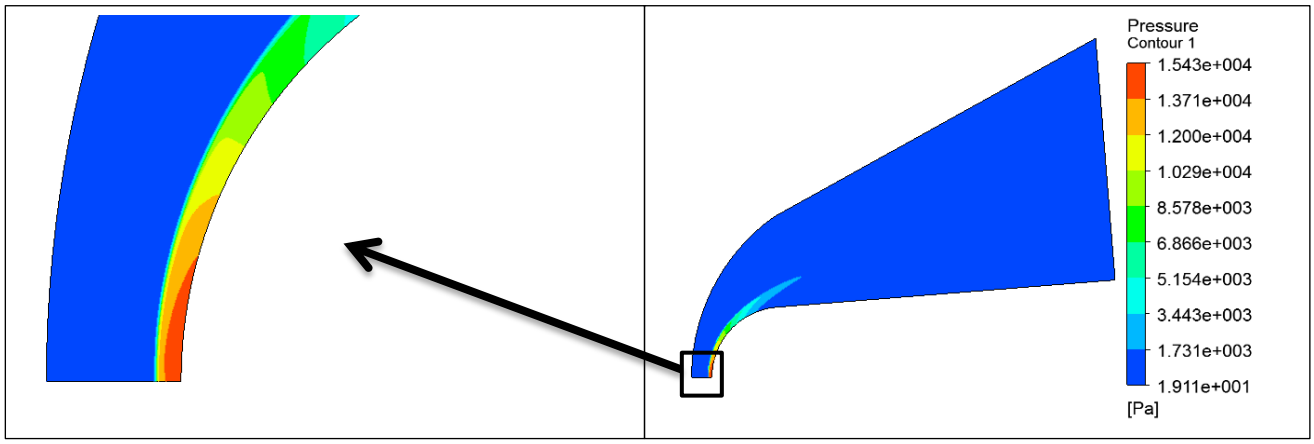

Figure 4-36: Pressure contour along conical body**.**

4.3.4 Mass fraction

We notice in **Fig 4.37** the formation of NO molecules where the flow is decelerated due to the compression waves that give more time for the recombination process, and also the **Fig4.37** shows that the O2 and N2 dissociation layer contract in the flap region due to the formation of NO molecules.

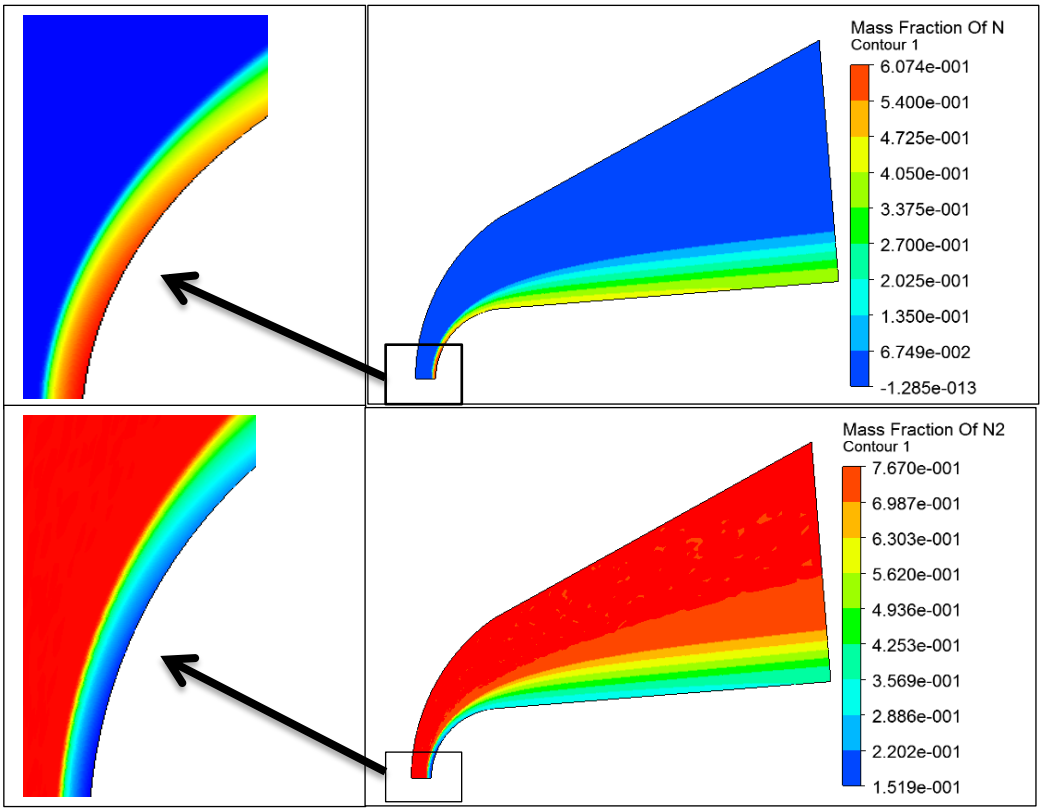

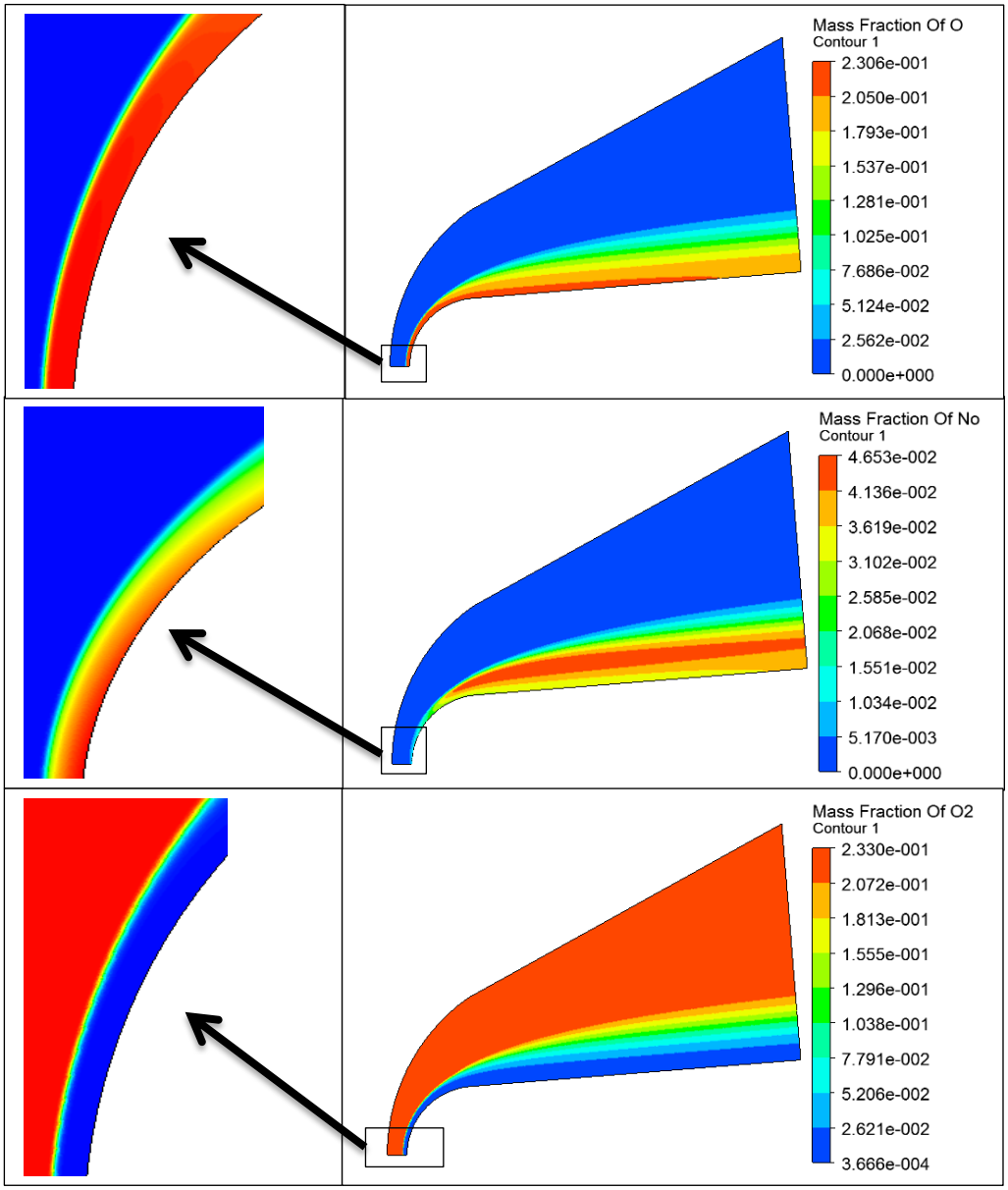

Figure 4-37: Mass fraction contour along conical body**.**

4.3.5 Validation

By comparing our result of **Fig 4.38** with J, MUYLAERT et al that of which shows the variation of the temperature along the relaxation range, one notices a good agreement between the two results in terms of pace and in quantitative term with an error of .2.2%

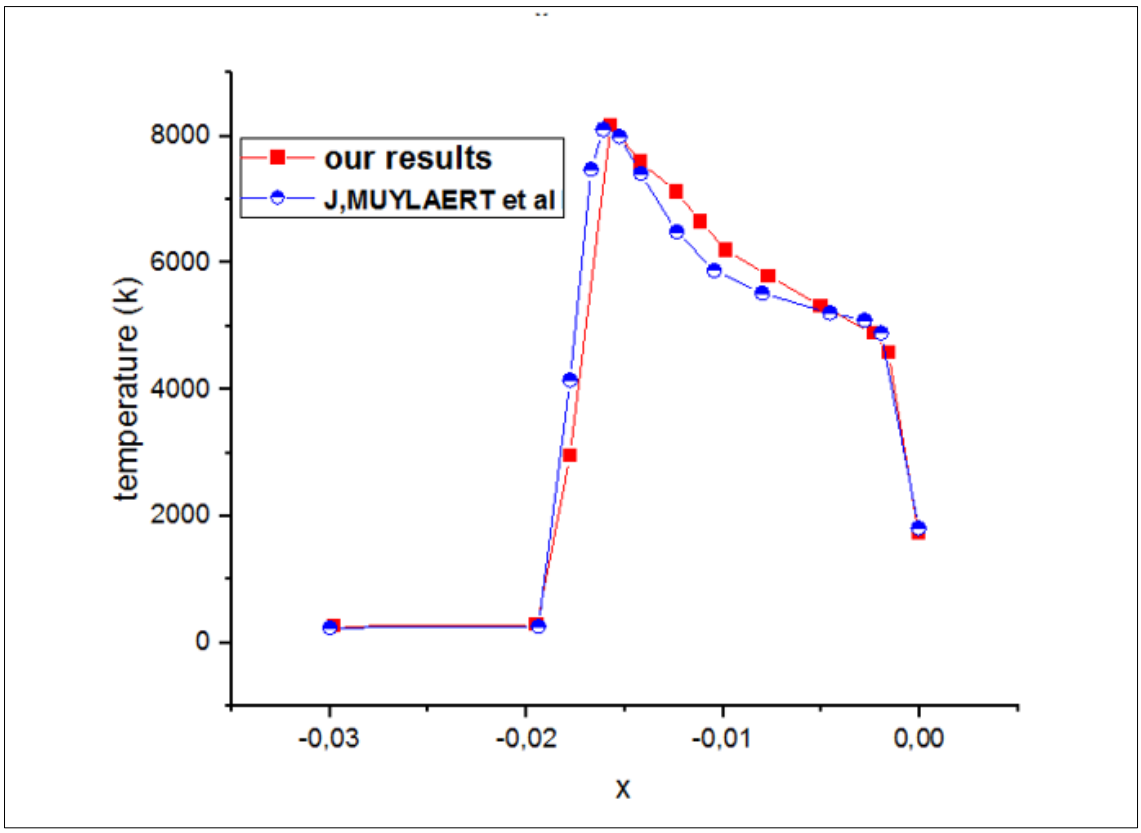

Figure 4-38: Temperature along the stagnation line compared to J, MUYLAERT et al**.) [58]**

4.3.6 Effect of altitude

At 71 km altitude (mach25.9 density ρ1 =7.2 x 1^{-05} kg/m3 ,T = 217 k , it was observed that the maximum temperature in the flow field reaches 24 000 K. However, the shock standoff distance is the shortest as shown in **Fig 4.39** ,because the wave compression is done more quickly compared to 61 km altitude (mach23.9 density ρ1 2.73 x 1^{-04} kg/m^3,T =244 k.

By comparing our result of **Fig 4.39** with [59]that of which shows the variation of the temperature along the relaxation range, we notice a good agreement between the two results in terms of pace and in quantitative term.

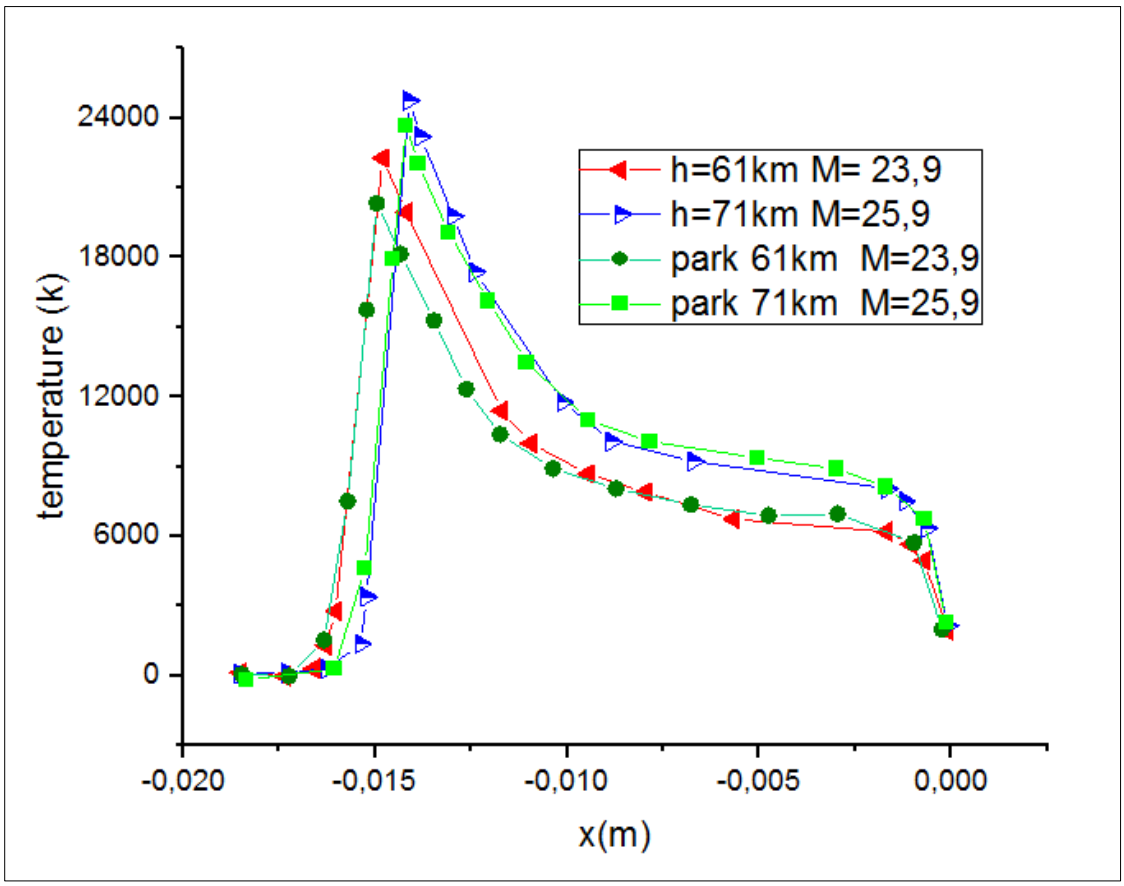

Figure 4-39: Comparison in temperature along stagnation line in different altitude and validation with Park**. [59]**

4.3.7 Results of circular conic body

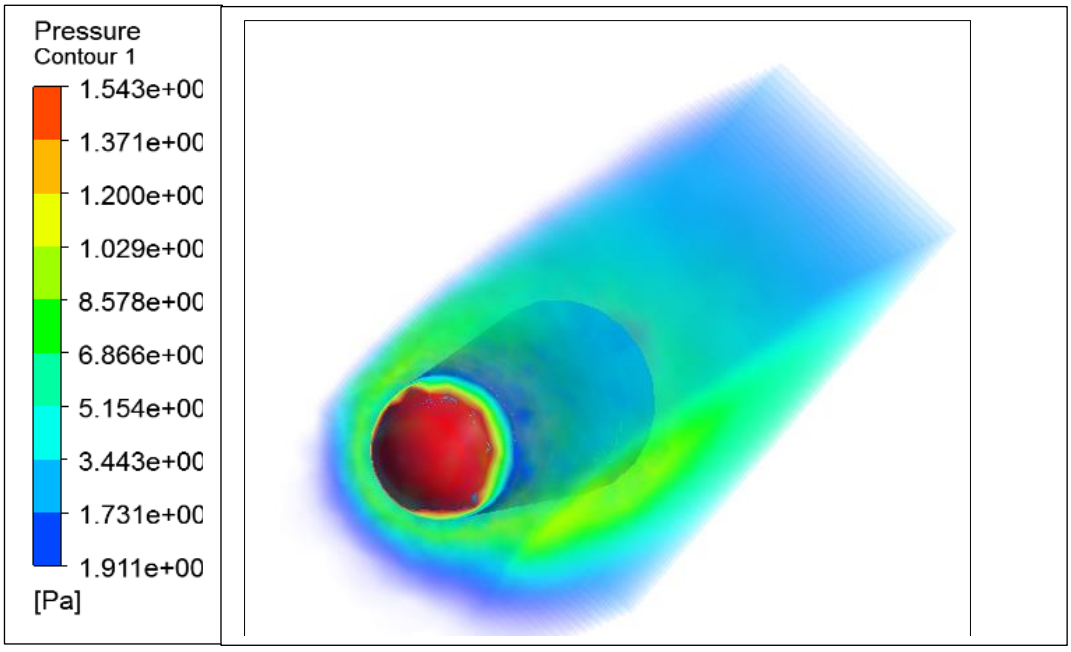

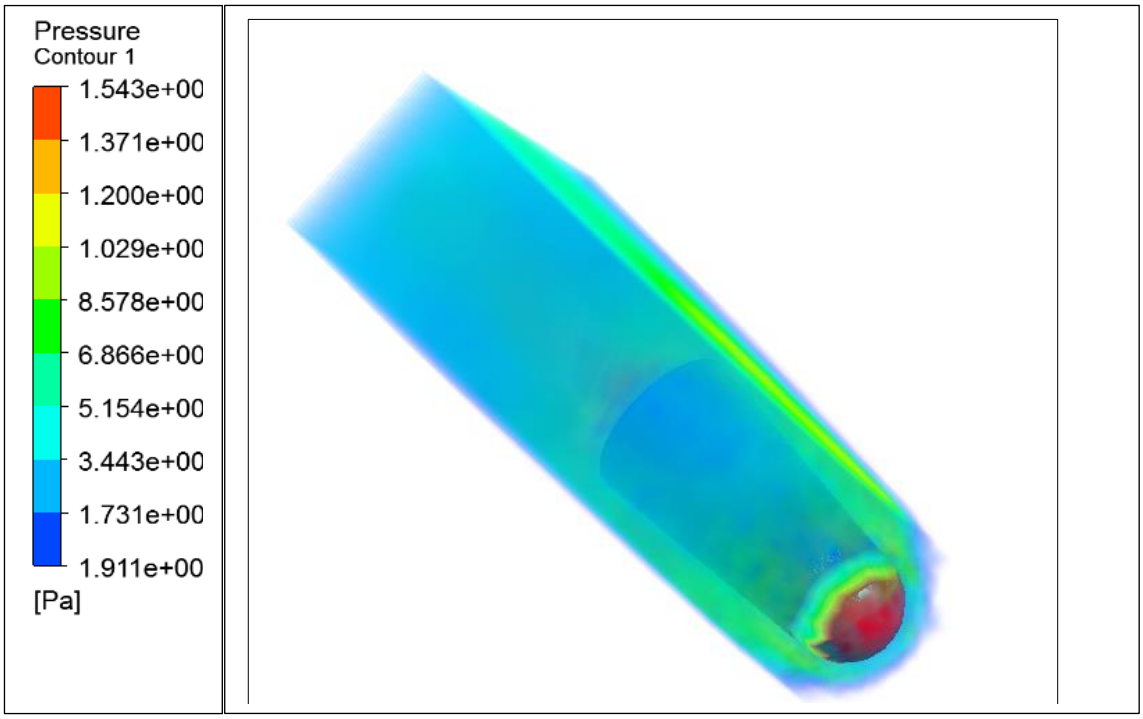

Figure 4-40: Pressure contour along circular conic body in 3D**.**

4.4 Results of capsule fire II

A general overview of the flowfield is presented in **Figs 4.41 and 4.42**, which show contours of translational temperature and pressure in the flowfield. The maximum temperature in the flowfield is around 30, 000 K occurring immediately after the shock wave. Due to dissociation and ionization reactions, the temperature decreases to around 10, 000 K in the shock layer. The pressure contours show the expected blunt body behavior with high pressure at the stagnation region reaching values close to 10, 000 Pa and an expansion around the shoulder of the spacecraft. The 2nd order scheme employed in the numerical calculation makes the contour lines very sharp. [60]

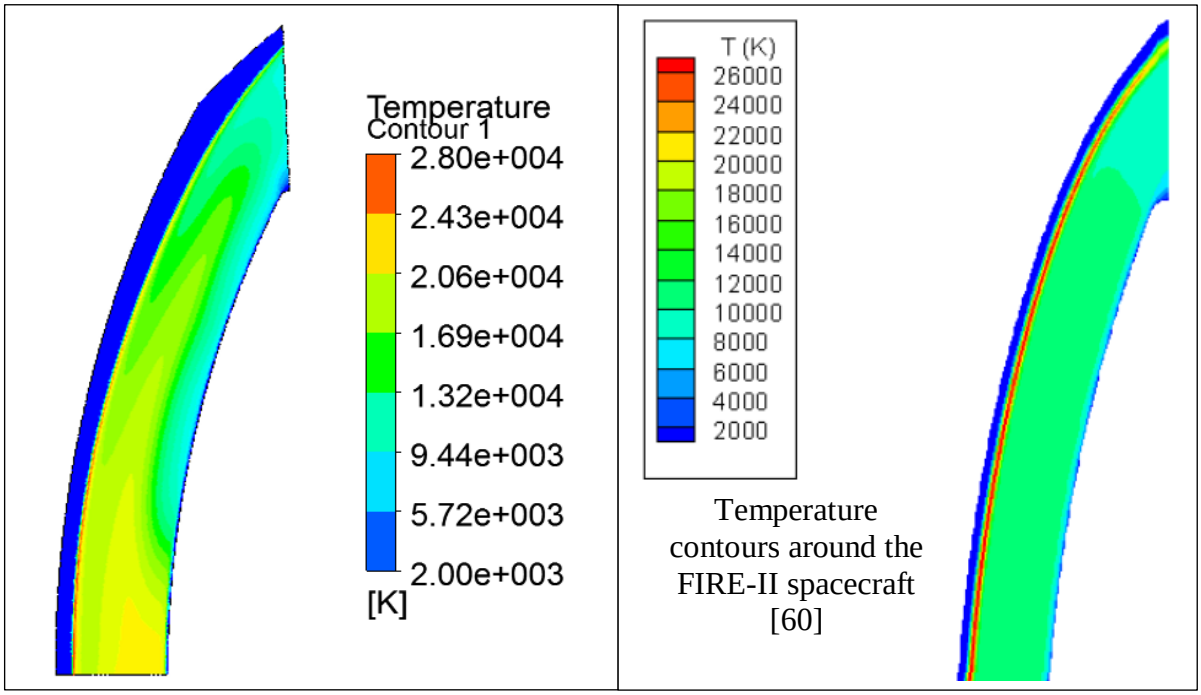

Figure 4-41: Comparison in temperature field along FIRE-II spacecraft between our results and SCALABRIN et al**. [60]**

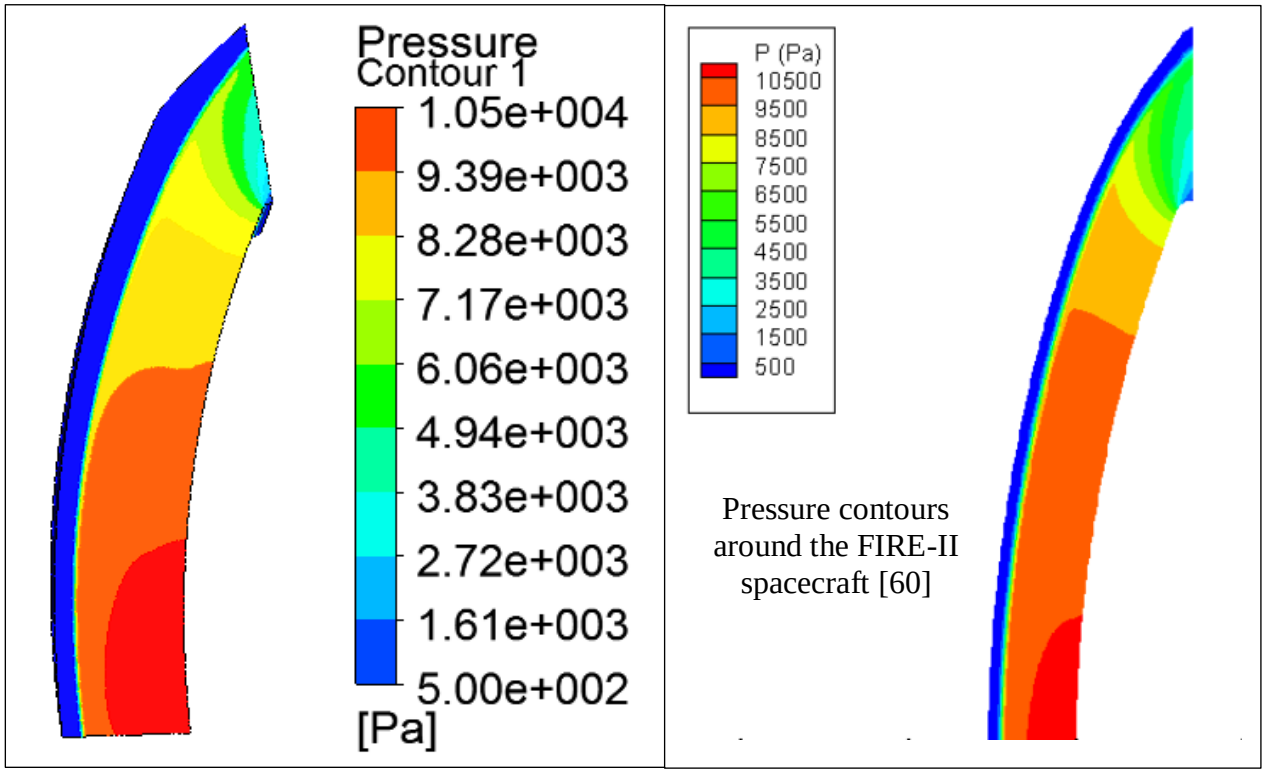

Figure 4-42: Comparison in pressure field along FIRE-II spacecraft between our results and SCALABRIN et al**. [60]**

4.5 Shuttle re-entry

4.5.1 Shuttle Mach number altitude map

Its altitude and velocity profile is shown in graph. A series of hypersonic flow simulations were conducted from mach25 to 0.5mach m/s through the re-entry stage, where the angle of attack was maintained at 40°

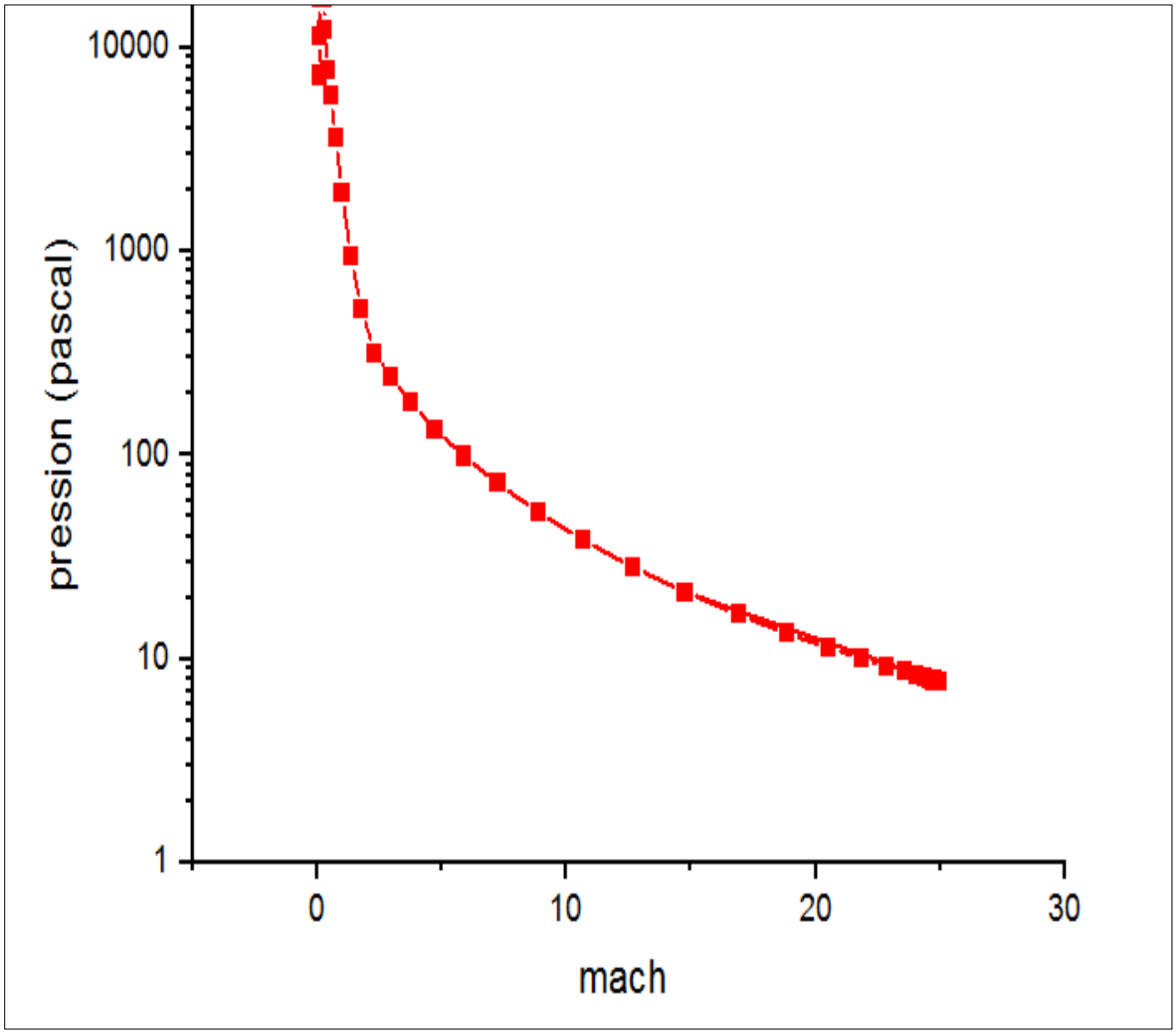

Figure 4-43: Pressure Mach number map**.**

Obtaining the altitude by using the equation

$$p = p_0 \exp\left(-\frac{7g}{2C_p T_0} z\right) \tag{4.1}$$

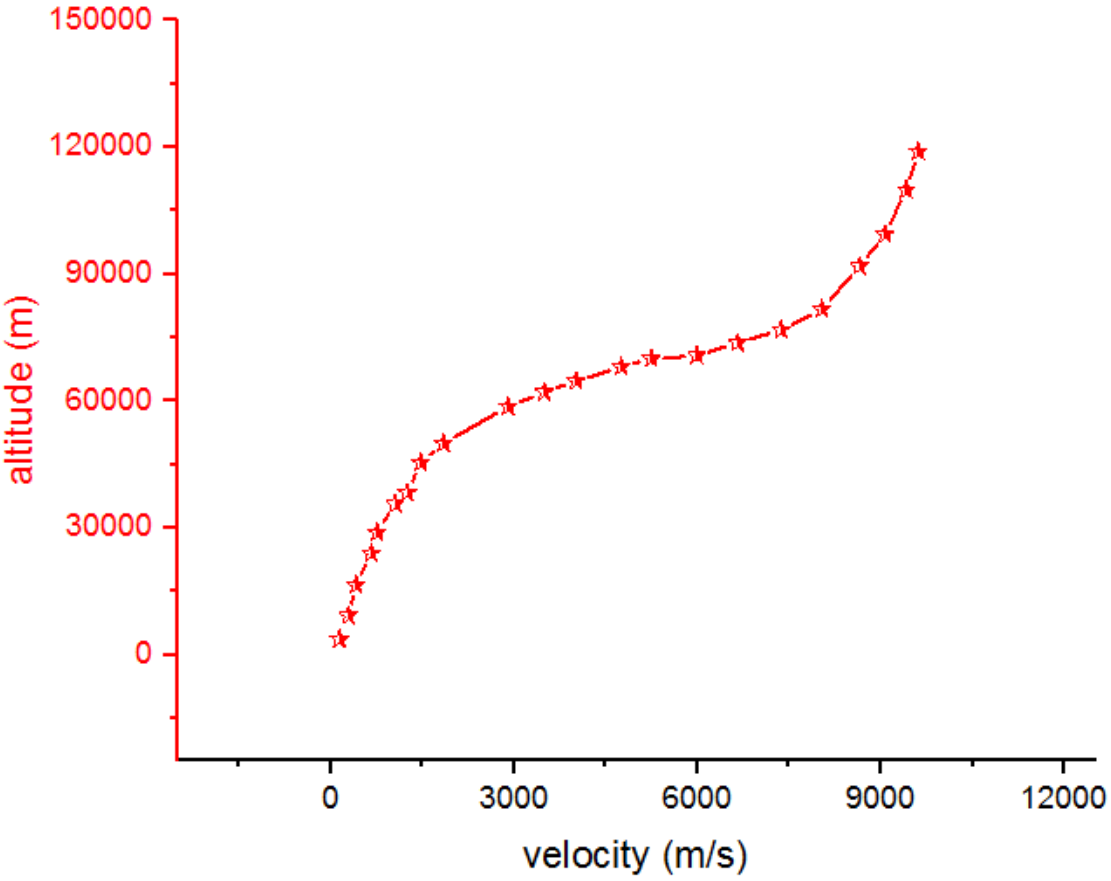

Figure 4-44: Velocity altitude map

4.5.2 Validation

By comparing our result of **Fig 4.45** with that of anderson **[7]**, we notice a good agreement between the two results in terms of pace and in quantitative term with an error of 1.3%

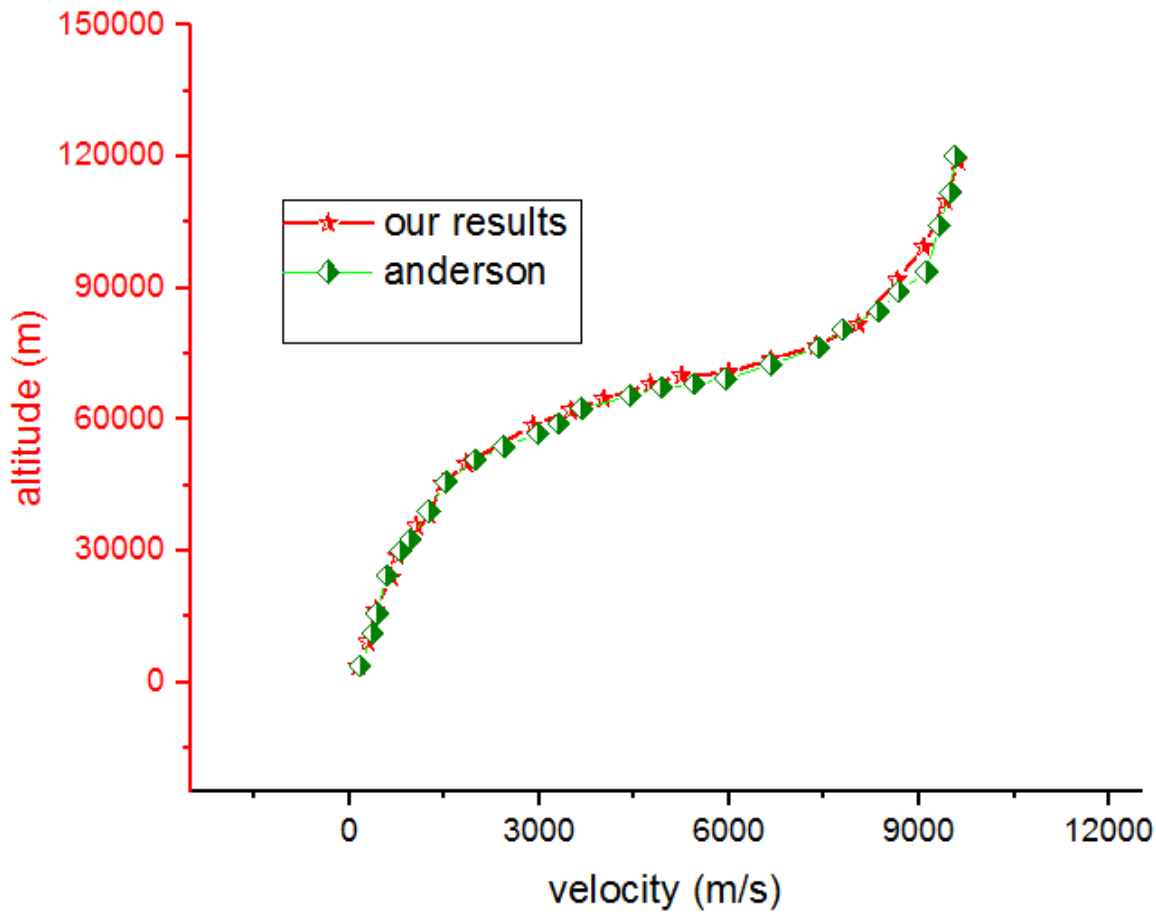

Figure 4-45: Comparison of velocity-altitude map with Anderson results **. [7]**

4.5.3 Altitude temperature velocity map

From this limit, the variation of the temperature changes shape and varies according to the processes of dissociation and ionization, which will take place in the flow **[61], [62] [63]**For example, when the speed is 9 Km/s, the reached temperature is 42829 K, if the speed increases to 14 Km / s the temperature behind the shock has the value of 100626 K. For the first case, the ionization is negligible by against.. In the second case, it is considerable. This is why in equilibrium, and according to Figure 8, we have noticed that the equilibrium temperature is of the order of 8500k for a speed of 9 km/s, against it is of 7300k at the entry speed of 13km/s, these gains in descent time, also in terms of the minimum equilibrium temperature reached due to the dominant ionization phenomenon at these conditions, this result allows us to deduce that the optimal re-entry speed of a spacecraft is about of 13km/s. **[64]**

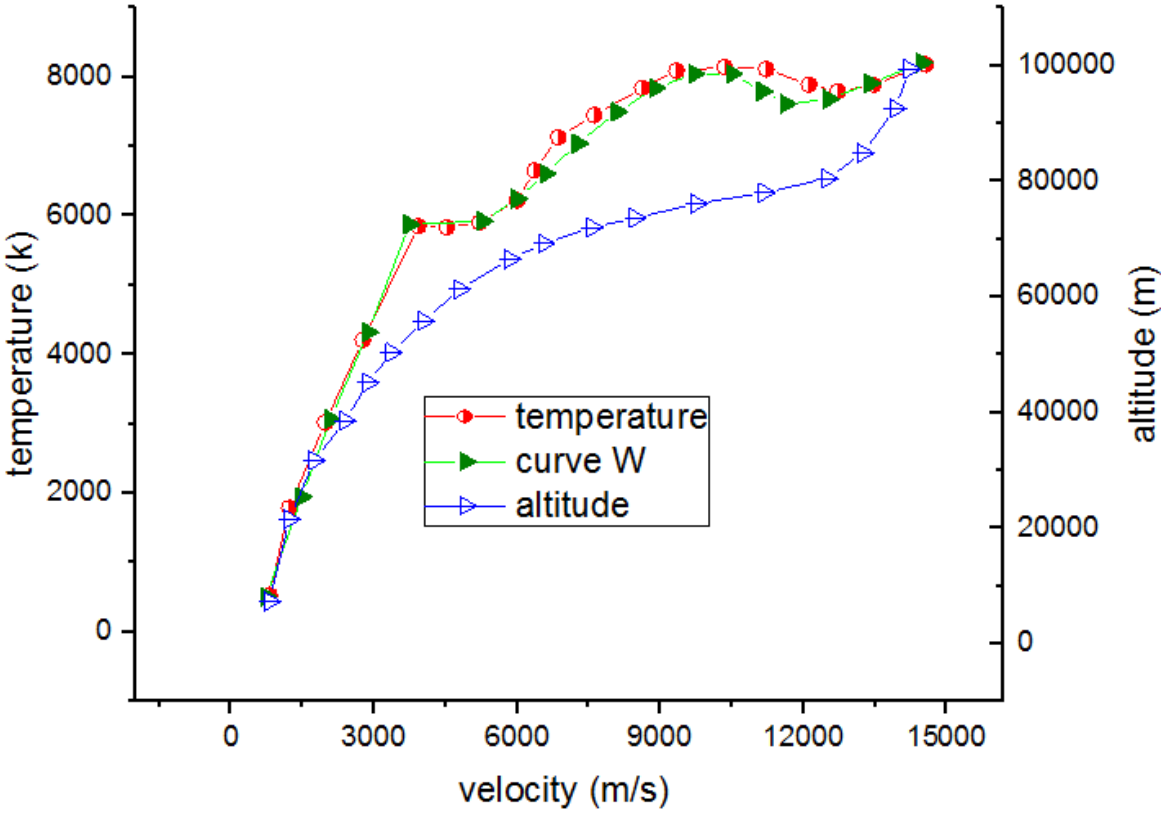

Curve W : velocity temperature map [63]

Figure 4-46: Velocity temperature altitude map**.**

4.5.4 Velocity temperature altitude Reynolds number map

During re-entry, the hypersonic regime is dominating from 120 km to 50 km and often after breakups usually occur during the hypersonic flow phase the early stage of a reentry features high Mach numbers and low Reynolds number where a viscous boundary layer is likely to be observed. At lower altitudes, the flow transitions to a turbulent, flow. As an illustration, Fig. 4.47 shows the transition from laminar to turbulent for a 10-meter object at Reynolds equal to 10^6. The laminar flow at the leading edge of the object transitions into a turbulent further as it moves downstream. The transition to turbulence in hypersonic is still not perfectly understood. It depends on the transition Reynolds number that in turn depends on a large number of flow parameters **[65].** Among them, the Mach number at the outer edge of the boundary layer (M). Studies found that the transition Reynolds number increases with the Mach number for M > 4, implying greater flow stability for hypersonic flows than for slower flow. Other key parameters such as the angle of attack, the environment, the wall temperature, and the object geometry also affect the turbulent transition.

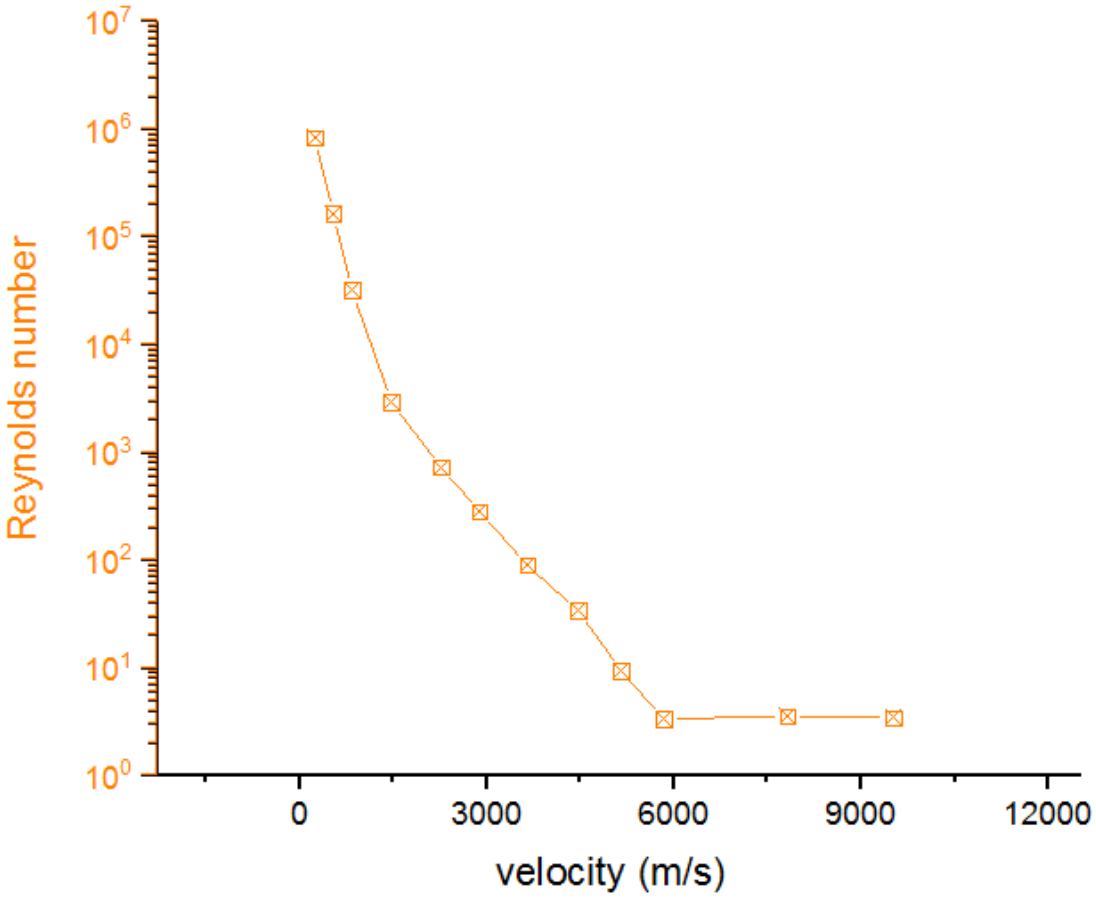

Figure 4-47: Velocity Reynolds number map**.**

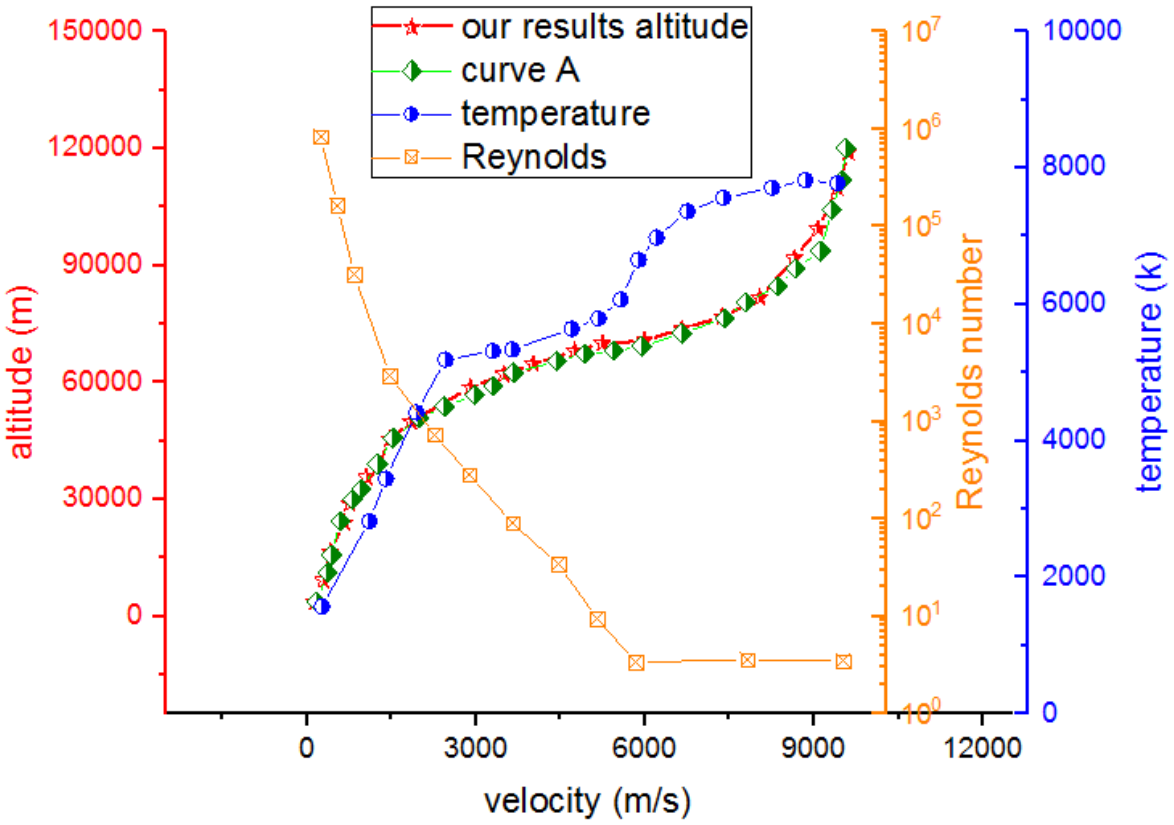

Curve A : Anderson velocity altitude map [7]

Figure 4-48: Velocity temperature altitude Reynolds number map**.**

CONCLUSION

This work devoted to the simulation of a hypersonic flow out of thermochemical equilibrium around a rounded body, encountered in the atmospheric re-entries of spacecraft, this type of flow is governed by the equations of Navier-Stocks coupled with the relaxation equations of physico-chemical phenomena. The fluid being air where it was simulated, in the shock layer, with a mixture of reactive gases, consisting of 11 species reacting with each other according to the Zeldovich and park models with 5, 17, 21, 31 elementary reactions in which a wave of intense shock. Particular attention is focused on the modeling of the chemical and vibrational imbalance taking into account the reaction models and the source terms as well as the different coupling modes.

We presented the study of a viscous two-dimensional and three- dimensional hypersonic flow which is in chemical imbalance around blunt body such as the Lobb sphere. And Cone flare body, conical circular body and capsule fire II with the consideration of turbulence models. This contribution is made using ANSYS 19 software where we focused on the behavior of the reactive flow and the physico-chemical phenomena that arise downstream of the intense shock wave that appears upstream of the obstacle. .

This study reveals and highlights many very important physical aspects for the modeling and simulation of the behavior of a hypersonic flow, these can be summarized in the following:

- The calculation of the flow parameters and the concentrations of the different chemical species are done step by step as a function of time until the state of equilibrium is reached.
- It was noticed that the greater the speed of the craft, the greater the temperature behind the shock and the greater the vibration energy (characterized by the vibration temperature), and among the physico-chemical phenomena that occur behind an intense shock for different flight Mach numbers at a constant altitude, there is a decrease in the temperature of the gas, the vibration of molecules and also other phenomena such as dissociation and ionization, the evolution towards equilibrium depends on the complexity of all these processes and the different exchanges between them.
- The position of the shock wave is localized in relation to the obstacle, this latter is of the order of 0.50 mm (Lobb sphere), result very close to the experimental result, in addition we were able to simulate the behavior of the flow in the relaxation range and determine the various parameters, namely the Mach number, the pressure and temperature field as well as the mass fractions some change. The variation of these parameters is influenced by the creation of the shock wave upstream of the obstacle as

well as by the appearance of physico-chemical phenomena which have an endothermic nature and which form a protective thermal shield of the wall.

- The shock standoff distance of the entry configuration can be reduced by thermochemical reactions but doesn't continue to decrease remarkably when ionization occurs. The increase of flow density after shockwave caused by ionization leads to a smaller shock stand-off distance. The shock stand-off distance calculated by the 11 species model is 4.2% smaller than that calculated by the 5 species model without considering ionization.
- Ionization reduces wall heat flux but increases wall pressure a little. The difference in wall pressures calculated by the 11 species and 5 species models is very small. The wall heat fluxes calculated by the 11 species model are smaller than those calculated by the 5 species model but more consistent with the experiment data.
- Another result of the study allow us to deduce that the optimal re-entry speed of shuttle spacecraft is 13 Km/s

Finally, our results are compared with those of the specialized scientific literature where we notice a good agreement.

Perspective

This study could be the subject of further study through certain perspectives that can be envisaged from different aspects, are those concerning the following points:

- Resume this study by a numerical calculation code OPEN FOAM.
- The study of the interaction between the fluid and the structure, the description of the movements of the structures in contact with the fluid itself in motion and more precisely the determination of how the fluid modifies the behavior of structures.
- Taking into account the phenomenon of radiation.
- Include the influence of the re-entry flight angles γ.

APPENDIX

Park's thermochemical model for a five species neutral air mixture the Park model considers a total of 17 reactions, i.e., 15 dissociation reactions (five for each molecule) and two Zeldovich (exchange).

TABLE A: Thermochemical model table.

Reaction	M	Pre-exponential Factor	Activation energy (j/kgmol)	Tempretture exponent(k)
Dissociation Reaction				
$O2 + M \leftrightarrow 2O$ + M	O	1e+19	4.947e+08	-1.5
	N	1e+19	4.947e+08	-1.5
	NO	1e+19	4.947e+08	-1.5
	$O2$	1e+19	4.947e+08	-1.5
	$N2$	1e+19	4.947e+08	-1.5
N2 + $M \leftrightarrow 2N$ + M	O	3e+19	9.412e+08	-1.6
	N	3e+19	9.412e+08	-1.6
	NO	3e+19	9.412e+08	-1.6
	$O2$	3e+19	9.412e+08	-1.6
	$N2$	3e+19	9.412e+08	-1.6
$NO + M \leftrightarrow O + N$ + M	O	1.1e+14	6.277e+08	0
	N	1.1e+14	6.277e+08	0
	NO	1.1e+14	6.277e+08	0
	$O2$	1.1e+14	6.277e+08	0
	$N2$	1.1e+14	6.277e+08	0
Recombination				
N2 + $O \leftrightarrow NO$ + N		1.8e+11	3.193e+08	0
NO + O $\leftrightarrow N + O2$		2400000	1.598e+08	1

Table B : CHEMICAL KINETICS MODEL OF PARK

.

Reactions	*Energy of reactions (kcal/mole)*	C $Cm^3/mole.\ sec$	*n*	θ_d
Dissociation reactions				
R_1: $O_2 + O \Leftrightarrow O + O + O$	-117.98	*8.25E+19*	-1.00	59500
R_2: $O_2 + N \Leftrightarrow O + O + N$	-117.98	*8.25E+19*	-1.00	59500
R_3: $O_2 + NO \Leftrightarrow O + O + NO$	-117.98	*2.75E+19*	-1.00	59500
R_4: $O_2 + O_2 \Leftrightarrow O + O + O_2$	-117.98	*2.75E+19*	-1.00	59500
R_5: $0_2 + N_2 \Leftrightarrow O + O + N_2$	-117.98	*2.75E+19*	-1.00	59500
R_6: $O_2 + O^+ \Leftrightarrow O + O + O^+$	-117.98	*8.25E+19*	-1.00	59500
R_7: $O_2 + N^+ \Leftrightarrow O + O + N^+$	-117.98	*8.25E+19*	-1.00	59500
R_8: $O_2 + NO^+ \Leftrightarrow O + O + NO^+$	-117.98	*2.75E+19*	-1.00	59500
R_9: $O_2 + O_2^+ \Leftrightarrow O + O + O_2^+$	-117.98	*2.75E+19*	-1.00	59500
R_{10}: $O_2 + N_2^+ \Leftrightarrow O + O + N_2^+$	-117.98	*2.75E+19*	-1.00	59500
R_{11}: $O_2 + e^- \Leftrightarrow O + O + e^-$	-117.98	*1.32E+22*	-1.00	59500
R_{12}: $N_2 + O \Leftrightarrow N + N + O$	-225.00	*1.11E+22*	-1.60	131200
R_{13}: $N_2 + N \Leftrightarrow N + N + N$	-225.00	*1.11E+22*	-1.60	131200
R_{14}: $N_2 + NO \Leftrightarrow N + N + NO$	-225.00	*3.70E+21*	-1.60	131200
R_{15}: $N_2 + O_2 \Leftrightarrow N + N + O_2$	-225.00	*3.70E+21*	-1.60	131200
R_{16}: $N_2 + N_2 \Leftrightarrow N + N + N_2$	-225.00	*3.70E+21*	-1.60	131200
R_{17}: $N_2 + O^+ \Leftrightarrow N + N + O^+$	-225.00	*1.11E+22*	-1.60	131200
R_{18}: $N_2 + N^+ \Leftrightarrow N + N + N^+$	-225.00	*1.11E+22*	-1.60	131200
R_{19}: $N_2 + NO^+ \Leftrightarrow N + N + NO^+$	-225.00	*3.70E+21*	-1.60	131200
R_{20}: $N_2 + O_2^+ \Leftrightarrow N + N + O_2^+$	-225.00	*3.70E+21*	-1.60	131200
R_{21}: $N_2 + N_2^+ \Leftrightarrow N + N + N_2^+$	-225.00	*3.70E+21*	-1.60	131200
R_{22}: $N_2 + e^- \Leftrightarrow N + N + e^-$	-225.00	*1.11E+24*	-1.60	131200
R_{23}: $NO + O \Leftrightarrow N + O + O$	-150.00	*4.60E+17*	-0.50	75500
R_{24}: $NO + N \Leftrightarrow N + O + N$	-150.00	*4.60E+17*	-0.50	75500
R_{25}: $NO + NO \Leftrightarrow N + O + NO$	-150.00	*2.30E+17*	-0.50	75500
R_{26}: $NO + O_2 \Leftrightarrow N + O + O_2$	-150.00	*2.30E+17*	-0.50	75500
R_{27}: $NO + N_2 \Leftrightarrow N + O + N_2$	-150.00	*2.30E+17*	-0.50	75500
R_{28}: $NO + O^+ \Leftrightarrow N + O + O^+$	-150.00	*4.60E+17*	-0.50	75500
R_{29}: $NO + N^+ \Leftrightarrow N + O + N^+$	-150.00	*4.60E+17*	-0.50	75500
R_{30}: $NO + NO^+ \Leftrightarrow N + O + NO^+$	-150.00	*2.30E+17*	-0.50	75500
R_{31}: $NO + O_2^+ \Leftrightarrow N + O + O_2^+$	-150.00	*2.30E+17*	-0.50	75500
R_{32}: $NO + N_2^+ \Leftrightarrow N + O + N_2^+$	-150.00	*2.30E+17*	-0.50	75500
R_{33}: $NO + e^- \Leftrightarrow N + O + e^-$	-150.00	*7.36E+19*	-0.50	75500

REFERENCES

REFERENCES

[1] WALLACE, John M. et HOBBS, Peter V. Atmospheric science: an introductory survey. Elsevier, 2006..

[2] KESHTIBAN, I. J., BELBLIDIA, F., et WEBSTER, M. F. Compressible flow solvers for low Mach number flows—a review. Int. J. Numer. Methods Fluids, 2004, vol. 23, p. 77-103..

[3] J. Anderson, Hypersonic and High-Temperature Gas Dynamics, Virginia: AIAA, 2006..

[4] D. Knight, J. Longo, D. Drikakis, D. Gaitonde, A. Lani, I. Nompelis and et. al, "Assessment of CFD capability.

[5] Sudharsan Thiruvenkadam, “A Computational model to characterize different flow.

[6] MINISCI, Edmondo. Space debris and asteroids (re) entry analysis methods and tools. Glasgow, UK: University of Strathclyde, 2015..

[7] Anderson, “Normal Shock waves , Compressible Fluid Flow”, Second Edition Chapter 3 pp. 88-125, Blacksburg, Virginia, 2019..

[8] SOUBRIE Tristan, « Prise en compte de l’ionisation et du rayonnement dans la modélisation des.

[9] OUCHENE samir, GHENDOUR Nabil, ALLOUCHE Rachid,RENANE Rachid, ”Simulation numérique d’écoulement hypersonique en hors équilibre thermochimique derriere l’onde de choc intense ” . 1st edition ,Université Saad Dahleb Blide institut d’Aéronautique et des étu.

[10] DOMINY, Robert Gerald. Rarefied hypersonic shock wave and blunt body flows. 1987..

[11] W. NIEHAUS , “Heat shield concept and materials for re-entry vehicles part reaction of air to hypersonic flow “,Defence documentation centre , Virginia, July 15, 1963..

[12] DINESH K PRABHU ,”High-temperature effects in hypersonic flows”, Vol. 20 pp.781-814, Division, National Aerospace Labo , Bangalore, India, MS received 31 August 1994; revised 21 January 1995 ..

[13] Eberhard Morgenroth, ,”Characteristic Time NonDimNumbers”, , ETH_SAMM L07.RTD, Institut für Umweltingenieurwiss. in Gujer10/29/2015..

[14] YANG, Jianlong et LIU, Meng. Numerical analysis of hypersonic thermochemical non-equilibrium environment for an entry con? figuration in ionized? ow. Chinese Journal of Aeronautics, 2019, vol. 12..

[15] D'Ambrosio, D., Colonna, G., and Capitelli, M., "Numerical Prediction of Non-Equilibrium Flows in Hypersonic Nozzles: State-to-State Kinetics versus Macroscopic Models," AIAA Paper 2003-3549, 2003..

[16] Sanjeev Kumar, M.Tech." Numerical Simulation of Chemically Reactive Hypersonic Flows", 1st edition A95-95357, European Computational Fluid Dynamics,Germany22. Dezember 2005..

[17] Blottner, F., Johnson, M., and Ellis, M., "Chemically Reacting Viscous Flow-Program for Multicomponent Gas Mixtures," Sandia Labs. TR SC-RR-70-754, Albuquerque, NM, 1971.

[18] Ideen Sadrehaghighi, Ph.D. "Turbulence Modeling",1 edition PhD in Mechanical Engineering , CFD Open Series , Mason, Ohio, États-Unis 200..

[19] CELIK, Ismail B. Introductory turbulence modeling. 1999..

[20] Park, Chul. "The limits of two-temperature kinetic model in air." 48th AIAA Aerospace Sciences Meeting Including the New Horizons Forum and Aerospace Exposition. 2010.

[21] Goodarz Ahmadi , "Introduction to turbulence modelling," , 13699-5725 Department of Mechanical and Aeronautical Engineering, Clarkson University Potsdam, 1994.

[22] Gerald Recktenwald,An ," Introduction to Turbulence Modeling ", edition 4 ,for CFD, Mechanical and Materials Engineering Department Portland State University, Portland, Oregon, February 19, 2020...

[23] L. Cutrone , F. Battista , "Assessment of Wall-functions k−ε Turbulence Models for the Prediction of the Wall Heat Flux in Rocket Combustion Chambers ",80125 Dipartimento di Ingegneria Aerospaziale, DIAS Universita degli Studi di Napoli "Federico II", Pia.

[24] Patrick M.Knupp, "Remarks on Mesh Quality" , NM87185 ,Aerospace Sciences Meeting and Exhibit,7- Sandia National Laboratories,Sandia 10January, 2007..

[25] BROATCH, A., GALINDO, J., NAVARRO, R., et al. Methodology for experimental validation of a CFD model for predicting noise generation in centrifugal compressors. International Journal of Heat and Fluid Flow, 2014, vol. 50, p. 134-144..

[26] BIRD, G. Low density aerothermodynamics. In : 20th Thermophysics Conference. 1985. p. 994..

[27] BIRD, G. Direct simulation of typical AOTV entry flows. In : 4th Thermophysics and Heat Transfer Conference. 1986. p. 1310..

[28] FARBAR, Erin D. Kinetic Simulation of Rarefied and Weakly Ionized Hypersonic Flow Fields. 2010. Thèse de doctorat..

[29] Gallis, M. A., and Harvey, J. K., "Ionization Reactions and Electric Fields in Plane Hypersonic ShockWaves," Progress in Astronautics and Aeronautics, AIAA, New York, 1992..

[30] BARTEL, TIMOTHY et JUSTIZ, CHARLES. DSMC simulation of ionized rarefied flows. In : 23rd Fluid Dynamics, Plasmadynamics, and Lasers Conference. 1993. p. 3095..

[31] JUSTIZ, CHARLES, SEGA, RONALD, DALTON, Charles, et al. A hybrid flow model for charged and neutral particles around spacecraft in Low Earth Orbit. In : 27th Thermophysics Conference. 1992. p. 2935..

[32] BLANCO, Ariel. The Rarefied Gas Electro Jet (RGEJ) Micro-Thruster for Propulsion of Small Satellites. 2017. Thèse de doctorat. University of Florida..

[33] APPLETON, J. P. et BRAY, K. N. C. The conservation equations for a non-equilibrium plasma. Journal of Fluid Mechanics, 1964, vol. 20, no 4, p. 659-672..

[34] BLANCO, Ariel et JOSYULA, Eswar. Numerical modeling of hypersonic weakly ionized external flowfields with Poisson's equation. AIAA Journal, 2020, vol. 58, no 8, p. 3464-3475.

[35] BOTTIN, Benoît. Thermodynamic properties of arbitrary perfect gas mixtures at low pressures and high temperatures. Progress in Aerospace Sciences, 2000, vol. 36, no 7, p. 547-579.

[36] JOSYULA, Eswar. Computation of hypersonic flow past blunt body for nonequilibrium weakly ionized air. In : 23rd Fluid Dynamics, Plasmadynamics, and Lasers Conference. 1993. p. 2995..

[37] LEE, J.-H. Basic governing equations for the flight regimes of aeroassisted orbital transfer vehicles. In : 19th Thermophysics Conference. 1984. p. 1729..

[38] FARBAR, Erin D. Kinetic Simulation of Rarefied and Weakly Ionized Hypersonic Flow Fields. 2010. Thèse de doctorat..

[39] Gnoffo, P. A., Gupta, R. N., and Shinn, J. L., "Conservation Equations and Physical Models for Hypersonic Air Flows in Thermal and Chemi- cal Nonequilibrium," NASA TP 2867, Hampton, VA, 1989..

[40] Landau, L., and Teller, E., “Zur Theorie der Schalldispersion,”Physikalische Zeitschrift der Sowjetunion, Vol. 10, No. 1, 1936,.

[41] Lee, J., “Basic Governing Equations for the Flight Regimes of Aero-Lee, J., “Basic Governing Equations for the Flight Regimes of Aero-Lee, J., “Basic Governing Equations for the Flight Regimes of Aero-Lee, J., “Basic Governing Equations for the Flight Reg.

[42] Bourdon, A., and Vervisch, P., “Electron-Vibration Energy Exchange Models in Nitrogen Plasma Flows,” Physical Review E, Vol. 55, No. 4,1997,.

[43] Alexandra Elbakyan , Hirsch, C. Structured and Unstructured Grid Properties”.Edition 42(249-277 chapter 6 ,Numerical Computation of Internal and External Flows, Elbakyan, 2007..

[44] Francois Duchaine, ”Génération du maillage structuré par Krigeage avec raffinement Francois Duchaine, ”Génération du maillage structuré par Krigeage avec raffinement Francois Duchaine, ”Génération du maillage structuré par Krigeage avec raffinement.

[45] ANSYS, Inc. Chapter 15. ”Reporting Mesh Statistics” , Technology Drive, April 15 2008.

[46] M. Cevdet Celenligil and James N. Moss, “Hypersonic rarefied flow about a delta wing - direct simulation and comparison with experiment”, Vol 30 N8 edition, NASA Langely research center, ,Hampton Virginia ,Augest 1992..

[47] A BOULAHIA,”Couche Limite hypersonique dans des écoulements visqueux en déséquilibre chimique” 1er edition,thèse de Doctorat, département physique, Université Mentouri, Constantine 2010..

[48] "ANSYS Help14.5"ANSYS Computing Platform Support Summary , Irvine October 2012.

[49] Jun Hyeok Chae, , Tapan K. Mankodi, , Seong Man Choi ,, Rho Shin Myong ,”Combined Effects of Thermal Non-equilibrium and Chemical Reactions on Hypersonic Air Flows Around An Orbital Re-entry Vehicle”, edition 4,International Journal of Aeronautical 2022.

[50] Paolo Baiocco, “PRE-X experimental re-entry lifting body design of flight test experiments for critical aerothermal phenemena”, edition 18 Saint-Médard-en-Jalles Cedex, France,2019..

[51] DR R.Kennethlobb," Experimental measurement of shock detachment distance on sphere fired in air at hypervelocity's".133 edition In W. C. Nelson, editor, Proc. of the AGARD-NATO in The High Temperature Aspect of Hypersonic Flow. Pergamum Press, 1962.

[52] V. Joly, F. Coquel, C. Marmignon, W. Aretz, S. Metz, and H. Wilhelmi. "Numerical modelling of heat transfer and relaxation in nonequilibrium air at hypersonic speeds". La Recherche Aerospatiale, Aachen university ,1994.

[53] G. Tchuen,. "Modélisation et simulation numérique des écoulements a haute enthalpie : influence du déséquilibre électronique". See also AIAA paper 2004–2462, PhD thesis, Université d'Aix-Marseille I, 2003..

[54] Paolo Baiocco, "PRE-X experimental re-entry lifting body design of flight test experiments for critical aerothermal phenemena", edition 18 Saint-Médard-en-Jalles Cedex, france,2019..

[55] Ideen Sadrehaghighi, Ph.D. "Turbulence Modeling",1 edition PhD in Mechanical Engineering , CFD Open Series , Mason, Ohio, États-Unis 2006..

[56] SANSON, Francois. On-ground risk estimation of reentering human-made space objects. 2019. Thèse de doctorat. Université Paris Saclay (COmUE)..

[57] TCHUEN, Ghislain, BURTSCHELL, Yves, et ZEITOUN, David E. Numerical study of non-equilibrium weakly ionized air flow past blunt bodies. International Journal of Numerical Methods for Heat & Fluid Flow, 2005, vol. 15, no 6, p. 588-610.

[58] J. Muylaert, L. Walpot, J. Häuser, P. Sagnier, D. Devezeaux, O. Papirnyk, D.Lourme, Standard model testing in the European high enthalpy facility F4 and extrapolation to flight, AIAA 1992-3905, 1992..

[59] C. Park, Nonequilibrium Hypersonic Aerothermodynamics, Wiley, New York,1990..

[60] SCALABRIN, Leonardo C. Numerical simulation of weakly ionized hypersonic flow over reentry capsules. 2007. Thèse de doctorat. University of Michigan, USA..

[61] J. M. Lamet. Transferts radiatifs dans les écoulements hypersoniques de rentrée atmosphérique terrestre » Thèse Docto-rat de L École Centrale Paris 21 Septembre 2009..

[62] T. Thierry et al Coarse-grain model for internal energy excitation and dissociation of molecular nitrogen. Chemical Physics. Volume 398, 4 April 2012, Pages 90-95..

[63] C. Park. Assessment of Two- Temperature Kinetic Model for Ionizing Air. NASA Ames Research Center, Moffett Field, California. JULY 1989.

[64] ALLOUCHE, Rachid, RENANE, Rachid, et HAOUI, Rabah. Prediction of the optimal speed of an aerospace vehicle by aerothermochemical analysis of hypersonic flow during atmospheric re-entry. Mechanics & Industry, 2020, vol. 21, no 2, p. 208.

[65] J. Anderson Jr, Hypersonic and High Temperature Gas Dynamics. AIAA Publications, AIAA, Reston, VA, 2000.